Research Frontiers 2018

SPring-8
SACLA

ISSN 2433-5126
SPring-8 Document D2019-006

SPring-8/SACLA
Research Frontiers 2018

CONTENTS

Reviews

Life Science

Physical Science

Chemical Science

Earth & Planetary Science

Industrial Applications

Note: The principal publication(s) concerning each article is indicated with all author's names in italics in the list of references.

PREFACE

I am Yoshiyuki AMEMIYA, who took over the role of the president of JASRI on June 17, 2019. I am very grateful to Dr. Yoshiharu DOI, the previous president, who guided JASRI with his prescient leadership for six years. I am fully determined to make every effort to serve JASRI so that it can continue fulfilling its responsibility of operating two world-leading accelerator-based light sources, SPring-8 and SACLA, located on the same campus, whose synergy produces groundbreaking results.

It is my great pleasure to publish this volume describing the activities of SPring-8 and SACLA in 2018. SPring-8 (Super Photon ring 8 GeV) welcomed over 17,000 users in 2018 who came to perform more than 2,000 experiments. Currently, SPring-8 users are publishing over 1,000 research papers per year. SACLA users published over 50 research papers in 2018. The ratio of papers in the top 1% of the citation index was as high as 4.3% for the papers published by SACLA users in 2017.

A number of SPring-8 and SACLA users were awarded prestigious prizes in 2018 and 2019 for their achievements in science and technology. Professor Makoto Fujita (The University of Tokyo) was awarded the Imperial Prize and Japan Academy Prize in 2019 for his achievement in the development of an X-ray structural determination technique that does not require crystallization. Following Professor Chikashi Toyoshima of The University of Tokyo in 2018, it is remarkable that SPring-8 users were successively awarded this most prestigious award in Japan. Professor Eiichi Takahashi (Tokyo Institute of Technology) was awarded the Medal with Purple Ribbon in Fall 2018 for his achievements in earth science. Professor Rie Umetsu was awarded the Saruhashi Award for her study on the physical properties of Heusler-type functional magnetic materials including half-metal-type magnets. This award is given to just one female Japanese scientist every year who is conducting outstanding research.

In this volume, two comprehensive reviews are reported by the groups of Professor Kiyoshi Ueda (Tohoku University) and Professor Stuart Hopper (Monash University). Active users of SPring-8 have also contributed the essence of their results as review articles in this volume. In addition, six articles are provided by active users of SACLA.

As part of its efforts to promote leading-edge sciences in Japan, SPring-8 has been collaborating with ESICMM (Elements Strategy Initiative Center for Magnetic Materials) over the past several years. In this project, a superconducting magnet was installed at BL25SU, and magnetic domains in a fractured surface of a Nd-Fe-B permanent magnet were studied at submicron spatial resolution. The article by Billington *et al.* in this issue describes this study, which may lead to the development of more powerful magnets in future.

I am very grateful to the many authors and experts who contributed their papers to this volume. Special thanks are due to Dr. Naoto Yagi and the members of the editorial board for their continuous efforts.

Y. Amemiya

Yoshiyuki Amemiya
President
Japan Synchrotron Radiation Research Institute (JASRI)

EDITOR'S NOTE

This is the 2018 issue of SPring-8/SACLA Research Frontiers that covers outstanding scientific outcomes of SPring-8 and SACLA in 2017 and 2018. The best scientific achievements are collected from more than 1,000 papers published using SPring-8 and SACLA each year.

There are two reviews in this issue. One is contributed by Professor Ueda and Dr. Fukazawa of Tohoku University. Professor Ueda has a long experience in synchrotron radiation science, particularly in atomic and molecular physics using soft X-rays. He has been an active user of soft X-ray beamlines at SPring-8, but since SACLA became in operation, he has been leading gas phase experiments using intense femtosecond pulses of SACLA. In such experiments, atoms are ionized by losing electrons in their inner shells, causing many interesting, previously unobserved phenomena within femtoseconds. These are experiments made possible only by using XFEL. This is a very fundamental research, but as long as we use intense X-rays as a measuring probe, it is always relevant.

The second review is contributed by Professor Hooper and Dr. Kitchen of Monash University, Australia, and Dr. Pearson of National Cerebral and Cardiovascular Center Research Institute, Osaka. Using propagation-based phase contrast imaging of newborn rabbits, the group have been working on the mechanisms of breathing immediately after birth, which led to a proposal of a new resuscitation method. They have also been developing new medical imaging techniques (see Kitchen *et al.* in this issue). This review focuses on the change of blood circulation after birth. Since oxygen, which is obtained through the placenta in utero, must be obtained in the lungs, blood circulation changes drastically after birth. However, how this is brought about has not been well understood. In recent experiments, they combined phase contrast imaging and angiography to visualize air and blood circulation simultaneously in the lungs. They discovered that the presence of gas in the lungs sends a signal to the brain to alter circulation. This finding is important for understanding various phenomena and anomalies that take place after birth in humans. Recently, Prof. Hooper was made a "Member of the Order of Australia" (AM) for his significant service to medical research in the field of fetal lung and cardiorespiratory development.

In this issue, I would like to particularly mention an article on an exotic insect found in Brazil. "Hidden morphological novelty enabling the evolution of female penis in the sex-role reversed cave insects" by Drs. Yoshizawa and Blanke is very interesting research in insect biology that sheds light on the evolution of an unusual insect. This work received an Ig Nobel Prize in 2017. Although the Ig Nobel Prize is conferred to "research that makes people LAUGH and then THINK," there is not much to laugh about in this article. High-resolution CT revealed interesting features of anatomy and gave clues towards the understanding of the curious path of evolution of the insect.

SPring-8/SACLA Research Frontiers is made of two parts. The first is scientific results (Scientific Frontiers) and the second is additional information on hard and soft infrastructures that support scientific research. Although some important numbers such as the operation time are given in the second part, other information and more complete statistical numbers on the operation of SPring-8 and SACLA are available on the website so that more updated information can be accessed (http://www.spring8.or.jp/en/about_us/spring8data/).

The full text of SPring-8/SACLA Research Frontiers is also available on the SPring-8 website (http://www.spring8.or.jp/). For the list of publications produced by SPring-8 users and staff, please visit the publication database at http://www.spring8.or.jp/en/science/publication_database/.

On behalf of all the editors, I would like to thank those who helped us by recommending excellent research results suitable for publication in this issue, and the users and staff of SPring-8 who contributed their reports to this issue.

Naoto Yagi
Japan Synchrotron Radiation Research Institute (JASRI)

EDITORIAL BOARD

SCIENTIFIC FRONTIERS

Ultrafast dynamics in atoms, molecules, and clusters induced by an XFEL pulse

In early 2012, an X-ray free-electron laser (XFEL) facility, the SPring-8 Angstrom Compact free electron LAser (SACLA) [1], started user operation in Japan. Intense pulses generated by SACLA, together with advanced imaging and spectroscopic techniques, have opened new avenues to solve new structures and to observe structural changes in any form of matter with an unprecedented combination of spatial and temporal resolutions. One of the promising studies using XFELs may generally be single-shot X-ray imaging based on the "before destroy" concept. However, target samples should be affected by ultrafast reactions occurring during XFEL pulse exposure. To utilize XFEL for "before destroy" imaging, it is indispensable to understand what happens in the matter during XFEL pulse exposure. The ultrafast reaction dynamics in atoms, molecules, and atomic clusters in the gas phase are not only fundamentally interesting but also fundamentally important for this purpose. Thus, we have been investigating the ultrafast reaction dynamics in atoms [2], molecules [3,4], and clusters [5,6,7] irradiated by XFEL pulses. In this article, we review some of our investigations that we carried out at SACLA during its first five years.

Experiment

A series of experiments have been carried out at SACLA **BL3** [8]. An XFEL beam was focused by a Kirkpatrick-Baez mirror system to a focal point of ~1 μm (FWHM) diameter. Target samples were introduced into a reaction chamber as a supersonic gas beam. XFEL pulse energies were measured by the beam position monitor located upstream of the beamline. The relative X-ray pulse energy passing through the interaction point was also measured shot-by-shot by a PIN photodiode.

Ions and electrons emitted from the gas-phase samples irradiated by very intense XFEL pulses were detected by the momentum spectrometers developed specifically for such XFEL experiments. Details of our setups are described in [9]. In brief, ions generated in the reaction volume were extracted towards an ion time-of-flight (TOF) spectrometer equipped with microchannel plates (MCPs) and a delay-line anode (RoentDek HEX80). Signals from the delay-line anode and MCPs were recorded by a digitizer and analyzed by a software discriminator. The arrival time and arrival position of each ion were determined. Three-dimensional momenta of individual ions were calculated using the detected position and TOF information of each ion. Electrons generated in the reaction volume were extracted towards a velocity map imaging (VMI) spectrometer equipped with MCPs and a phosphor screen. Electron detection images on the phosphor screen were recorded using a CCD camera synchronized with the arrival of the XFEL pulse in the interaction chamber. The measured two-dimensional projection allows us to obtain the momentum distributions of the ejected electrons using the inverse Abel transformation.

Multiphoton multiple ionization dynamics in xenon atom

Figure 1 depicts the charge state distribution of Xe ions generated by irradiating Xe atoms with an XFEL pulse at a photon energy of 5.5 keV and a peak fluence of 47 μJ/μm^2 [2]. We compared the theoretical charge state distributions at this peak fluence with the experimental distributions. The photon energy of 5.5 keV is above the L-shell threshold for charge states of up to +23 according to the calculations [2]. Thus, direct two-photon ionization barely contributes to charge formation because not only is its cross section very small but also one-photon ionization is always available up to +23. There is no apparent signature of resonance-enabled ionization enhancement because the fluence is insufficient to

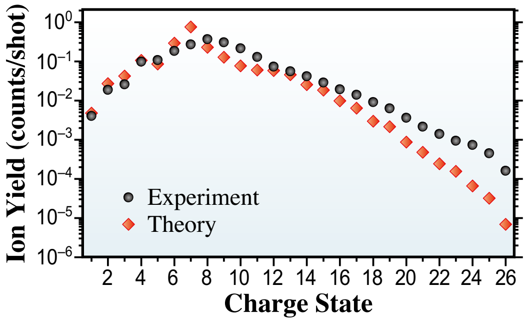

Fig. 1. Experimental and theoretical charge state distributions of Xe at a photon energy of 5.5 keV. The peak fluence is 47 μJ/μm^2. [2]

form high charge states that involve resonance excitation. The discrepancy between theory and experiment may be attributed to the nonrelativistic treatment and lack of shake-off in the current theoretical model. The shake-off process can further ionize valence electrons after photoionization, and some decay channels might be absent without relativity. The inclusion of both relativity and shake-off tends to produce higher charge states. In spite of these limitations, the theoretical results are in reasonable agreement with experimental results, at least semiquantitatively.

The charge state distribution varies with the peak fluence. The peak fluence dependence of the ion yield for each charge state indicates contributions from multiphoton processes. According to the peak fluence dependence and theoretical calculations, the observed high charge states with ≥ 24 are produced via five-photon absorption. Understanding of the ionization dynamics of heavy atoms exposed to intense XFEL pulses will provide us with useful input for future molecular imaging experiments using XFELs.

Charge and nuclear dynamics in iodine-containing molecules

In the case of the irradiation of molecules by XFEL pulses, in addition to multiphoton absorption and charge buildup we observed in atoms, charge redistribution and bond rupture occur, resulting in the generation of several ions from a single molecule. Ions released from a single molecule must have a momentum correlation. As the first molecular sample, we used the iodomethane (CH_3I) molecule, which is the smallest organic molecule that contains a heavy iodine atom. Figure 2 depicts an example of correlations between the momenta of C^{n+} and I^{m+} released from CH_3I irradiated by an XFEL pulse [3]. The photon energy was 5.5 keV and the peak fluence was 26 μJ/μm^2. Here, the momentum correlation coefficient k_{mn} is the average ratio of the momenta of C^{n+} and I^{m+}. The experimental results are well reproduced by a simple Coulomb explosion model with a few physically meaningful empirical constants that account for the concerted dynamics of nuclear motion *vs* charge creation and redistribution. According to the results of model calculations, we found that it takes ~9 fs for the charge to be created at the iodine site, while it takes ~3 fs for the charge to be redistributed among the molecules. Also, we found that the C–I bond length increases by ~10%, whereas the C–H bond distance increases by a factor of three in 10 fs. In this way, the electron and nuclear motions during XFEL pulse exposure can be captured.

As the next target sample, we adopted a larger molecule, 5-iodouracil ($C_4N_2O_2H_3I$, 5IU) [4]. 5IU is an iodine-substituted molecule of uracil, which is one of the RNA bases. Thus, 5IU is considered to be the smallest building block of biomolecules. Figure 3 depicts momentum correlations among three ions released from 5IU. To observe the correlations, a triple product was calculated from the observed momenta, giving the cosine of the polar angle:

$$\cos(\varphi) = \frac{(\boldsymbol{p}_{\mathrm{A}} \times \boldsymbol{p}_{\mathrm{B}}) \cdot \boldsymbol{p}_{\mathrm{C}}}{|\boldsymbol{p}_{\mathrm{A}} \times \boldsymbol{p}_{\mathrm{B}}||\boldsymbol{p}_{\mathrm{C}}|},$$

where $\boldsymbol{p}_{\mathrm{A}}$, $\boldsymbol{p}_{\mathrm{B}}$, and $\boldsymbol{p}_{\mathrm{C}}$ are the momentum vectors of ions A, B, and C, respectively. The experimental distributions, denoted as $SP_3(A,B,C)$, are depicted in the left column of Fig. 3. Note that the distribution function SP_3 for three randomly oriented and uncorrelated vectors is flat against $\cos(\varphi)$ and thus the curves presented directly reflect the deviation from isotropic emission. Coulomb explosion, when it occurs preferentially in the plane, results in the distributions of $SP_3(A,B,C)$ peaked at $\cos(\varphi) = 0$. As seen in the figure, the combinations $SP_3(I^{q+},H^+,X)$, where X stands for H^+, O^+, N^+, or C^+. I^{q+}, H^+, N^+, and O^+, tend to be ejected preferentially in the plane, but this is not necessarily the case for C^+. The discrepancies between the experimental and simulated $SP_3(I^{q+},H^+,C^+)$ for high q are probably due to the existence of molecular and neutral fragments, which are not considered in the simulation.

To interpret the experimental results and quantify the underlying dynamics, we carried out classical molecular dynamics (MD) simulations of Coulomb explosion within a parametric model of charge buildup and redistribution. Good agreement between the experimental and simulation results was found when selecting the internal temperature, charge buildup time, and charge redistribution rate of 300 K, 10 fs, and 0.5 fs^{-1}, respectively. The simulation results are shown in the right column of Fig. 3. The time dependence of

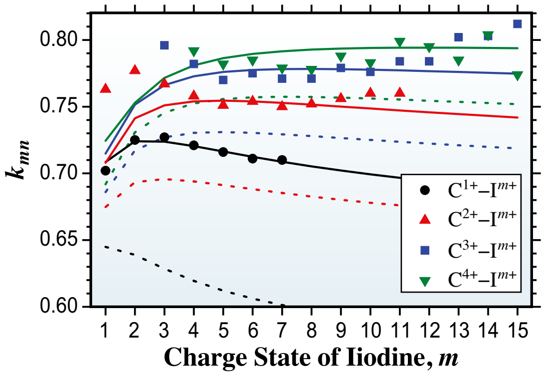

Fig. 2. Momentum correlation coefficient k_{mn} for I^{m+}–C^{n+} coincidences at a photon energy of 5.5 keV. The peak fluence is 26 μJ/μm^2. [3]

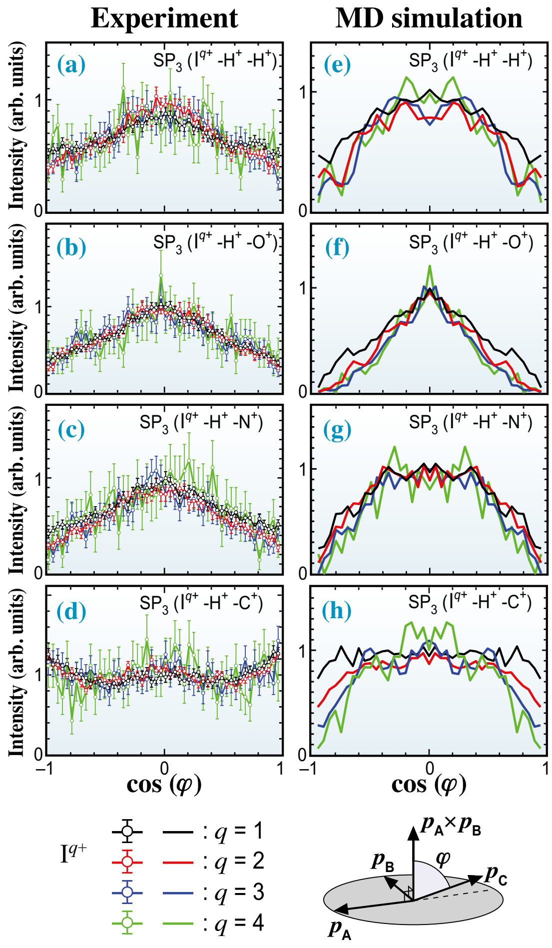

Fig. 3. Distributions of normalized scalar triplet products of momentum vectors SP$_3$(A,B,C) plotted as a function of cos(φ). Black, red, blue, and green lines indicate q = 1, 2, 3, and 4, respectively. [4]

the interatomic distances, deduced from the MD simulations, suggests that within 10 fs, the displacements are large for hydrogens and are considerably smaller, within 10% of the bond length variation, for other heavier atoms.

Nanoplasma dynamics in atomic clusters

It is known that nanoplasma is formed when clusters (i.e., atomic or molecular aggregates) are irradiated by intense lasers with longer wavelengths, e.g., near infrared (NIR) lasers. What will happen to clusters exposed to intense XFEL pulses? Figure 4 depicts the electron spectra of Ar clusters with different average cluster sizes <N> exposed to an XFEL pulse at a photon energy of 5 keV [5]. The peak fluence of the XFEL pulses was ~50 μJ/μm^2. In the spectrum for <N>~100, we can identify the broad peak around 150–250 eV due to the LMM Auger electrons emitted after the KLL Auger process. The intensity of electron emission below 150 eV increases with the cluster size. This trend is interpreted in the following manner, with the help of theoretical calculations that reproduce the experimental spectra as shown in Fig. 4. The discrepancies between the experimental and theoretical spectra, caused by the uncertainties of the cluster size and size distributions, do not affect the following discussion. When the cluster is exposed to intense XFEL pulses, atoms in the cluster are ionized by photoionization and subsequently proceeding Auger decays. The charge state of the cluster increases with the number of ionized atoms. As a result, the LMM Auger electrons are decelerated by the positive potential from the highly charged cluster and form a plateau in the electron spectra. The decelerated electrons are eventually trapped by the cluster ions. The LLM Auger electrons and the secondary electrons produced by the low-energy electron impact are also trapped. As a result, we expect that a nanoplasma is formed. The peak at zero kinetic energy is due to thermal emission, which is evidence of nanoplasma formation. Note that nanoplasma formation can always occur whenever matter is exposed to an intense XFEL pulse.

For further investigation, we employed pump–probe measurements using the XFEL pulse as a pump and the NIR laser pulse as a probe [7]. To observe ultrafast phenomena, we used an arrival timing monitor [10] to compensate for the temporal jitter between the two laser pulses. Time-resolved yields of ions released from Xe clusters (<N>~5000) were measured. The photon energies of the XFEL and NIR laser pulses were 5.5 keV and 1.5 eV, respectively. The peak fluences of the XFEL and NIR laser pulses were 30 μJ/μm^2 and 15 nJ/μm^2, respectively.

Figure 5 depicts Xe$^+$ and Xe^{2+} yields as a function of pump–probe delay. Let us first focus on the Xe^{2+} yield [7]. In Fig. 5, a gradual increase in Xe^{2+} yield with the time delay can be observed. The electrons in

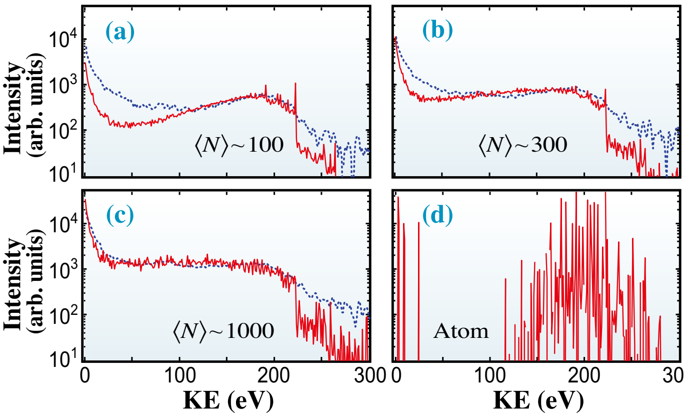

Fig. 4. Electron spectra of Ar clusters at a photon energy of 5 keV. The peak fluence was ~50 μJ/μm^2. Blue dotted lines are the experimental results and red solid lines are the corresponding theoretical results. [5]

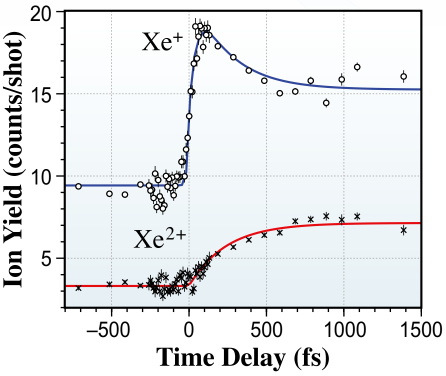

Fig. 5. Xe$^+$ and Xe^{2+} yields as a function of the time delay of the NIR-probe pulse (1.5 eV) with respect to the XFEL-pump pulse (5.5 keV). The peak fluences of the XFEL and NIR laser pulses were 30 μJ/μm^2 and 15 nJ/μm^2, respectively. [7]

the nanoplasma produced by XFEL irradiation acquire kinetic energy from the additional NIR laser field and further ionize neutral Xe to Xe$^+$ and Xe$^+$ to Xe^{2+} by collisional ionization processes. The gradual increase in Xe^{2+} yield indicates the following. Quasi-free electrons in the nanoplasma are so dense that they shield the electric field inside the nanoplasma when the nanoplasma is formed. Then, the electron density decreases with time owing to the nanoplasma expansion. With the decrease in electron density, the nanoplasma starts to absorb NIR light more efficiently via the surface plasmon resonance effect.

In contrast to the gradual increase in Xe^{2+} yield, the Xe$^+$ yield shows a sharp rise at a time delay of zero, followed by a slower decrease as a function of the time delay. This behavior indicates that the NIR pulse probes another much faster process, which is the transient population of highly excited states of neutral atomic fragments that can be ionized by the NIR pulse. The highly excited states are populated during the XFEL pulse of 10 fs. Such a short time indicates that the excitations are created during nanoplasma formation and not afterwards when they can be produced by, for example, the three-body recombination of quasi-free plasma electrons. The most probable mechanism is the inelastic scattering of the Auger electrons emitted during the initial cascade from neutral atoms in a cluster. The population of neutral excited states is expected to be depleted by a variant of interatomic Coulombic decay (ICD) in which two excited atoms exchange energy, ionizing one of them and deexciting the other. As many highly excited xenon atoms are created in the cluster, a cascade of such ICD processes is expected. The present experiments allow us to gain a fundamental insight into the ultrafast reactions induced by XFEL pulses, which should also be of crucial relevance for the use of XFEL pulses to determine the structure of nanosize objects "before destroy." The present femtosecond time-resolved method is versatile and can be widely applied to study electron and nuclear dynamics induced by the interaction of hard XFEL pulses with any form of matter.

Chemical dynamics in the atomic clusters

When clusters are irradiated by an XFEL pulse with relatively low fluence, a series of oligomer formations, i.e., chemical dynamics triggered by X-rays, are observed.

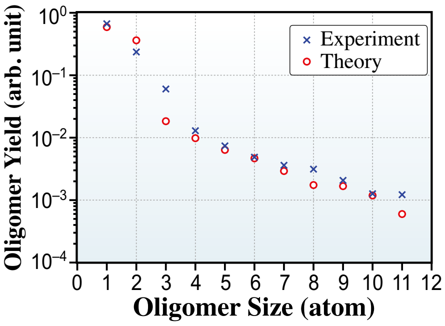

Fig. 6. Ar fragment yield as a function of the oligomer size at the photon energy of 5.5 keV and a peak fluence of 4.1 μJ/μm^2. [6]

Figure 6 depicts the yield of fragments from an Ar cluster ($\langle N \rangle \sim 1000$) as a function of the oligomer size at a photon energy of 5.5 keV and a peak fluence of 4.1 μJ/μm^2 [6]. Using a dedicated molecular dynamics simulation tool, we found that van der Waals bonding, the oligomer formation mechanism, and charge transfer among the cluster constituents significantly affect ionization dynamics induced by an XFEL pulse. The oligomer formation is due to bond formation between neutral atoms and an atomic ion, both during the early stage of cluster ionization when the first ions appear, and during cluster fragmentation when cluster components begin to move apart. Our results clearly demonstrate that XFEL pulses can be used not only to damage and destroy molecular assemblies but also to modify and transform their molecular structure.

Hironobu Fukuzawa[a,b], Kiyoshi Ueda[a,b,*]

[a] Institute of Multidisciplinary
Research for Advanced Materials,
Tohoku University
[b] RIKEN SPring-8 Center

*Email: kiyoshi.ueda@tohoku.ac.jp

References

[1] T. Ishikawa *et al*.: Nat. Photonics **6** (2012) 540.
[2] H. Fukuzawa *et al*.: Phys. Rev. Lett. **110** (2013) 173005.
[3] K. Motomura *et al*.: J. Phys. Chem. Lett. **6** (2015) 2944.
[4] K. Nagaya *et al*.: Phys. Rev. X **6** (2016) 021035.
[5] T. Tachibana *et al*.: Sci. Rep. **15** (2015) 10977.
[6] Y. Kumagai *et al*.: Phys. Rev. Lett. **120** (2018) 223201.
[7] Y. Kumagai *et al*.: Phys. Rev. X **8** (2018) 031034.
[8] M. Yabashi *et al*.: Appl. Sci. **7** (2017) 604.
[9] H. Fukuzawa *et al*.: Nucl. Instrum. Meth. Phys. Res. A **907** (2018) 116.
[10] T. Katayama *et al*.: Struct. Dyn. **3** (2016) 034301.

Review Article

Imaging the increase in pulmonary blood flow at birth

Introduction

Before birth the human fetus lives in a liquid environment with liquid-filled lungs that play no role in the exchange of oxygen and carbon dioxide [1]. Instead, gas exchange occurs across the placenta and the fetal lungs receive only a small fraction of the blood flow they receive after birth [2]. However, at birth the airways are cleared of liquid to allow the lungs to take over the role of gas exchange. Fetal vascular shunts close to separate the pulmonary and systemic circulations and, as a consequence, blood flow through the lungs markedly increases to equal blood flow through the entire body [3]. Undertaking these changes is a major physiological challenge for the infant that is unparalleled by any other event that the infant may experience during of its life. Thus, it is truly amazing that most infants make these changes with an apparent ease that belies the magnitude of the changes.

Fetal circulation

The fetal circulation is very different to adults. Adults have two circulations; the pulmonary, which circulates blood through the lungs and the systemic, which circulates blood through the rest of the body. These two circulations are separated by the heart, allowing them to work at very different pressures (mean of ~15 mmHg *vs* ~100mmHg, respectively), but are connected in series. As such, flow through both circulations must always be equal so that blood doesn't pool in either circulation. The right ventricle pumps blood through the lungs (pulmonary circulation) whereas the left ventricle pumps blood around the body (systemic circulation) (Fig. 1). Blood returning from the body supplies blood for the right ventricle to pump (called preload) whereas the supply of blood for the left ventricle comes from the lungs.

In the fetus, the pulmonary and systemic circulations are interconnected by the presence of vascular shunts, making it very different from the adult. Both ventricles contribute to blood flow in the systemic circulation, with the left ventricle supplying blood to the upper body and the right ventricle supplying blood to the lower body and placenta [3]. Most of the blood pumped by the right ventricle (~90%) by-passes the lungs and directly enters the descending aorta, through a shunt called the ductus arteriosus. This is largely because the resistance to blood flow through the lungs is very high during fetal life (Fig. 1) and pulmonary blood flow (PBF) is low. As a result, the volume of blood returning to the left ventricle (preload) from the lungs is small and is unable to supply the left ventricle with sufficient blood to pump [3]. Instead, the left ventricle receives most of its preload from the highly oxygenated blood returning from the placenta (Fig. 1). This blood passes from the umbilical vein through a shunt (ductus venosus) into the inferior vena cava and then passes through another shunt (foramen ovale) to enter the left atrium, before entering the left ventricle (Fig. 1) [4]. As the left ventricle receives a high proportion of oxygenated blood from the placenta and, as its output is directed mainly towards the brain, the brain receives blood that is more highly oxygenated than organs in the lower body (Fig. 1).

Changes to the fetal circulation at birth

At birth, the resistance to blood flow through the lungs massively decreases (30-50 fold) so that it can accept the entire output of the right ventricle [3]. The fetal vascular shunts (ductus arteriosus, ductus venosus and foramen ovale) must close to separate the pulmonary and systemic circulations, allowing them to work at very different pressures (see above). All of these changes are precipitated by two seemingly innocuous events; (i) the baby taking its first few breaths and (ii) clamping and cutting of the umbilical cord.

Phase contrast X-ray imaging experiments at SPring-8 BL20B2, demonstrated in newborn's breathing efforts are overwhelmingly responsible for clearing the airways of liquid and aerating the lung [5,6]. This, in turn, stimulates a large decrease in the resistance to blood flow through the lungs and a big increase (30-50 fold) in PBF, allowing the lungs to accept the entire output of the right ventricle. Clamping the umbilical cord disconnects the low resistance placental circulation from the fetal circulation, causing a large increase in resistance [3]. As a result, pressure in the systemic circulation rapidly increases and, combined with the large decrease in pulmonary vascular resistance, blood flow through the ductus arteriosus reverses during diastole (between heart beats) [7]. Thus, blood begins to flow from the aorta and into the lungs, contributing up to 50% of PBF for ~30 minutes after birth (called left-to-right shunting) [8]. However, blood flow gradually diminishes with time after birth as the ductus arteriosus narrows and then eventually closes [8].

Clamping of the umbilical cord at birth causes the ductus venosus to close due to a loss of blood flow, but it also removes umbilical venous return as a source of blood supply for the left ventricle (via the foramen ovale) [3]. As a result, if umbilical cord clamping occurs before the infant has aerated its lungs and its PBF has increased, then the left ventricle is deprived of blood to pump and cardiac output markedly decreases (by 30-50%) [3]. This can have serious consequences for the infant, potentially contributing to hypoxic/ischemic injury to the brain. On the other hand, if lung aeration precedes umbilical cord clamping, the increase in PBF can immediately replace umbilical venous return as the primary source of preload for the left ventricle, thereby preventing a reduction in cardiac output after birth [7]. In addition, the increase in pulmonary venous return to left atrium increases left atrial pressure above right atrial pressure, causing the foramen ovale to close, which eventually fuses with the intra-atrial septa.

Increase in Pulmonary blood flow at birth

With respect to infant survival after birth, the increase in PBF plays two critical roles. It facilitates the switch to pulmonary gas exchange by directing a high rate of blood flow across the lung's gas exchange surface to meet the infant's oxygen uptake requirements. The increase in PBF is also vital for maintaining cardiac output after birth, as it takes over from umbilical venous return as the primary source of preload for the left ventricle. Thus, a persisting high pulmonary vascular resistance is a major cause of death and disease in newborn infants [9], which reinforces the need to understand the mechanisms by which PBF increases after birth.

Although the precise mechanisms are unknown, lung aeration is the primary trigger for the increase in PBF after birth. It was widely believed that increased release of vasodilators, particularly nitric oxide (NO) in response to an increase in oxygenation associated with lung aeration, is the primary mechanism for the increase in PBF [2]. Increasing oxygen levels in the fetus stimulates an increase in PBF, although the increase is not sustained [2]. Furthermore, ventilation of the lung with a gas devoid of oxygen (with 100% nitrogen) or with low oxygen levels that do not increase oxygenation, can stimulate a large increase in PBF [10]. However, as the increase in PBF is greater with higher oxygen levels, increased oxygenation levels likely contributes to the increase in PBF at birth, but is not the primary mechanism [3,10]. Other potential mechanisms include an increase in lung recoil caused by the formation of an air/liquid interface and the creation of surface tension within the lung following aeration [11]. An increase in recoil within adjacent alveoli decreases the pressure within the interstitial tissue separating the alveoli, as it does in the intrapleural space (space between lung and chest wall). As such, the capillaries located within lung tissue would be expected to expand leading to an increase in vessel caliber and a reduction in resistance. Although simulating the increase in lung recoil induced by lung aeration increases PBF, the increase is considerably smaller than the increase at birth [11]. As such, additional, as yet undefined, mechanisms likely also contribute to the increase in PBF at birth.

Experiments at SPring-8 BL20B2 has discovered what is likely to be the primary underlying mechanism

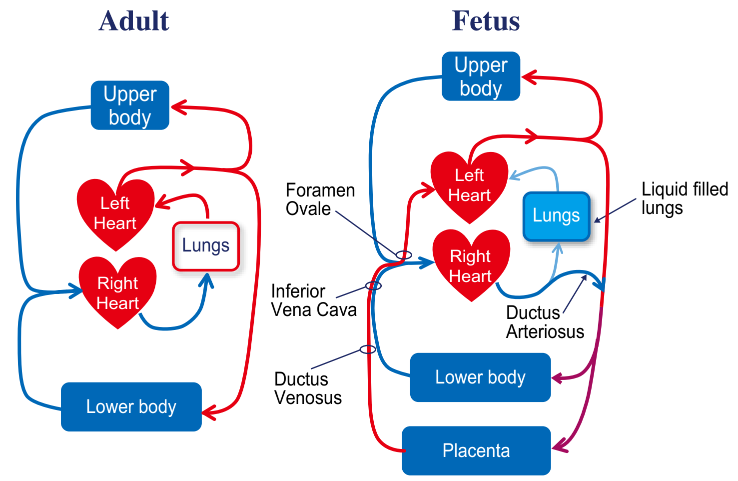

Fig. 1. Diagrammatic representation of the adult and fetal circulations. In the adult, the pulmonary and systemic circulations are separated by the heart and each ventricle provides blood flow through only one circulation; the left provides all systemic blood flow, whereas the right provides all pulmonary blood flow. In the fetus, the two circulations are interconnected by vascular shunts (foramen ovale and ductus arteriosus) that allow both the left and right ventricles to contribute to blood flow in the systemic circulation. Blood flow through the lungs is very low as most right ventricular output by-passes the lungs and flows through the ductus arteriosus. As such pulmonary blood flow provides little venous return for the left ventricle, which instead comes from the placenta via the ductus venosus and foramen ovale.

for the increase in PBF at birth [12-14]. By combining phase contrast X-ray imaging and angiography, the spatial relationship between lung aeration and the increase in PBF at birth was investigated. In view of the known effect that oxygenation and lung recoil has on PBF, it was hypothesized that the increase in PBF would be restricted to aerated lung regions [14]. However, contrary to this hypothesis, the experiments showed that partial aeration of the lung caused a global increase in PBF (Fig. 2). Furthermore, the increase in PBF occurred equally and simultaneously in all parts of the lung, irrespective of their state of aeration (Fig. 2 and Fig. 3). This effect of partial lung aeration on the global increase in PBF also occurred when the ventilation gas was changed to 100% nitrogen [12]. This discounted the suggestion that the increase in PBF in unaerated regions occurred in response to an increase in oxygenation caused by recirculation of well oxygenated blood from aerated regions into unaerated lung regions. On the other hand, partial lung aeration with 100% oxygen caused a larger increase in PBF in aerated regions compared to unaerated regions [12]. This indicates that increased oxygenation contributes to the increase in PBF, but the effect of oxygen is localized to aerated lung regions.

Realization that partial lung aeration causes rapid and global vasodilation of the lung, which occurs simultaneously and equally in both aerated and unaerated regions, led to the hypothesis that a neural reflex mediates the effect of lung aeration on PBF [13]. Studies in adult lung have previously described the juxta-capillary receptor (J-receptor), which is sensitive to lung edema and when activated triggers an increase in breathing rate (tachypnoea) [15]. The receptors are thought to be located within the juxta-capillary tissue between adjacent alveoli and to signal via afferent C-fibers passing within the vagal nerve trunk. As lung aeration at birth involves lung liquid leaving the distal airways and entering the peri-alveolar tissue, the accumulation of lung liquid within lung tissue simulates lung edema and may activates these J-receptors. The receptors signal the brain via the vagus which then initiates global dilation of the lung, presumably via efferent parasympathetic nerves. This hypothesis was tested by examining the effect of partial lung aeration on the global increase in PBF in newborn rabbits following bilateral trans-section of the vagus nerves [13]. Sectioning of the vagus nerves blocked the global increase in PBF caused by partial lung aeration (Fig. 3), which is consistent with the suggestion that signaling via the vagus nerve plays a vital role in the increase in PBF at birth. Interestingly, partial aeration of the lung with 100% oxygen increased PBF just in the aerated lung region, indicating that the increase in PBF at birth results from a hierarchy of mechanisms that either have global or localized effects. That is, the initial movement of liquid out of the airways into lung tissue activates receptors (possibly J-receptors) to initiate a global increase in PBF via a neural reflex. However, this increase in PBF is modulated at the local level by increased oxygenation, which is likely mediated by NO release.

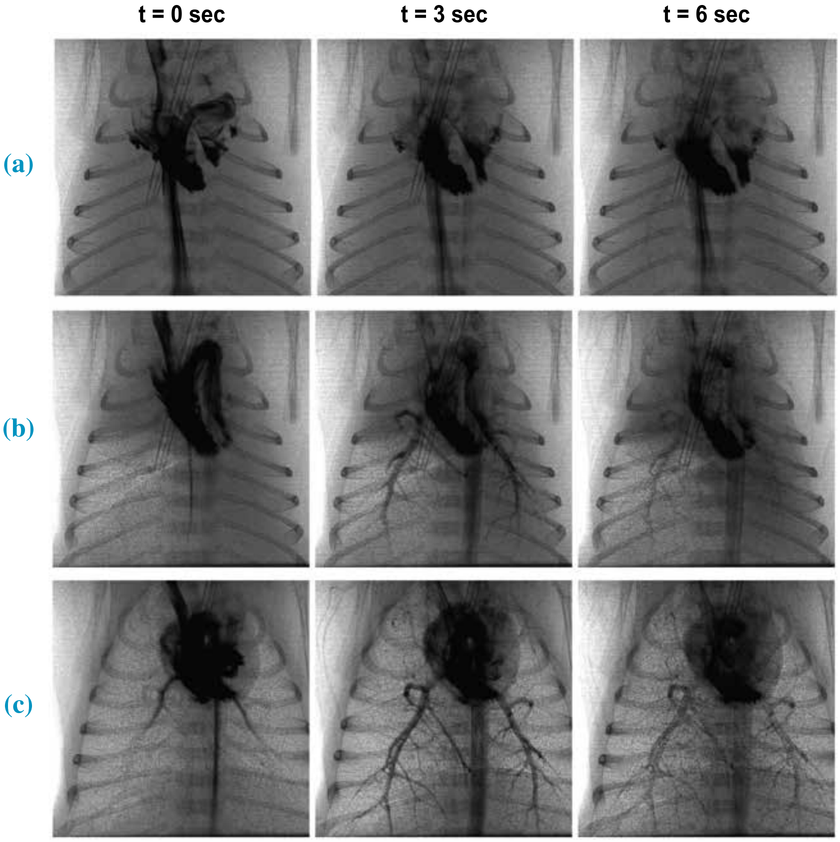

Fig. 2. Simultaneous phase contrast X-ray imaging and angiography of a newborn rabbit before lung aeration **(a)**, after aeration of one lung **(b)** and after aeration of both lungs **(c)**. An iodine solution was used as a contrast agent and was injected into a major vein leading to the heart. A series of images were acquired starting (t=0 sec) from the moment that iodine was first ejected from the heart to show the transit time of iodine through the pulmonary circulation; images displayed were acquired at t = 0, 3 and 6 secs. Aeration of the lung is clearly identified in the lung as regions of higher intensity with the presence of speckle. Note that before lung aeration (a), very little iodine enters the pulmonary circulation, but this markedly increases following aeration of one lung (b) with the increase occurring equally in both aerated and unaerated regions.

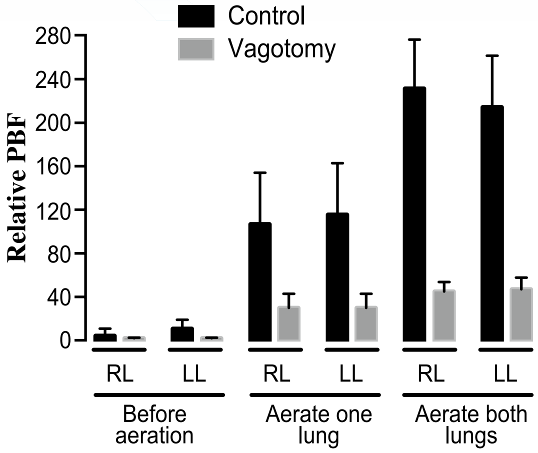

Fig. 3. Effect of vagotomy (cutting of both vagus nerves) on relative pulmonary blood flow before lung aeration, following aeration of one lung and following aeration of both lungs in newborn rabbits. Note that in controls (black bars) pulmonary blood flow increases in both lungs following aeration of only one lung. However, this increase in greatly reduced in vagotomized (gray bars) newborn rabbits. Data has been redrawn from [13].

Partial lung aeration and a global increase in PBF: What are the broader considerations?

In the healthy adult lung, ventilation (in and out movement of gas) of lung regions is closely "matched" with the level of blood flow (perfusion) through those lung regions. This is termed "ventilation/perfusion matching" and is regulated by changing oxygenation levels within localized lung regions. Ventilation/perfusion matching in the lung plays an important role in optimizing the lung's gas exchange potential by ensuring that when ventilation within a region changes, this region receives a matching change in blood flow. In the diseased lung, ventilation/perfusion matching can be reduced, resulting in a "mismatch". This is where lung regions with little or no ventilation receive large amounts of blood flow, which are commonly referred to as pulmonary shunts. Clearly, shunting blood through non-ventilated regions of the lung will greatly reduce the gas exchange efficiency of the lung.

While a ventilation/perfusion "mismatch" is thought to be problematic in adults, the presence of large pulmonary shunts in newborns immediately after birth should be viewed differently and may be beneficial for the infant. Indeed, while survival at birth depends on only part of the lung being ventilated, good cardiac output is essential for survival and to prevent brain injury, particularly when oxygenation levels are low. Thus, as a high PBF is essential to maintain left ventricular output, it is vital that the increase in PBF is not limited by whether or not the lung is fully aerated. Thus, it is logical that the increase in PBF at birth is not linked to the rate and degree of lung aeration, particularly as the lung can take some time to fully aerate [5,6].

Summary

The increase in PBF is vital for survival after birth as it enhances the efficiency of pulmonary gas exchange and is critical for maintaining cardiac output. However, until recently the primary mechanisms underpinning the increase in PBF were unclear. Imaging experiments at SPring-8 BL20B2 have provided a new understanding for how lung aeration triggers the increase in PBF at birth. By demonstrating that the increase in PBF is not spatially related to lung aeration and that the effect of oxygen is mediated locally, this implicated the involvement of a neural reflex. The role of this neural reflex was confirmed in subsequent experiments, but much further research is required to detail the specific pathways involved.

Stuart B. Hooper[a,b,*],
James T. Pearson[c]
and Marcus J. Kitchen[d]

[a] The Ritchie Centre, Hudson Institute of Medical Research, Australia
[b] Dept. of Obstetrics and Gynaecology, Monash University, Australia
[c] Department of Cardiac Physiology, National Cerebral and Cardiovascular Center Research Institute, Japan
[d] School of Physics and Astronomy, Monash University, Australia

*Email: stuart.hooper@monash.edu

References

[1] S.B. Hooper, R. Harding: Clin. Exp. Pharmacol. Physiol. **22** (1995) 235.
[2] Y. Gao, J.U. Raj: Physiol Rev. **90** (2010) 1291.
[3] S.B. Hooper *et al.*: Pediatr. Res. **77** (2015) 608.
[4] A.M. Rudolph: Ann. Rev. Physiology. **41** (1979) 383.
[5] S.B. Hooper *et al.*: FASEB J. **21** (2007) 3329.
[6] M.L. Siew *et al.*: J. Appl. Physiol. **106** (2009) 1888.
[7] S. Bhatt *et al.*: J. Physiol. **591** (2013) 2113.
[8] K.J. Crossley *et al.*: J Physiol. **587** (2009) 4695.
[9] E.M. Ostrea *et al.*: Pediatr. Drugs **8** (2006) 179.
[10] D.F. Teitel *et al.*: Pediatr. Res. **27** (1990) 372.
[11] S.B. Hooper: Exp. Physiol. **83** (1998) 833.
[12] J.A. Lang *et al.*: J. Physiol. **594** (2016) 1389.
[13] J.A. Lang *et al.*: J. Physiol. **595** (2017) 1593.
[14] J.A. Lang *et al.*: J. Appl. Physiol. **117** (2014) 535.
[15] A.M. Roberts *et al.*: Circ. Res. **58** (1986) 512.

Crystal structures of the gastric proton pump reveal the mechanism for proton extrusion

After intaking food, the pH inside our stomach reaches around 1. This acidic environment, generated by the gastric proton pump H$^+$,K$^+$-ATPase [1], is indispensable for food digestion and is also an important barrier to pathogen invasion via the oral route. However, excess stomach acidification induces ulcers, which considerably impair the health of those affected. Acid suppression in combination with antibiotics is a widely recognized treatment to eradicate *Helicobactor pylori*, a strong risk factor for gastric cancer. Proton pump inhibitors (PPIs) and a recently developed class of acid suppressants called K$^+$-competitive acid blockers (P-CABs) are commonly used for the treatment of acid-related diseases. Gastric H$^+$,K$^+$-ATPase therefore continues to be a prominent target for the treatment of excess stomach acidification.

Similarly to other P-type ATPases, gastric H$^+$,K$^+$-ATPase mediates the uphill transport of H$^+$ and K$^+$ fueled by ATP hydrolysis (Fig. 1), which is accomplished by the cyclical conformation changes of the enzyme. H$^+$,K$^+$-ATPase is composed of two subunits. The catalytic α-subunit is highly homologous to those of related P2-type ATPases such as Na$^+$,K$^+$-ATPase and sarco(endo)plasmic reticulum Ca^{2+}-ATPase (SERCA). In addition, H$^+$,K$^+$-ATPase requires an accessory β-subunit for functional expression as an αβ-complex.

We determined the crystal structures of gastric H$^+$,K$^+$-ATPase in a luminal-open E2P conformation bound to vonoprazan or SCH28080, representative P-CABs, which were analyzed to 2.8 Å resolution at SPring-8 **BL32XU** and **BL41XU** [2]. The α-subunit comprises 10 transmembrane helices (M1-M10), in which a cation-binding site is located, and three cytoplasmic domains – the nucleotide (N), phosphorylation (P), and actuator (A) domains (Fig. 2(a)). The β-subunit has a single TM helix and a large ectodomain with three of the six *N*-linked glycosylation sites visualized in the structure. The electron density maps define the binding mode of vonoprazan (now available for clinical treatment) and SCH28080 (a prototype of P-CAB), and the residues coordinating them, in a luminal-facing conduit that extends to the cation-binding site (Figs. 2(b) and 2(c)). The binding sites of these P-CABs were previously thought to overlap owing to similar inhibitory actions. Our structures show that they do indeed partially overlap but are also distinct. The binding mode of P-CABs determined in the crystal structure is consistent with mutagenesis studies, providing the molecular basis for P-CAB binding to H$^+$,K$^+$-ATPase, which will be useful for the structure-based development of novel PPIs.

According to the transport scheme, the luminal-open E2P state is an intermediate state occurring just after proton release and allows subsequent K$^+$ binding. In fact, the cation-binding site is exposed to the luminal bulk medium when bound P-CAB is removed from our structures. Similarly to other P2-type ATPases

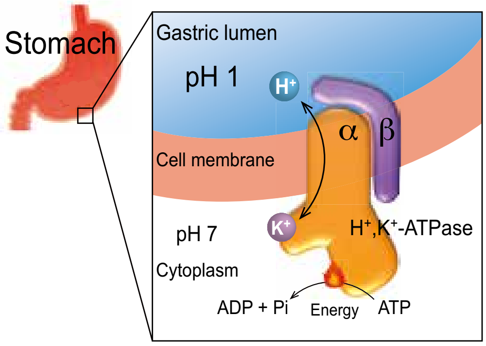

Fig. 1. Gastric proton pump H$^+$,K$^+$-ATPase.

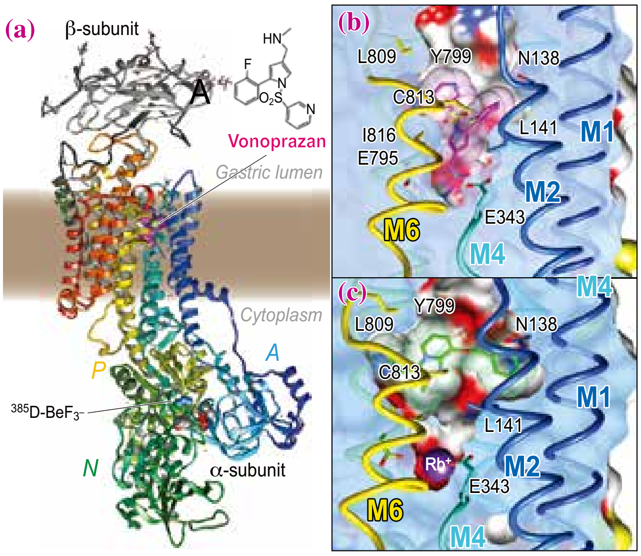

Fig. 2. Overall structure of gastric H$^+$,K$^+$-ATPase **(a)**. The color of the α-subunit gradually changes from the N terminus (blue) to the C terminus (red), and is gray for the β-subunit. Vonoprazan bound to the transmembrane region is shown as a magenta sphere. The sectional surfaces of vonoprazan- **(b)** and SCH28080- **(c)** bound structures are shown. Several amino acids important for P-CAB binding are indicated in the figure.

and cation-transporting proteins, H^+,K^+-ATPase also utilizes conserved acidic amino acids of its cation-binding site in M4 and M6 for H^+ transport, except for a lysine residue in M5. This invariant lysine (Lys791) in H^+,K^+-ATPase is replaced with serine in Na^+,K^+-ATPase, and is thus predicted to be important for proton transport. In our structure, the carboxyl residue of Glu820 is surrounded by other polar amino acids (Figs. 3(a) and 3(b)). The juxtaposition of the two glutamates (Glu795 and Glu820, 2.5 Å between their closest oxygens) indicates that at least one of these acidic residues is protonated. Because the charge-neutralized Glu795Gln mutant shows an ATPase activity profile comparable to the wild-type enzyme, in this case, Glu795 is likely to be protonated. Therefore, these two glutamate residues interact through a hydrogen bond. Glu820 also receives hydrogen bonds from Asn792 (3.0 Å) and a water molecule (3.5 Å). In addition to this hydrogen bond network around Glu820, the ε-amino group of Lys791 interacts intimately with the carboxylate of Glu820 (3.1 Å). Thus, the Glu820 carboxyl is situated in an unusual environment with extensive polar interactions that could lower its pK_a value. A reduction of pK_a values in juxtaposed carboxyl groups of two adjacent acidic residues occurs in the catalytic centers of many other enzymes; for example, two aspartate residues 2.5 Å apart in the catalytic center of pepsin were estimated to have pK_a values of 1.2 and 4.7 [3]. Therefore, H^+,K^+-ATPase Glu820 is a strong candidate for the proton release site, which enables the generation of the pH 1 solution in the stomach.

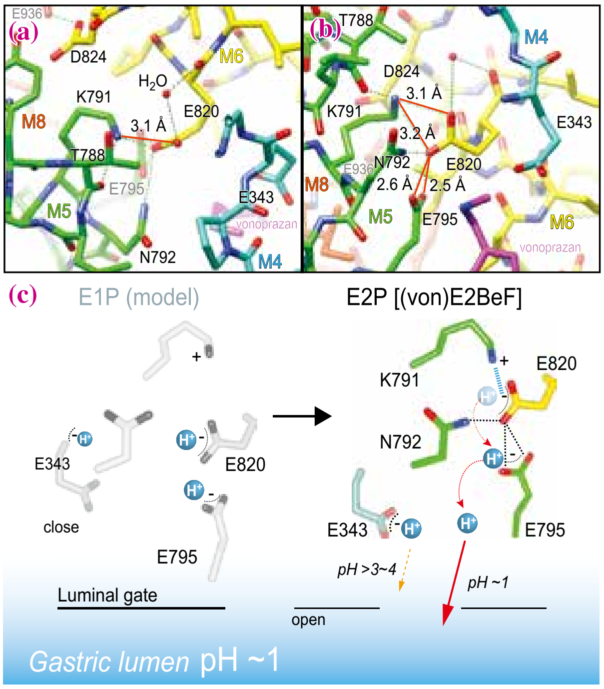

Fig. 3. Close-up of the cation-binding site in H^+, K^+-ATPase, viewed approximately perpendicular to the membrane from the cytoplasmic side **(a)** and parallel to the membrane from the M4 side **(b)**. Dotted lines are drawn between residues within 3.5 Å of neighboring atoms. The interactions between Glu795 and Glu820 (hydrogen bonds) and between Lys791 and Glu820 (salt bridges) are highlighted as red lines with the distances between them indicated. **(c)** Model for proton extrusion into the acidic solution. In the H^+-occluded E1P state (left), all three glutamates in the cation-binding site are protonated; otherwise, H^+ would be incorporated into the cation-binding site owing to its high concentration in the stomach when the luminal gate opens. In the luminal-open E2P state (right, based on the present structure), the H^+-binding affinity of the Glu820 carboxyl is greatly reduced because of its juxtaposition with Glu795, a hydrogen bond to Asn792, and a salt bridge with Lys791. As a consequence, a single H^+ is expelled into the luminal acidic solution.

Kazuhiro Abe

Cellular and Structural Physiology Institute (CeSPI),
Graduate School of Pharmaceutical Sciences,
Nagoya University

Email: kabe@cespi.nagoya-u.ac.jp

References

[1] E.C. Rabon and M.A. Reuben: Annu. Rev. Physiol. **52** (1990) 321.
[2] *K. Abe, K. Irie, H. Nakanishi, H. Suzuki and Y. Fujiyoshi: Nature* ***556*** *(2018) 214.*
[3] A.R. Seilecki *et al.*: J. Mol. Biol. **214** (1990) 143.

High-resolution crystal structure of the LH1-RC complex from *Thermochromatium tepidum*

Photosynthesis is a process by which light energy from the sun is converted into chemical energy indispensable for the survival of living organisms on the earth. Photosynthetic bacteria can also perform this process (Fig. 1), although they do not evolve oxygen as a side product. In order to perform photosynthesis efficiently, photosynthetic organisms have developed various light-harvesting pigment-protein complexes to compensate for the low light energy density available on the surface of the earth. In purple photosynthetic bacteria, there are usually two kinds of light-harvesting (LH) antennas named LH1 and LH2, which absorb light energy first and then transfer them to the reaction center (RC) to initiate photochemical reactions. LH2 is a group of peripheral antenna with different numbers of the α/β-subunits to form octamers or nonamers in different bacteria, whereas LH1 is the core antenna and encircles the RC to form an integral pigment-membrane protein supercomplex called LH1-RC supercomplex. RC contains 3-4 subunits (L, M, H and Cyt) and LH1 consists of 14-17 pairs of α/β-subunits or $\alpha/\beta/\gamma$-subunits, giving rise to a total molecular weight over 400 kDa for the LH1-RC supercomplex. The RC complex from a purple bacterium is the first membrane protein whose structure was determined in 1985 [1], and from then on, several techniques have been employed to determine the structure of the LH1-RC supercomplex in the last decades. Recently, several structures of the LH1-RC complexes were reported by either X-ray crystallography [2] or cryo-electron microscope (cryo-EM) [3] from different species of bacteria at various resolutions. However, the high-resolution crystal structure of this supercomplex has not been determined until recently.

We purified the LH1-RC supercomplex from a thermophilic photosynthetic bacterium *Thermochromatium tepidum* isolated from Mammoth Hot Springs in Yellowstone National Park, and crystallized, determined its structure at a resolution of 1.9 Å [4]. The diffraction data was collected at SPring-8 **BL41XU** at a wavelength of 1.0 Å with a beam size of 35×22 μm^2. The initial structure was solved by the molecular replacement method using the previous structure determined at 3.0 Å [2] as the search model with calcium ions, lipid and solvent molecules omitted. Incorporation of cofactors, lipids and detergent molecules and model modification were manually performed and the final structure was refined to 1.9 Å resolution [4].

The overall structure shows that the RC contains Cyt, L, M and H subunits and is surrounded by 16 heterodimers of the LH1 α/β-subunits containing 32 bacteriochlorophyll (BChl) *a* and 16 spirilloxanthin molecules, forming a completely closed elliptical ring [4] (Fig. 2). Compared with the previously determined structures of isolated RC [5] and LH1-RC complex [2], relatively large deviations were found in some regions of the RC subunits and the N- and C-termini of the LH1 subunits. Owing to the high resolution achieved, a number of cofactors and structural details were identified for the first time. These include a number of lipids and additional ubiquinone molecules, a large amount of water molecules that form a potential proton transfer pathway to the secondary electron acceptor Q_B, detailed coordinating environment for 16 Ca^{2+} ions in LH1, etc.

The differences found in the RC structure between the current "intact" LH1-RC supercomplex and previously reported isolated RC-only complex include the N-terminal region and a loop region (residues 172-196) of the Cyt subunit, and a loop region of the H subunit (residues 44-58). Similar differences are found between a recently reported cryo-EM structure of LH1-RC from *Blc. viridis* [3] and those of the isolated RC-only complex [5]. These differences are considered to arise from the interactions of the RC subunits with the surrounding LH1 subunits in the intact supercomplex that are absent in the isolated RC-only complex. Thus, the RC structure represents its native state more closely.

Q_A and Q_B are menaquinone-8 (MQ8) and ubiquinone-8 (UQ8) molecules bound to the M, L subunits of RC respectively, and serve as the primary and secondary electron accepters of the electron

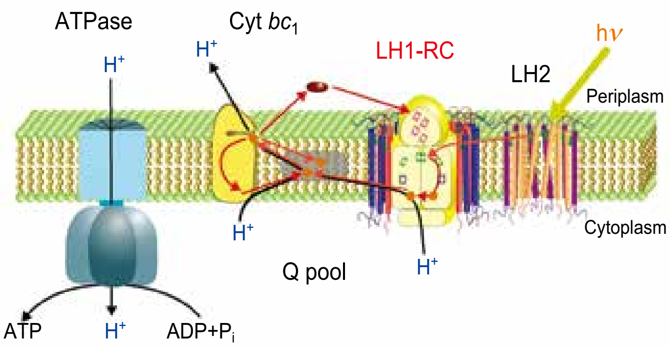

Fig. 1. Schematic illustration of a photosynthetic unit in the intracellular membrane of purple bacteria. Red arrows show the energy transfer from LH2 to LH1 and the cyclic electron-transport pathway.

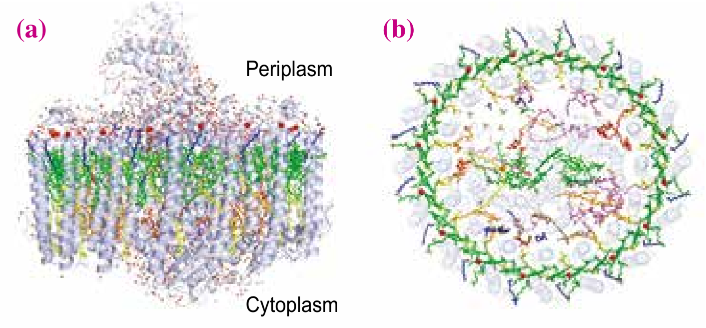

Fig. 2. Side view **(a)** and top view **(b)** of the LH1-RC super-complex from *Tch. tepidum*. Color codes: protein subunits, gray; BChls, green; spirilloxanthin, yellow; Ca^{2+} ions, red; water, raspberry.

transfer chain. In our structure, we identified one MQ8 and five UQ8s, among which, the MQ8 and one UQ8 are located in the Q_A and Q_B-binding sites respectively. The additional four UQ8s are located in the gap region between RC and LH1 (Fig. 3(a)). In particular, one of these UQ8 molecules was found to insert its isoprenoid tail into a potential channel formed by the LH1 α/β-subunits, which suggests that it is undergoing transport between the inside and outside of the ring through this possible exchange channel. This channel has been suggested in the previous studies [2], however, the present result provides the direct experimental evidence for the transport of UQ8s through this channel. Since there are 16 pairs of the LH1 α/β-subunits, there are potentially 16 such channels to facilitate the transport of the UQ8 molecules.

The *Tch. tepidum* LH1-RC supercomplex has two special features compared with other mesophilic counterparts, namely, red-shift of LH1 Qy transition and enhanced thermostability of the supercomplex. These features have been suggested to be brought about by the binding of Ca^{2+} ions. However, the detailed binding environments of the Ca^{2+} ions have not been determined unambiguously in the medium resolution due to the flexibility of the region surrounding the Ca^{2+}-binding site [2]. In the high resolution structure, all ligands including water molecules were identified; they include the side chain of Asp49, the carbonyl oxygens of α-Trp46, α-Ile51 and (n+1) β-Trp45, and two water molecules, giving rise to a six-coordination structure. A large number of interactions were found between the LH1 α/β-polypeptides that are mediated by the Ca^{2+}-binding site; this may greatly contribute to the tight connection of the neighboring LH1 α/β-polypeptides (Fig. 3(b)), resulting in the higher thermostability. Since the α-Trp46 and (n+1) β-Trp45 residues coordinated to the Ca^{2+} ions are also hydrogen-bonded with the neighboring BChl, binding of the Ca^{2+} ions may stabilize this region, resulting in the red-shift of the Qy absorption.

The novel features of LH1-RC supercomplex revealed by this high-resolution structure provide important information regarding the energy transfer between LH1 and RC, the exchange of Q_B molecule and shuttling of UQ8s through LH1 to the cytochrome bc_1 complex, proton transfer pathways to Q_B, and the possible effects of Ca^{2+}-binding on the LH1 red-shift and thermostability of the LH1-RC supercomplex. This information greatly advances our understanding on the bacterial photosynthetic reactions and will also provide important clues for the development of artificial photosynthetic systems.

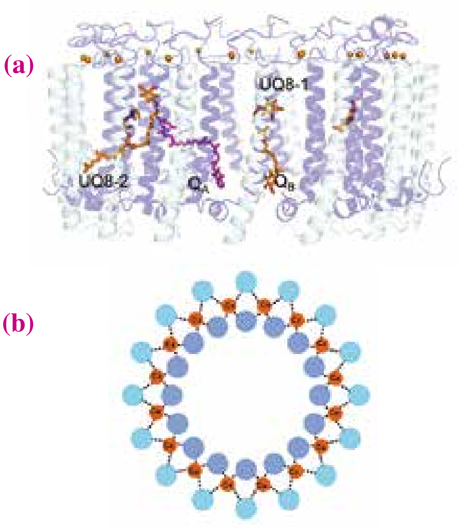

Fig. 3. **(a)** Distribution of the menaquinone (magenta) and ubiquinone (orange) molecules over the LH1-RC supercomplex. **(b)** Schematic model for the coordinating pattern of the 16 Ca^{2+} ions in the LH1 complex.

Long-Jiang Yu and Jian-Ren Shen*

Research Institute for Interdisciplinary Science,
Okayama University

*Email: shen@cc.okayama-u.ac.jp

References

[1] J. Deisenhofer *et al.*: Nature **318** (1985) 618.
[2] S. Niwa *et al.*: Nature **508** (2014) 228.
[3] P. Qian *et al.*: Nature **556** (2018) 203.
[4] *L.-J. Yu, M. Suga, Z.-Y. Wang-Otomo and J.-R. Shen: Nature* ***556*** *(2018) 209.*
[5] T. Nogi *et al.*: Proc. Natl. Acad. Sci. USA **97** (2000) 13561.

Structural basis of signal recognition and regulation at the full-length glucagon receptor

Class B G-protein-coupled receptors (GPCRs), which are therapeutic targets for treatment of various diseases, consist of an extracellular domain (ECD) and a transmembrane domain (TMD) [1]. The human glucagon receptor (GCGR), a member of class B GPCR family, is activated by the peptide hormone glucagon and plays critical roles in glucose homeostasis. Thus, GCGR has been considered as an attractive drug target for type 2 diabetes [2] (Fig. 1). Due to conformational flexibility and diversity, structural determination of full-length class B GCGR structure remains challenging. To better understand the ligand recognition and signal transduction mechanisms of class B GPCRs, we have determined the crystal structures of the full-length GCGR in complex with different ligands [3,4].

To obtain crystals of the full-length GCGR, the fusion partner T4L was inserted into the second intracellular loop (ICL2) of GCGR, and the receptor C terminus was truncated by 45 residues. To further improve protein stability, the antigen-binding fragment (Fab) of an inhibitory antibody, mAb1, and a negative allosteric modulator NNC0640 were used to purify and co-crystallize with the receptor. The GCGR-NNC0640-mAb1 complex structure was determined at 3.0 Å resolution by collecting data at SPring-8 **BL41XU** and the Linac Coherent Light Source (LCLS) in the SLAC National Accelerator Laboratory [3]. To further solve the peptide-bound structure of GCGR, we designed a partial agonist NNC1702 by introducing four point mutations in glucagon. Collecting data at BL41XU, the structure of the GCGR-NNC1702 complex was also determined at 3.0 Å [4].

The overall architecture of GCGR comprises an α-β-β-α fold of the ECD and seven transmembrane α-helices (Fig. 2(a,b)). In the GCGR-NNC0640-mAb1 structure, NNC0640 binds to the receptor on the external surface of the TMD, forming hydrogen-bond interactions with S350$^{6.41b}$, T353$^{6.44b}$ and N404$^{7.61b}$ in helices VI and VII (Fig. 2(c)). The binding mode of NNC0640 suggests that this negative allosteric modulator most likely inhibits receptor function by blocking the conformational changes of helices VI and VII.

In the peptide-bound GCGR structure, the C terminus of the peptide NNC1702 binds to the receptor ECD, and its N terminus penetrates into the ligand-binding pocket within the TMD, consistent with the previously proposed two-domain peptide binding model of class B GPCRs [1] (Fig. 2(b)). Additionally, the middle region of NNC1702 makes extensive contacts with the first extracellular loop (ECL1), the second extracellular loop (ECL2) and the stalk region that connects the ECD and TMD (Fig. 2(d)). The GCGR-NNC1702 structure, for the first time, provides a detailed molecular map for the interactions between a class B GPCR and its peptide ligand, which would benefit drug design and development targeting GCGR.

Comparing the two GCGR structures, there is a 90° orientation change of the ECD relative to the TMD (Fig. 3(a,b)). This introduces questions about inter-domain conformational flexibility required for

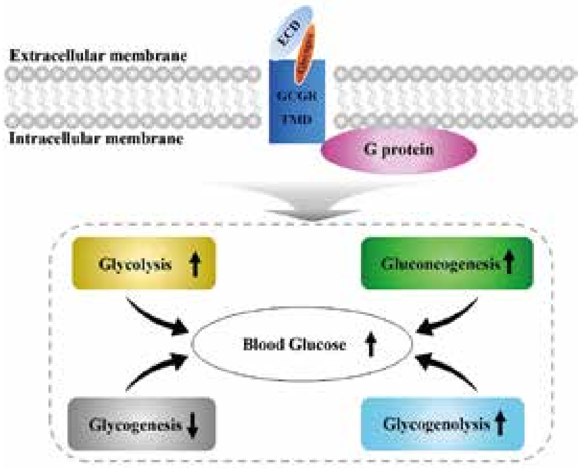

Fig. 1. Schematic illustration of the roles of GCGR in glucose regulation. Once activated by its endogenous ligand glucagon, GCGR increases blood glucose level, and is involved in modulating glucose homeostasis in human body.

the receptor binding to different ligands. Remarkably, the stalk and ECL1 adopt completely different conformations in the two structures. In the GCGR-NNC0640-mAb1 structure, the stalk and ECL1 form a compact β-sheet structure, stacking on top of the ligand-binding pocket of the TMD (Fig. 3(c)). In contrast, these two regions depart from each other and form an α-helix and a loop-α-helix-loop conformation respectively in the peptide-bound structure, acting as two 'arms' holding the peptide ligand tightly (Fig. 3(d)). These differences suggest that the structure rearrangement of the stalk and ECL1 may play a role in modulating peptide binding and receptor activation, which was further supported by our extensive studies of hydrogen–deuterium exchange, disulfide crosslinking, ligand binding, cell signaling and molecular dynamics simulations. Based on these findings, we proposed a dual-binding-site trigger model of GCGR activation. This model extends the previously established two-domain peptide binding model of class B GPCRs by including the interactions between the middle region of the peptide and the stalk and ECL1 as another trigger of receptor activation in addition to the binding of the peptide N terminus to the receptor TMD.

In summary, we reported two crystal structures of the full-length GCGR at different conformational states. These structures reveal molecular details of the receptor binding to different types of ligands, providing structural basis for drug development of diabetes. Additionally, the insights into the full-length GCGR structures shed light on the molecular mechanisms of receptor activation modulation, and thereby greatly expand our understanding about signal transduction of class B GPCRs.

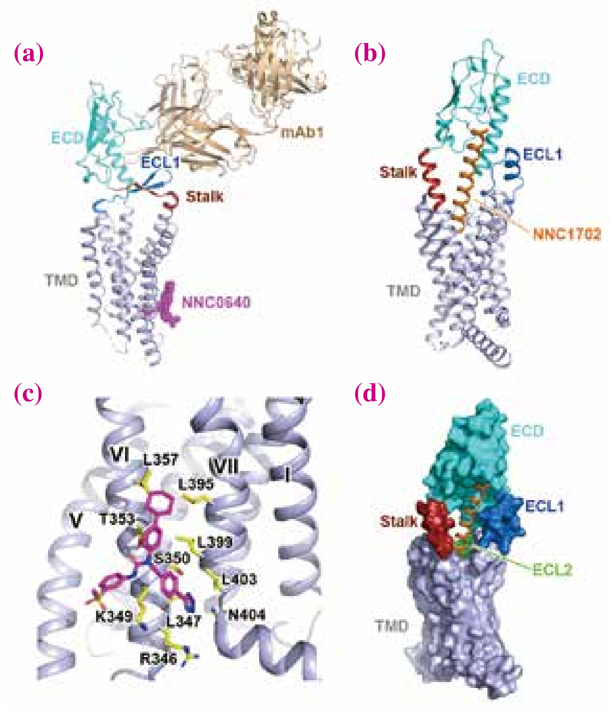

Fig. 2. Structures and ligand binding modes of GCGR. **(a)** Structure of the GCGR–NNC0640–mAb1 complex. **(b)** Structure of the GCGR-NNC1702 complex. **(c)** Binding pocket of NNC0640. **(d)** Binding mode of NNC1702.

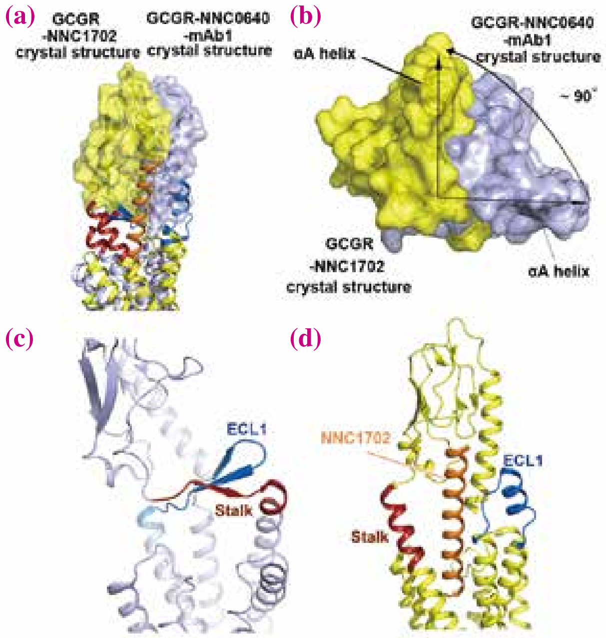

Fig. 3. Conformational changes of the stalk and ECL1. **(a)** Comparison between the two GCGR structures. **(b)** Extracellular view of the ECDs. **(c)** Conformation of the stalk and ECL1 in the GCGR-NNC0640-mAb1 structure. **(d)** Conformation of the stalk and ECL1 in the GCGR-NNC1702 structure.

Anna Qiao, Qiang Zhao and Beili Wu*

Shanghai Institute of Materia Medica,
Chinese Academy of Sciences, China

*Email: beiliwu@simm.ac.cn

References

[1] K. Hollenstein *et al.*: Trends Pharmacol. Sci. **35** (2014) 12.
[2] Y.M. Cho *et al.*: Pharmacol. Ther. **135** (2012) 247.
[3] *H. Zhang, A. Qiao, D. Yang, L. Yang, A. Dai, C. de Graaf, S. Reedtz-Runge, V. Dharmarajan, H. Zhang, G.W. Han, T.D. Grant, R.G. Sierra, U. Weierstall, G. Nelson, W. Liu, Y. Wu, L. Ma, X. Cai, G. Lin, X. Wu, Z. Geng, Y. Dong, G. Song, P.R. Griffin, J. Lau, V. Cherezov, H. Yang, M.A. Hanson, R.C. Stevens, Q. Zhao, H. Jiang, M.W. Wang and B. Wu: Nature.* ***546*** *(2017) 259.*
[4] *H. Zhang, A. Qiao, L. Yang, N. Van Eps, K.S. Frederiksen, D. Yang, A. Dai, X. Cai, H. Zhang, C. Yi, C. Cao, L. He, H. Yang, J. Lau, O.P. Ernst, M.A. Hanson, R.C. Stevens, M.W. Wang, S. Reedtz-Runge, H. Jiang, Q. Zhao and B. Wu: Nature* ***553*** *(2018) 106.*

Crystal structure of the human Frizzled-4 receptor

10 Frizzled receptors (FZDs) belong to a class of unconventional G-protein-coupled receptors (GPCRs) that function in WNT signal transductions and are gatekeeping proteins in regulating the fundamental signaling axis in embryonic development and tumorigenesis [1] (Fig. 1). Thus, the FZDs have been recognized as promising cancer drug targets for decades yet no drugs have been yielded from efforts toward discovering anti-FZD therapeutics. Uncovering the structures of extracellular soluble region in FZDs, the cysteine-rich domain (CRD) and its complex with WNT led to the discovery of small-molecule ligands and biologics targeting on this region [2]. However, until now, there has been no reported ligand targeting on the transmembrane domain of FZDs, the traditional pocket on which numerous GPCR drugs act. In order to understand why no one has been able to develop good tool ligands or drug molecules for FZDs and to tackle the mystery of FZD signaling, we solved the intact transmembrane domain structure of Frizzled4 receptor (FZD4) at 2.4 Å resolution [3].

As a representative of the Frizzled family, FZD4 mediates the canonical WNT signaling. It harbors a multi-domain architecture including the family-conserved extracellular CRD, a 7-helical transmembrane bundle (7TM or TMD), and a hinge domain that we previously defined for Smoothened (SMO) [4], a close homology of Frizzled. Uniquely for FZD4, it also recognizes Norrin protein to mediate the canonical β-catenin signaling. Structural investigation of FZD4 will provide the first insight to understand the structure-function relationship of other FZDs which are emerging cancer drug targets.

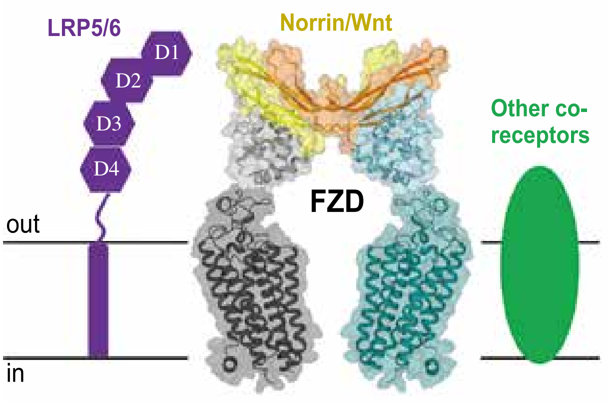

Fig. 1. Simplified illustration of Wnt (Norrin)-Frizzled signaling pathway. Wnt (or Norrin) induced Frizzled signaling requires clustering of transmembrane components such as Frizzled, LRP5/6 and other co-receptors. The intact signalosome also requires intracellular components such as Axin, DVL, GSK and other factors.

To generate a stable human FZD4 protein amenable for structure determination in the absence of a ligand (apo state), we screened hundreds of constructs, optimized purification procedures, and tried thousands of possible crystallization methods. It turns out to be extremely challenging to obtain diffraction-quality crystals, likely due to the lack of a tool ligand to lock the flexible region in the protein. During the course of crystal optimization, the efficient feedback from SPring-8 data collection results provided us the right direction. Finally, with introduction of stabilizing mutations and further optimization of crystallization conditions we were able to collect a complete data set at SPring-8 **BL41XU**. We solved the structure of FZD4 in the apo state, which is the first structure of the Frizzled family GPCRs and the first apo structure of a ligand-regulated GPCR as far as we know.

It is surprisingly observed that the traditional orthosteric ligand binding site is very narrow making it hard for small molecules to enter or bind (Fig. 2). More importantly, such a narrow and hydrophilic pocket is highly conserved among 10 FZDs, but not in SMO. These findings improved our understanding of the FZD ligand and signaling, and showed that ligand design for this pocket may require special considerations that could be inspired by this crystal structure.

Although both FZD4 and SMO belong to Class-F GPCRs, and they share similar overall architecture, the Frizzled and SMO are distinguishable in several ways: (1) from the structure perspective, the helix VI extension and ECL3 in FZD4 are much shorter than that in SMO (Fig. 3(a)). In SMO, the long helix VI extension and ECL3 create a large interface for CRD interaction and contribute to the stable “straight-up” conformation of CRD relatively to TMD. In contrast, such a short ECL3 in FZD4 may result in flexible CRD connection leading to swinging dynamics in the extracellular region as seen in MD simulations of the full-length model [3]. This comparison suggests different ways of CRD connection and extracellular ligand recognition. Additionally, the intracellular end of helix V in FZD4 moves outward from the helical bundle by about 13°. These differences between FZD4 and SMO are consistent with the varied upstream and downstream signaling of these two receptors. (2) Family-conserved residues such as Y250$^{2.39f}$ (transplanting the B&W numbering system

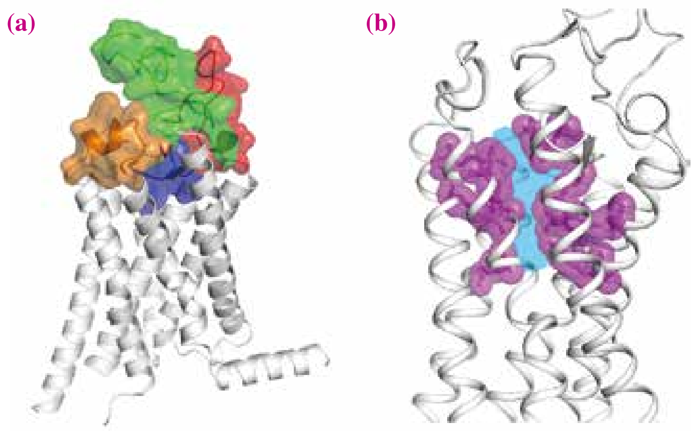

Fig. 2. **(a)** Overall structure of ΔCRD-Frizzled4. The hinge domain, ECL1, ECL2, ECL3 are colored in green, red, blue, and orange, respectively. **(b)** Highlight of the narrow pocket at the transmembrane domain. Residues constituting the transmembrane pocket are represented in stick-ball in magenta.

from Class A GPCRs), F440$^{6.36f}$ and W494$^{7.55f}$ adopt different conformations in the two structures (Figs. 3(b,c)). It is conceivable that these residues play important roles in downstream signaling, and evolution has endowed these key residues distinct conformations for respective function. (3) Molecular dynamics simulations at microsecond-time scale and mutational analysis uncovered two coupled, dynamic kinks located at helix VII that are involved in FZD4 activation. However, residues constituting these two kinks are conserved in 10 FZDs but not in SMO, suggesting that FZDs and SMO may undergo different conformational changes while being activated.

In addition to the discovery of a vacant and narrow pocket, the structure also reveals an unusual packing in transmembrane helices, providing new insight into a potential activation mechanism of this family of receptors. Such a remarkable structure provides a more accurate template to redirect the efforts on Frizzled drug discovery.

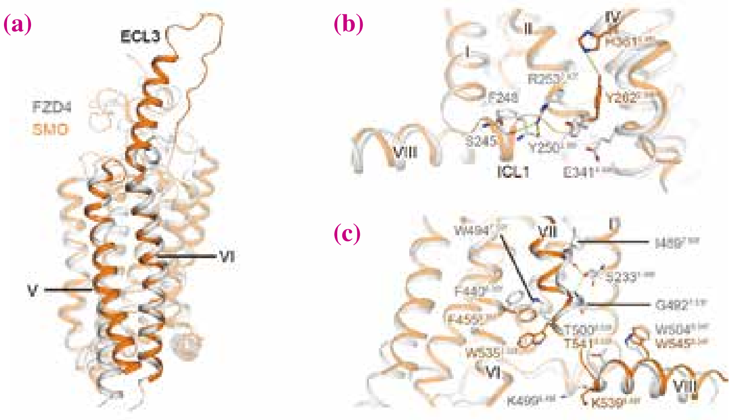

Fig. 3. **(a)** Comparison of ΔCRD-FZD4 (gray) with ΔCRD-SMO (orange, truncated from PDB: 5L7D). **(b)** and **(c)**, Conformational rearrangement of Y2.39f, F6.36f and W7.55f were observed between FZD4 and SMO.

Shifan Yang and Fei Xu*

iHuman Institute, ShanghaiTech University, China

*Email: xufei@shanghaitech.edu.cn

References

[1] R. Nusse and H. Clevers: Cell **169** (2017) 985.
[2] X. Zhang *et al*.: Trends Biochem. Sci. **43** (2018) 1033.
[3] *S. Yang, Y. Wu, T.-H. Xu, P.W. de Waal, Y. He, M. Pu, Y. Chen, Z.J. DeBruine, B. Zhang, S.A. Zaidi, P. Popov, Y. Guo, G.W. Han, Y. Lu, K. Suino-Powell, S. Dong, K.G. Harikumar, L.J. Miller, V. Katritch, H.E. Xu, W. Shui, R.C. Stevens, K. Melcher, S. Zhao and F. Xu: Nature* ***560*** *(2018) 666*.
[4] X. Zhang *et al*.: Nat. Comm. **8** (2017) 15383.

Structural basis of type IVb pilus-mediated bacterial adhesion to the intestinal epithelium

Initial attachment and subsequent colonization of the host cell surface are critical events that allow bacterial pathogens to survive in the host environment and exert their pathogenic effects. For efficient attachment and colonization, enteric pathogens have evolved numerous surface organelles, with filamentous protein polymers termed pili or fimbriae being the most prominent [1]. Enterotoxigenic *Escherichia coli* (ETEC) (Fig. 1(a)), a major pathogen causing diarrhea in travelers and children in developing countries, expresses a long, rod-like proteinaceous fiber called colonization factor antigen/III (CFA/III), which is an operon-encoded type IVb pilus (T4bP) synthesized through the assembly of its major and minor type IV pilin subunits, CofA and CofB, respectively.

Despite its known importance in bacterial pathogenesis, little is known about the structure and adhesion mechanisms of CFA/III. Therefore, we first determined the crystal structure of the CFA/III major pilin subunit, CofA, at a resolution of 0.90 Å by single-wavelength anomalous dispersion (SAD) phasing using five sulfurs in the protein. Given the counterbalance between anomalous signal strength and the undesired X-ray absorption of the solvent, we collected diffraction data selectively at a wavelength of 1.5 Å on SPring-8 **BL38B1**, which were sufficient to perform successful sulfur SAD phasing [2]. The determined CofA structure adopts an α/β-roll fold typical of type IVb pilin protein (Fig. 1(b)) and shows high similarity to that of another type IVb pilin, TcpA, which is the major pilin subunit of the toxin-coregulated pilus from *Vibrio cholerae*, including the spatial distribution of key residues critical for pilus assembly. Although this allows us to build a pilus-filament model of CofA via computational docking using a previously proposed filament model of TcpA as a structural template, the lack of structural information regarding the minor pilin subunit, CofB, hampers the acquisition of comprehensive data on CFA/III pilus. Therefore, the crystal structure of CofB was determined at a resolution of 1.88 Å by the SAD method using SeMet-derivatized crystals of CofB. The diffraction quality of CofB crystals was initially very poor. However, several post-crystallization protocols including dehydration of the crystals substantially improved the resolution limit of these crystals from ~4.0 Å to ~2.0 Å when measured at BL38B1 [3]. The determined CofB structure shows novel three-domain architecture, where each domain is connected by a short linker loop (Fig. 1(c)). In addition to the N-terminal type IVb pilin-like domain, the C-terminal region of CofB is composed of two characteristic β-strand-rich domains that were subsequently revealed to homotrimerize in solution by domain-swapping to form a pilus assembly initiator complex. This initiator complex efficiently promotes T4bP assembly (Fig. 2) [4]. We also noted that at the distal pilus end, the CofB C-terminal β-strand-rich domain adopts an H-type lectin fold that bears substantial structural similarity with that of trimeric discoidin I from *Dictyostelium discoideum* (Fig. 2).

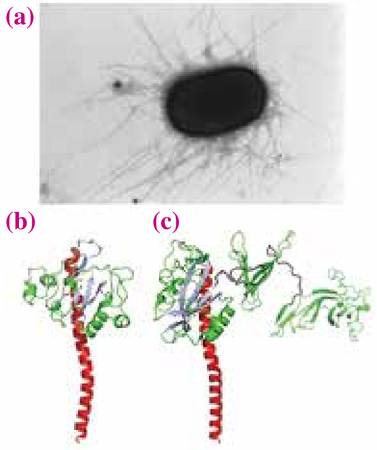

Fig. 1. Type IVb pili of enterotoxigenic *Escherichia coli* (ETEC). **(a)** Transmission electron micrograph of wild-type ETEC 31-10 strain. **(b)** Full-length structure of CFA/III major pilin CofA. **(c)** Full-length structure of CFA/III minor pilin CofB. Because the conserved N-terminal hydrophobic segment (1-28) of each pilin was truncated to solubilize the protein, the corresponding N-terminal segment was modeled using the full-length PAK pilin structure of type IVa pilin (PDB entry: 1OQW) as a template.

As H-type lectins generally bind N-acetylgalactosamine (GalNAc) molecules at the conserved binding pocket of their trimeric interfaces, it was initially thought that CofB may function as a lectin, targeting the small intestine mucosal glycome. However, we unexpectedly found that, in order to attach to the target cell surface, CFA/III pilus requires additional interaction with a protein named CofJ, a secreted protein of unknown function encoded by the CFA/III operon, at the expected binding interfaces of the CofB trimer located at its pilus-tip [5]. Interaction analyses indicated that the N-terminal flexible 24 residues of CofJ were responsible for the CofB-CofJ interaction. We subsequently elucidated the crystal structure of the corresponding N-terminal region (namely CofJ (1-24) peptide) in complex with CofB at a resolution of 3.52 Å on SPring-8 **BL26B1** (Fig. 3(a)). In each CofB trimeric interface, the complex structure clearly revealed that the CofJ (1-24) peptide fragment from Ser5 to Pro15 was bound to the groove, initially considered as a sugar binding pocket, sandwiched between 2 CofB C-terminal H-type lectin domains. This intriguing binding feature reasonably explains the fact that it precludes GalNAc binding and suggests functional "repurposing" of the H-type lectin domain of CofB for efficient attachment of ETEC to the target cell surface.

Based on the data from analytical ultracentrifugation which demonstrated that the CofJ-CofB complex in solution exists as a heterotetramer with one intact CofJ molecule and three CofB molecules, we generated a structural model of the CofJ-CFA/III pilus, in which a secreted protein CofJ was situated further above the minor pilin CofB at the tip of T4bP (Fig. 3(b)). Cell adherence assay with the CFA/III-positive HB101 strain carrying the recombinant plasmid which harbored all CFA/III operon genes except *cofJ* (Δ*cofJ* strain) indicated a marked reduction in bacterial adherence to Caco2 cells, where the observed reduction recovered noticeably when recombinant CofJ was added (Fig. 3(c)). These results strongly support the notion that the secreted protein CofJ serves as an anchor, bridging the host cell surface and the pilus-tip of T4bP during the process of ETEC adherence [5]. Initial attachment is a critical step common to all enteric pathogens. Thus, the interplay between secreted protein and T4bP of ETEC shown in this study may constitute an attractive therapeutic target for vaccination and/or antiadhesive treatment against ETEC infection.

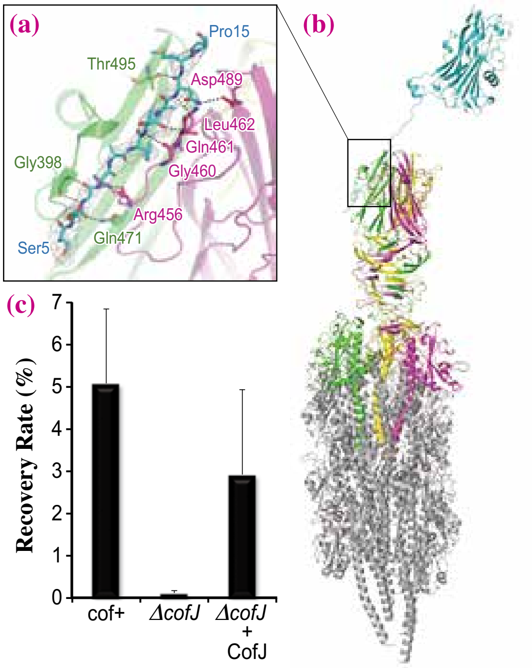

Fig. 3. Interplay of a secreted protein CofJ with CFA/III for bacterial adhesion to target cell surface. **(a)** Binding interface of CofJ(1-24)-CofB complex. A 2mFo-DFc omit map contoured at 1.0 σ corresponding to the region of the peptide binding groove is shown. **(b)** Structural model of CofJ-CFA/III pilus complex, with the CofJ monomer situated further above the minor pilin CofB homotrimer at the pilus tip. The model was built by superposing the CofJ(1-24)-CofB crystal structure onto the CFA/III pilus model. The CofJ(1-24) segment was then modeled and connected with the CofJ globular domain, the crystal structure of which was previously solved using its Dy derivative crystal at SPring-8 BL38B1. **(c)** CFA/III-mediated *E. coli* adherence to Caco-2 cells. Adherence values correspond to the recovery rate after incubation for 3 h. cof+ is an *E. coli* strain HB101 harboring all CFA/III operon genes on the plasmid pTT240 and Δ*cofJ* is a *cofJ* deletion mutant.

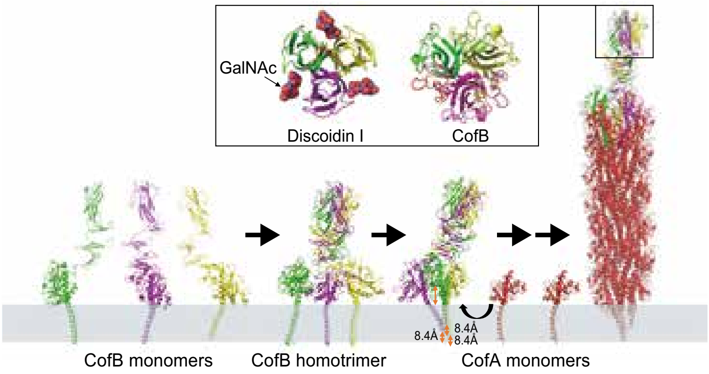

Fig. 2. Proposed mechanism for initiation of CFA/III assembly by CofB homotrimer. Three CofB monomers with their N-terminal α-helices initially embedded deeply in the inner membrane form a homotrimeric complex by association of C-terminal two β-strand-rich domains. Three cycles of extraction (~8.4 Å) of the N-terminal α-helix, possibly occurring in collaboration with inner membrane proteins, bring the α-helices into close proximity. This structural "tip" complex allows for easy docking of the major pilin CofA by shape and charge complementarity. Of note, the C-terminal domain of CofB has substantial structural similarity with H-type lectin domain of discoidin I from *Dictyostelium discoideum* (PDB entry: 2WN3).

Kazuki Kawahara[a,*], Hiroya Oki[a] and Shota Nakamura[b]

[a] Graduate School of Pharmaceutical Sciences,
Osaka University
[b] Research Institute for Microbial Diseases,
Osaka University

*Email: kkkazuki@phs.osaka-u.ac.jp

References

[1] K.A. Kline *et al*.: Cell Host Microbe. **5** (2009) 580.
[2] S. Fukakusa *et al*.: Acta Cryst. **D68** (2012) 1418.
[3] K. Kawahara *et al*.: Acta Cryst. **F71** (2015) 663.
[4] K. Kawahara *et al*.: J. Mol. Biol. **428** (2016) 1209.
[5] *H. Oki, K. Kawahara, T. Maruno, T. Imai, Y. Muroga, S. Fukakusa, T. Iwashita, Y. Kobayashi, S. Matsuda, T. Kodama, T. Iida, T. Yoshida, T. Ohkubo and S. Nakamura: Proc. Natl. Acad. Sci. USA* ***115*** *(2018) 7422.*

Structural mechanisms underlying anion selectivity and high-speed gating in anion channelrhodopsins

Light is one of the most useful resources for energy and information, and most animals capture light using rhodopsin family proteins. Rhodopsin family proteins are mainly classified into two groups: microbial (type I) and animal (type II). They are both characterized by seven transmembrane (TM) helices that bind a chromophore retinal, but their functions are very different. Animal rhodopsins primarily work as G-protein-coupled receptors, whereas microbial rhodopsins have more divergent functions such as ion pumps, ion channels, sensors, adenylyl/guanylyl cyclases, and phosphodiesterases. Recently, these rhodopsin family proteins have attracted broad attention as powerful tools to control intracellular signalings, ion concentrations, and cyclic nucleotide concentrations in a light-dependent manner (termed optogenetics) [1]. Among these proteins, ion-pump and ion-channel rhodopsins are the most well-established optogenetics tools. Because the inward flow of cations or the outward flow of anions across the cell membrane depolarizes the membrane potential and vice versa, the light-mediated activation of these pumps and channels modulates neuronal excitability. As membrane-depolarizing, excitatory optogenetics tools, the most common proteins currently used are cation channelrhodopsins (CCRs). Since the first discovery of *Chlamydomonas reinhardtii* ChR1 (*Cr*ChR1) and ChR2 (*Cr*ChR2) in 2002-3, many variants have been engineered and isolated. The currently available CCRs offer a wide choice of absorption spectra, conductances, light sensitivities, channel kinetics, and so on. As compared with excitatory optogenetics tools, the development of membrane-hyperpolarizing, inhibitory optogenetics tools has been lagging behind. Light-induced neuronal inhibition was first achieved by inward Cl$^-$ pumps and outward H$^+$ pumps such as *Natronomonas pharaonis* halorhodopsin (*Np*HR) and archaerhodopsin-3 (AR3). However, the application of these inhibitory optogenetics tools has been limited because of their low conductance and low light sensitivity. In 2014-5, CCR-based artificial anion channelrhodopsins (ACRs), such as iC++ and iChloC, were engineered, and naturally occurring anion channelrhodopsins, including *Gt*ACR1 and *Gt*ACR2, were isolated from chlorophyte algae [2]. These ACRs can translocate 10^4-10^5 ions per second and have a 10^2-10^4-fold higher light sensitivity than previously used inhibitory tools such as *Np*HR and AR3, and now they are widely applied to neuroscience research in a wide range of animals including mice, flies, and fish. Both designed and natural anion-conducting channelrhodopsins (dACRs and nACRs) have since been applied as inhibitory optogenetic tools, but each also exhibits performance tradeoffs that underscore their limitations. For example, dACRs offer a much wider range of kinetics than nACRs; on the other hand, nACRs exhibit larger photocurrents. Therefore, molecular and structural understanding of both dACRs and nACRs will be critical not only to understand the mechanisms underlying fundamental channel properties including channel kinetics and conductance, but also to enable the creation of new optogenetics tools.

To identify dACRs and nACRs that are suitable for structural studies, we screened all reported dACRs and nACRs, and found that iC++ (dACR) and *Gt*ACR1 (nACR) show excellent expression and thermostability, which are important for crystallization. The crystals of both iC++ and *Gt*ACR1 were obtained using the lipidic cubic phase (LCP) crystallization method, and diffraction datasets were collected at SPring-8 **BL32XU** and the GM/CA-CAT beamlines 23ID-B and 23ID-B of APS. Finally, the structures of iC++ at two pHs (8.5 and 6.5) and *Gt*ACR1 were determined at 2.9, 3.2, and 2.9 Å resolutions, respectively [3] (The *Gt*ACR1 structure was reported in detail in an accompanying paper [4]).

Both iC++ and *Gt*ACR1 form a dimer, and each monomer is composed of an N-terminal extracellular domain and a 7-TM domain. The overall architectures of iC++ and *Gt*ACR1 are similar, including the shape of their ion-conducting pathways (Fig. 1). Both ACRs have two extracellular vestibules, extracellular vestibules

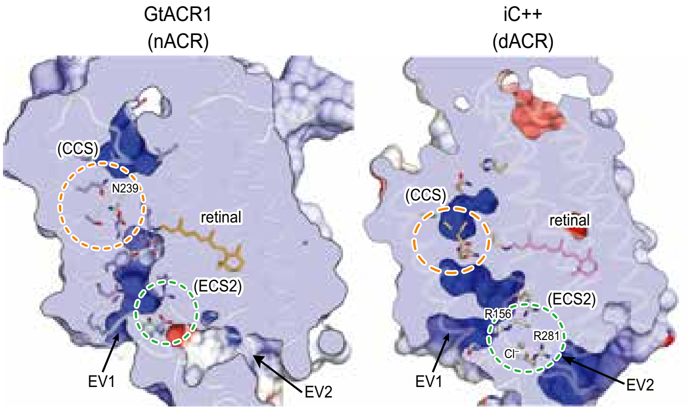

Fig. 1. Structural comparison of ion-conducting pathways between GtACR1 and iC++. Green and orange circles represent ECS2 and CCS, respectively.

1 and 2 (EV1 and EV2), and only EV1 extends to the central constriction site (CCS) of the ion-conducting pathway. EV2 is occluded at extracellular constriction site 2 (ECS2) in both iC++ and *Gt*ACR1. To analyze whether these structurally similar motifs (ECS2 and CCS) have the same functions, we performed an all-atom molecular dynamics (MD) simulation and patch clamp analyses of iC++ and *Gt*ACR1. The extensive computational and electrophysiological analyses revealed that the functions of these constriction sites are indeed very different. In iC++, ECS2 is formed by a Cl^--mediated hydrogen bond between Arg 156 and Arg 281. However, the interaction is often broken, and Arg 281 is oriented towards an extracellular bulk solvent during the simulation. It is observed that Arg 281 sometimes catches Cl^- floating in the solution, drags it into the extracellular vestibule, and forms a transient interaction with Arg 156. These results suggest that the residues at ECS2 of iC++ are involved in anion conduction, and the electrophysiological analysis of Arg 156 and Arg 281 supports the idea. In contrast, the interaction at ECS2 of *Gt*ACR1 is more stable, and mutational analysis suggests that they are important to regulate the closing of the channel. The stability and functions of CCS are also different between iC++ and *Gt*ACR1. The interactions at CCS of iC++ are weaker than those of *Gt*ACR1, and mutational analysis suggests that they work as a main determinant of ion selectivity. However, the mutations introduced to the residues at CCS of *Gt*ACR1 do not significantly affect ion selectivity but accelerate channel closing, indicating that they are more involved in the regulation of channel kinetics. Further electrophysiological analyses revealed that, unlike iC++, the anion selectivity of *Gt*ACR1 is mainly determined by the positively charged amino acid residues near the ion-conducting pathway; there are 12 positively charged amino acids positioned close to the ion-conducting pathway, and 3 of these 12 mutants show a leakage current of cations (Fig. 2). This suggests that these positively charged residues cooperatively contribute to anion selectivity in *Gt*ACR1.

Notably, one of the CCS mutants of *Gt*ACR1 tested above (N239Q) has a powerful effect on current decay kinetics while it maintains a photocurrent amplitude comparable to that of wild-type *Gt*ACR1. It is assumed that this mutant protein can be used as an inhibitory optogenetic channel with unprecedented speed and temporal resolution for single-spike inhibition in neurons. Thus, we combined N239Q and the R83Q mutation, which we had found to be effective for increasing the photocurrent amplitude, and named the R83Q/N239Q mutant as FLASH (Fast, Light-activated Anion-Selective rHodopsin). Since a recently described nACR (ZipACR) showed the fastest reported anion channel kinetics thus far [5], we compared FLASH and ZipACR, first using HEK293 cells and cultured neurons, and later using acute slices of mouse hippocampus, a living mouse, and a living worm. In all systems, more efficient inhibition was observed from FLASH-expressing cells and neurons, suggesting that FLASH is the ACR of choice for inhibitory optogenetic experiments.

In summary, the current study reported the first crystal structures of a dACR (iC++) and a comparison of the iC++ structure with that of an nACR (*Gt*ACR1), not only to provide insight into their ion conductance, channel gating, and anion selectivity, but also to enable engineering of the first ACR integrating all the key features of a large photocurrent magnitude and fast kinetics alongside exclusive anion selectivity.

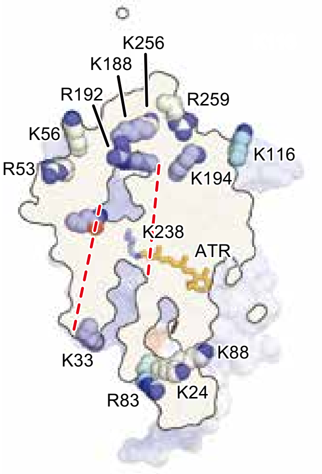

Fig. 2. Positively charged residues positioned close to the ion-conducting pathway of GtACR1. The mutants of K188, R192, and K256 show significantly lower anion selectivities.

Hideaki E. Kato[a,b,†]

[a] Department of Molecular and Cellular Physiology,
School of Medicine, Stanford University, USA
[b] JST / PRESTO

Email: hekato@bio.c.u-tokyo.ac.jp

[†] Present address: Komaba Institute for Science,
The University of Tokyo

References

[1] O.P. Ernst *et al.*: Chem. Rev. **114** (2014) 126.
[2] K. Deisseroth and P. Hegemann: Science **357** (2017) eaan5544.
[3] *H.E. Kato, Y.S. Kim, J.M. Paggi, K.E. Evans, W.E. Allen, C. Richardson, K. Inoue, S. Ito, C. Ramakrishnan, L.E. Fenno, K. Yamashita, D. Hilger, S.Y. Lee, A. Berndt, K. Shen, H. Kandori, R.O. Dror, B.K. Kobilka & K. Deisseroth: Nature* ***561*** *(2018) 349.*
[4] *Y.S. Kim, H.E. Kato, K. Yamashita, S. Ito, K. Inoue, C. Ramakrishnan, L.E. Fenno, K.E. Evans, J.M. Paggi, R.O. Dror, H. Kandori, B.K. Kobilka & K. Deisseroth: Nature* ***561*** *(2018) 343.*
[5] E.G. Govorunova *et al.*: Sci. Rep. **7** (2017) 43358.

Observation of enzymatic reactions by time-resolved X-ray crystallography using photosensitive caged substrate

Enzymes can catalyze various kinds of chemical reactions with high efficiency and selectivity under mild conditions. The elucidation of the mechanism of the catalytic reactions of enzymes is therefore crucial for understanding how nature designs active site structures for efficient catalytic reactions. The combination of X-ray structural analysis of the static state and time-resolved spectroscopic analysis of dynamic information is an invaluable strategy to reveal the molecular mechanism of enzyme-catalyzed reactions. However, a method for the direct observation of enzyme structures during their catalytic reactions can be a much more powerful tool for completely understanding the mechanism of enzymatic reactions. X-ray free electron lasers (XFELs) have provided a new method for time-resolved (TR) protein X-ray crystallography, which has great potential for observation of enzyme structures along with catalytic reactions. An experimental technique using XFELs, serial femtosecond crystallography (SFX), in which diffraction images are collected from a continuous flow of microcrystals with random orientation, opened a new avenue for TR crystallography [1]. The SFX technique was combined with pump-probe TR crystallography, in which photoirradiation is utilized as a reaction trigger. This TR-SFX technique has already led to major achievements in the analysis of structural dynamics in several photosensitive proteins such as photosystem II [2] and bacteriorhodopsin [3]. Thus, we consider that a system for the initiation of enzymatic reactions by photoirradiation will assist the TR-SFX characterization for enzymatic reactions.

In this project, we utilized a photosensitive caged compound as a reaction trigger in a TR-SFX experiment and applied this system to the structural characterization of the intermediate in a reaction catalyzed by nitric oxide reductase isolated from the fungus *Fusarium oxysporum* (P450nor). P450nor has a heme that is ligated by cysteine thiolate as an active site and catalyzes the reduction of nitric oxide (NO) to nitrous oxide (N_2O) ($2NO+NADH+H^+ \rightarrow N_2O+NAD^++H_2O$). Since N_2O is a powerful greenhouse gas as well as a major ozone-depleting substance, the mechanism of N_2O generation from NO has intrigued researchers. On the basis of spectroscopic studies, the reaction mechanism was proposed as shown in Fig. 1 [4]. The enzyme is in the ferric state with a water molecule as the sixth ligand in the resting state. The binding of the first NO molecule induces the dissociation of the water ligand, producing a ferric NO-bound form as the initial reaction intermediate. Then, the ferric NO-bound species is reduced with hydride (H^-) from NADH to form the second intermediate called intermediate *I* (*I*). Although *I* is in a two-electron reduced state, the protonation state is still under debate. Finally, a second NO molecule electrophilically attacks *I* to generate N_2O. To completely understand the NO reduction mechanism, study of the TR structure is highly desirable.

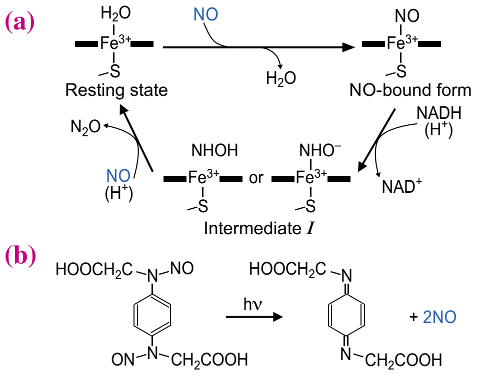

Fig. 1. **(a)** Proposed mechanism of NO reduction reaction catalyzed by P450nor. The protonation state in intermediate *I* is still under debate. **(b)** Chemical structure of caged NO used in this project. In the current TR experiments, photolyzed NO from caged NO initiates the P450nor-catalyzed NO reduction.

For the initiation of the P450nor-catalyzed reaction in TR-SFX experiments, we used caged NO (N,N'-bis(carboxymethyl)-N,N'-dinitroso-p-phenylenediamine sodium salt), which quantitatively releases NO on the microsecond time scale upon UV irradiation (Fig. 1). Prior to the TR-SFX experiments, we tested whether the P450nor reaction system with caged NO works or not by TR spectroscopic analysis. Using P450nor microcrystals soaked into a solution containing NADH and caged NO, we measured the changes in TR visible absorption induced by UV irradiation (Fig. 2) [5]. A positive difference peak at 437 nm was observed 20 ms after UV irradiation, indicating that NO released from caged NO reacts with the resting enzyme to form the ferric NO-bound species. Another positive peak at 450 nm was detected with the concomitant decay of the peak at 437 nm in the second time scale. These spectral changes indicate the formation of *I* upon the reduction of the ferric NO-bound form with NADH. Furthermore, the N-N stretching band of N_2O at 2,228 cm^{-1} was observed after UV irradiation of the sample by microscopic infrared spectroscopy at SPring-8 **BL43IR**, showing that P450nor catalyzes NO reduction to yield N_2O even in the crystalline state. These spectroscopic data demonstrate that P450nor produces N_2O through the formation of a ferric NO-bound form and *I* in the crystalline state, as observed in the solution sample. However, the rate of *I* formation was two orders of magnitude lower in the crystalline sample than in the solution (Fig. 2). It is plausible that the slow accommodation of NADH into the active site of P450nor in the crystal is due to the packing effect. Thus, kinetic analysis of the crystalline sample by TR spectroscopy is important to determine the measurement points in the TR-SFX experiment.

We carried out the TR-SFX experiment using a lipidic cubic-phase injector with a hydroxyethyl cellulose matrix at SACLA **BL3**. The current system for TR-SFX allows us to carry out measurements for a time window of up to 20 ms. Therefore, we focused on the characterization of the formation of the ferric NO-bound species, the initial reaction intermediate, in the TR-SFX experiment on the basis of the kinetic information. Figure 3 shows the structures of P450nor before caged NO photolysis and 20 ms after caged NO photolysis, both of which were determined at a resolution of 2.1 Å at ambient temperature [5]. In the structure at 20 ms, there is a clear positive electron density at the heme distal coordination sphere in the F_o(20 ms) – F_o(without UV irradiation) difference electron density map, which is assignable to the NO ligand. The NO coordination geometry in the NO-bound structure determined by TR-SFX shows a slightly bent Fe-N-O structure (158°). In the case of the NO-bound structure determined at SPring-8 **BL26B2**, the orientation of NO is more bent (147°) (Fig. 3). Since the reduction of the ferric NO-bound form generally induces the conformational change of the Fe-NO moiety to a bent conformation, the structure determined at SPring-8 could be partially reduced by X-ray irradiation, but the structure determined by TR-SFX is the ferric NO-bound form without any X-ray reduction. Thus, we can conclude that the method using a photosensitive caged compound with pump-probe TR-SFX is a powerful tool for dynamic structural analyses of enzymes during their catalytic reactions. Various caged compounds including caged ATP and photoinduced electron donors are available, allowing us to further elucidate the dynamic aspects of proteins based on time-resolved structural analysis.

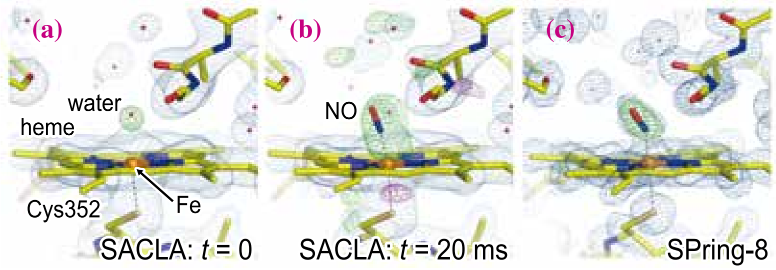

Fig. 3. Active site structure of P450nor determined at SACLA and SPring-8. **(a)** The structure determined by TR-SFX before UV irradiation at ambient temperature. A water molecule coordinates to a heme iron. **(b)** Structure determined by TR-SFX 20 ms after caged NO photolysis at ambient temperature. Green mesh represents the F_o(20 ms) – F_o(without UV irradiation) difference electron density map, which indicates the presence of a NO ligand at the sixth coordination sphere of the heme. **(c)** NO-bound structure determined by synchrotron crystallography at 100 K. The NO-bound form was prepared by soaking NO gas into P450nor crystal in the absence of NADH. Green mesh represents the $F_o - F_c$ electron density map.

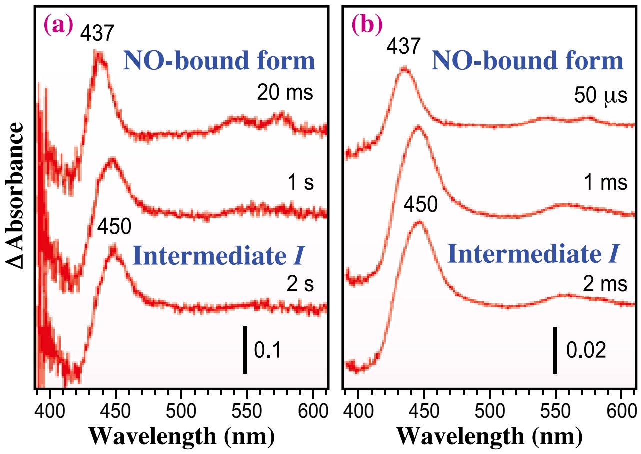

Fig. 2. TR visible absorption difference spectra of P450nor after caged NO photolysis in the crystalline state **(a)** and solution state **(b)**. The difference spectra were obtained by subtracting the spectrum recorded before UV irradiation to induce the caged NO photolysis. The spectra showed that NO released from caged NO upon UV irradiation reacts with ferric P450nor to form a ferric NO-bound state, which is followed by the formation of intermediate *I* in both crystalline and solution samples.

Takehiko Tosha[a,*] and Minoru Kubo[a,b]

[a] RIKEN SPring-8 Center
[b] Graduate School of Life Science, University of Hyogo

*Email: ttosha@spring8.or.jp

References

[1] H. Chapman *et al.*: Nature **470** (2011) 73.
[2] M. Suga *et al.*: Nature **543** (2017) 131.
[3] E. Nango *et al.*: Science **354** (2016) 1552.
[4] Y. Shiro *et al.*: J. Biol. Chem. **270** (1995) 1617.
[5] *T. Tosha, T. Nomura, T. Nishida, N. Saeki, K. Okubayashi, R. Yamagiwa, M. Sugahara, N. Takanori, K. Yamashita, K. Hirata, G. Ueno, T. Kimura, T. Hisano, K. Muramoto, H. Sawai, H. Takeda, E. Mizohata, A. Yamashita, Y. Kanematsu, Y. Takano, E. Nango, R. Tanaka, O. Nureki, O. Shoji, Y. Ikemoto, H. Murakami, S. Owada, K. Tono, M. Yabashi, H. Ago, S. Iwata, H. Sugimoto, Y. Shiro, M. Kubo: Nat. Commun.* ***8*** *(2017) 1585.*

Missing piece of two-component signal transduction systems unveiled by SEC-SAXS

To adapt to changes in the chemical and physical factors of their environment, all organisms have signal transduction systems that sense each environmental factor. In this study, we focused on a signal transduction system of root nodule bacteria (rhizobia) coexisting with legumes, which senses oxygen (O_2) levels in the soil.

The rhizobia mediate nitrogen fixation, which converts nitrogen (N_2) in the atmosphere into ammonia (NH_3), which is nitrogen nutrition available for plants. Although NH_3 in chemical fertilizers is industrially produced at a very high pressure and temperature, the rhizobia can generate ammonia at an ordinary temperature and pressure by their nitrogen fixation reaction. This reaction is catalyzed by nitrogen fixation enzymes, but these enzymes cannot function in the presence of O_2 owing to their lability to O_2. Therefore, the rhizobia have an O_2-sensing protein system, in which FixL functions as an oxygen sensor and FixJ controls the biosynthesis of nitrogen fixation enzymes in response to the O_2 concentration sensed by FixL (Fig. 1) [1], resulting in the synthesis of nitrogen fixation enzymes in anaerobic environments. The FixL/FixJ system is a so-called "two-component signal transduction system (TCS)" that consists of two types of proteins [2]. Since TCSs are ubiquitous in all living systems, except for animals including humans, it has attracted increasing attention as a development target of antimicrobial agents and plant growth promoters without side effects in animals. From this background, although numerous researchers have studied TCSs with interest for many years, it has been impossible to clarify the molecular mechanism of how living organisms sense and adapt to environmental factors in detail. This is mainly because the whole structures of TCS proteins have not yet been elucidated.

We aimed to clarify the detailed molecular mechanism of the signal transduction system involved in sensing environmental factors by elucidating the overall structure of O_2-sensing FixL/FixJ protein systems.

In this study, the structures of full-length FixL and FixJ proteins were determined by small-angle X-ray scattering (SAXS) and X-ray crystallography. To obtain accurate SAXS data, we established new equipment, SEC-SAXS, at SPring-8 **BL45XU** [3], in which size-exclusion column chromatography (SEC) equipment for protein purification and an SAXS measurement system are assembled. The system makes it possible to measure the SAXS of a fresh protein sample free from any protein aggregation, immediately after elution from a column has been enabled. Such a combined measurement system was recently installed in the synchrotron radiation facilities of the Asia-Oceania countries, although it has already been introduced in Western countries.

Figure 2 shows the newly unveiled three-dimensional structures of FixL and FixL-FixJ complexes determined by the SEC-SAXS method and X-ray crystal structure analysis at SPring-8 **BL26B2** [4,5]. These analyses provided some novel insights into the structure. FixL forms an intertwined homodimer, and there was no significant difference between the overall structures of O_2-binding and O_2-unbinding to the heme of FixL. Therefore, it is suggested that the intramolecular signal transduction in FixL caused by O_2 sensing is propagated by local structural changes (Fig. 3). For the FixL-FixJ complex, it was also found that only the receiver domain of a phosphate group in FixJ interacts with the FixL, and another domain is flexible without interacting with the FixL. Because phosphate transfer is a common function for all TCSs, the interaction between the FixL

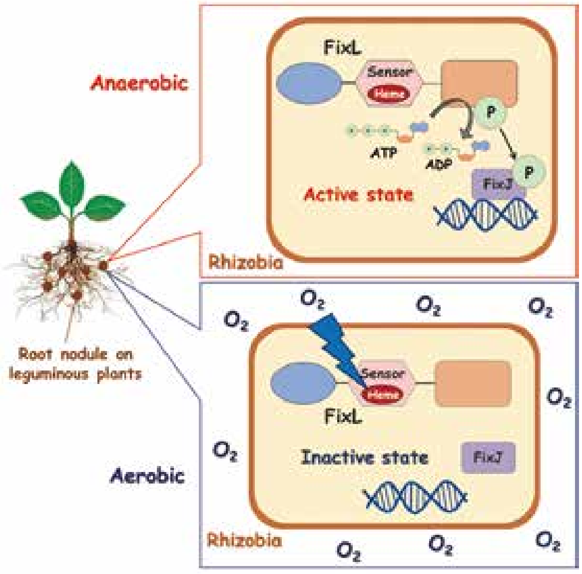

Fig. 1. O_2-sensing protein system FixL/FixJ in rhizobia. O_2 is sensed in rhizobia by a heme molecule in the sensor domain of FixL. Under an anaerobic condition, FixL does not bind O_2, and a phosphate group is generated by ATP hydrolyzation. The phosphate group is transferred from FixL to FixJ. The phosphorylated FixJ acts as a transcriptional factor for the biosynthesis of nitrogen fixation enzymes. Under an aerobic condition, O_2 is sensed by the heme molecule in the FixL, and FixJ does not act as transcriptional factor.

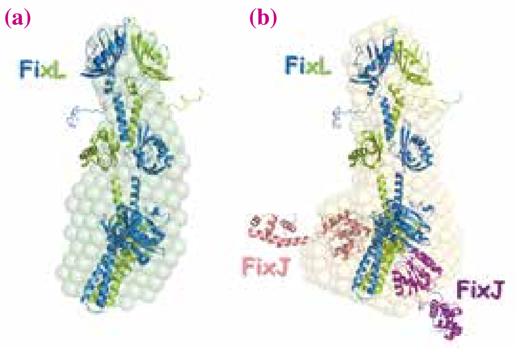

Fig. 2. Structure of the full-length FixL **(a)** and its complex with the full-length FixJ. **(b)** As revealed in this study, FixL forms a homodimer, shown as blue and green ribbons. FixJ is shown in pink and magenta.

and FixJ in this study is considered to be a common characteristic of TCS proteins. In addition, in the other proteins belonging to TCSs, protein domains with various physiological functions are fused to the domain corresponding to the flexible structure. Therefore, it is considered that TCS proteins became able to cope with various environmental factors by diversifying this flexible domain during the process of evolution.

FixL/FixJ is indispensable for the supply of nitrogen nutrients essential to the growth of soybeans, the host plant. Soybeans are a highly nutritious and useful plant, as reflected in its scientific name *Glycine max* (meaning that glycine, a kind of amino acid, is maximum). *Bradyrhizobium japonicum* solution is sprayed onto soybean seed stock at an industrial scale. Our results may open the path for genetic modification of this rhizobial TCS to improve crop yields.

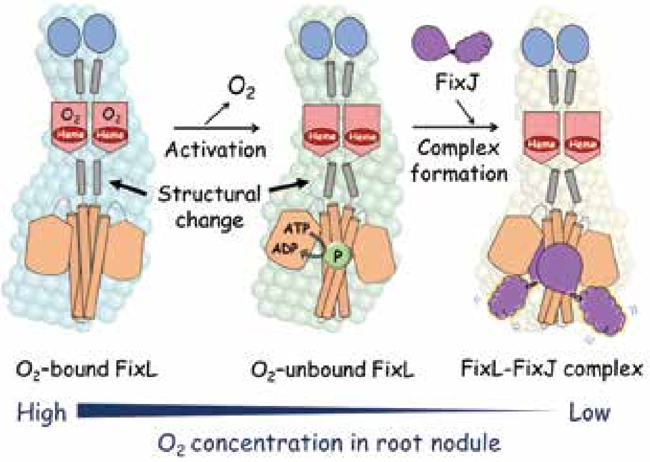

Fig. 3. Schematic diagram of the molecular mechanism of the O_2-sensing FixL/FixJ system. Our results suggest that there are no large changes in the overall structure of the full-length FixL upon O_2 dissociation from the heme. However, the orientation of the coiled-coil helices between the heme-containing sensor domain (pink) and the histidine kinase domain (orange) may change. Such a localized structural change could alter the distance between the ATP-binding site and a phosphate receiving site in the histidine kinase domain. At a low O_2 concentration, FixL and FixJ form a complex, and a phosphorylation site of FixJ approaches the phosphorylated site of FixL, which mediates phosphotransfer.

Hitomi Sawai* and Yoshitsugu Shiro

Cellular Regulation Lab., Graduate School of Life Science,
University of Hyogo

*Email: sawai@sci.u-hyogo.ac.jp

References

[1] M.A. Gilles-Gonzalez *et al*.: Nature **350** (1991) 170.
[2] Y. Gotoh *et al*.: Curr. Opin. Microbiol. **13** (2010) 232.
[3] T. Fujisawa *et al*.: J. Appl. Crystallogr. **33** (2000) 797.
[4] G. Ueno *et al*.: J. Struct. Funct. Genomics **7** (2006) 15.
[5] *G.S.A. Wight, A. Saeki, T. Hikima, Y. Nishizono, T. Hisano, M. Kamaya, K. Nukina, H. Nishitani, H. Nakamura, M. Yamamoto, S.V. Antonyuk, S.S. Hasnain, Y. Shiro, H. Sawai: Sci. Signal.* ***11*** *(2018) eaaq0825.*

CT dose reduction factors in the thousands using X-ray phase contrast

In X-ray imaging and computed tomography (CT), photon shot noise (Poisson noise) can be reduced by increasing radiation dose, but dose must be minimized for use with animals or humans or for high throughput applications.

Phase contrast imaging techniques can enhance image contrast by an order of magnitude or more using phase shifts (i.e., refraction) of X-rays. Propagation-based imaging (PBI) is the simplest phase contrast technique, whereby Fresnel diffraction fringes arise at the interfaces of an object upon propagation of the X-ray beam downstream from the object. This effect simultaneously enhances image contrast and spatial resolution. To recover information about an object from such images, Paganin *et al.* [1] developed a noise-robust algorithm for homogenous samples (TIE-Hom). Beltran *et al.* [2] and Croton *et al.* [3] extended TIE-Hom for multi-material samples. This approach has been shown to improve the signal-to-noise ratio (SNR) by up to 200-fold over conventional CT with minimal loss of spatial resolution [2,4]. These algorithms essentially smooth away the Fresnel fringes, whilst simultaneously reducing noise. A more complete description behind this huge gain in SNR has recently been suggested by Gureyev *et al.* [5] based on the quantum nature of image noise and the evolution of spatial Fourier spectra upon free-space propagation. The present article explores how such gains can be traded for massive reductions in radiation exposure, as reported by Kitchen *et al.* [4].

Experimental data was acquired in hutch 3 of SPring-8 **BL20B2** with a beam energy of 24 keV. The dose (air kerma) rate to the sample was fixed at 13.5±0.1 mGy/s. Twelve separate CT datasets of a newborn rabbit thorax were acquired to investigate the dependence of image quality on: (1) sample-to-detector propagation distance; (2) exposure time, and; (3) the effect of applying the TIE-Hom algorithm.

CT datasets were acquired at sample-to-detector distances of 0.16 m, 1.0 m and 2.0 m, and using four different exposure times of 1 ms, 10 ms, 100 ms, and 300 ms per projection at each distance. The shortest distance of 0.16 m was the closest we could safely position the detector to minimize phase contrast. A total of 1801 projections were recorded for each 180° CT scan. This gave a dose range from 24.3±0.1 mGy (1 ms exposures) to 7.29±0.01 Gy (300 ms exposures). We note that the lower dose is comparable to clinical CT scanners, but with much higher spatial resolution.

Figure 1 shows a reconstructed slice through the lungs at the smallest and largest propagation distances, and the effect of applying TIE-Hom phase retrieval algorithm. Figure 2 shows close-up images with absorption contrast at 0.16 m in (a) and with phase retrieval from a phase contrast dataset recorded at a distance of 2 m in (b), both at the lowest radiation exposure. With absorption contrast, the lungs are barely visible against the noise. Conversely, with phase retrieval the lungs are revealed with such high contrast and resolution that individual alveoli are readily visible.

Figure 3 shows the gain in SNR for phase retrieved CT, relative to that of the absorption CT, at each propagation distance as a function of exposure time. We discovered an unexpected effect that the SNR gain is consistently highest at the shortest exposure times, leading to large potential for dose reduction [4].

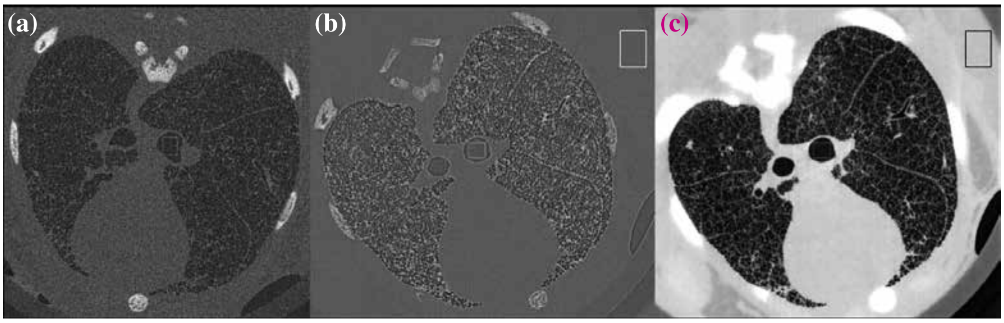

Fig. 1. CT reconstruction of rabbit kitten lungs. **(a)** Absorption contrast CT reconstruction at a sample-to-detector distance of 0.16 m. **(b)** Phase contrast CT at 2 m; **(c)** and with phase retrieval (TIE-Hom) at 2 m. Dark areas represent air-filled airways and bones appear bright. Black and white boxes indicate regions of interest for SNR analysis. The exposure time was 10 ms per projection for all images. Image dimensions: (a) 18.4 mm×18.5 mm; (b) and (c) 20.7 mm×18.5 mm.

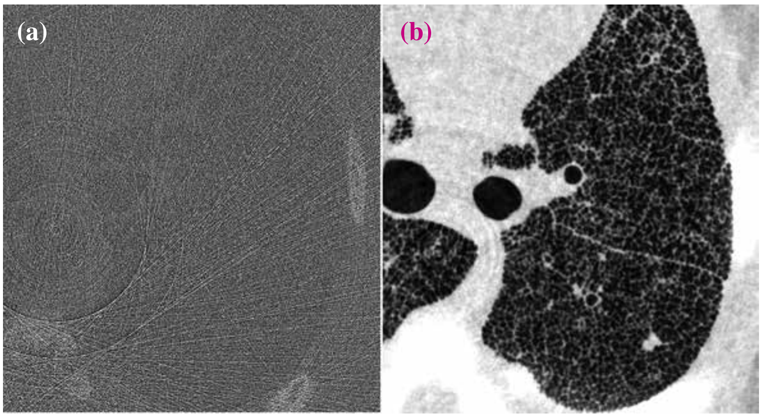

Fig. 2. High resolution lung CT reconstructions from absorption contrast data **(a)** and phase retrieved data (**(b)** 2 m propagation) at the lowest dose of 24.3±0.1 mGy (1 ms per projection). Voxel size = 15.3 μm. Small black circular objects are cross-sections through individual alveoli (~160 μm diameter). Image dimensions: 10 mm×11 mm.

The dose was reduced by a maximum of 300-fold in the experiment due to detector limitations. The SNR of the 1 ms phase retrieved data was still larger than the absorption contrast SNR at 300 ms by factors of 1.28±0.02; 5.16±0.05; and 9.6±0.2 at 0.16 m, 1.0 m and 2.0 m, respectively. From our noise analysis equations derived in [4] we can estimate the remaining dose reduction factor as the square of these numbers. This gives the expected dose reduction factors at 0.16 m, 1.0 m and 2.0 m of $300\times1.28^2=490\pm20$; $300\times5.16^2=7{,}990\pm30$; and $300\times9.6^2=27{,}600\pm30$, respectively. Our model for noise analysis shows that the dose reduction factors can potentially be in the hundreds of thousands, as discussed in [4].

The ability to improve CT image quality by factors in the tens to hundreds, or to reduce radiation exposure by factors in the hundreds to thousands, would have a dramatic impact on high-throughput low-dose imaging for clinical diagnostics and industrial non-destructive testing applications. Using less radiation will enable higher throughput imaging with fewer motion artifacts and be safer for human imaging or for longitudinal preclinical studies. The demonstrated dose reduction also lowers the requirements for brightness of micro-focus X-ray sources that can be used for medical phase-contrast X-ray imaging, thus potentially opening the way for the introduction of this method into routine clinical practice.

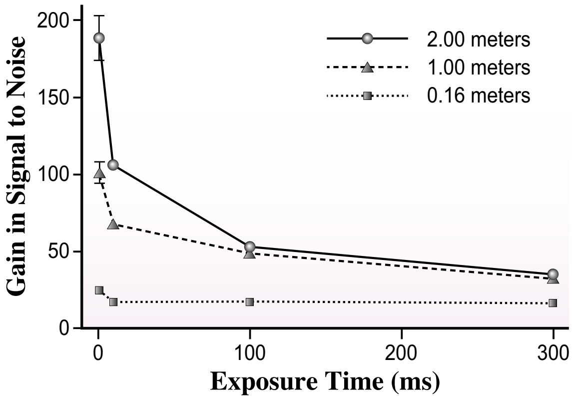

Fig. 3. Plots of the gain in SNR with phase retrieval CT as a function of exposure time.

Marcus J. Kitchen[a,*], Timur E. Gureyev[a,b,c]
and Stuart B. Hooper[d,e]

[a] School of Physics and Astronomy, Monash University, Australia
[b] ARC Centre of Excellence in Advanced Molecular Imaging, University of Melbourne, Australia
[c] Faculty of Health Sciences, the University of Sydney, Australia
[d] The Ritchie Centre, Hudson Institute for Medical Research, Australia
[e] Department of Obstetrics and Gynaecology, Monash University, Australia

*Email: marcus.kitchen@monash.edu

References

[1] D. Paganin *et al.*: J. Microsc. **206** (2001) 33.
[2] M.A. Beltran *et al.*: Opt. Express **18** (2010) 6423.
[3] L.C.P. Croton *et al.*: Sci. Rep. **8** (2018) 11412.
[4] *M.J. Kitchen, G.A. Buckley, T.E. Gureyev, M.J. Wallace, N. Andres-Thio, K. Uesugi, N. Yagi, S.B. Hooper: Sci. Rep.* ***7*** *(2017) 15953.*
[5] T.E. Gureyev *et al.*: J. Opt. Soc. Am. A **34** (2017) 2251.

Hidden morphological novelty enabling the evolution of female penis in the sex-role reversed cave insects

The discovery of a female penis in the Brazilian cave insect genus *Neotrogla* (order Psocodea, family Prionoglarididae, tribe Sensitibillini) received considerable attention by the scientific community and the public (Fig. 1) [1]. Similar female penis is also known from the African cave insect genus *Afrotrogla* (also a member of Sensitibillini) [2]. During copulation, the females of *Neotrogla* (and probably *Afrotrogla*) receive nutritious semen from the males using the female penis, and the semen forms a capsule within the female's sperm storage organ (spermatheca) (Fig. 1(d)). The female *Neotrogla* consume the contents of this seminal capsule not only for fertilization but also as nutrition. In the majority of animals, males are more active for mating (conventional sex-role). In contrast, to compete for this nutritious semen, the female *Neotrogla* evolved a more active role during mating than males (sex-role reversal), which is considered to be the major evolutionary pressure (reversed sexual selection) facilitating the evolution of female penis.

Although there are other more examples of sex-role reversed animals, the genera *Neotrogla* and *Afrotrogla* are the only ones known to date in which a female penis has evolved [3]. Due to the systematic position of these two genera (Fig. 3), an independent origin of the female penis has to be assumed (since the genus *Sensitibilla*, the sister group of *Afrotrogla*, lacks female penis) [2]. Therefore, in addition to the reversed sexual selection caused by sex-role reversal, there must be at least an additional key factor which facilitated the evolution of a female penis. In search of such a potential factor, we focused on a specialized structure (spermathecal plate) located at the entrance of the spermatheca.

In order to examine the detailed structure of this minute spermathecal plate, we used synchrotron μCT (SR-μCT) imaging, as well as light microscopes and confocal scanning laser microscopy. High resolution SR-μCT was carried out at SPring-8 **BL47XU** using a beam energy of 8 keV in absorption-contrast mode. The tomography system consists of a full field X-ray microscope with Fresnel zone plate optics. The field of view and the effective pixel size are 0.11 mm × 0.11 mm and 0.0826 μm × 0.0826 μm, respectively.

As a result, we identified the existence of a tiny switching valve (about 0.3 mm wide) at the entrance of the spermatheca (Fig. 2) [4]. The valve system is composed of an inlet duct, a closure element, actuator muscles to incline the closure element, resilin patches (a rubber-like protein) supporting the closure element, and two plates forming two insemination slots. This valve system serves to direct the seminal flow provided from the male into one of two slots

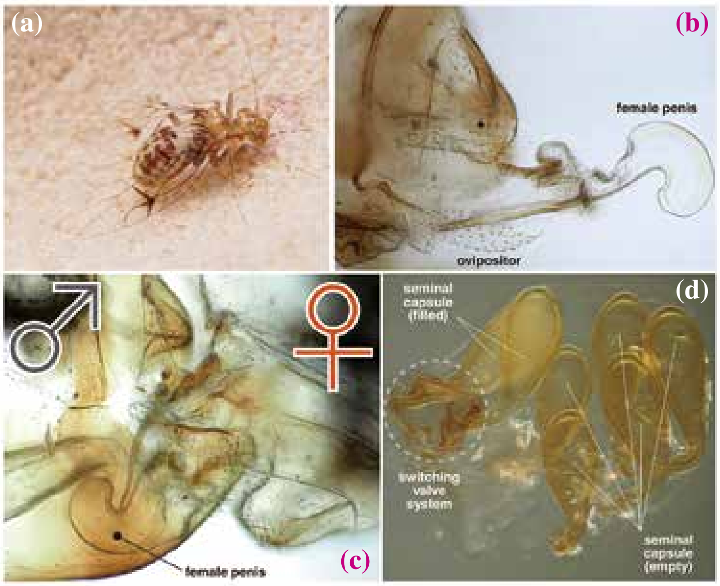

Fig. 1. **(a)** *Neotrogla brasiliensis* photographs in a cave in Brazil. **(b)** Female penis of *N. curvata*. **(c)** Male and female terminal abdomens of *N. curvata* in copula. **(d)** Light microscopy photograph of the spermatheca, including the switching valve system and seminal capsules.

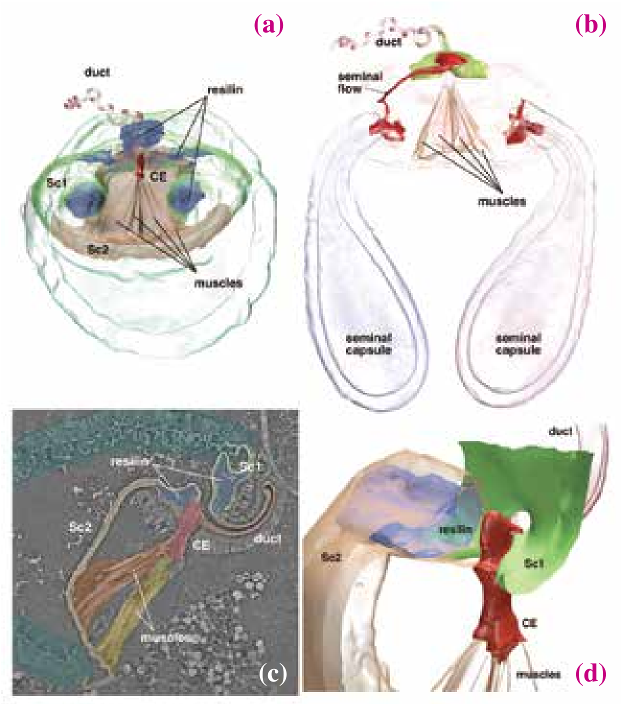

Fig. 2. Morphology of the spermatheca and spermathecal plate of *Neotrogla*. **(a)** 3D segmentation of the spermathecal plate with no seminal capsule. Abbreviations. CE: closure element; Sc1 and 2: body sclerite 1 and 2. **(b)** 3D segmentation of the spermathecal plate with two seminal capsules and showing seminal flow. **(c)** Muscle attachment to CE. **(d)** Detail of CE.

of insemination (Fig. 2(b)). The existence of similar spermathecal plate is also confirmed in *Afrotrogla* and *Sensitibilla* (i.e., all genera of Sensitibillini), although its detailed structure and function have not been examined. This represents the first discovery of a functional biological switching valve in the animal kingdom.

The females of close relatives of Sensitibillini can only receive one seminal capsule at a time. In contrast, by using the switching valve, the females of Sensitibillini can hold two seminal capsules at a time (Fig. 1(d) and Fig. 2(b)). Therefore, the switching valve makes it possible for female Sensitibillini to receive more nutrition from the males, rendering the female-female competition for the nutritious semen more intense in comparison to other sex-role reversed animals. In addition, independent origins of the female penis, which is an extremely rare evolutionary event, were identified in Sensitibillini, even though this is a small group of cave insects containing three genera and eleven named species, only (Fig. 3) [2]. It is very likely that the evolution of this switching valve was a prerequisite for the reversal of the genital organs in Sensitibillini.

Many mechanical solutions engineered by humans do not exist in nature. The switching valve discovered in *Neotrogla* is constructed in a fundamentally different manner than engineered switching valves (Fig. 2) such as those in the oil and gas industry or for changing the water flows in the shower. This micrometer-sized structure could inspire alternative valve technologies on a micrometer/nanometer scale.

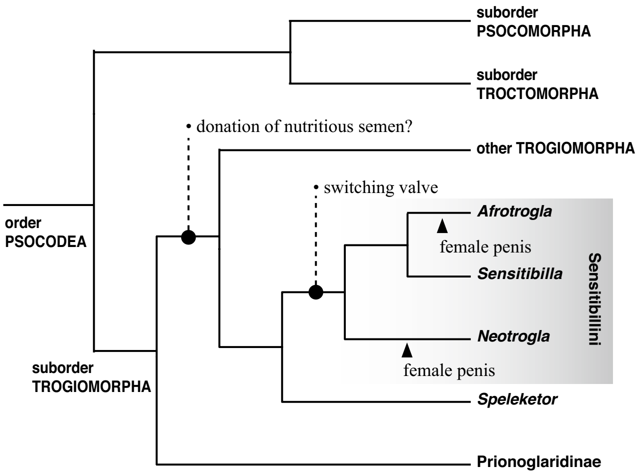

Fig. 3. Phylogeny of Psocodea and assumed history of character evolution related to the origin of female penis.

Kazunori Yoshizawa[a,*] and Alexander Blanke[b]

[a] Systematic Entomology, School of Agriculture, Hokkaido University
[b] Institute for Zoology, University of Cologne

*Email: psocid@res.agr.hokudai.ac.jp

References

[1] K. Yoshizawa *et al*.: Curr. Biol. **24** (2014) 1006.
[2] K. Yoshizawa *et al*.: Biol. Lett. **14** (2018) 20180533.
[3] Y. Kamimura and K. Yoshizawa: Sex Role Reversal in Encyclopedia of Animal Cognition and Behavior (Springer, 2007).
[4] *K. Yoshizawa, Y. Kamimura, C. Lienhard, R.L. Ferreira and A. Blanke: eLife 7 (2018) e39563.*

Revealing the pressure-induced layer-sliding transition in Ta_2NiSe_5 by X-ray diffraction under high pressure

Many exotic phenomena such as insulator-metal transitions and high-temperature superconductivity are found in various compounds. To understand the electronic state behind them correctly, precise crystal structural analysis is essential. In condensed matter physics, despite pressure being one of the most fundamental tuning parameters for controlling the electronic state, structural analysis using diffraction data under pressure is extremely difficult.

Powder X-ray diffraction (XRD) using a diamond anvil cell (DAC) to apply pressure to the sample is the standard method of revealing the crystal structure under pressure. For elucidating the pressure-induced phase transition mechanism, precise integration of the scattering intensity of the sample is the most important issue for precise crystal structure analysis. However, in the case of powder XRD, it is very difficult to precisely obtain the intensity, since the powder XRD data under pressure generally has a weak signal and, furthermore, is often affected by a preferred orientation effect, which causes a significant change in the scattering intensity ratio. Therefore, there was limited scope to discuss the change in the lattice constant and symmetry on the basis of powder XRD analysis. On the other hand, in the case of single-crystal XRD, a much stronger signal than that in powder XRD is expected and the preferred orientation effect is not a problem. Therefore, it is greatly desired to establish experimental and analytical methods for single-crystal XRD under high-pressure conditions.

We performed single-crystal XRD measurement under high-pressure conditions to precisely determine the crystal structure of the layered chalcogenide Ta_2NiSe_5. Interestingly, this compound shows an insulator-metal transition at 3 GPa and superconductivity at 8 GPa and 1.2 K. However, since the crystal structure above 3 GPa has not yet been precisely determined, the electronic state has also not been revealed.

We employed SPring-8 **BL22XU** beamline, which is equipped with high-pressure XRD facilities such as a goniometer with a closed-cycle helium refrigerator, a helium gas compression system for DAC and a pressure determination system employing ruby luminescence (Fig. 1). Because of these many attachments around the sample, an incident X-ray is scattered from not only the target sample but also such attachments. Therefore, we developed our in-house analytical software so as to obtain the scattering intensity individually from different scatterers and succeeded in precise integration only from the target sample and structural analysis based on it. XRD patterns were measured within the pressure range from 0 to 8 GPa and the temperature range from 10 to 300 K.

Figure 2 shows a comparison of the crystal structure in the low- and high-pressure phases. Ta_2NiSe_5 crystallizes as a layered structure and each layer consists of $TaSe_6$ octahedra and $NiSe_4$ tetrahedra (Fig. 2(a)). In the low-pressure phase there are two layers in a unit cell (Figs. 2(b) and 2(c)) since the upper and lower layers are related by *C*-centered lattice symmetry and shifted relative to each other by 1/2 $\boldsymbol{a}$.

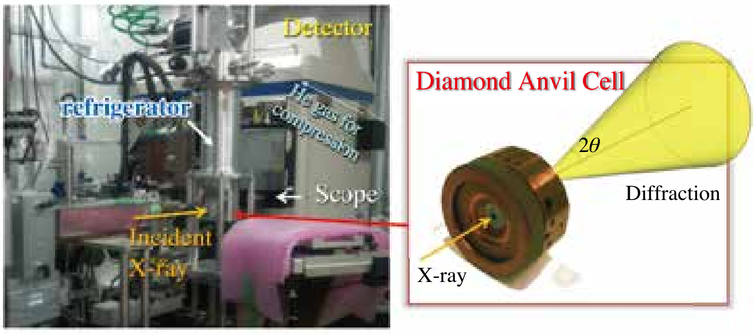

Fig. 1. High-pressure X-ray diffraction facilities in the beamline BL22XU.

On the other hand, there is only one layer in the unit cell in the high-pressure phase (Figs. 2(d) and 2(e)). This means the entire layer "slides" by 1/2 ***a*** at 3 GPa as shown schematically in Fig. 2(f). Furthermore, we revealed that the positional relationship of interlayer Se ions plays an important role in this structural phase transition. There are no other compounds that show the layer-sliding transition at a relatively low pressure comparable to 3 GPa while maintain sufficient crystallinity to enable single-crystal structural analysis. Thus, we conclude that the pressure-induced layer-sliding transition is a unique phenomenon derived from the special layered structure of Ta_2NiSe_5. In recent years, Ta_2NiSe_5 has attracted great interest as a promising exotic insulator state called an "excitonic insulator" caused by the Bose-Einstein condensation of excitons. Our structural analysis will provide important information for discussing the relationship between the excitonic insulator state and superconductivity under pressure.

In this work, we showed that crystal structure analysis with sufficient precision is possible even for relatively complex substances by single-crystal XRD under high pressure. In the near future, it will be possible to elucidate the electronic state of various substances with novel physical properties under high pressure by using our developed analysis method.

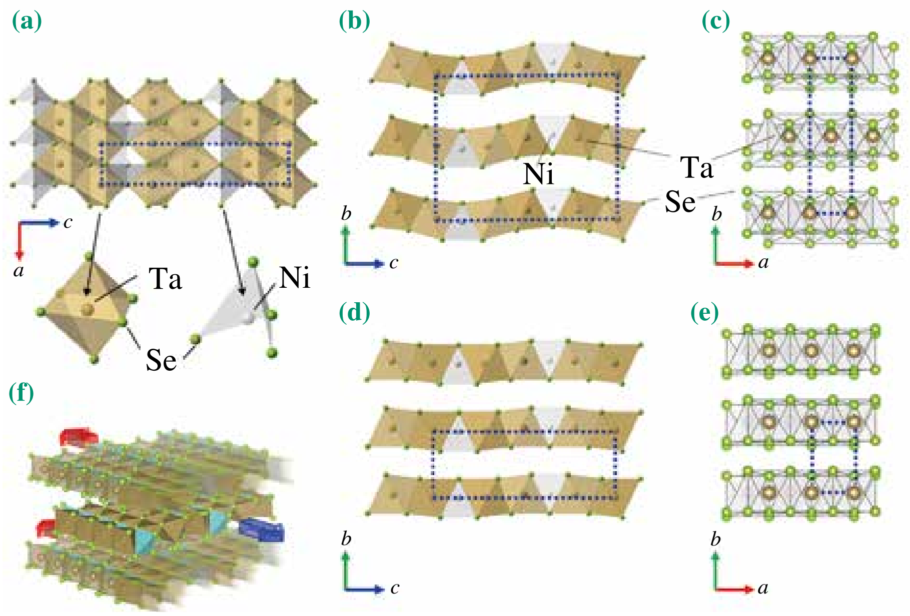

Fig. 2. **(a)** In-plane crystal structure viewed from the *b*-axis (common to phases below and above 3 GPa). **(b)** and **(c)** Crystal structures of phases below 3 GPa viewed from the (b) *a*- and (c) *c*-axes. **(d)** and **(e)** Crystal structure obtained above 3 GPa viewed from the *a*- and *c*-axes, respectively. The dotted blue line indicates the unit cell for each structure at the given pressure. **(f)** Schematic picture of layer sliding.

Akitoshi Nakano and Hiroshi Sawa*

Department of Applied Physics, Nagoya University

*Email: z47827a@cc.nagoya-u.ac.jp

References

[1] *A. Nakano, K. Sugawara, S. Tamura, N. Katayama, K, Matsubayashi, T. Okada, Y. Uwatoko, K. Munakata, A. Nakao, H. Sagayama, R. Kumai, K. Sugimoto, N. Maejima, A. Machida, T. Watanuki and H. Sawa: IUCrJ.* **5** *(2018) 158.*
[2] T. Watanuki *et al*.: Philos. Mag. **87** (2007). 2905
[3] Y. Wakisaka *et al*.: Phys. Rev. Lett. **103** (2009) 02640.

Extreme disorder-phonon competition and liquid-like thermal conduction in $AgCrSe_2$

Thermal transport is one of the most fundamental properties of matter. Materials with small thermal conductivity are desirable for a great diversity of applications such as thermal insulation, optical phase-change memory devices and efficient thermoelectric energy conversion [1]. Thus, a persistent challenge is to reduce the thermal conductivity of solids as much as possible. In general, acoustic phonons of solids are the major heat-carriers so that several strategies are proposed to enhance the scattering of acoustic phonons for suppressing thermal conduction, such as disorder scattering, anharmonic phonon interactions, uncorrelated or concerted rattling modes, interfaces and grain boundaries [1]. Disorder-phonon coupling has been frequently employed to achieve ultralow thermal conductivities in leading thermoelectrics, for example, Zn_4Sb_3 [2] and Cu_2Se [3]. It is true that the thermal conduction can be effectively suppressed in this way, but it still remains unknown that to what extent the acoustic phonons can be scattered. Such an issue is also fundamentally critical, given that it may define the physical lower limit of thermal conductivity in solids.

It is known that $AgCrSe_2$ undergoes a superionic transition at T_C of about 450 K, above which Ag ions become disordered, with high ionic conductivity [4]. In order to examine the atomic structures, we performed high-energy X-ray diffraction at SPring-8 **BL04B2**. The obtained diffraction data, $S^X(Q)$, were converted into pair distribution function, $G^X(r)$, in real space.

$AgCrSe_2$ crystallizes in a hexagonal structure with alternative Ag layers and $CrSe_6$ octahedral layers repeating along the c axis, as shown in Fig. 1(a). Ag atoms lie in the equivalent tetrahedral interstitial sites in between $CrSe_6$ layers. In the ground state, it is expected that only one specific site is fully occupied and as temperature rises, an increasing number of Ag ions immigrate to another site owing to the jump diffusion. At T_C of about 450 K, the occupation of Ag ions undergoes an order-to-disorder transition to the high-temperature phase with 50% occupation at each site while the space group of crystal symmetry changes from $R3m$ to $R\bar{3}m$. The crystallographic changes are evidenced at X-ray scattering structure factor $S^X(Q)$ by the disappearance of Bragg peaks (003) and (006) as well as the weakening of $(10\bar{5})$, as shown in the inset of Fig. 1(b).

Shown in Fig. 2(a) are $G^X(r)$ at selected temperatures. The uniform nearest neighboring Ag–Ag distance splits into three sets due to the occupational disorder and the next nearest neighboring Ag-related correlations sequentially become diverse as well. This is responsible for the special temperature dependence of $G^X(r)$. With the guide of the partial PDF of Ag-related correlations shown in the lower part of Fig. 2(a), it can be seen that heights of Ag-related peaks are much more susceptible to the change of temperature, such as those at 4.5, 13 and 19 Å. As a representative, the integrated intensity of the peak at 4.5 Å is plotted in Fig. 2(b), which exhibits a well-defined critical-like behavior, in contrast to the 3.5 Å peak where contributions of Ag-related pairs are marginal. It is suggested that the disorder of atomic occupation of silver is saturated above T_C.

The occupational disorder has a direct influence on atomic dynamics because the transverse acoustic (TA) phonons are exclusively contributed by atomic motions of silver (Fig. 3(d)). In other words, there is a maximized competition between the local and global atomic motions. At higher temperatures, the

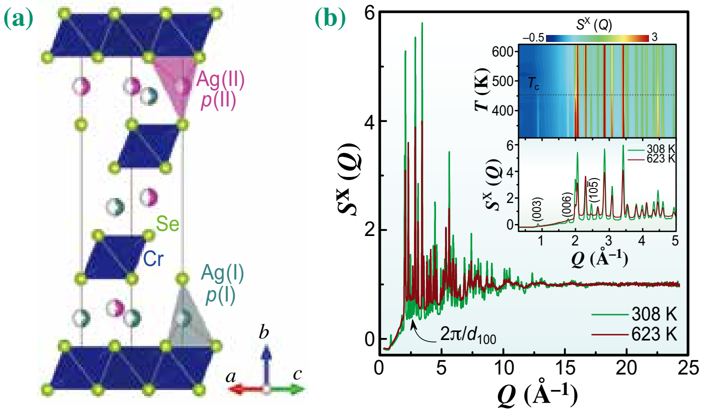

Fig. 1. **(a)** The crystal structure of $AgCrSe_2$. **(b)** The structure factor, $S^X(Q)$, obtained in X-ray scattering at 308 and 623 K. The diffuse scattering appears at about 2.0 Å^{-1}. The inset highlights $S^X(Q)$ at the small-Q region for temperature evolution (upper) and two end temperatures (lower).

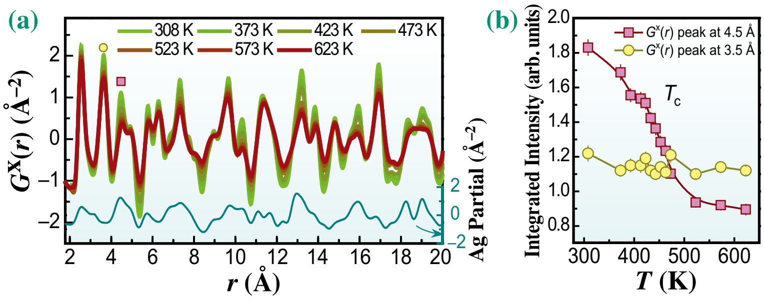

Fig. 2. **(a)** The experimental X-ray PDF, $G^X(r)$. Underneath is the superposition of partial $G^X(r)$ for Ag-involved pairs calculated on the $R3m$ crystal model. **(b)** The integrated intensity of $G^X(r)$ for the Ag-correlation-poor peak at 3.5 Å and the Ag-correlation-rich peak at 4.5 Å, which are labeled by a circle and a square in (a), respectively.

system is dominated by the local dynamics so that it is understandable that the global counterpart vanishes. Figure 3(a) and b shows inelastic neutron scattering $S(Q,E)$ with incident energy (E_i) of 5.931 meV at 150 and 520 K, respectively. It can be seen that pronounced diffuse scattering exists at $Q \sim 2.0$ Å^{-1}. At 150 K, the diffuse scattering appears just in the vicinity of the elastic line and TA phonons are fairly sharp. Nevertheless, the diffuse scattering becomes dominant at 520 K at the expense of Bragg peaks and TA phonons. Their evolution as a function of temperature is plotted in Fig. 3(c). TA phonons are softened and gradually merged into the diffuse scattering around T_C.

It is well-known that a solid conducts heat through both transverse and longitudinal acoustic phonons, but a liquid employs only longitudinal vibrations. As a result, a solid is usually thermally more conductive than a liquid. The present observation provides a unique example where a solid mainly conducts heat via longitudinal acoustic phonons. Moreover, it has important implications on tailoring the properties of thermoelectrics [5].

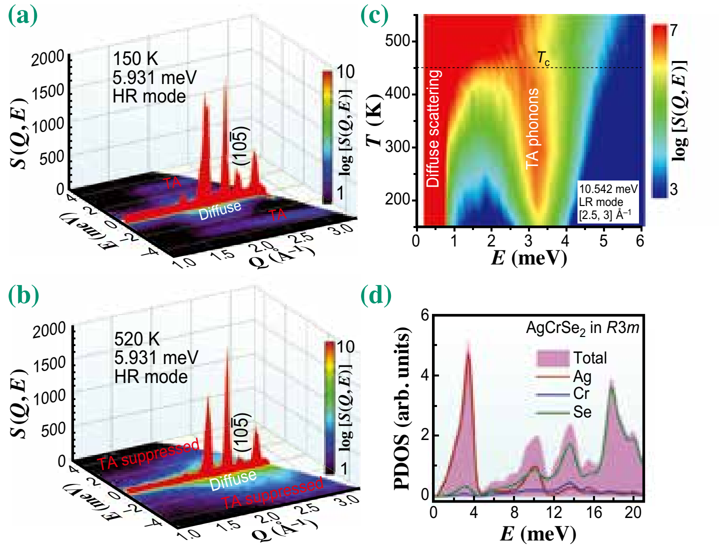

Fig. 3. **(a)** and **(b)** $S(Q,E)$ surface plots at 150 and 520 K at $E_\text{i} = 5.931$ meV obtained in inelastic neutron scattering measurements performed at AMATERAS of J-PARC. **(c)** Contour plot of $S(Q,E)$ as a function of temperature with $E_\text{i} = 10.542$ meV at Q of [2.5, 3] Å^{-1}. **(d)** Calculated phonon density of state (PDOS) of AgCrSe$_2$.

Bing Li

Institute of Metal Research,
Chinese Academy of Sciences, China

Email: bingli@imr.ac.cn

References

[1] J.G. Snyder and E.S. Toberer: Nat. Mater. **7** (2008) 105.
[2] G.J. Snyder *et al.*: Nat. Mater. **3** (2004) 458.
[3] H. Liu *et al.*: Nat. Mater. **11** (2012) 422.
[4] D.W. Murphy and H.S. Chen: J. Electrochem. Soc. **124** (1977) 1268.
[5] *B. Li, H. Wang, Y. Kawakita, Q. Zhang, M. Feygenson, H.L. Yu, D. Wu, K. Ohara, T. Kikuchi, K. Shibata, T. Yamada, X.K. Ning, Y. Chen, J.Q. He, D. Vaknin, R.Q. Wu, K. Nakajima and M.G. Kanatzidis: Nat. Mater.* **17** *(2018) 226.*

Microscopic origin of heat properties in ScN epitaxial film revealed by inelastic X-ray scattering spectroscopy

A challenge of next-generation devices (e.g., solar cells, thermoelectric devices, power devices) is to reduce the amount of energy wasted. In power devices, for instance, the applied high electric field easily causes overheating, resulting in operating failures. In thermoelectric devices and solar cells, lower energy loss is required for higher efficiency. In particular, in the coming years, these devices will be required to be compact while maintain their performance, and hence detailed knowledge of their heat properties and thermal management will be important for designing and fabricating these devices.

Phonons are the particles that carry heat in semiconductors and insulators. These particles have infinite lifetime in the harmonic approximation. However, once a particle merges with another particle or decays into two particles (as shown in Fig. 1(a)), the harmonic approximation is no longer satisfied, and the phonon has a finite lifetime. Thermal conductivity is directly correlated to the phonon lifetime; in other words, a (in)finite phonon lifetime corresponds to (in)finite thermal conductivity. On the one hand, in power device applications, good thermal conductivity (i.e., a long phonon lifetime) is desired. On the other hand, in thermoelectric applications, poor thermal conductivity (a short phonon lifetime) leads to a good thermoelectric figure of merit.

The phonon lifetime is a function of the phonon mode and momentum. The recent development of density functional theory (DFT) calculations now provides both the microscopic phonon lifetime, including the phonon-mode and momentum dependences, and the macroscopic thermal conductivity. Experimentally, the phonon lifetime with momentum dependence at a specific phonon mode has been estimated by observation of the phonon linewidth in inelastic neutron and X-ray scattering profiles [1,2]. Compared with neutron scattering, the attenuation length of X-rays is generally much smaller (<~1 mm), and tunable by changing the incident angle (α, Fig. 1(b)), which enables measurements of the phonon properties of films. In the previous literature, however, phonon lifetimes of bulk materials were estimated, and there have been no reports of the momentum-dependent phonon lifetime in epitaxial films.

We have observed the phonon lifetime of ScN, a promising thermoelectric material among the nitride semiconductors, using high-resolution inelastic X-ray spectroscopy (IXS) at SPring-8 **BL35XU** [3]. This material has a rocksalt structure, in which no phonon modes should be observed in the first-order Raman scattering, and therefore detailed phonon information remains unknown. In this study, we used an epitaxially grown ScN (110) film (thickness of 40 μm) on a sapphire substrate (m-plane). After optimizing the incident angle with respect to the surface of the film ($\alpha = 1.1–1.7°$ was used in the measurements), we obtained information only from the ScN film without artifacts from the substrate (as shown in Fig. 2, these spectra correspond to the phonon dispersion relation along the [q00] (right) and [qq0] (left) directions). Note that the obtained spectra in Fig. 2 are well reproduced by the DFT calculations.

To discuss the phonon lifetime in ScN, we estimated the profile linewidth of the longitudinal optical phonon mode along the [q00] direction (black dots in Fig. 3(a). The corresponding phonon dispersion is indicated by red arrows in Fig. 2). The phonon lifetime is short near the Γ point (around 0.2 ps) but long around the X point (more than ~3 ps). This indicates that phonon scattering (Fig. 1(a)) frequently occurs at Γ but rarely happens at X. Similar to the phonon dispersion in Fig. 2, the phonon lifetime is also reproduced by the DFT calculations (red line in Fig. 3(a)). Owing to this agreement, we can obtain the detailed phonon scattering process as shown in Figs. 3(b-d). Similar agreement between observation and calculations is obtained in the transverse phonon mode along the [q00] direction (the corresponding phonon dispersion is indicated by black arrows in Fig. 2).

The agreement between the experimental observation and DFT calculations of the phonon lifetime enables us to discuss the macroscopic thermal conductivity; the DFT calculation indicates that the thermal conductivity is 43 W/m/K at $T = 300$ K, which well reproduces the observed thermal conductivity, 36.4 W/m/K. This good agreement indicates that

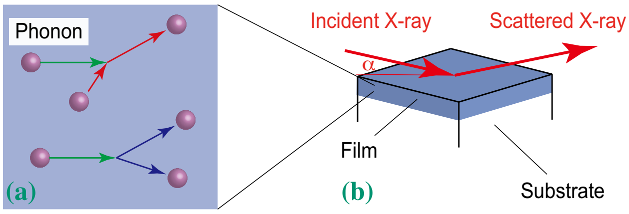

Fig. 1. **(a)** Phonon-phonon scattering mechanisms that reduce the thermal conductivity. **(b)** Schematic of experimental setup; thin film on substrate and path of X-ray used in the experiment.

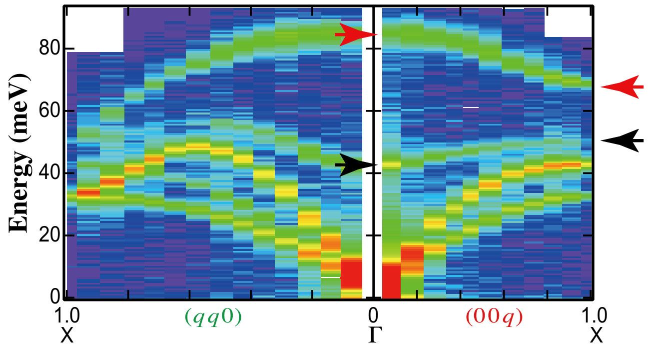

Fig. 2. Phonon dispersion curves in ScN film observed by inelastic X-ray scattering spectroscopy.

the origin of macroscopic thermal conductivity can be explained by the macroscopic phonon scattering mechanism as shown in Fig. 1(a). In the previous reports, this material has relatively low thermal conductivities of 10–20 W/m/K. However, our study reveals that the material has potentially higher thermal conductivity from the viewpoints of both observation and calculations. Through the comparison of the carrier and thermal conductivities in the literature, we found that impurities and defects may have reduced the thermal conductivity in the previous reports.

The present work demonstrates that the microscopic mechanism of thermal properties in a thin film, which is similar to an actual device environment, can be clarified by comparing the IXS profiles with the results of thermal conductivity measurements and calculated data. The achievements of this study are expected to be used to evaluate the thermal properties of leading-edge energy-efficient/energy creation devices such as thermoelectric devices that convert heat into electricity, highly efficient power semiconductor devices with low energy loss, and next-generation solar cells.

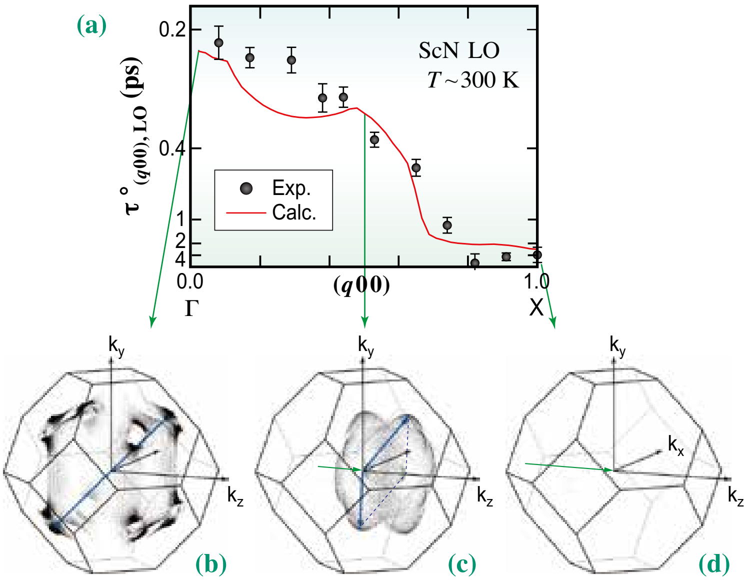

Fig. 3. **(a)** Experimentally obtained phonon lifetime (black solid circles) and lifetime in the DFT calculations (red line). **(b)-(d)** Plot of the calculated phonon-phonon scattering mechanism. The blue arrows in (b) and (c) show one pair of decay phonons from the original (q00) phonon (green arrow). Near the X point, phonon scattering (black dots) rarely occurs, as shown in (d). Blue and green arrows in (b)-(d) correspond to the phonon scattering mechanism depicted in Fig. 1(a) with the same colors.

Hiroshi Uchiyama

Japan Synchrotron Radiation Research Institute (JASRI)

Email: uchiyama@spring8.or.jp

References

[1] O. Delaire *et al.*: Nat. Phys. **10** (2011) 614.
[2] D.J. Voneshen *et al.*: Nat. Mater. **12** (2013) 1028.
[3] *H. Uchiyama, Y. Oshima, R. Patterson, S. Iwamoto, J. Shiomi and K. Shimamura: Phys. Rev. Lett.* ***120*** *(2018) 235901.*

Nature of charge density waves in the cuprate high-T_c superconductors

In conventional metals, the valence electrons are spread uniformly throughout the material. But in some substances, such as high-temperature superconductors (HTSCs), the electrons can form periodic modulations known as charge density waves (CDWs) which deform the underlying atomic crystal lattice of the metal. In 2012, researchers discovered this electronic state in the HTSC $YBa_2Cu_3O_{6+\delta}$, triggering intense debate about whether this behavior has the same origin as charge correlations discovered in another HTSC family, $La_{2-x}Ba_xCuO_4$, over twenty years ago [1,2]. Now, an international research team lead by Brookhaven National Laboratory has used state-of-the-art inelastic X-ray scattering (IXS) instrumentation at SPring-8 **BL43LXU** to examine the CDW correlations in $La_{2-x}Ba_xCuO_4$ through its interaction with collective lattice motions. The researcher found strong experimental evidence to support a unified CDW mechanism in high-temperature superconductors [3].

The research started by determining the collective lattice motions, also known as phonons, of $La_{1.875}Ba_{0.125}CuO_4$ at the room temperature. As shown in Fig. 1, two phonon modes, M1 and M2, are experimentally identified, and in agreement with the first principle calculations. From the calculations, the researchers ascertain that these modes are primarily associated with *z*- and *y*-direction motions of the La and Cu atoms. By gradually cooling the sample down, the researchers are able to track the temperature dependent changes of these phonons down to –265°C. Figure 2 shows representative experimental spectra at different temperature and different *K*. Strong temperature dependence is seen at the CDW wavevector $K = 0.23$ in reciprocal lattice units (r.l.u.), whereas the $K = 0.09$ and 0.35 r.l.u. show no obvious temperature dependence. By carefully analyzing and fitting the experimental data, the researcher discovered a large phonon softening associated with precursor CDW fluctuations. Significantly, as shown in Fig. 3, the phonon softening wavevector of the precursor CDW changes from 0.238 r.l.u. at –265°C to 0.3 r.l.u. at room temperature.

In cuprates, the origin of the CDW is under debate between reciprocal space pictures such as Fermi-surface nesting and real space pictures with strong magnetic and Coulomb interactions. In the first class of scenarios, the most important property of the

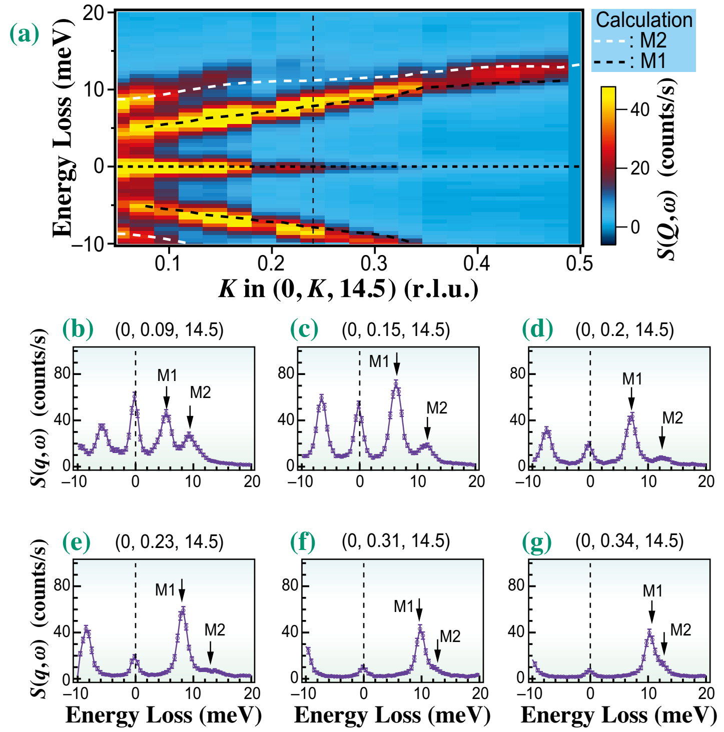

Fig. 1. **(a)** Color map around (0, *K*, 14.5) for $K = 0 \rightarrow 0.5$ r.l.u., showing two phonon modes labeled M1 and M2 that match theoretical predictions shown as dashed lines. **(b)-(g)** Representative experimental spectra at $K = 0.09$, 0.15, 0.2, 0.23, 0.31 and 0.34 r.l.u., respectively.

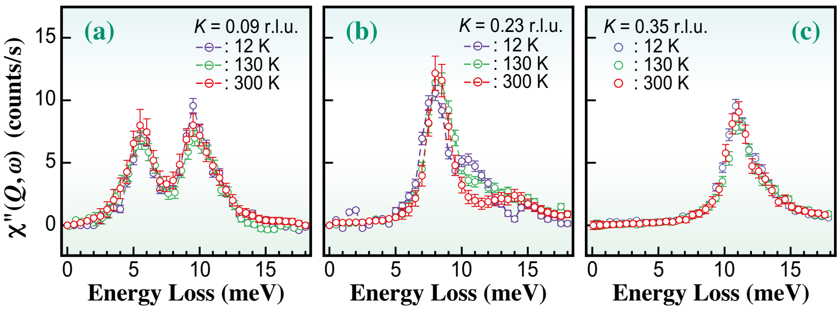

Fig. 2. Temperature dependence of the $La_{1.875}Ba_{0.125}CuO_4$ phonon spectra. **(a)–(c)** Elastic-line-subtracted and Bose-factor-corrected IXS spectra at K = 0.09, 0.23, and 0.35 r.l.u., respectively. Purple, green, and red circles correspond to data at 12, 130, and 300 K, respectively. Strong temperature dependence is seen at 0.23 r.l.u., whereas the K = 0.09 and 0.35 r.l.u. show no obvious temperature dependence.

ground state is the wave vector. Here, the temperature dependence of the incommensurability shown in Fig. 3 does not match theoretical expectations based on the Fermi surface. These scenarios would predict that the CDW wave vector should either decrease at higher temperatures or be temperature independent, neither of which is observed here. Instead, real space pictures are likely more important. These include those based on the competition between minimizing the number of broken magnetic bonds and kinetic energy and Coulomb repulsion between the doped holes. In such scenarios, the ordering wave vector arises from a balance between different ordering tendencies and is not a crucial defining parameter of the mechanism. These scenarios are more compatible with our observed variation of the CDW wave vector with temperature, which implies that the CDW wave vector is not solely defined by doping. It should be noted that a similar conclusion has been put forward based on STM studies of $Bi_2Sr_2CaCu_2O_{8+x}$, where the authors found that the local CDW wave vector is doping independent and that the change of the wave vector is due to “phase slips” in the CDW domain boundaries and hence not a fundamental property of the CDW [4].

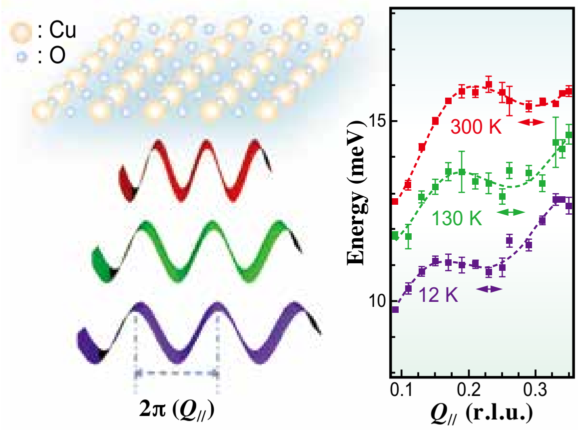

Fig. 3. Illustration of CDW periods associated with different wavevectors, $Q_{//}$. Phonon dispersions of M2 at 12, 130, and 300 K along (0 K 14.5) are shown as purple, green, and red squares. Dashed lines are guides to the eye, and arrows indicate the Q associated with the CDW-related phonon softening. Dispersions at 130 and 300 K are offset by 1.5 and 3 meV, respectively, for clarity.

Hu Miao* and Mark P. M. Dean

Condensed Matter Physics and Materials Science Dept.,
Brookhaven National Laboratory, USA

*Email: hmiao@bnl.gov

References

[1] R. Comin and A. Damascelli: Annu. Rev. Condens. Matter Phys **7** (2016) 369.
[2] H. Miao *et al.*: Proc. Natl. Acad. Sci. USA **114** (2017) 12430.
[3] *H. Miao, D. Ishikawa, R. Heid, M. Le Tacon, G. Fabbris, D. Meyers, G.D. Gu, A.Q. R. Baron and M.P.M. Dean: Phys. Rev. X* ***8*** *(2018) 011008.*
[4] A. Mesaros *et al.*: Proc. Natl. Acad. Sci. USA **113** (2016) 12661.

Three-dimensional observation of magnetic domain structure by scanning hard X-ray microtomography

Over a century ago, Weiss theoretically predicted that ferromagnets have internal structures called magnetic domains: magnetization directions are uniform in an individual domain and may be different in different domains. Afterward, researchers found that magnetic domain structures reflect the fundamental magnetic properties of materials. Since the first experimental confirmation of the presence of a domain structure by Bitter, observation of the magnetic domain structure has been an important technique for understanding the magnetic characteristics of systems including practical magnetic materials. Today, observation at a high spatial resolution of a few 10 nm to 100 nm is possible with various magnetic microscopy techniques: magnetic force microscopy (MFM), magneto-optical Kerr microscopy, photoemission electron microscopy (PEEM), and scanning transmission soft X-ray microscopy (STXM). However, most of the existing techniques are limited to observations at the sample surface, where the magnetic domain structures are two-dimensional. The magnetic domain structure inside a bulk sample generally has a three-dimensional (3D) distribution and is closely related to the magnetic properties of the bulk system. For example, the 3D network domains inside sintered permanent magnets are related to the mechanism of magnetization reversal and the emergence of high coercivity. Elucidating 3D magnetic domains in a permanent magnet is an important task in materials science. Moreover, visualizing the topographic spin arrangement in spintronic materials is an intriguing subject in fundamental physics. Such research will also greatly contribute to technological applications. To date, only a few studies of 3D domain observations have been reported [1-3], including the successful 3D vectorial reconstruction of magnetic domains of $GdCo_2$ alloys via X-ray ptychography imaging by Donnelly *et al.* [3] In this study, we present another X-ray tomographic technique that allows observation of the internal magnetic domain structure in a micrometer-size ferromagnetic sample [4]. The technique is based on a scanning hard-X-ray nanoprobe using X-ray magnetic circular dichroism (XMCD). We demonstrate the 3D distribution of a single component of the magnetization vector in a GdFeCo microdisk, which has been reconstructed with a spatial resolution of 360 nm. This technique is applicable to practical magnetic materials including permanent magnets with sintered microstructures. 3D visualization of the magnetic domain formation process under external magnetic fields will be feasible.

Figure 1 shows the experimental setup for the scanning hard-X-ray microtomography constructed at the X-ray nanospectroscopy station of SPring-8 **BL39XU** [5]. The hard X-ray radiation from the in-vacuum standard undulator was monochromatized with a Si 111 double-crystal monochromator. A 0.45-mm-thick diamond X-ray phase retarder was used to generate circularly polarized X-ray beams of switchable photon helicity. Two elliptical mirrors in the Kirkpatrick-Baez configuration were used to focus the circularly polarized X-ray beam in the vertical and horizontal directions. The resulting X-ray beam size

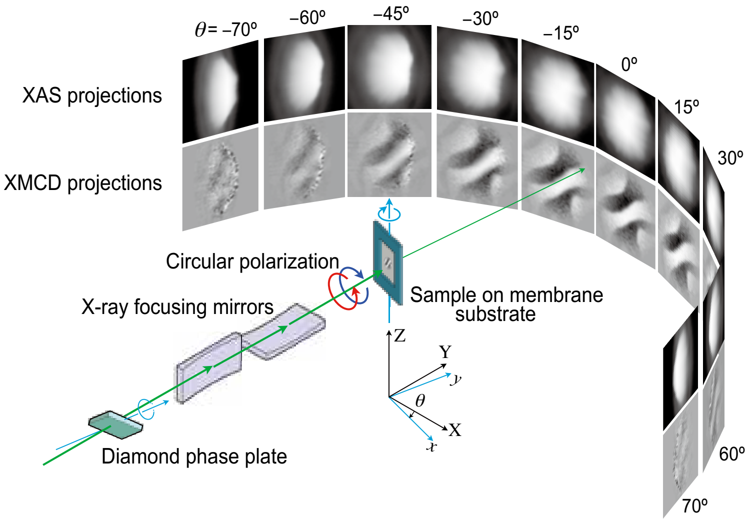

Fig. 1. Experimental setup of scanning hard-X-ray magnetic tomography. A cartoon scheme of a collection of XAS projections and magnetic contrast via XMCD projections at various angles is also shown.

was 130 (horizontal) × 140 (vertical) nm^2 in full width at half maximum (FWHM) at the sample position. To demonstrate the magnetic tomography technique, a microdisk made of $Gd_{22}Fe_{68}Co_{10}$ alloy was used as a sample. This material exhibits perpendicular magnetic anisotropy and maze-like domain structures with stripe widths of 2–3 μm. The sample was grown on a SiN membrane substrate by magnetron sputtering and then patterned into a disk shape by optical lithography and Ar ion milling. The diameter and thickness of the disk are approximately 7 and 3 μm, respectively. The microdisk sample was mounted on high-precision stages with X-Y translations and a vertical (Z)-axis rotation. X-ray absorption (XAS) images were taken by scanning the sample two-dimensionally in the plane perpendicular to the incident X-ray beam. Scanning magnetic images were simultaneously recorded by monitoring the XMCD signals using the helicity-modulation technique [4]. Figure 1 shows a cartoon scheme of taking images for tomographic reconstruction; the projected XAS and XMCD images were collected as a function of the rotation angle θ of the sample.

Figure 2 shows the 3D reconstruction of the GdFeCo magnetic microdisk. To reconstruct 3D XAS images, the standard algorithm of the algebraic reconstruction technique (ART) was applied to 37 projection images collected at angles from –70 to +70° with a step of 5°. The XAS reconstruction revealed that the sample was mostly homogeneous in composition. To reconstruct a 3D magnetic image, a modified ART algorithm was applied to XMCD projections taken at the same angles as those in XAS. In the modified ART, strong uniaxial anisotropy of the sample is assumed and a correction for the cosθ dependence of the XMCD amplitude is included [4]. In Fig. 2, a cutaway view of the XMCD reconstruction result demonstrates the 3D distribution of the magnetization inside the GdFeCo disk. The color scales correspond to the direction and the amplitude of magnetization perpendicular to the film. Five striped magnetic domains were clearly observed. The spatial resolution of the 3D XMCD reconstructed image was estimated to be 360 nm from the widths of the observed domain boundaries [4].

Our scanning hard-X-ray microtomography technique is applicable to various kinds of ferromagnetic samples including sintered permanent magnets. We are developing magnetic tomographic measurements under an external magnetic field for 3D observation of the evolution of magnetic domains in a bulk. The present setup has a relatively large sample space, making it suitable for introducing a specially designed magnet to allow tomographic measurement under a variable magnetic field. Additionally, the scanning X-ray setup can easily be modified for X-ray fluorescence microtomography and used to study the correlation between the magnetic domains and the elemental distribution via chemical and magnetic 3D imaging. Furthermore, in this study, a sample with uniaxial magnetic anisotropy was assumed and the distribution of only one component of the magnetization vector was obtained. Improvement in the experimental procedure, as well as in the reconstruction algorithm, is ongoing to achieve magnetic vector tomography [2,3].

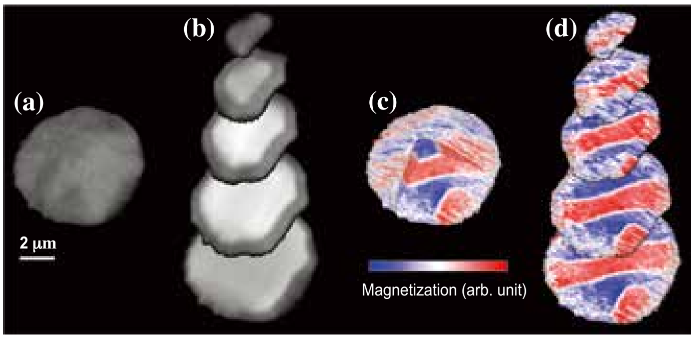

Fig. 2. 3D reconstruction images of GdFeCo microdisk. **(a)** Density distribution obtained by X-ray absorption tomography. **(b)** Cross-sectional images of the density distribution. **(c)** Magnetization distribution obtained by XMCD tomography. **(d)** Cross-sectional images showing the magnetization distribution inside the micrometer-size sample.

Motohiro Suzuki[a,*] and Teruo Ono[b]

[a] Japan Synchrotron Radiation Research Institute (JASRI)
[b] Institute for Chemical Research, Kyoto University

*Email: m-suzuki@spring8.or.jp

References

[1] I. Manke *et al.*: Nat. Commun. **1** (2010) 125.
[2] T. Tanigaki *et al.*: Nano Lett. **15** (2015) 1309.
[3] C. Donnelly *et al.*: Nature **547** (2017) 328.
[4] *M. Suzuki, K.-J. Kim, S. Kim, H. Yoshikawa, T. Tono, K. T. Yamada, T. Taniguchi, H. Mizuno, K. Oda, M. Ishibashi, Y. Hirata, T. Li, A. Tsukamoto, D. Chiba and T. Ono: Appl. Phys. Express **11** (2018) 036601.*
[5] M. Suzuki *et al.*: J. Phys. Conf. Ser. **430** (2013) 012017.

Direct band bending observation by angular-resolved HAXPES for semiconductor films in contact with metal nanoparticles

Systematic combinations of metals and semiconductors are widely applied and important for devices such as sensors, power devices, solar cells, and photocatalysts for solar energy conversion and environmental purification. In photocatalysis, photocatalytic activity is improved by the surface adsorption of metal or metal oxide co-catalysts. For example, volatile organic compounds (VOCs) are decomposed by photoexcited TiO_2. This decomposition is accelerated by surface loading with nanoscale Pt (Pt/TiO_2). For solar energy conversion, Pt/TiO_2 is used to split water for the stoichiometric production of hydrogen and oxygen under ultraviolet light irradiation, in which a nanoscale Pt co-catalyst attached to TiO_2 plays a significant role in improving chemical reaction rates [1]. Although the nanoscale Pt functions as an effective co-catalyst for TiO_2, it cannot be universally applied to all semiconductors. For example, a Pt co-catalyst does not enhance photocatalytic H_2 production in water splitting over semiconductor photocatalysts such as TaON and Ta_3N_5 [2]. This suggests that the difference in photocatalytic activity is responsible for the difference in the electronic states of both nanoscale co-catalysts and semiconductors after the formation of metal-semiconductor junctions. However, this phenomenon has not been clarified experimentally.

The position of the energy band can be directly measured by photoelectron spectroscopy. In hard X-ray photoemission spectroscopy (HAXPES), raising the X-ray photon energy for excitation extends the analysis depth compared with the case of XPS measurements. Thus, band bending in semiconductors from the bulk to the surface can be measured dynamically by angular distribution of HAXPES peak (angle-resolved HAXPES), which reflects depth profile of the electronic structures [3].

In this paper, we describe the direct observations of band bending near the surfaces of films of bare TiO_2, nanoscale metal-adsorbed TiO_2, bare N-doped Ta_2O_5 (N-Ta_2O_5), and nanoscale metal-adsorbed N-Ta_2O_5 by angular-resolved HAXPES, which was conducted at SPring-8 **BL47XU** using a photon energy of 7940 eV. Our results clearly showed that the Mott-Schottky rule for metal-semiconductor junctions was not applicable to semiconductors with adsorbed nanoscale metals, because the electrostatic potentials between them are mainly dominated by the electric dipole in the ground state. The data presented in this report provides new insights into electrostatic interactions at the junctions in the ground state [4].

Figure 1 shows HAXPES spectra for Ti $2p_{3/2}$ and Ta $3d_{5/2}$ core state photoemissions. The bare TiO_2 films at take-off-angles of 65° (bulk phase; maximum analysis depth of *ca.* 31 nm) and 10° (surface; maximum analysis depth of *ca.* 6 nm) produced similar spectra without any significant shifts. On the other hand, the peak for N-Ta_2O_5 at take-off-angles of 10° (surface; maximum analysis depth of *ca.* 5 nm) shifted by 0.4 eV to a higher binding energy than that at a take-off-angle of 65° (bulk phase; maximum analysis depth of *ca.* 24 nm). However, upon deposition with nanoscale Pt, markedly different spectra were observed. For example, the film (Pt/TiO_2) exhibited upward band bending by 0.07 eV with the binding energy peak for a nearby surface (take-off-angle of 10°) positioned higher than that for the bulk (angle of 65°). In addition, the peak position of Ti $2p_{3/2}$ bulk (65°) of bare TiO_2 was shifted negatively by 0.25 eV by the deposition of Pt (Pt/TiO_2) as shown in Fig. 1(a). A strong electrostatic interaction was also obtained for a N-Ta_2O_5 film deposited with Pt (Pt/N-Ta_2O_5). The large downward band bending observed in a bare N-Ta_2O_5 film (0.40 eV) was also greatly reduced to 0.05 eV by the surface deposition of nanoscale Pt. Almost the same phenomenon was observed using other metal nanoparticles such as Au and Rh. In general, the degree

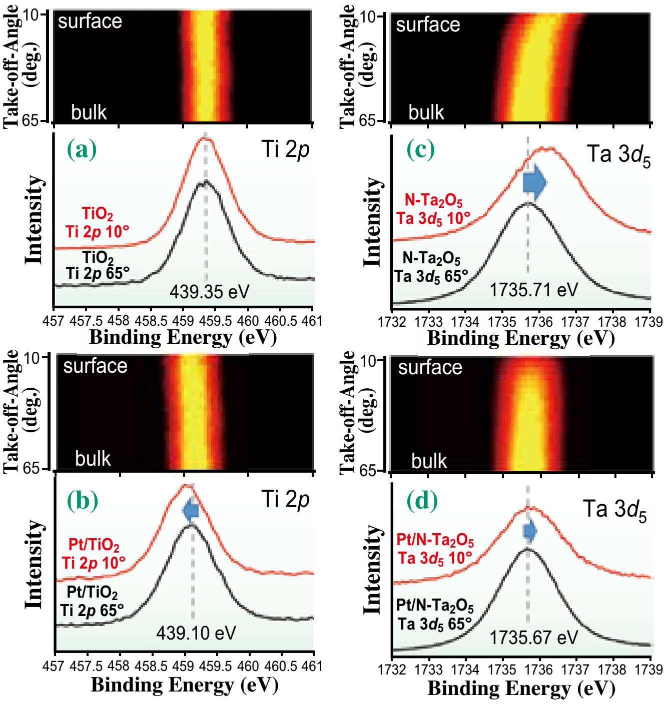

Fig. 1. Series of Ti $2p_{3/2}$ spectra measured on **(a)** TiO_2 and **(b)** Pt/TiO_2 using angular-resolved HAXPES [take-off angles 10° (red line) and 65° (black line)]. The upper panel shows a single shot of Ti $2p_{3/2}$ peaks from a 2D image for take-off angles from 10° to 65°. Series of Ta $3d_{5/2}$ spectra measured on **(c)** N-Ta_2O_5 and **(d)** Pt/N-Ta_2O_5 by angular-resolved HAXPES (take-off angles of 10° and 65°). The upper panel shows a single shot of Ta $3d_{5/2}$ peaks from a 2D image of take-off angles from 10° to 65°. Adapted from Ref. 4 with permission from the PCCP Owner Societies.

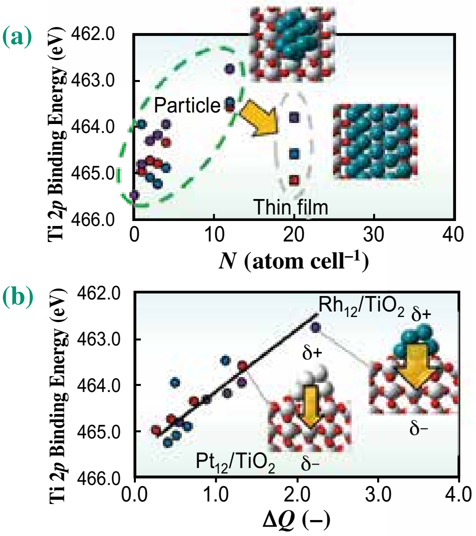

Fig. 2. **(a)** Binding energy of the Ti $2p_{3/2}$ peak for metal particles or thin films on TiO_2 calculated using DFT [red circles: Pt particles on TiO_2; blue circles: Au particles on TiO_2; purple circles: Rh particles on TiO_2; red squares: thin Pt film on TiO_2; blue squares: thin Au film on TiO_2; purple squares: thin Rh film on TiO_2] **(b)** Relation between calculated binding energy of Ti $2p_{3/2}$ peak and intensity of charge transfer (ΔQ) between metal particles and TiO_2 film [red circles: Pt particles on TiO_2; blue circles: Au particles on TiO_2; purple circles: Rh particles on TiO_2]. [4]

and direction of band bending in metal-semiconductor junctions can be explained by the difference in their work functions using the Mott-Schottky model [5]. The work functions of Pt, Au, and Rh are 5.65 eV, 5.1 eV, and 4.9 eV, respectively, which are greater than that of TiO_2 (4.5 eV). Therefore, the upward band bending in the metal/TiO_2 films observed by HAXPES was consistent with the Mott-Schottky rule. However, the peak shift cannot be explained by the Mott-Schottky rule. This result indicated that there is a strong interaction between the metal nanoparticles and the semiconductor in the ground state.

To clarify the reason for the peak shift upon the adsorption of metal nanoparticles, we attempted to simulate the phenomenon by density function theory (DFT) calculation. Results of the DFT calculation are shown in Fig. 2. It was found that all of the Ti $2p_{3/2}$ peaks of TiO_2 films with metals were shifted negatively from that for the bare TiO_2 film (Fig. 2(a)). Figure 2(b) shows the calculated binding energies of the Ti $2p_{3/2}$ peak as a function of the intensity of the charge transfer between TiO_2 and the metals. This result indicated that the negative peak shift of Ti $2p_{3/2}$ is determined by the amount of charge transfer from the nanoscale metal to TiO_2. This charge transfer forms the dipole moment at the interface and thus results in a shift of the electrostatic potential.

Figure 3 is a schematic drawing of the summarized results, which can be conducted by angle-resolved HAXPES. As a result of charge migration from the nanoscale metal to the semiconductor, the electric dipole formed at the surface modifies the electrostatic potential in the ground state, resulting in band bending and a band shift (Fermi level shift) as shown in Fig. 3(b). This illustrates a major difference from the Mott-Schottky rule normally observed in a solid-state junction composed of a bulk metal and a semiconductor as shown in Fig. 3(a). Although we usually use a co-catalyst such as nanoparticle metals to improve the catalytic activity of a semiconductor photocatalyst, the semiconductor band potentials can be affected by them. Therefore, if we use metal nanoparticles as photocatalysts, devices, and so forth, we will have to consider the electric dipole from the nanoparticles.

In conclusion, angle-resolved HAXPES measurements can simultaneously evaluate the electronic states of both the surface and bulk of a semiconductor film. From the HAXPES and DFT results, it was revealed that the dipole moment from metal nanoparticles strongly affects semiconductor properties such as the band position and bending.

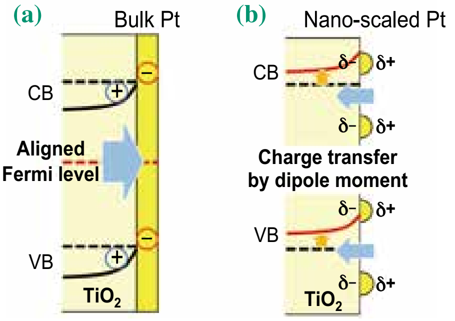

Fig. 3. Schematic illustration of metal and n-type semiconductor (TiO_2) contact: **(a)** between the bulk metal and TiO_2 (ideal state according to Mott-Schottky rule); **(b)** between nanoscale metal and TiO_2 (charge migration from metal to semiconductor with dipole moment). Black solid line shows CB and VB after contact between the bulk metal and semiconductor; black dashed line shows CB and VB before contact between the metal and semiconductor; red solid line shows CB and VB after contact between the nanoscale metal and semiconductor. δ shows polarization of materials.

Shunsuke Sato* and Takeshi Morikawa

Toyota Central R&D Labs., Inc.

*Email: ssato@mosk.tytlabs.co.jp

References

[1] A. Furube *et al.*: J. Phys. Chem. B **103** (1999) 3120.
[2] M. Hara *et al.*: Chem. Commun. (2003) 300.
[3] E. Ikenaga *et al.*: J. Electron Spectrosc. Relat. Phenom. **190** (2013) 180.
[4] *S. Sato, K. Kataoka, R. Jinnouchi, N. Takahashi, K. Sekizawa, K. Kitazumi, E. Ikenaga, R. Asahi and T. Morikawa: Phys. Chem. Chem. Phys.* ***20*** *(2018) 11342.*
[5] R. Tung: Mater. Sci. Eng. R **35** (2001) 1.

Experimental determination of the topological phase diagram by soft X-ray angle-resolved photoemission spectroscopy

The discovery of topological insulators represents significant progress in topological band theory [1]. They are characterized by a nontrivial Z_2 topological invariant (ν_0: $\nu_1\nu_2\nu_3$); each of these four invariants takes a value of either 0 or 1, indicating 16 phases with three general classes according to Ref. 1. This nontrivial Z_2 invariant can be realized only if the conduction and valence bands are inverted by spin-orbit coupling (SOC). In the three-dimensional case, the band inversion gives rise to topological surface states (TSSs) inside the energy gap. Owing to the bulk-edge correspondence, investigations of the in-gap TSS in principle can reveal the band topology of the bulk states. In fact, surface-sensitive angle-resolved photoemission spectroscopy (ARPES) with vacuum ultraviolet (VUV) light has achieved great success in confirming the Dirac-cone-like TSS in a number of chalcogenides and obtained excellent agreement with the predicted nontrivial Z_2 topology [1].

However, searches of the topological phase are still challenging in low-carrier semimetals such as rare-earth monopnictides LnX (Ln: La or Ce; X: P, As, Sb, or Bi). The main difficulty comes from two issues. One is that a band calculation can lead to controversial conclusions about their band topology [2], since the magnitude of band gaps can often be misestimated in such low-carrier systems, and thus the experimental determination is crucial. Secondly, despite this, the experimental confirmations have so far been limited to the observation of the surface dispersions predicted by calculations [3,4]. In this study, we present an alternative approach to determine the band topology by means of bulk-sensitive soft X-ray ARPES (SX-ARPES) [5]. For this demonstration, we adopt a series of materials of CeX. By the paradigmatic investigation of the electronic structures from CeP to CeBi as a function of their SOC, we draw the topological phase diagram and unambiguously reveal the topological phase transition from a trivial to a nontrivial regime induced by the band inversion.

Single crystalline CeX's were grown by the Bridgman method. Bulk-sensitive SX-ARPES measurements were performed at SPring-8 **BL25SU**. The total experimental energy resolution was set to about 70–90 meV for photon energies ($h\nu$) of 500–760 eV. All samples were cleaved at a pressure of 5×10^{-8} Pa at approximately 60 K, exposing shiny surfaces corresponding to the (001) plane of the NaCl crystal structure.

We start with comparing the bulk electronic structures of the CeX's. By tuning $h\nu$ in the SX range, we observe their bulk band dispersions selectively cut along the high-symmetry X-Γ-X line (Fig. 1). By systematically examining the electronic structures, we find the SOC effect and its evolution. We find three important consequences of the SOC. Firstly, valence bands at Γ point originating from pnictogen p orbitals split into the $p_{1/2}$ and $p_{3/2}$ states. The magnitude of the splitting varies substantially across the series of compounds. Secondly, the SOC also induces valence band splitting at the X point. The large SOC pushes the X1 (X2) band up (down) in energy [red (green) arrows in Fig. 1]. The splitting becomes significant with increasing SOC. Thirdly, for CeSb and CeBi, the

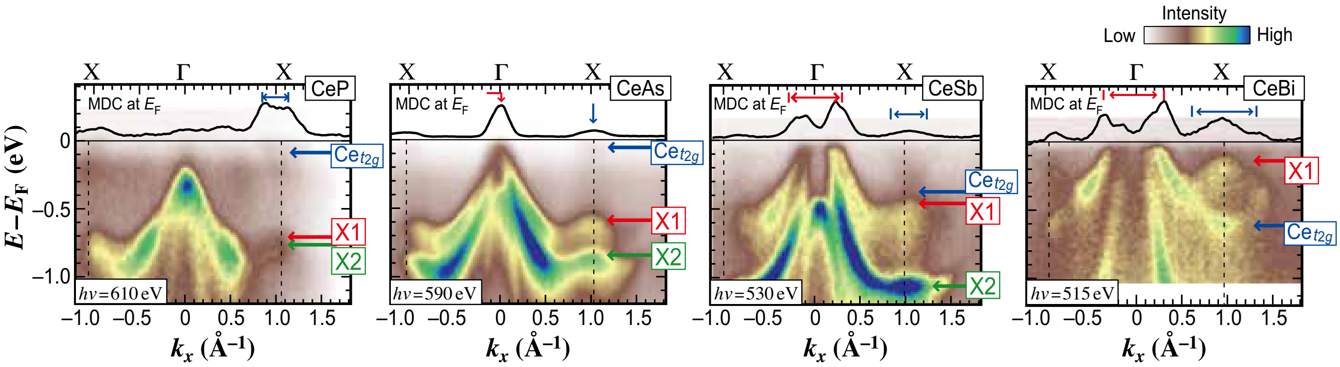

Fig. 1. SX-ARPES band maps and (inset) their momentum distribution curves (MDCs) for CeX's obtained at $h\nu$ of (CeP) 610 eV, (CeAs) 590 eV, (CeSb) 530 eV, and (CeBi) 515 eV, cut along the high symmetry X-Γ-X line in the 3D Brillouin zone. The hole X1 ($Ce_{t_{2g}}$ electron) bands are shown by red (blue) arrows.

higher-lying $p_{3/2}$ bands at the Γ point are pushed above E_F due to the large SOC, and hole pockets appear [red arrows in inset].

The third effect triggers a dynamical change in the Ce$_{t2g}$ electron band. The SOC evolution of the hole pockets should increase the size of the electron pocket at the X point to compensate their carriers, since the CeX series materials have a similar low carrier density. This carrier compensation is necessary in the semimetallic structure of CeX's. This electron band evolution is captured by blue arrows in Fig. 1. For CeAs, both the hole and electron pockets are quite small. With the increasing size of the hole pocket at the Γ point from CeAs to CeBi, the electron band bottom appears to decrease energy. This eventually leads to the band inversion in CeBi.

On the basis of the SX-ARPES results, one can now draw the topological phase diagram of CeX's (Fig. 2). The topological phase transition is elucidated by SOC in collaboration with the carrier compensation of the semimetallic structures. CeSb is trivial but close to a phase transition state, whereas CeBi is classified into a nontrivial phase owing to the band inversion. The band inversion process visualized by SX-ARPES is the most fundamental feature of the topological matter; therefore, the presented nontrivial topology of CeBi is identified without surface information.

In summary, we performed bulk-sensitive SX-ARPES on CeX series materials and determined the topological phase diagram. Our experiment unambiguously demonstrated the topological transition from a trivial to a nontrivial phase across the border between CeSb and CeBi in the presented phase diagram. Moreover, the mechanism is explained by SOC in concert with the carrier-compensated semimetallic band structures. This work demonstrates a new capability of SX-ARPES to clarify the band topology, which can be widely applied for solid states as a complementary tool to surface-sensitive ARPES.

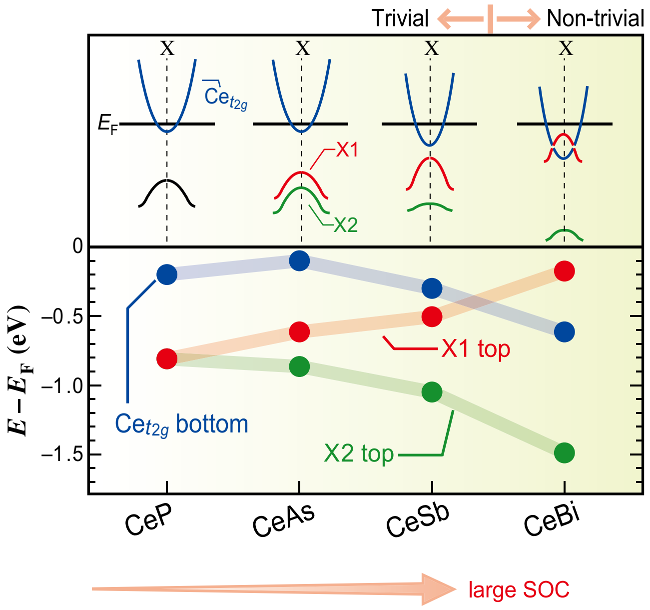

Fig. 2. Experimentally determined topological phase diagram with the energy positions of (blue) Ce$_{t2g}$, (red) X1, and (green) X2 bands. (Inset) Schematics of the band structures around X point.

Kenta Kuroda* and Takeshi Kondo

The Institute for Solid State Physics,
The University of Tokyo

*Email: kuroken224@issp.u-tokyo.ac.jp

References

[1] M.Z. Hasan and C.L. Kane: Rev. Mod. Phys. **82** (2010) 3045.
[2] P.-J. Guo *et al*.: Phys. Rev. B **93** (2016) 235142.
[3] X.H. Niu *et al*.: Phys. Rev. B **94** (2016) 165163.
[4] L. Meng *et al*.: Phys. Rev. Lett. **117** (2016) 127204.
[5] *K. Kuroda, M. Ochi, H.S. Suzuki, M. Hirayama, M. Nakayama, R. Noguchi, C. Bareille, S. Akebi, S. Kunisada, T. Muro, M.D. Watson, H. Kitazawa, Y. Haga, T.K. Kim, M. Hoesch, S. Shin, R. Arita and T. Kondo: Phys. Rev. Lett. **120** (2018) 086402.*

Tensile-strain-dependent spin states in epitaxial $LaCoO_3$ thin films

In transition metal compounds, charge, spin, and orbital degrees of freedom induced by a strong electron correlation realize various physical phenomena such as superconductivity, metal-insulator transition, and charge ordering [1]. The perovskite-type cobalt oxide $LaCoO_3$ is one of the most interesting materials because of its various electron degrees of freedom. Since the spin state of $LaCoO_3$ is sensitive to the crystal field, a spin crossover from the low-spin (LS) to high-spin (HS) state occurs upon increasing the temperature [2]. Epitaxial strain can also affect the spin states, and ferromagnetism is observed in $LaCoO_3$ thin films at lower temperatures ($\lesssim$85 K) [3-5]. In previous studies, the spin states of thin films were considered by the orderings of 3*d* electrons on the basis of resonant X-ray diffraction [3-5]. However, direct observations of the electronic structures are important to clarify the spin states. Since it is difficult to determine the spin states by conventional techniques such as X-ray absorption spectroscopy (XAS), we performed resonant inelastic soft X-ray scattering (RIXS) with the Co $2p \rightarrow 3d \rightarrow 2p$ process (*L* edge) [6]. RIXS is one of the most powerful techniques for clarifying the spin states by observing the *d*-*d* excitations.

$LaCoO_3$ epitaxial thin films (30 nm thickness) were fabricated on LSAT(110) and LSAT(111) $[(LaAlO_3)_{0.3}(SrAl_{0.5}Ta_{0.5}O_3)_{0.7}]$ substrates by pulsed laser deposition. The same substrates with different orientations enable us to observe the pure strain effects on XAS and RIXS spectra. The lattice constant of the LSAT substrate is 3.868 Å, whereas that of the $LaCoO_3$ bulk is 3.804 Å, indicating that tensile strains are applied to the $LaCoO_3$ epitaxial thin films grown on the LSAT substrates. The magnitudes of the tensile strains from the LSAT(110) and LSAT(111) substrates are 1.0% and 0.5%, respectively (strains are defined as the ratio of the cubic root of the unit cell volume) [3,4]. The XAS and RIXS experiments were performed at SPring-8 **BL07LSU** HORNET [7]. The RIXS measurements were performed with soft X-rays from 770 to 810 eV (Co $L_{3,2}$ edge). In this range of X-ray energies, the energy resolution is ~300 meV. A charge-coupled device (CCD) detector was set at 90° relative to the incident X-ray with horizontal polarization to suppress elastic scattering (see inset in Fig. 1(b)).

Co $L_{3,2}$ edge XAS spectra measured with the total electron yield (TEY) mode are shown in Fig. 1(a). The peaks at approximately 779 and 794 eV correspond to the Co L_3 and L_2 edges, respectively. Although the magnitude of the strain is different between LSAT(110) and LSAT(111), the XAS spectra are similar. To investigate the strain effect on the electronic structures from *d*-*d* excitations, we performed RIXS measurements. We selected energies of A: L_3 – 2.9 eV, B: L_3 – 1.5 eV, C: L_3 – 1.0 eV, D: L_3, E: L_3 + 1.7 eV, and F: L_2 as the excitation energies. The RIXS spectra of the $LaCoO_3$ thin films are shown in Fig. 1(b). These spectra are normalized with the intensity of the highest

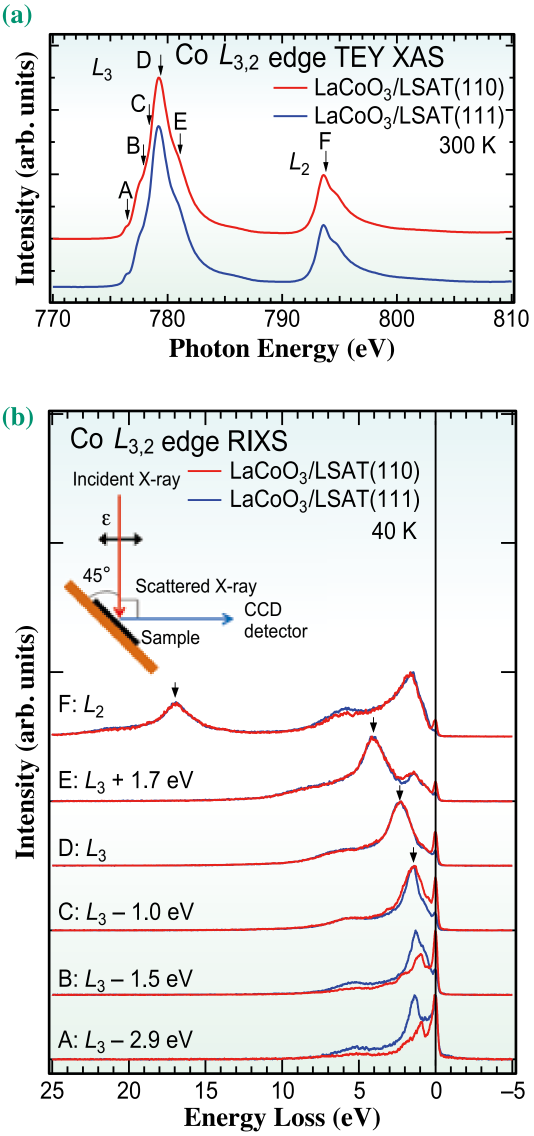

Fig. 1. Co $L_{3,2}$ edge **(a)** TEY XAS and **(b)** RIXS spectra of $LaCoO_3$ thin films grown on LSAT (110) and LSAT(111) substrates. All RIXS spectra are normalized by the intensity of the highest peak. The inset shows a schematic diagram of the experimental setup of RIXS.

peak. The thick solid line shows the center of the elastic scattering peaks, whereas the arrows indicate the fluorescence peaks. Other peaks from 0 to 4 eV correspond to the *d*-*d* excitations. In the spectra with the energies of A and B, the peaks of *d*-*d* excitations can be clearly observed. The *d*-*d* excitations are markedly different between the thin films on LSAT(110) with 1.0% tensile strain and LSAT(111) with 0.5% tensile strain, indicating that the spin states of $LaCoO_3$ change with the magnitude of the tensile strain. On the other hand, in the spectra excited by higher energies (C, D, E, and F), the peaks of *d*-*d* excitations are not clear owing to the overlapping with the larger florescent peak. Then, we selected the excitation energy A: L_3 – 2.9 eV and analyzed the spectra by impurity Anderson model calculations in O_h and D_{2h} local symmetries.

The experimental RIXS spectra excited with A: L_3 – 2.9 eV (776.5 eV) measured at 40 and 300 K and the theoretical spectra with several electronic states are shown in Fig. 2. The peaks observed at approximately 0.3 eV are assigned to the excitations from the HS ground states. On the other hand, the peaks observed at 1.3 eV correspond to the excitations from the LS ground states. However, the peaks at 1.0 eV in $LaCoO_3$/LSAT (110) cannot be explained by either the LS or HS state with O_h symmetry. From the comparison with the theoretical spectra, the peak for the HS state is shifted to 1.0 eV by lowering the symmetry from O_h to D_{2h}, indicating that the spin state of $LaCoO_3$/LSAT(110) consists of the HS states with different local symmetries, i.e., a mixture of O_h and D_{2h} symmetries.

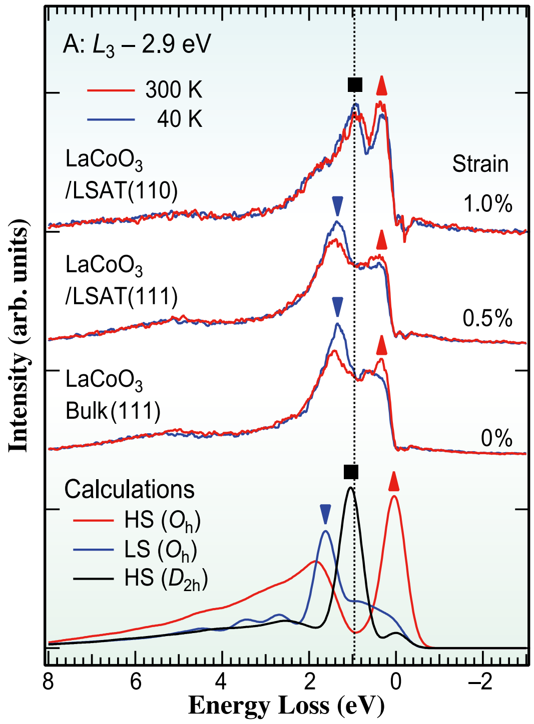

Fig. 2. Experimental RIXS spectra excited with A: L_3 – 2.9 eV (776.5 eV) measured at 40 and 300 K and the theoretical spectra in O_h and D_{2h} symmetries.

In this study, we performed RIXS measurements and revealed that the spin states of Co ions were different between the bulk crystal and thin film crystals. Although it is difficult to observe the strain effects on the spin states by conventional XAS measurements, a clear difference can be observed by RIXS.

Yuichi Yokoyama[a,b] and Hiroki Wadati[b,*]

[a] National Institute for Materials Science, NIMS
[b] Institute for Solid State Physics, The University of Tokyo

*Email: wadati@issp.u-tokyo.ac.jp

References

[1] M. Imada *et al*.: Rev. Mod. Phys. **70** (1998) 1039.
[2] M.W. Haverkort *et al*.: Phys. Rev. Lett. **97** (2006) 176405.
[3] J. Fujioka *et al*.: Phys. Rev. Lett. **111** (2013) 027206.
[4] J. Fujioka *et al*.: Phys. Rev. B **92** (2015) 195115.
[5] Y. Yamasaki *et al*.: J. Phys. Soc. Jpn. **85** (2016) 023704.
[6] *Y. Yokoyama, Y. Yamasaki, M. Taguchi, Y. Hirata, K. Takubo, J. Miyawaki, Y. Harada, D. Asakura, J. Fujioka, M. Nakamura, H. Daimon, M. Kawasaki, Y. Tokura and H. Wadati: Phys. Rev. Lett.* ***120*** *(2018) 206402.*
[7] Y. Harada *et al*.: Rev. Sci. Instrum. **83** (2012) 013116.

Shedding light on the coercivity mechanism in Nd-Fe-B sintered magnets through high-field magnetic domain observations

Nd-Fe-B sintered magnets are being used everywhere in modern life because they are the best permanent magnets we currently have. However, from an industrial perspective the next-generation of green-energy applications such as electric vehicles and wind turbines will require higher-performance permanent magnets than those currently available. In order to make technological progress, understanding their coercivity mechanism and its relationship with the microstructure is vitally important. Elucidating the coercivity mechanism requires detailed knowledge of where reversed magnetic domains are nucleated and how they propagate.

Some recent studies have implied that the fractured and polished surfaces of Nd-Fe-B permanent magnets reflect the interior and exterior magnetic states, respectively, because the coercivity of the fractured surface is very similar to the bulk, while the coercivity of the polished surface is drastically reduced. This degradation is thought to occur because the polishing process introduces numerous defects that facilitate the nucleation of additional reversed magnetic domains which, essentially, mask the true magnetic domain distribution. Contrary to the polished surface, the magnetic $Nd_2Fe_{14}B$ grains are not directly exposed; they are covered by a thin-film-like grain boundary phase due to the dominant grain boundary fracturing. Although magnetic domains in the polished surface of these materials have been investigated extensively, observations of the fractured surface have proven to be particularly challenging because of the technical difficulties in imaging the rough surface under magnetic fields large enough to saturate the magnet.

For the purpose of imaging element-specific magnetic distributions under high magnetic fields, a scanning soft X-ray absorption microscope has been developed at SPring-8 **BL25SU** [1] under the ESICMM (Elements Strategy Initiative Center for Magnetic Materials) project. Figure 1 shows a photograph of the scanning soft X-ray microscope apparatus. Circularly polarized soft X-ray photons, which are generated by twin helical undulators, are focused using a Fresnel zone plate to a beam size of about 100 nm at the sample surface. The scanning X-ray microscope utilizes total electron yield (TEY) detection of absorbed circularly polarized soft X-rays in order to observe magnetic domains through the X-ray magnetic circular dichroism effect. The TEY method is advantageous because it allows us to observe magnetic domains in the surface of non-transmittable samples. Crucially, this new instrument has a focal depth of ±5 μm from

Fig. 1. Photograph of the scanning soft X-ray absorption microscope apparatus equipped with an 8 T superconducting magnet. This apparatus is installed at the b-branch of BL25SU. (UHV = ultra-high vacuum)

the focal point and is equipped with a superconducting magnet that can generate a maximum field of 8 T, thereby significantly advancing the previous limit of 0.5 T and permitting the observation of magnetic domains in the fractured surfaces of granular materials.

To unmask the interior magnetic domain structure of Nd-Fe-B sintered magnets that represents the bulk, the soft X-ray absorption microscope was employed to track the reversal of individual grains in the polished and fractured surfaces [2]. As the applied field is varied, significant differences in the reversal behavior of the polished and fractured surfaces were observed and intergranular correlations could be identified. Figures 2(a) and 2(b) show the magnetic domain images recorded in the polished and fractured surfaces, respectively, of a Nd-Fe-B sintered magnet near their respective coercive fields. In the polished surface, large regions are covered by a maze-like domain pattern and, as the applied magnetic field is varied, the domain walls can easily move because of the fine balance between the external field and the magnetostatic stray field at the surface. The maze-like multiple-domain structure in the polished surface reflects the reduced magnetic anisotropy, as evidenced by the narrow domain widths, and this is clearly a consequence of the surface damage. In contrast, the demagnetization process of the fractured surface occurs grain-by-grain where most of the grains completely reverse their magnetization without exhibiting the maze-like domain pattern and the domain walls are able to travel through multiple whole grains for small changes in applied field.

The scanning soft X-ray absorption microscope that we have developed provides a new opportunity for element-specific magnetic domain imaging and spectroscopy under much higher applied magnetic fields than those previously available. This instrument has provided a comprehensive, state-of-the-art experimental description and comparison of the magnetic domains in both the interior and exterior regions of a Nd-Fe-B sintered magnet. Furthermore, we anticipate that the advanced capabilities of this measurement system will be particularly advantageous for observing magnetic domain structures formed from other kinds of first-order phase transitions and possible metamagnetic transitions induced by strong magnetic fields. Finally, improving the spatial resolution to less than 50 nm and increasing the applied magnetic field are possibilities for future technical developments.

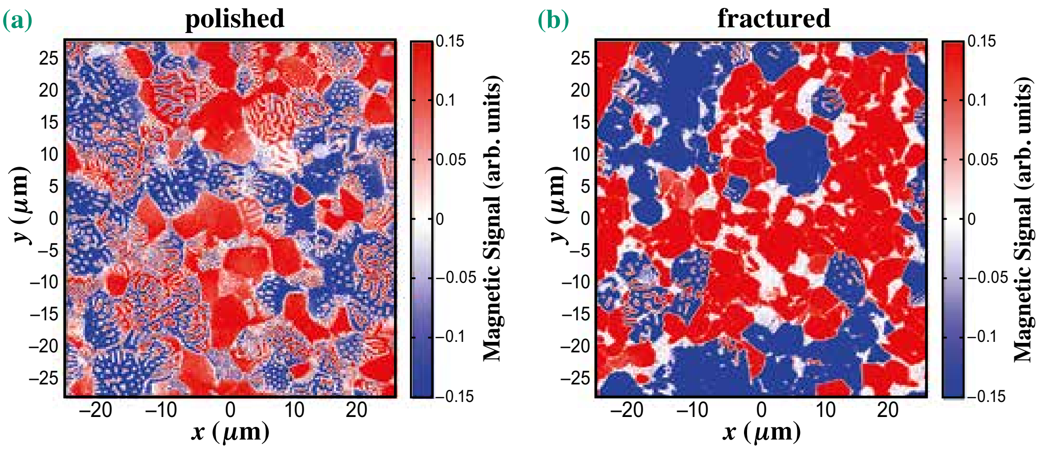

Fig. 2. Magnetic domain images of **(a)** the polished surface and **(b)** the fractured surface of a Nd-Fe-B sintered magnet close to their respective coercive fields.

D. Billington[a,b,†], Y. Kotani[a], K. Toyoki[a,b], T. Nakamura[a,b,*]

[a] Japan Synchrotron Radiation Research Institute (JASRI)
[b] Elements Strategy Initiative Center for Magnetic Materials (ESICMM)

*Email: naka@spring8.or.jp

[†] Present address: School of Physics and Astronomy,
Cardiff University, UK

References

[1] *Y. Kotani, Y. Senba, K. Toyoki, D. Billington, H. Okazaki, A. Yasui, W. Ueno, H. Ohashi, S. Hirosawa, Y. Shiratsuchi and T. Nakamura: J. Synchrotron Rad.* ***25*** *(2018) 1444.*
[2] *D. Billington, K. Toyoki, H. Okazaki, Y. Kotani, T. Fukagawa, T. Nishiuchi, S. Hirosawa and T. Nakamura: Phys. Rev. Mater.* ***2*** *(2018) 104413.*

Charge and lattice fluctuations in molecule-based spin liquids

Electron spin is one of the fundamental properties of electrons. A magnetic moment is caused by electron spins. Electron spins tend to align in a crystal, affecting the magnetic behavior. On the other hand, there is no consensus on the magnetic behavior induced by three electron spins accommodated into the corners of an isosceles triangle (Fig. 1(a)). One reason for this is because there is no stable alignment condition even at zero Kelvin. Such situation is called the "spin liquid" [1]. The spin liquid has been attracting attention because of its potential properties arising from quantum fluctuations. To obtain evidence for the spin liquid, physicists and chemists have focused on crystalline materials having triangular, kagome and pyrochlore lattices.

A metal-dithyolene complex salt, $EtMe_3Sb[Pd(dmit)_2]_2$, whose 2D layer belongs to the triangular lattice, is one of the candidate compounds exhibiting spin liquid behavior (Figs. 1(b) and 1c)). Magnetic and transport property measurements revealed the absence of any ordering near absolute zero Kelvin [2-4]. Nevertheless, anomalous behaviors that suggest the release of a small amount of entropy near liquid-helium temperature were observed in the transport and magnetic measurements [2-4]. Furthermore, a slight deviation from the isosceles triangular lattice was revealed, whereas the 2D layers in two nonmagnetic insulators ($Et_2Me_2Sb[Pd(dmit)_2]_2$ and $EtMe_3P[Pd(dmit)_2]_2$) were close to the isosceles triangular lattice. These contradictory properties were elucidated by vibrational spectroscopy focusing on the C=C stretching modes denoted as A–D modes (Fig. 2(a)).

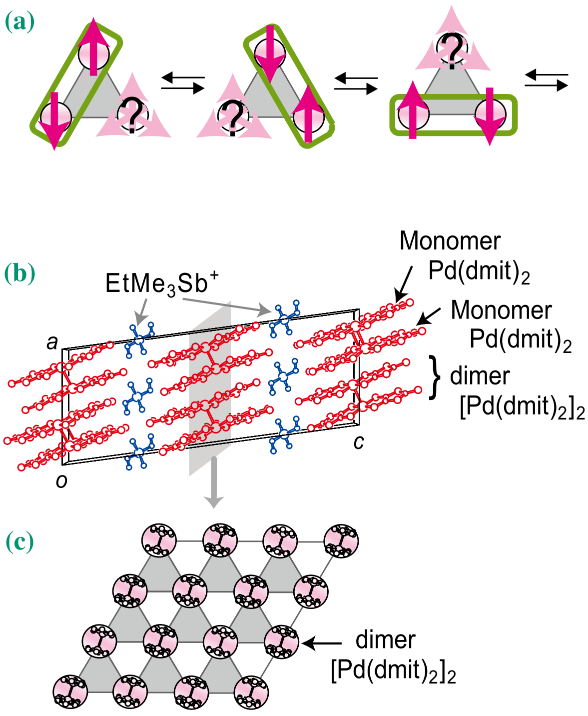

Fig. 1. **(a)** Frustration of electron spins in isosceles triangle. **(b)** Crystal structure of $EtMe_3Sb[Pd(dmit)_2]_2$ viewed along the *b* axis. **(c)** Schematic views of molecular arrangement in the 2D layer, which is parallel to the *ab*-plane. A triangular lattice is formed by dimers consisting of two monomers.

Some vibrational modes of molecule-based conducting materials are sensitive to a slight change in intermolecular interactions and molecular charges, which is useful for analyzing the fluctuation of a hidden ordered state. To capture all C=C stretching modes as much as possible, the polarization dependence of the infrared spectra and the dependence of the excitation energy in Raman spectra were examined [5]. The thickness of a platelike crystal is smaller than 50 μm. When the polarization direction is parallel to the thickness direction, the narrow infrared beam at SPring-8 **BL43IR** is suitable for such a material. We also observed the C=C stretching modes in three related compounds that are in the antiferromagnetic state at low temperatures.

Figures 2(b) and 2(c) show the conductivity spectra and Raman spectra, respectively. The conductivity spectrum corresponds to the infrared spectrum. When dimers are regularly arranged in the 2D layer, the number of C=C stretching modes should be four (= A_D–D_D modes, which are identical to A–D modes, respectively (Fig. 2(a)). A_D in the Raman spectra corresponds to regularly arranged dimers (Fig. 3(a)), whereas A_T and D_O do not. A_T is assigned to one of the C=C stretching modes of a tetramer (Fig. 3(a)), where the A_D modes of two neighboring dimers in the tetramer are combined. A_T is observed as a weak and non-negligible shoulder of the B mode (Fig. 2(b)). This phenomenon is ascribed to fluctuating tetramers rather than static tetramers. The D_O mode corresponds to the C=C stretching modes of an octamer, where the D_D modes of four contiguous dimers are combined. Because the static octamer consists of two shrunk and two expanded dimers (Fig. 3(a)), D_O should exhibit separate peaks, which is inconsistent with the broad linewidth in Fig. 2(c). The broad linewidth is ascribed to the dynamical repetition of the expansion and contraction of dimers due to the fluctuating octamer. Our experimental result reveals the dynamical alternation among dimers, tetramers and octamers (Fig. 3(a)). The dynamical alternation induces the charge fluctuation in the 2D layer. The broad linewidth in the B mode (Fig. 2(b)), whose frequency is sensitive to the monomer charge, is ascribed to the charge fluctuation.

The dynamical alternation is ascribed to the competition among dimers, tetramers and octamers due to the degeneracy among these three ordered states (Fig. 3(b)). As shown in the energy diagram of molecular orbitals (Fig. 3(b)), the highest occupied molecular orbital (HOMO) and the lowest unoccupied molecular orbital (LUMO) of a normal dimer become the LUMO (H–H) and HOMO (L+L) in a tight dimer, respectively. The singly occupied orbital of [Tight dimer]$^{-}$ (H–H) is antibonding, whose energy should be decreased by the formation of any ordering. One of the ordered states is the antiferromagnetic ordering by the regular arrangement of tight dimers. Another ordered state is a tetramer. The highest occupied orbital of [Tetramer]$^{2-}$ consists of H–H orbitals, which form the valence bond order in a crystal. L+L orbitals form the next highest occupied orbital of [Tetramer]$^{2-}$, which induces the charge separation. The valence bond order and charge separation are cooperative with each other. The other ordered state is the octamer. A similar cooperative mechanism is applied to the formation of an octamer. When the energy levels among the three ordered states are identical, the system becomes stable owing to the dynamical exchange between them. This mechanism resolves the contradictory phenomena previously observed in the transport and magnetic measurements [2-4]. This mechanism is also consistent with the slight deviation from the isosceles triangular lattice.

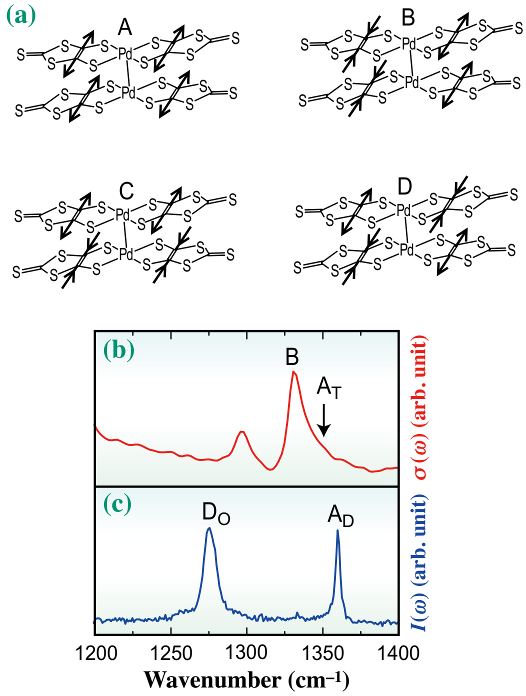

Fig. 2. **(a)** Four C=C stretching modes (A–D modes) in a tight dimer ($[Pd(dmit)_2]_2$). **(b)** Conductivity spectra ($\sigma(\omega)$) calculated from the infrared reflectance spectra obtained at BL43IR. The incident light was polarized along the interlayer direction of a single crystal. **(c)** Raman spectra ($I(\omega)$) obtained using spectrometer in the Institute for Molecular Science.

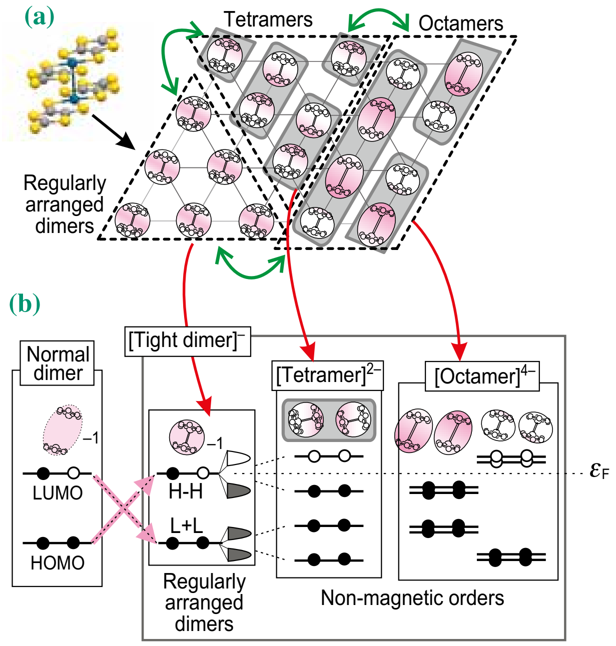

Fig. 3. **(a)** Coexistence between regularly arranged dimers, tetramers and octamers in triangular lattice, which can be interchanged at approximately the liquid helium temperature. **(b)** Energy diagrams of normal dimer, tight dimer, tetramer and octamer. Interchange of energy levels occurs between normal and tight dimers. Magenta contours in (a) and (b) denote the electron density of the singly occupied orbital of [Tight dimer]$^{-1}$ and the highest occupied orbitals of [Tetramer]$^{2-}$ and [Octamer]$^{4-}$.

Takashi Yamamoto[a,b,c]

[a] Graduate School of Science and Engineering,
Ehime University
[b] Geodynamics Research Center, Ehime University
[c] RIKEN / Wako

Email: yamataka@ehime-u.ac.jp

References

[1] L. Balents: Nature **464** (2010) 199.
[2] S. Yamashita *et al.*: Nat. Comm. **2** (2911) 275.
[3] M. Yamashita *et al.*: Science **328** (2010) 1246.
[4] T. Itou *et al.*: Nat. Phys. **6** (2010) 673.
[5] *T. Yamamoto, T. Fujimoto, T. Naito, Y. Nakazawa, M. Tamura, K. Yakushi, Y. Ikemoto, T. Moriwaki and R. Kato: Sci. Rep.* ***7*** *(2017) 12930.*

Roles of mesoscale dynamics in shear viscosity of high alcohol revealed by γ-ray quasielastic scattering

High alcohols, in which a hydrophilic OH group is attached to an end of a hydrophobic long alkyl chain, are among the simplest amphiphilic molecules. The molecular structure of the high alcohol 3,7-dimethyl-1-octanol (dmOcOH) investigated in this work is drawn in the inset of Fig. 1. In the neat liquid state, the OH groups aggregate through strong intermolecular hydrogen bonding, and the alkyl chains expelled from the hydrogen-bonding network also cluster together. The liquid structure of this high alcohol thus consists of two domains, namely, the polar OH and nonpolar alkyl domains. The domain structure of this high alcohol resembles those of surfactant systems, which are the origin of their large structural viscosity. The shear viscosity of liquids in general has practical applications in chemical engineering, mechanical engineering, and other fields, but its molecular origin is yet to be resolved. It is thus interesting to know how the domain structure of high alcohols is related to their shear viscosity.

The domain structure of high alcohols appears as a low-q peak in the X-ray structure factor. Figure 1 shows the X-ray diffraction pattern of dmOcOH. A strong peak at 13 nm^{-1}, which is hereafter called “main peak,” is common to various liquids in general. In addition, a small peak is observed at 4.5 nm^{-1}, which is hereafter called the “prepeak.” The prepeak originates from the scattering contrast between the polar and nonpolar domains, and it represents the domain structure of the high alcohol.

The shear viscosity of a liquid is a dynamic property reflecting the microscopic structural relaxation. The time scale of the microscopic relaxation responsible for shear viscosity can be evaluated from the frequency-dependent complex shear viscosity, called “viscoelastic relaxation.” On the other hand, the structural relaxation at a given wavenumber is determined through the measurement of the intermediate scattering function at the given wavenumber. From the comparison between the viscoelastic relaxation and the intermediate scattering function, we can infer the length scale of the microscopic structure that governs the shear viscosity. Based on this scheme, a molecular dynamics (MD) simulation study performed by one of us (TY) suggested the significant contribution of domain dynamics to the shear viscosity of high alcohols [1]. In this work, we determine the relaxation times of the intermediate scattering functions of liquid dmOcOH at both the prepeak and the main peak using γ-ray quasielastic scattering spectroscopy, and compare them with the viscoelastic relaxation times to examine the mechanism suggested by the previous MD study [2].

The γ-ray quasielastic scattering measurement was performed at SPring-8 **BL09XU**. The Mössbauer γ-ray emitted from the ^{57}Fe nucleus excited by synchrotron radiation was utilized. The energy of the Mössbauer γ-ray of ^{57}Fe is 14.4 keV, whose wavelength, 0.084 nm, is suitable for the structural analysis of molecular systems. Owing to the narrow band width of the Mössbauer γ-ray, 4.7 neV, we can measure the intermediate scattering function in the corresponding time scale of around 100 ns.

A schematic picture of the experimental equipment is drawn in Fig. 2. Thin foils of α-^{57}Fe are inserted on both the upstream and downstream sides of the sample. The incident beam of the synchrotron radiation, on passing through the ^{57}Fe foil on the upstream side, generates a monochromatic Mössbauer γ-ray, which is then scattered quasielastically by the sample and enters the detector. At the same time, the direct incident beam is scattered by the sample, which also gives a Mössbauer γ-ray on passing through the ^{57}Fe foil on the downstream side. The former γ-ray is broadened by the sample, whereas the latter is not. When the energies of the γ-rays from the upstream and downstream foils are sufficiently different, the interference between these two γ-rays is detected as a beating pattern in the time domain, and the line broadening is used to determine the temporal decay of the beat signal.

Some experimental ingenuity is introduced to improve the measurement efficiency. For instance, magnetic fields of different directions are applied to the ^{57}Fe foils on each side to selectively allow different nuclear excitations between the nuclear energy levels

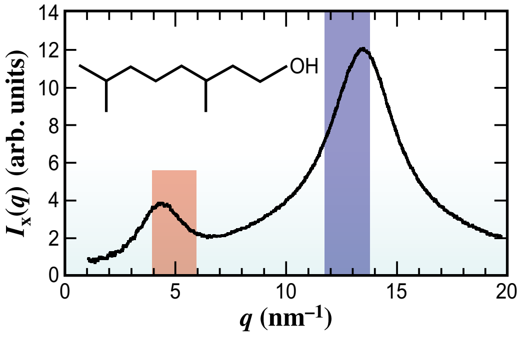

Fig. 1. X-ray structure factor of 3,7-dimethyl-1-octanol, whose molecular structure is indicated in the inset. The q-ranges of the quasielastic scattering measurements are indicated with red (prepeak) and blue (main peak) zones.

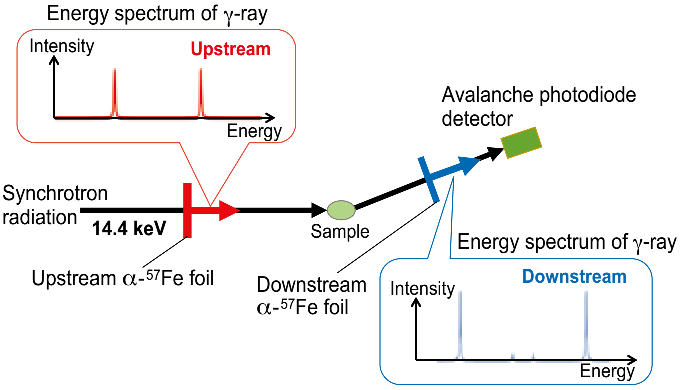

Fig. 2. Schematic picture of γ-ray quasielastic scattering measurement using time domain interferometry.

with the hyperfine splitting. Details of the experiment are given in the literature [3].

The frequency-dependent complex shear viscosity was determined by shear impedance spectroscopy at four different temperatures. In Fig. 3(a), the complex shear viscosity normalized to its zero-frequency limit, η_0, is plotted against the reduced frequency, $2\pi\eta_0\nu$. The spectra at different temperatures appear to fall on a master curve, indicating that the relaxation frequency is inversely proportional to η_0. In addition, the spectrum appears to consist of two relaxation modes. The curves in Fig. 3(a) show the fitting using the sum of the Cole-Davidson and the Debye functions, which reproduces the experimental spectra fairly well. From the reduced relaxation frequencies and the temperature dependence of η_0, the relaxation times of both modes are determined as the functions of temperature, which are plotted in Fig. 3(b) as the open symbols.

The time-domain interference signal of the γ-ray is analyzed assuming the KWW functional form of the intermediate scattering function, $I(q,t)$, as

$$I(q,t) \propto \exp\left(-\left(\frac{t}{\tau(q)}\right)^{\beta(q)}\right)\ ,$$

and the parameters $\beta(q)$ and $\tau(q)$ are determined for both peaks as the functions of temperature. Since the viscoelastic relaxation is related to $I^2(q,t)$ according to the mode-coupling theory, the mean relaxation times of $I^2(q,t)$ are calculated and compared with the viscoelastic relaxation times in Fig. 3(b).

Figure 3(b) demonstrates that the mean relaxation times of $I^2(q,t)$ at the prepeak and the main peak agree well with those of the slow and fast modes of the viscoelastic relaxation, respectively. This suggests that the mesoscale dynamics of the domain structure contributes to the shear viscosity of high alcohols through the slower mode of the viscoelastic relaxation, while the contribution of the short-range dynamics is also present as the faster mode.

Our present study experimentally demonstrated the role of the mesoscopic structure of high alcohols in their macroscopic rheological property for the first time, and we hope that it will be a first step toward controlling the macroscopic shear viscosity by microscopic molecular design.

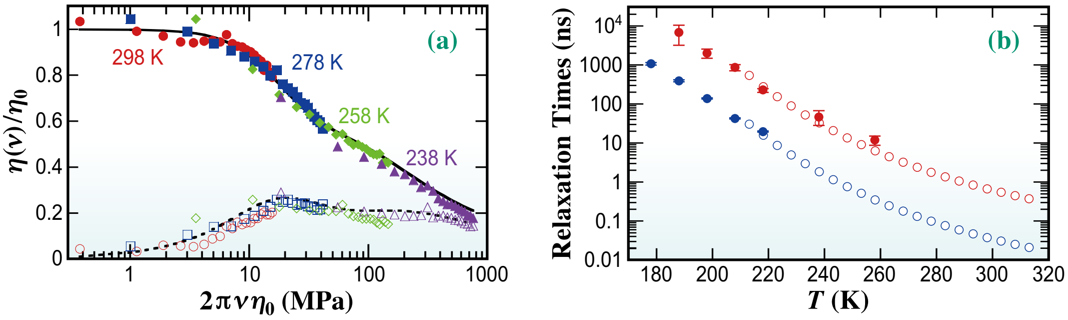

Fig. 3. **(a)** Frequency dependence of viscosity at four different temperatures. The real and imaginary parts are plotted with the filled and open symbols, respectively. Both axes are reduced to the steady-state shear viscosity, η_0. **(b)** The relaxation times of the slower (red) and faster (blue) modes of viscoelastic relaxation, plotted with the open symbols, are compared with those of the squared intermediate scattering functions (filled symbols) at the prepeak (red) and the main peak (blue).

Tsuyoshi Yamaguchi[a,*] and Makina Saito[b]

[a] Graduate School of Engineering, Nagoya University
[b] Institute for Integrated Radiation
and Nuclear Science, Kyoto University

*Email: yamaguchi.tsuyoshi@material.nagoya-u.ac.jp

References

[1] T. Yamaguchi: J. Chem. Phys. **146** (2017) 094511.
[2] *T. Yamaguchi, M. Saito, K. Yoshida, T. Yamaguchi, Y. Yoda and M. Seto: J. Phys. Chem. Lett.* ***9*** *(2018) 298.*
[3] M. Saito *et al.*: Sci. Rep. **7** (2017) 12558.

Stabilization of the superionic conducting phase of silver iodide by size and pressure effects

Enhancement of the performance and safety of batteries has been recently highlighted because of the widespread use of mobile electronic devices such as laptop computers and smartphones. At present, organic liquid electrolytes are generally used for batteries, and they have safety problems such as liquid spill and ignition. Although all-solid-state batteries, which contain solid electrolytes instead of organic liquids, have been actively investigated in order to overcome these problems, the ionic conductivity of solid electrolytes is generally lower than that of liquid electrolytes. Silver iodide (AgI) is known not only as one of the most traditional solid electrolytes but also as one of the fastest ionic conductors. Above 147°C, bulk AgI exists as the α-phase, which shows very high Ag^+ conductivity of more than 1 S/cm owing to the sublattice melting of Ag^+. Below 147°C, however, the α-phase undergoes a structural phase transition to the poorly conducting β/γ-phases, limiting the application of AgI as a solid electrolyte. Various methods have been attempted to stabilize the α-phase down to a lower temperature. For example, in bulk AgI, the phase transition temperature is decreased by applying a moderate pressure. It was reported that the α-phase exists stably down to 100°C at 0.3 GPa [1]. In our previous studies, it was revealed that the phase transition temperature from the α-phase to the β/γ-phases decreased with decreasing particle size of AgI [2,3]. Although the α-phase was stabilized down to 40°C in AgI nanoparticles with a diameter of 11 nm, there are still no reports on the stabilization of the α-phase at room temperature. As reported here, we investigated the phase transition behavior of AgI nanoparticles under pressure through synchrotron powder X-ray diffraction (PXRD) and observed the stabilization of the α-phase down to room temperature by a combination of pressure and size effects.

The AgI nanoparticles used in this work were prepared by liquid-phase synthesis in accordance with previous research [2]. Their mean diameter and size distribution were estimated to be 11.4 ± 4.5 nm through transmission electron microscopy (TEM, Figs. 1(a) and 1(b)).

First, the phase transition behavior of the AgI nanoparticles under ambient pressure was investigated through variable-temperature PXRD measurements at SPring-8 **BL02B2** with synchrotron radiation of $\lambda = 0.581$ Å. A powdered sample was loaded into 0.3 mm borosilicate glass capillaries, and the measurement temperature was controlled using a nitrogen gas flow. At the beginning of the measurement, it was indicated that the as-synthesized AgI nanoparticles consisted of β/γ-phases at ambient temperature and pressure (Fig. 1(c)). It should also be noted that the crystal sizes of the β- and γ-phases (13.4 and 10.2 nm, respectively) calculated using the

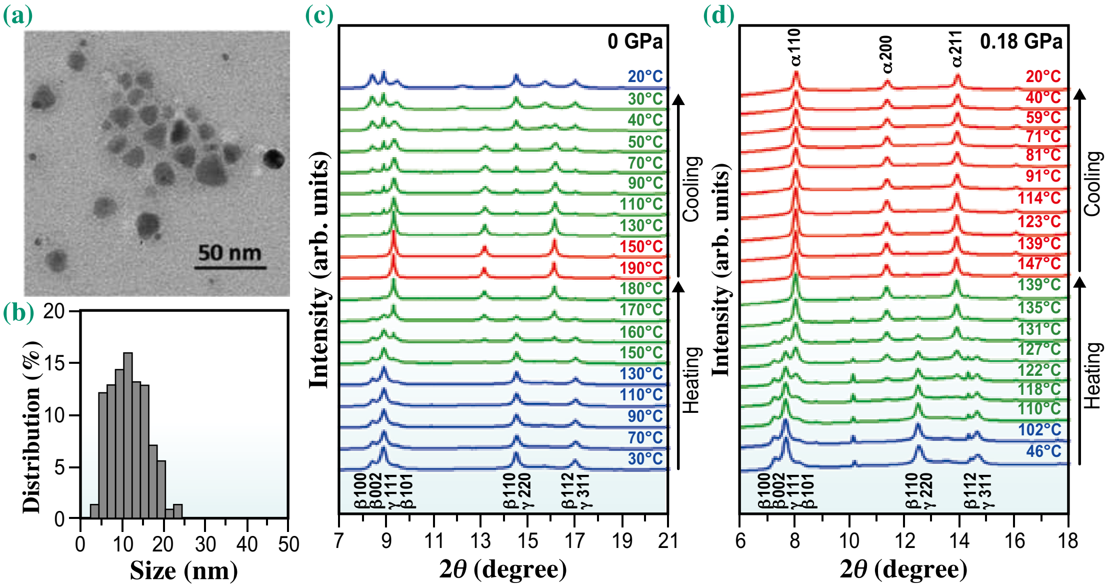

Fig. 1. **(a)** TEM image and **(b)** size distribution of the AgI nanoparticles. Variable-temperature synchrotron PXRD patterns for the AgI nanoparticles **(c)** at ambient pressure and **(d)** at 0.18 GPa. Blue and red curves denote PXRD patterns corresponding to only β/γ-phases and the α-phase, respectively. Green curves correspond to a mixture of these phases [4].

Scherrer equation were in good agreement with the mean diameter determined by TEM observation. In the heating process, the AgI nanoparticles consisted of β/γ-phases up to 130°C, and the β/γ-phases gradually changed to the α-phase between 150 and 190°C. In the cooling process, on the other hand, the α-phase gradually changed to the β/γ-phases below 130°C, and the phase transition was completed at 20°C while a small amount of the α-phase remained at 30°C. To determine the phase transition temperatures from the PXRD results, the fraction of the α-phase at each temperature was calculated by Rietveld refinement of the PXRD patterns and is plotted against temperature in Fig. 2(a). By defining the phase transition temperature as the temperature at which the fraction of the α-phase reaches 50%, the phase transition temperatures in the heating and cooling processes were estimated to be 162 and 39°C, respectively. These values are consistent with the phase transition temperatures determined from the onsets of peaks in differential scanning calorimetry (DSC) as shown in Fig.2(b).

Next, the phase transition behavior of the AgI nanoparticles under pressure was investigated through variable-temperature PXRD measurements at SPring-8 **BL10XU** with synchrotron radiation of $\lambda = 0.497$ Å. A powdered sample was loaded into the hole of a rhenium gasket on a diamond anvil cell with sodium chloride as the pressure transmitting medium and pressure marker. The measurement pressure was controlled using a gas membrane and was calibrated using the equation of states of sodium chloride. The measurement temperature was controlled using an electric resistance heater on the cell. As shown in Fig. 1(d), in the heating process at 0.18 GPa, the initial β/γ-phases gradually changed to the α-phase between 110 and 147°C, which was a lower temperature than at ambient pressure. In the cooling process, in contrast, the diffraction patterns did not change and only the α-phase was observed, even at 20°C, at 0.18 GPa. This is the first observation of the stabilization of the α-phase at room temperature. As with the case of the ambient-pressure data, the fraction of the α-phase at each temperature was calculated by Rietveld refinement of the PXRD patterns and is plotted against temperature in Fig. 2(a). At 0.18 GPa, the transition temperature in the heating process was estimated to be 123°C, which is lower than that under ambient pressure by 39°C. According to the phase diagram of bulk AgI [1], the transition temperature decreased by 41°C at 0.18 GPa. This value is consistent with the result for our nanoparticles. Thus, it can be concluded that the stabilization of the α-phase at room temperature under pressure observed in the AgI nanoparticles originates from both size and pressure effects.

In summary, we investigated the pressure effect on the phase transition behavior of AgI nanoparticles with a diameter of 11.4 ± 4.5 nm through variable-temperature synchrotron PXRD measurements under pressure. The α-phase was stabilized down to 20°C by applying a moderate pressure of 0.18 GPa to the AgI nanoparticles as a result of the combination of pressure and size effects.

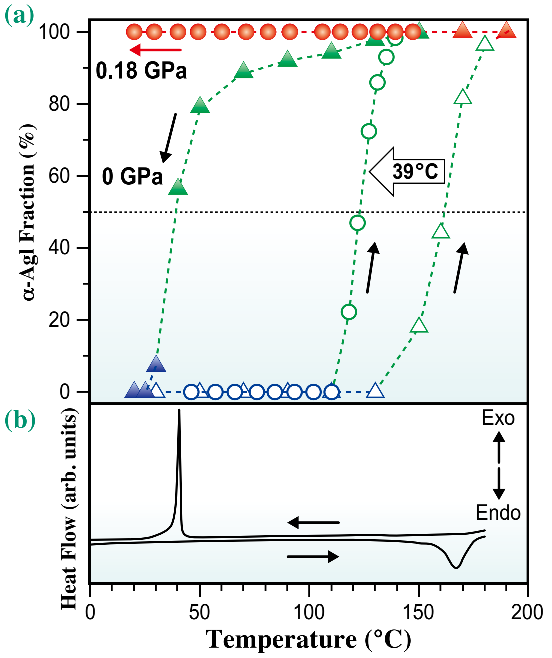

Fig. 2. **(a)** Temperature dependence of the fraction of the α-phase at ambient pressure (triangles) and at 0.18 GPa (circles). Open and closed symbols represent the heating and cooling processes, respectively. Blue, green, and red colors correspond to those in Figs. 1(c) and 1(d). **(b)** DSC thermograms of the AgI nanoparticles at ambient pressure [4].

Takayuki Yamamoto[a,*], Mitsuhiko Maesato[b]
and Hiroshi Kitagawa[b]

[a] Department of Materials Design Innovation Engineering, Nagoya University
[b] Division of Chemistry, Kyoto University

*Email: yamamoto.takayuki@material.nagoya-u.ac.jp

References

[1] B.E. Mellander *et al*.: Phys. Scr. **22** (1980) 541.
[2] R. Makiura *et al*.: Nat. Mater. **8** (2009) 476.
[3] S. Yamasaki *et al*.: Chem. – Asian J. **8** (2013) 73.
[4] *T. Yamamoto, M. Maesato, N. Hirao, S. I. Kawaguchi, S. Kawaguchi, Y. Ohishi, Y. Kubota, H. Kobayashi and H. Kitagawa: J. Am. Chem. Soc.* ***139*** *(2017) 1392.*

Synthesis of H_2-rich molecular compounds by laser heating at high pressures

As hydrogen has an exceptional energy density by weight, finding new methods for capturing hydrogen in a dense state has been subject to intense investigation for decades. High-pressure techniques have revealed the potential of molecular clathrates and metal-organic frameworks to act as desirable hydrogen-storage materials, and the claim of high-temperature superconductivity in H_2S has reignited the interest in dense hydrogen-bearing materials [1]. For instance, recent structure-searching calculations predicted that compounds of hydrogen (H_2) and iodine (I_2) with various stoichiometries could be stable at pressures above 30 gigapascals (GPa), with emergent superconducting phases above 100 GPa [2].

Studying this system experimentally is however far more challenging as hydrogen iodide (HI) is unstable and readily decomposes upon exposure to laser or X-ray radiation. Early work on HI at high pressures claimed the existence of an insulator-to-metallic transition at 50 GPa. However, work by our group has shown that at room temperature HI decomposes above 10 GPa, returning to its constituent elements [3]. However, this apparent instability of HI, could ultimately lead to the formation of new H-I compounds at higher pressure and/or temperature. Theoretical simulations predict the possible formation of numerous new hydrogen-rich configurations; $HI(H_2)_2$, H_2I, and $(H_2)_2I$, none of which were experimentally observed.

The synthesis of new H_2-I_2 compounds was explored using high-pressure X-ray diffraction at SPring-8 **BL10XU**, combined with *in situ* laser heating and Raman spectroscopy [4]. Mixtures of HI-H_2 were synthesized in diamond-anvil cells by direct reaction between solid I_2 and dense fluid H_2. After loading, samples were then irradiated with green laser light (532 nm) to photodissociate I_2, which reacts vigorously with the surrounding fluid H_2 media, resulting in a mixture of liquid HI and H_2. Through varying the initial quantity of I_2, we were able to control the mixture ratio of HI and H_2. Samples were then compressed to approximately 30 GPa before irradiation with up to 50 W of 1064 nm laser light.

As seen in Fig. 1, laser-heating leads to the appearance of relatively weak, but well-defined diffraction lines, in addition to those from iodine. Initial analysis of the diffraction data indicated a single, strong, electron-density peak corresponding to HI, arranged in a primitive cubic lattice. The spacing between HI molecules was clearly much larger than the combined radii of HI, suggesting the presence of additional H_2 molecules, however they cannot be observed by X-ray diffraction.

In order to estimate the stoichiometry of this compound, the volume-per-formula-unit was compared with various compositions from the summation of the atomic equations of state for I_2 and H_2 which suggested the surprising composition of $HI(H_2)_{13}$. Structures with this AB_{13} composition have been observed in a number of systems: from intermetallic compounds to binary colloidal crystals and Brazilian gem opals. Two forms of AB_{13} structure are known and differ by the arrangement of their B spheres. To distinguish between the two packing types we performed molecular dynamics (MD) density functional theory calculations at 300 K and 30 GPa. The average positions from the simulation clearly show H_2 molecules adopting an icosahedral $(H_2)_{13}$ distribution as found in the $Fm\bar{3}c$ polymorph (Fig. 2).

Through Raman spectroscopic studies (Fig. 3), a single HI vibrational mode is observed in agreement with one unique HI molecular environment from our assigned structure. The $(H_2)_{13}$ intramolecular vibrational mode is red-shifted compared with that of

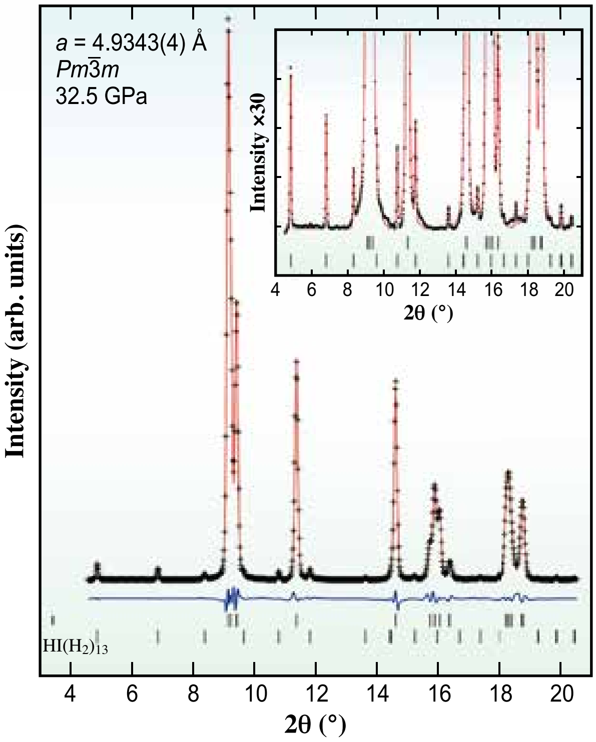

Fig. 1. High-pressure X-ray diffraction pattern collected from a laser-heated mixture of H_2 and I_2 at 32.5 GPa (λ = 0.4141 Å) collected at BL10XU.

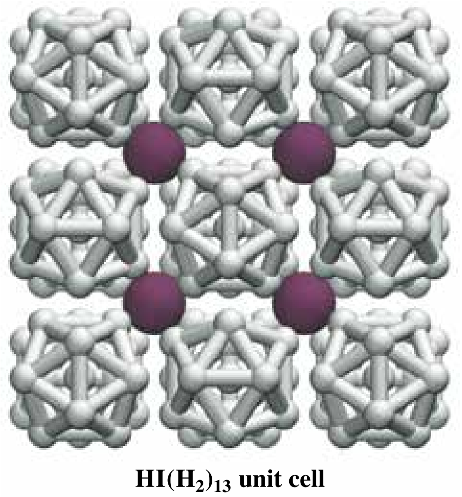

Fig. 2. $HI(H_2)_{13}$ crystal structure with the orientation of icosahedral clusters highlighted with "bonds" between H_2 positions to guide the eye.

pure H_2 and its pressure-evolution mirrors that of the HI vibrational mode. The similarities in the behavior of the two modes suggest strong intermolecular coupling between HI and H_2. In the MD calculations we observe that the nearest approach between non-bonded H atoms involves the hydrogen in HI. Radial-distribution functions for H_2 molecules also indicate the icosahedral symmetry adopted by the clusters and furthermore confirm that the $(H_2)_{13}$ clusters are well separated and act as individual objects in the crystal structure.

We observed diffraction peaks from $HI(H_2)_{13}$ over a remarkably large pressure range, from 9 GPa on decompression to 130 GPa on compression. Amongst the hydrogen halides only HBr and HI have been experimentally proven to decompose into their constituent elements. Decomposition occurs when intermolecular distances are short enough to lead to the spontaneous formation of H_2 molecules. In $HI(H_2)_{13}$, HI molecules are widely dispersed amongst $(H_2)_{13}$ clusters and this hinders the decomposition mechanism, stabilizing the compound by more than an order of magnitude. This remarkable change in stability makes $HI(H_2)_{13}$ among the most stable bimolecular compounds at high pressures, comparable to $Xe(N_2)_2$ and $Xe(H_2)_8$, which are stable up to 180 and 255 GPa, respectively.

Among molecular hydrogen storage materials, $HI(H_2)_{13}$ shows a relatively high weight-percent H_2 content, 17.7%, which compares favorably to other materials such as $H_2(H_2O)_2$ (5.3 H_2 wt%), $H_2(H_2O)$ (11.2 H_2 wt%), and $Xe(H_2)_8$ (10.9 H_2 wt%), although it falls short of the record 33.4 wt% found in $(H_2)_4CH_4$. The formation of $HI(H_2)_{13}$ also poses an interesting question as to whether this structure type could be stable for other molecules that satisfy the geometric size ratio compatible with the $(H_2)_{13}$ supramolecular building block. In a subsequent molecular dynamics study we demonstrated the stability of a number of so-far unobserved AB_{13} compounds, including the hydrogen halides and the noble gas xenon [5]. Further experimental studies will test these predictions in the search for more hydrogen-rich compounds.

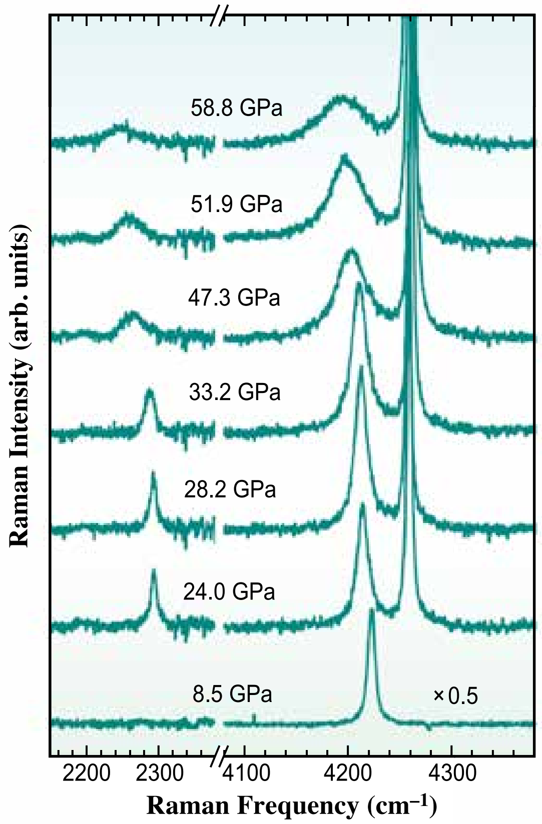

Fig. 3. Raman spectra of $HI(H_2)_{13}$.

Jack Binns*, Philip Dalladay-Simpson and Ross Howie

Center for High Pressure Science and Technology
Advanced Research, Shanghai, China

*Email: jack.binns@hpstar.ac.cn

References

[1] A.P. Drozdov *et al.*: Nature **525** (2015) 73.
[2] A. Shamp and E. Zurek: J. Phys. Chem. Lett. **6** (2015) 4067.
[3] J. Binns *et al.*: Phys. Rev. B **96** (2017) 144105.
[4] *J. Binns, P. Dalladay-Simpson, M. Wang, G.J. Ackland, E. Gregoryanz and R.T. Howie: Phys. Rev. B* ***97*** *(2018) 024111.*
[5] G.J. Ackland *et al.*: Phys. Rev. Mater. **2** (2018) 093601.

High-T_c superconducting phases of $FeSe_{1-x}S_x$ at high pressure

In condensed matter physics, it is one of the important problems to understand the mechanism of unconventional superconductivity which is not described by the standard BCS theory. The phase diagrams of such unconventional superconductors have a common feature, i.e. the superconducting phase exists near the magnetic order. Recently-discovered Fe-based superconductors also have this feature. From this point, it is thought that the spin fluctuations enhanced near the verge of the magnetic order are related to the mechanism of the unconventional superconductors. On the other hand, recent studies suggest that the nematic order that spontaneously breaks rotational symmetry of the system exists in the Fe-based superconductors and its quantum fluctuations may play an essential role for the superconductivity. However, this remains unclear because the nematic order usually coexists with the magnetic order [1]. To solve this issue, FeSe which uniquely exhibits a nonmagnetic nematic order is a key system. FeSe has the simplest crystal structure among Fe-based superconductors and shows the tetragonal-to-orthorhombic structural transition (nematic transition) at T_s~90 K as well as the superconductivity at T_c~9 K. It is reported that by partially substituting Se with isovalent S, a nematic quantum critical point can be reached, at which the electronic nematic transition temperature T_s is suppressed to absolutely zero [2]. By applying physical pressure, T_s is suppressed as in the case of S-substitution system. However, the magnetic order is induced before the nematic order is completely suppressed. This pressure-induced magnetic order has a dome shape in the pressure phase diagram. When the magnetic order is suppressed in high-pressure region, high-T_c superconductivity at $T_c = 38$ K is realized [3]. These results indicate that pressure and S-substitution have different effects on the electronic states of FeSe. Thus, it is important to explore how the ground state of FeSe changes when chemical pressure by S-substitution and physical pressure is controlled as independent parameters. We have performed high-pressure studies in high-quality single-crystalline $FeSe_{1-x}S_x$ up to 8 GPa. We find a systematic change of the pressure phase diagram in FeSe by the S-substitution. Our results imply that the respective role of nematic and magnetic fluctuations can be elucidated from the precise control of pressure and substitution in this system [4].

High-pressure resistivity measurements

First, the transport measurements under high pressure up to 8 GPa in high-quality single crystals of $FeSe_{1-x}S_x$ (x=0.04, 0.08, 0.12 and 0.17) are conducted with a constant-loading type cubic anvil apparatus invented by Uwatoko group at Institute for Solid State Physics in The University of Tokyo. Each sample is grown by the chemical vapor transport technique. From the anomalies in the resistivity curve, we assigned the phase transition temperatures, T_s, T_c, as well as the magnetic transition temperature T_m. From this we establish the temperature(T)-pressure(P)-S-substitution(x) 3-dimensional (3D) electronic phase diagram. As shown in Fig. 1, the electronic nematic

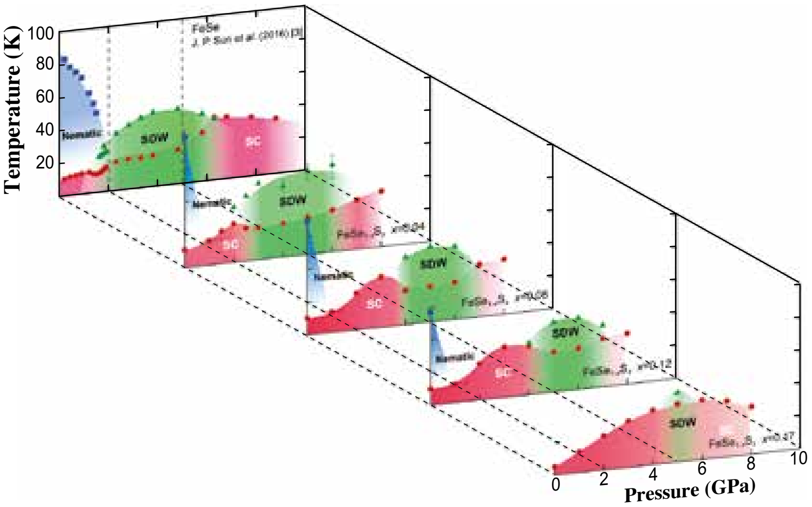

Fig. 1. The T-P-x 3D electronic phase diagram of $FeSe_{1-x}S_x$ established by this work. The overlap of the nematicity and magnetism is separated by S-substitution. Furthermore, it is also shown that the high-T_c superconductivity occurs near the magnetic phase.

phase and pressure-induced magnetic phase overlap in low-pressure region of the electronic phase diagram of FeSe, but these two orders separate with each other by increasing the S-content. Besides, at the region where both two orders are absent, a new high-T_c superconducting phase is observed. Highest T_c is achieved close to the verge of magnetic phase, which suggests the pressure-induced magnetic phase has an intimate link with high-T_c superconductivity in this system.

Synchrotron X-ray diffraction measurements

To understand more about the nature of the pressure-induced high-T_c superconducting phase, the crystal structure of $FeSe_{1-x}S_x$ at high pressure needs to be clarified. Synchrotron X-ray diffraction measurements of $FeSe_{1-x}S_x$ ($x = 0.08$) under pressure have been performed at SPring-8 **BL22XU** by using a diamond anvil cell. In this content, the transport measurements reveal the magnetic order between 4 and 6 GPa (Fig. 2(a)). The upper parts of Figs. 2(b) and 2(c) show the results of the temperature dependence of (331) Bragg peak at 3 and 4.9 GPa, respectively. At 4.9 GPa, the split of the Bragg peak by the tetragonal-orthorhombic structural transition is clearly observed near the temperature where the resistivity anomaly by magnetic transition appears (Fig. 2(c)). This result is consistent with the previous synchrotron X-ray diffraction measurements of FeSe [5]. This confirms that the dome-shaped magnetic order in the pressure phase diagram of $FeSe_{1-x}S_x$ is accompanied with the tetragonal-orthorhombic structural transition. In contrast, at 3 GPa where the new high-T_c superconductivity is observed by the transport measurements, no split of the Bragg peak is observed, indicating that the crystal structure remains tetragonal down to the lowest temperature (Fig. 2(b)). This demonstrates that in $FeSe_{1-x}S_x$ nematic and magnetic phases are separated completely and that the high-T_c superconductivity appears in the non-magnetic tetragonal phase.

These results show that in FeSe-based system it is possible to control the electronic nematicity and the magnetism in the electronic phase diagram by the combination of S-substitution (chemical pressure) and physical pressure. These two different pressures have different effects on the electronic state of FeSe. In this system, the high-T_c superconductivity appears in the vicinity of pressure-induced magnetic phase, which suggests that the non-magnetic electronic nematic fluctuations alone cannot induce high-T_c superconductivity, but the pressure-induced magnetism with orthorhombicity has an intimate relationship with the high-T_c superconductivity.

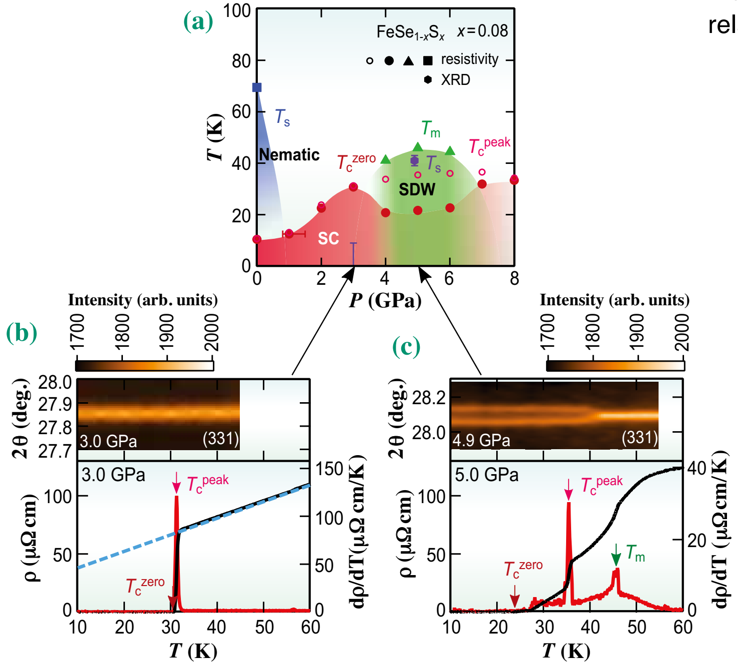

Fig. 2. Temperature-pressure phase diagram for $x = 0.08$. **(a)** T-P phase diagram of $FeSe_{1-x}S_x$ ($x = 0.08$) together with T_s determined by the high-pressure synchrotron X-ray diffraction (XRD) in a diamond anvil cell (purple hexagon with error bars). **(b,c)** Temperature-dependence of Bragg intensity as a function of 2θ angle is indicated in color scale for 3.0 GPa (b) and 4.9 GPa (c). Temperature dependence of resistivity $\rho(T)$ and $d\rho/dT$ are also shown with the same horizontal axis. The red (green) arrows indicate T_c (magnetic transition temperature, T_m). The blue dashed line in (b) is a T-linear fit to the normal-state $\rho(T)$ at 3.0 GPa.

Kohei Matsuura*, Yuta Mizukami
and Takasada Shibauchi

Department of Advanced Materials Science,
The University of Tokyo

*Email: matsuura@qpm.k.u-tokyo.ac.jp

References

[1] R.M. Fernandes *et al.*: Nature Physics **10** (2014) 97.
[2] S. Hosoi *et al.*: Proc. Natl. Acad. Sci. USA **113** (2016) 8139.
[3] J.P. Sun *et al.*: Nat. Commun. **7** (2016) 12146 .
[4] *K. Matsuura, Y. Mizukami, Y. Arai, Y. Sugimura, N. Maejima, A. Machida, T. Watanuki, T. Fukuda, T. Yajima, Z. Hiroi, K.Y. Yip, Y.C. Chan, Q. Niu, S. Hosoi, K. Ishida, K. Mukasa, S. Kasahara, J.-G. Cheng, S.K. Goh, Y. Matsuda, Y. Uwatoko and T. Shibauchi: Nat. Commun.* ***8*** *(2017) 1143.*
[5] K. Kothapalli *et al.*: Nat. Commun. **7** (2016) 12728.

Three-dimensional atomic imaging of dopant sites in As-doped Si using spectro-photoelectron holography

A significant problem of the impurity doping techniques for semiconductor devices is the electrical activation of dopants with a high concentration. It is known that individual dopant atoms occupying a substitutional site in a crystal matrix provide carriers, making the dopant electrically active. However, in the doped regions with a high concentration, not all dopant atoms are active owing to the deactivation of excess dopant atoms by the formation of various clusters and other defect structures. With the aim of developing process technologies to overcome the problem, the atomic level dopant structures have been investigated by both theoretical and experimental approaches, although the direct observation of their three-dimensional (3D) structures has been difficult. As a different approach, dopants in Si have been examined using soft X-ray photoelectron spectroscopy (SXPES), in which particular chemical bonding states were correlated with electrical activity [1].

Photoelectron holography is a method of examining element-specific local 3D atomic structures applicable to nonperiodic structures [2]. Recently, the development of reconstruction algorithms has greatly improved the quality of reconstructed atomic images. Furthermore, a high energy resolution electron analyzer has allowed the visualization of local dopant atomic structures having different chemical bonding states. In this work, we report the 3D imaging of structures for As doped into a Si surface using spectro-photoelectron holography combined with first-principles simulations [3].

The sample was prepared by As^+ ion implantation followed by activation annealing and surface etching [3]. The As concentration and carrier concentration near the surface were evaluated as $1.5 \times 10^{20}\,cm^{-3}$ and $7.5 \times 10^{19}\,cm^{-3}$, respectively; thus, the activation rate was 50%. The spectro-photoelectron holography measurements were performed at SPring-8 **BL25SU**. Soft X-rays were incident to the sample at a 5° glancing angle, as shown in Fig. 1(a). The principle of photoelectron holography is summarized in Fig. 1(b). Part of each photoelectron wave emitted from the excited atom is scattered by surrounding atoms and the scattered wave interferes with the original direct photoelectron wave. The resulting interference pattern, i.e., the photoelectron hologram, appears in the angular distribution of the photoelectrons. An entire photoelectron hologram was obtained with an electron analyzer (Scienta-Omicron DA30) capable of measuring the angular distribution with high energy resolution. The 3D atomic image reconstruction was conducted using the SPEA-L1 algorithm [4]. First-principles calculations were performed to calculate the stability, core-level shifts, and dynamical properties of As doped in Si using the STATE-Senri program [5]. First-principles molecular dynamics (MD) simulations were carried out to evaluate atomic fluctuations at room temperature.

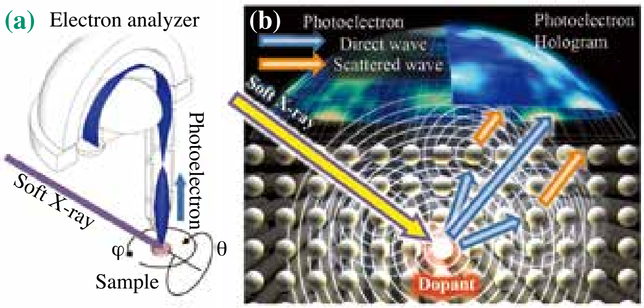

Fig. 1. **(a)** Experimental setup at BL25SU. **(b)** Schematic diagram summarizing the principles of photoelectron holography. [3]

Figure 2 shows the obtained As 3*d* spectrum containing three components labeled BEH, BEM, and BEL (Fig. 2(d)), which are attributed to three distinct atomic sites, and the corresponding photoelectron holograms (Figs. 2(a-c)). The hologram associated with the BEH peak is very clear and its pattern is similar to that of the Si 2*p* hologram (not shown here).

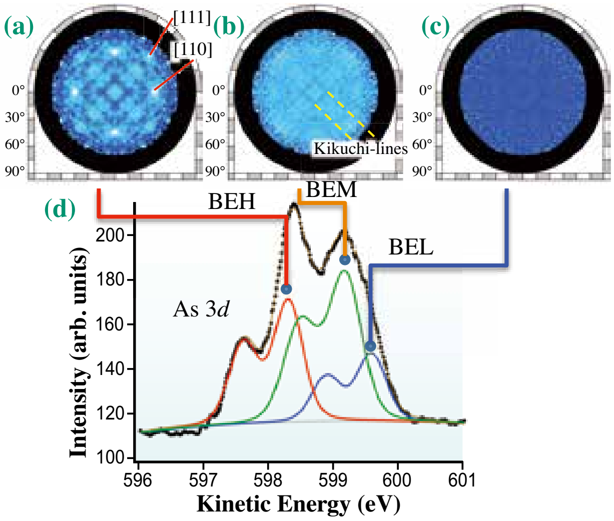

Fig. 2. Holograms generated from the spectra labeled **(a)** BEH, **(b)** BEM, and **(c)** BEL, and **(d)** As 3*d* core-level photoelectron spectra with labels. [3]

Although the pattern associated with the BEM peak is less intense, Kikuchi lines are clearly evident. The pattern from the BEL peak is unclear and has little structure.

The atomic images of these sites were reconstructed, as shown in Figs. 3(a-c) and Figs. 2(e-g), which correspond to the BEH and BEM peaks, respectively. The atomic image for the BEH peak indicated that the As atoms were located at substitutional sites in the Si lattice. However, the atomic image of the first nearest neighbor (NB) was quite weak as shown in Fig. 3(b). Our first-principles MD simulations suggested that this is due to the slightly larger amplitude of thermal oscillations of As atoms relative to Si atoms, as shown in the structural image of Fig. 3(d). On the other hand, for the BEM peak, atomic images of (1/2, 1/2, 0) in Fig. 3(e) were elongated. On the basis of the result that atomic images of the first NB are visible (Fig. 3(f)), we conclude that As atoms occupy the substitutional sites, the same as in the BEH case, even though the positions of As atoms thermally fluctuate.

To investigate the structural difference between BEH and BEM, we observed electrical activation and chemical shifts. Comparing the relative peak intensity ratio (Fig. 2(d)) with electrical activation rate (~50%), and considering our previous work of SXPES indicating that electrically active As has a larger binding energy [1], the As giving the BEH peak was determined to be electrically active. On the other hand, As atoms giving the BEM peak are considered to form As cluster structures. We evaluated their binding energy shifts for As 3d core-levels by first-principles calculations. Comparing the theoretical values for candidate clusters reported so far with the experimental values, we concluded that the As atoms giving the BEM peak form As$_n$V($n=2-4$) cluster structures, as shown in Fig. 3(h) for the case of $n=2$. Based on the structureless hologram (Fig. 2(c)), the As atoms responsible for the BEL peak are thus considered to be located in either amorphous or disordered structures.

In conclusion, the 3D atomic structures of As doped into a Si crystal were successfully revealed. This work demonstrated the potential of spectro-photoelectron holography for the analysis of dopants in semiconductors.

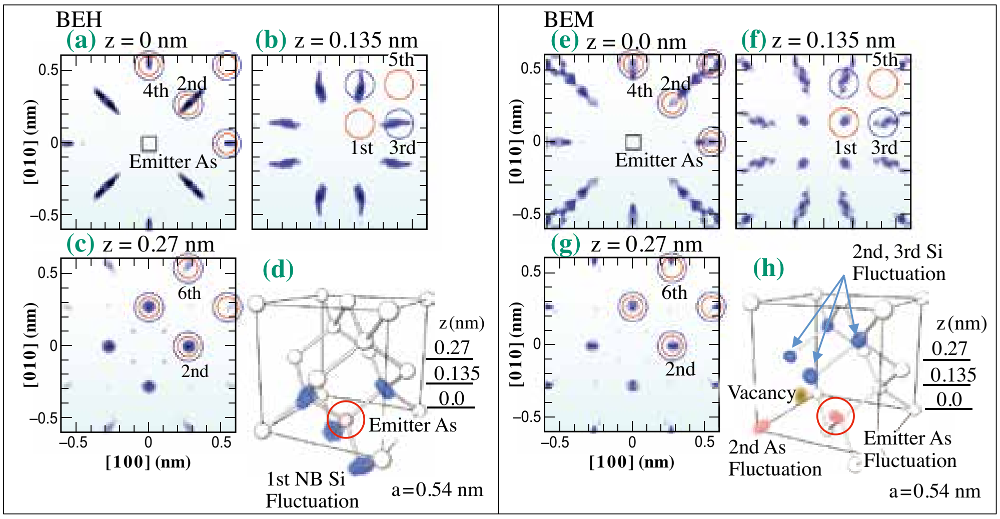

Fig. 3. Atomic images reconstructed from the holograms for the BEH and BEM spectra. The BEH cross sections are labeled as z = **(a)** 0, **(b)** 0.135 (= a/4), and **(c)** 0.27 nm (= a/2), a: lattice constant. The candidate structure is shown in **(d)**. Those for the BEM are shown in **(e)-(h)** in the same manner. In the structural images, (d) and (h), "emitter As" atoms are red, notable Si atoms and vacancies near the emitters are blue and brown, respectively, and fluctuating atoms appear blurry. [3]

Kazuo Tsutsui[a,*], Tomohiro Matsushita[b]
and Yoshitada Morikawa[c]

[a] Institute of Innovative Research,
Tokyo Institute of Technology
[b] Japan Synchrotron Radiation Research Institute (JASRI)
[c] Department of Precision Science and Technology,
Osaka University

*Email: ktsutsui@ep.titech.ac.jp

References

[1] K. Tsutsui *et al*.: J. Appl. Phys. **104** (2008) 093709.
[2] A. Szöke: AIP Conf. Proc. **147** (1986) 361.
[3] *K. Tsutsui, T. Matsushita, K. Natori, T. Muro, Y. Morikawa, T. Hoshii, K. Kakushima, H. Wakabayashi, K. Hayashi, F. Matsui, T. Kinoshita: Nano Lett.* ***17*** *(2017) 7533.*
[4] T. Matsushita *et al*.: J. Phys. Soc. Jpn. **87** (2018) 061002.
[5] Y. Hamamoto *et al*.: Phys. Rev. B **93** (2016) 245440.

The origin of water's anomalous properties revealed by X-ray lasers

Water, both common and necessary for life on earth, behaves very strangely in comparison with other substances. How water's density, specific heat, viscosity and compressibility respond to changes in pressure and temperature is completely opposite to other liquids that we know. We all are aware that all matter shrinks when it is cooled resulting in an increase in the density. We would therefore expect that water would have high density at the freezing point. However, if we look at a glass of ice water (Fig. 1), everything is upside down, since we expect that water at 0°C being surrounded by ice should be at the bottom of the glass, but of course as we know ice cubes float. Strangely enough for the liquid state, water is the densest at 4 degrees C, and therefore it stays on the bottom whether it's in a glass or in an ocean. This is why life can exist at the bottom of a lake and an ocean during winter even when the surface is frozen. If we cool water below 4 degrees, it starts to expand again. If we continue to cool pure water (where the rate of crystallization is low) to below 0, it continues to expand – the expansion even speeds up when it gets colder. Many more properties such as compressibility and heat capacity become increasingly strange as water is cooled. As we know it so far there is no life without water.

The microscopic origin of the anomalous properties of water has been elusive and there has been an intense debate for over a century. One major hypothesis, that has strong indirect support from theoretical work, is that there could exist two different liquid states, high-density liquid (HDL) and low-density liquid (LDL). The phase boundary between the two phases would be at high pressures. This liquid-liquid transition (LLT) line is proposed to end with decreasing pressure and increasing temperature in a liquid-liquid critical point (LLCP) and its extension into the one-phase region corresponds to the Widom line [1,2]. At the Widom line, the density fluctuations would reach a maximum (see Fig. 2). The challenge has been that water crystallization has prevented measurements of the bulk liquid phase below the homogeneous nucleation temperature of ~232 K and above ~160 K, leading to a 'no-man's land' devoid of experimental results regarding the structure.

A new technique using ultrafast single-shot X-ray diffraction probing with free-electron lasers and fast cooling of micron-sized droplets in a vacuum showed the existence of metastable bulk liquid water down to temperatures of 227 K and allowed us to venture into a 'no-man's land' [3,4]. The measurements were performed at SACLA **BL3** beamline and the NCI beamline of PAL-XFEL [5]. The results obtained from the experiment is summarized in Fig. 3. The small angle X-ray scattering (SAXS) intensity initially increases upon cooling, then reaches the maximum at around 229 K, and subsequently decreases for lower temperatures. Isothermal compressibility and correlation length can be derived from the SAXS intensities and it was found that they also reach a maximum at 229 K. From the wide angle X-ray scattering (WAXS) measurement, it was also seen that the continuous increase of structures with local tetrahedral coordination became more enhanced upon deep supercooling, which shows an accelerated transition towards a LDL dominated structure. The derivative with respect to the temperature of the position of the structure factor also shows maxima at 229 K. It is fully consistent with the picture drawn from the SAXS measurement. This is the first experimental evidence of the existence of the Widom line and this is fully consistent with the LLCP hypothesis, which can explain the origin of water's anomalous properties [5]. There are fluctuations that extend from the LLCP all the way up to ambient pressures and temperature causing water behave in a strange way. We can call the Widom line the smoke from the fire being the LLCP. This is the strongest experimental evidence of the LLCP. Another remarkable finding of the study is that the unusual properties were different between

Fig. 1. A glass of ice water with a thermometer measuring 4 degrees C at the bottom.

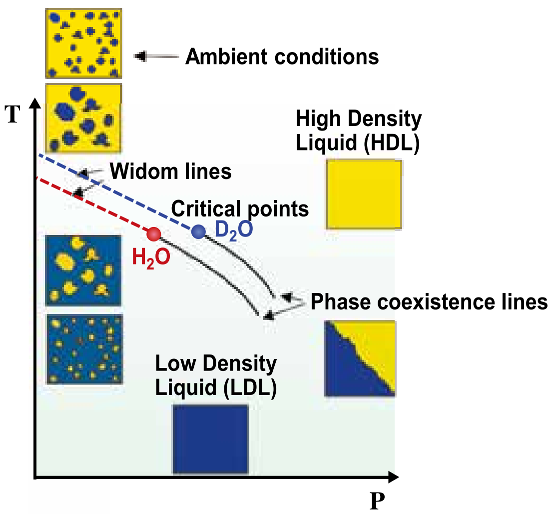

Fig. 2. Schematic picture of a hypothetical phase diagram of liquid water, showing the Widom lines, liquid-liquid critical points, and phase separation lines of H_2O and D_2O.

normal and heavy water, and was more enhanced for the lighter water, thus showing the importance of nuclear quantum effects [4].

With the help of ultra-short X-ray pulses, we were able to X-ray unimaginably fast before the ice froze and could observe how it fluctuated between the two states. For decades there have been speculations and different theories to explain these remarkable properties and why they got stronger when water becomes colder. Now we have found such a maximum, which means that there should also be a critical point at higher pressures.

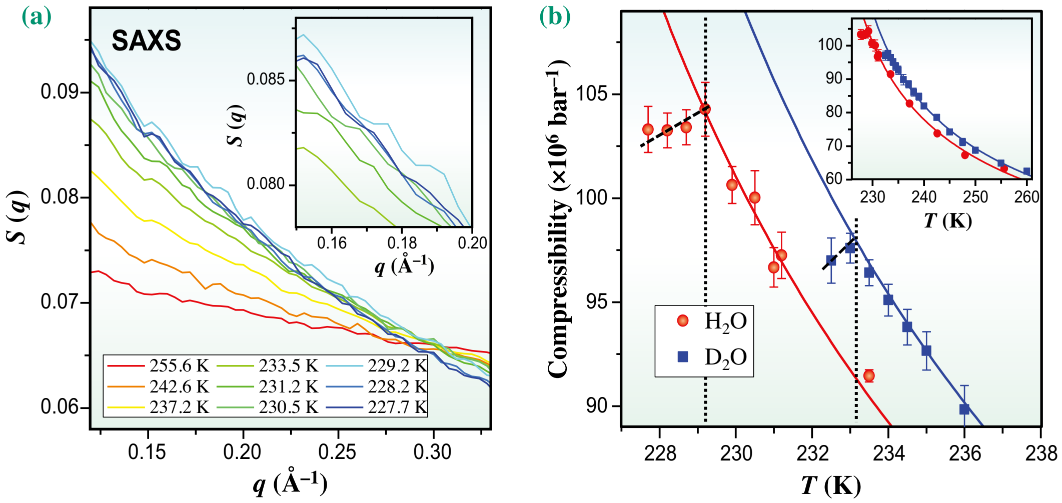

Fig. 3. **(a)** Temperature dependent scattering structure factor, $S(q)$ of H_2O at the SAXS region. The inset shows the magnified view from $q = 0.15$ to 0.2 Å^{-1}. **(b)** Temperature dependent isothermal compressibility of H_2O (red) and D_2O (blue).

Kyung Hwan Kim[a], Alexander Späh[b] and Anders Nilsson[b,*]

[a] Department of Chemistry, POSTECH, Korea
[b] Dept. of Physics, AlbaNova University Center, Stockholm University, Sweden

*Email: andersn@fysik.su.se

References

[1] O. Mishima, H.E. Stanley: Nature **396** (1998) 329.
[2] P.H. Poole *et al.*: Nature **360** (1992) 324.
[3] J.A. Sellberg *et al.*: Nature **510** (2014) 381.
[4] K.H. Kim *et al.*: Phys. Rev. Lett. **119** (2017) 075502.
[5] *K.H. Kim, A. Späh, H. Pathak, F. Perakis, D. Mariedahl, K. Amann-Winkel, J.A. Sellberg, J.H. Lee, S. Kim, J. Park, K.H. Nam, T. Katayama and A. Nilsson: Science* ***358*** *(2017) 1589.*

How to make materials more resistant to extreme deformation

Understanding of the fracture phenomena of a material under extreme conditions of pressure and/or temperature is crucial for a wide variety of scientific fields ranging from applied science and technological developments to fundamental science such as laser-matter interactions and geology. This universal process is particularly important for the development of new materials. Indeed, the properties related to the fracture of materials depend on the way forces are applied to materials as the properties are difficult to define physically. Such properties include the bulk modulus, young's modulus, and spall strength. A method of directly estimating spall pressure may facilitate the efficient evaluation of the spall property to explore novel materials. As an example, there is a large amount of debris around the Earth traveling at an average velocity of ~10 km/s and can hit spacecraft and satellites. If one can test and develop new materials that have different behaviors of dynamic fracture, one can make them more robust or with specific properties (e.g., void size). We have been attempting to bridge the gap between the fundamental study of dynamic fracture and the needs of engineers in materials design, system certification, and manufacturing as discussed in [1].

Several experimental techniques have been developed over the last few decades to study the dynamical damage of a material using macroscopic information, such as the evolution of the free surface velocity and/or information obtained from postmortem examination of the sample. However, a gap exists between the information retrieved at the macroscopic scale from experiments and that obtained from large-scale simulations performed at the atomic scale. In Ref. 2, a new experimental technique is presented, which allows the direct ultrafast real-time monitoring of dynamic fracture (spallation) at the atomic scale with picosecond time resolution. This is achieved in coupling an optical high-power laser ($I \sim 2.5\times10^{12}$ W·cm^{-2}), which generates a shock wave inside the sample (5-µm-thick polycrystalline tantalum), with an X-ray beam (10 keV photon energy) used as a probe. The experimental setup is displayed in Fig. 1 and the experiment has been performed at SACLA **BL3**.

Experimental results are presented in Fig. 2. We were able to directly measure an extension of the tantalum lattice of ~8 to 10% just before fracture occurred at an ultrahigh strain rate of $\sim2\times10^8$-3.5×10^8 s^{-1} using X-ray diffraction. The spall strength has also been determined to be approximately –16.8 GPa. These results have been directly compared with large-scale molecular dynamics simulations and are in good agreement with simulated data (see Fig. 3). This not only paves the way toward the direct measurement of the spall strength of materials as a function of strain rate but also highlights the usefulness of these facilities for investigating various physical problems such as high-speed crack dynamics, uncommon stress-induced solid-solid phase transitions, and so forth.

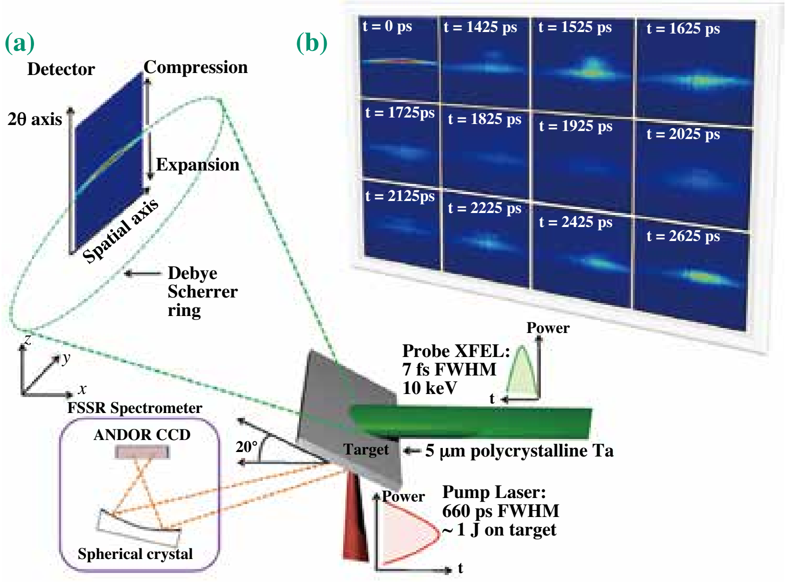

Fig. 1. Pump-probe experiment at SACLA BL3. **(a)** Experimental configuration. **(b)** Experimental results.

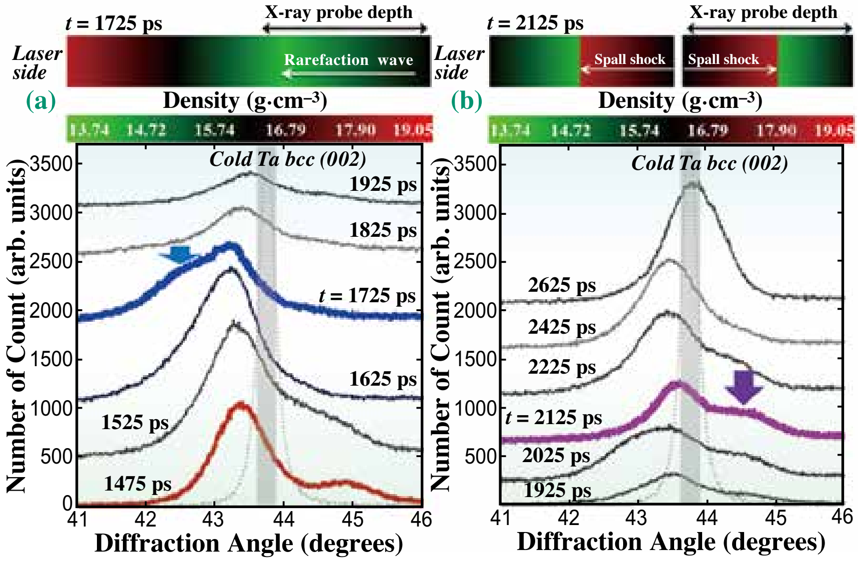

Fig. 2. Experimental profiles of stretching and postspallation compression in a Ta sample. **(a)** Observed stretching (blue curve) of the (002) plane of Ta in the experiment. **(b)** Observed compression wave (purple curve) due to the relaxation of tension after spallation.

As a conclusion, it is interesting to note that the repetition rate of the SACLA platform is non-negligible. This means that it is possible, during one experimental campaign, to test many different materials. This makes it easy to investigate the atomic structures of new materials and select those having the desired macroscopic properties over a wide range of strain rates and deformations. Then, in the next cycle of development, the obtained knowledge about specific relationships between these mechanical properties and atomic structures can be used in the design of the next generation of materials. In this way, XFEL facilities may accelerate the development of new materials by bridging the gap in the understanding of the relationships between atomic structures and material properties.

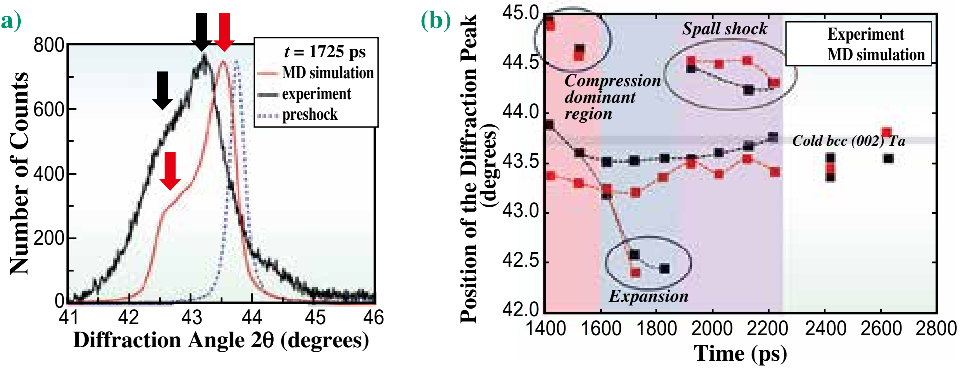

Fig. 3. Comparison between experimental results and those obtained in large-scale atomistic simulation. **(a)** Direct comparison between the diffraction signal obtained in the experiment (black) and simulation (red). **(b)** Dynamical comparison of the position of the peak in the experiment and simulation.

Bruno Albertazzi[a,*], Norimasa Ozaki[b]
and Vasily Zhakhovsky[c]

[a] LULI, École Polytechnique, CNRS, France
[b] Photon Pioneers Center, Osaka University
[c] Dukhov Research Institute of Automatics,
ROSATOM, Russia

*Email: bruno.albertazzi@polytechnique.edu

References

[1] B.N. Cox *et al.*: J. Mech. Phys. Solids **53** (2005) 565.
[2] *B. Albertazzi, N. Ozaki, V. Zhakhovsky, A. Faenov, H. Habara, M. Harmand, N. J. Hartley, D. Ilnitsky, N. Inogamov, Y. Inubushi, T. Ishikawa, T. Katayama, M. Koenig, A. Krygier, T. Matsuoka, S. Matsuyama, E. McBride, K. Migdal, G. Morard, T. Okuchi, T. Pikuz, O. Sakata, Y. Sano, T. Sato, T. Sekine, T. Seto, K. Takahashi, H. Tanaka, K. A. Tanaka, Y. Tange, T. Togashi, K. Tono, Y. Umeda, T. Vinci, M. Yabashi, T. Yabuuchi, K. Yamauchi and R. Kodama: Sci. Adv.* **3** *(2017) e1602705.*

Element selectivity in second-harmonic generation by using a soft-X-ray Free Electron Laser

Significant developments of lasers have led us to discover novel optical responses of matter. A well-known example is the nonlinear effect that generates a signal from specific environments, such as inside a nonlinear crystal and a surface/interface system, that have hardly been probed in usual optical experiments. Nowadays, laser pulses of soft and hard X-rays can be used in experiments at X-ray free electron laser (XFEL) facilities such as the SPring-8 Angstrom Compact Free Electron Laser (SACLA). The energy of photons covers various absorption edges of elements and it can be tuned to satisfy the resonance condition in the interaction between light and matter. The resonance effect has been used to perform X-ray spectroscopy or X-ray scattering experiments with element selectivity. Using ultrahigh-intensity laser pulses of an XFEL, one can now examine the core-level resonance of the nonlinear optical effect (Fig.1).

In the present research, we investigated second-harmonic generation (SHG), one of the nonlinear optical frequency conversions, in the soft X-ray region [1]. The demonstration was performed at SACLA-SXFEL **BL1**. The FEL was operated at a nominal electron beam energy of 400 MeV in the experiment. The SXFEL beamline was chosen owing to the advantages of photon-energy tuning in the EUV-soft X-ray region and ultrahigh brilliance, enabling the examination of nonlinear optics at various photon energies. The sample was a non-centrosymmetric crystal of $GaFeO_3$. The resonance enhancement of SHG signals was expected when the photon energy with double the frequency 2ω was above the absorption edge of a sample. Thus, the SHG resonance condition ($2\omega = \omega_{ng}$) was satisfied by the energy difference between the Fe 3*p* level and the unoccupied band, as shown in Fig. 2.

Figure 3(a) shows an overview of the beamline and the measurement system. The measurement was made in the reflection geometry. The reflected light from the sample was incident on the grating and the diffracted intensity was measured using a microchannel plate (MCP) detector that could be moved along the energy-dispersion direction. The spectral intensities of the reflected light (I_ω and $I_{2\omega}$) were measured at various MCP positions, as shown in Fig.3.

Figure 3(b) shows the Fe 3*p* absorption spectrum of the $GaFeO_3$ crystal, showing the Fe 3*p* absorption edge above 54 eV. The photon energy of the SXFEL pulse was set to half of the Fe 3*p* absorption edge. Figure 3(c) shows the variation of the reflected intensity at a photon energy of $\hbar\omega = 27.5$ eV with respect to the incident intensity I_0. The dashed line represents the fitted curves obtained by using the power law $\propto I_0^\beta$. The exponent coefficient is $\beta = 1.0$, which verifies the linearity of the ω component. The intensity of the 2ω component ($2\hbar\omega = 55$ eV) clearly shows its nonlinear dependence on I_0, as shown in Fig. 3(d). Moreover, the 2ω signal intensity significantly decreases when the photon energy is tuned to $2\hbar\omega = 53$ eV ($\hbar\omega = 26.5$ eV), which is below the Fe 3*p* absorption edge (Fig. 3(e)). From the power-law fitting, the exponent coefficients are $\beta = 1.8$ ($2\hbar\omega = 55$ eV), $\beta = 2.0$ ($2\hbar\omega = 57$ eV), and $\beta = 2.0$ ($2\hbar\omega = 59$ eV). The experimental values consistently match the quadratic intensity dependence ($\beta = 2$) of the SHG light. These

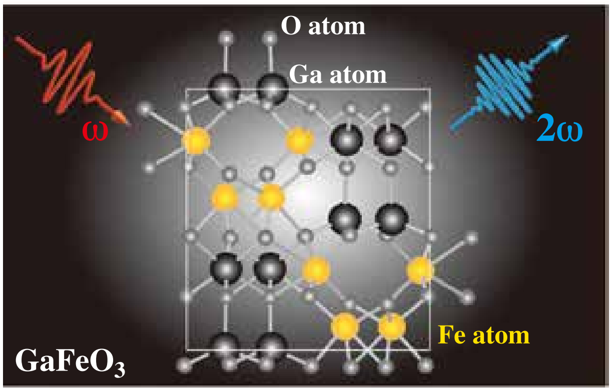

Fig. 1. Schematic drawing of second-harmonic generation in a $GaFeO_3$ crystal using Fe 3*p* resonance.

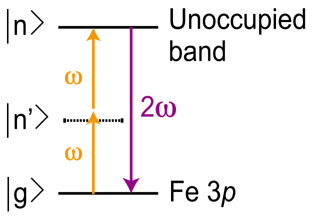

Fig. 2. Energy diagram of SHG in $GaFeO_3$. The notations g, n', and n represent the ground state, intermediate state, and excited state, respectively.

results unambiguously indicate the detection of SHG light from the $GaFeO_3$ crystal.

In summary, we demonstrated the possibility of element selectivity in SHG spectroscopy measurements in the soft X-ray range. We observed, for the first time, SHG in the reflected beam from a nonlinear crystal in the soft X-ray range. For a surface system, SHG in the soft X-ray region was observed at the XFEL facility of FERMI@ELETTRA in the transmission geometry [2]. The resonant SHG scheme is expected to promote new understanding of various samples, such as strongly correlated systems and the interfaces of heterojunctions in spintronics.

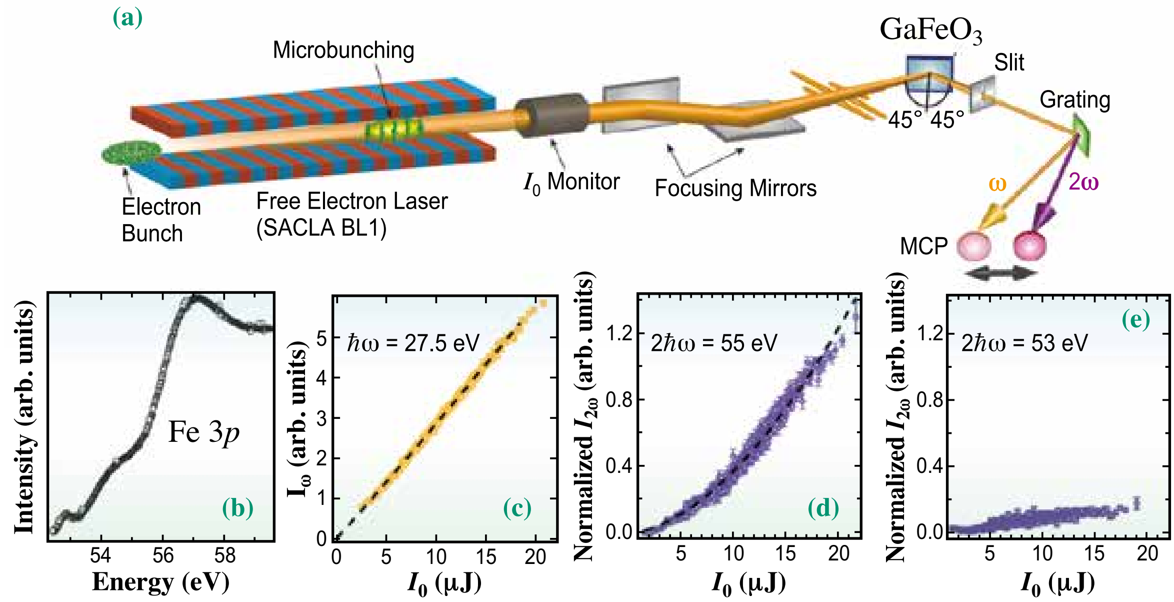

Fig. 3. **(a)** Schematic drawing of the SHG measurement at the SXFEL beamline in SACLA. **(b)** Fe 3*p* absorption spectrum of the $GaFeO_3$ crystal taken at BL-5B (UVSOR). **(c)** Intensity plot of the ω component, I_ω, of the reflected SXFEL pulses with respect to I_0 at the photon energy $\hbar\omega = 27.5$ eV. **(d)** Plot of $I_{2\omega}$ at $2\hbar\omega = 55$ eV. **(e)** Plot of $I_{2\omega}$ at $\hbar\omega = 53$ eV. The dashed lines shown in (c) and (d) are the fitted curves.

Iwao Matsuda

The Institute for Solid State Physics,
The University of Tokyo

Email: imatsuda@issp.u-tokyo.ac.jp

References

[1] *Sh. Yamamoto, T. Omi, H. Akai, Y. Kubota, Y. Takahashi, Y. Suzuki, Y. Hirata, K. Yamamoto, R. Yukawa, K Horiba, H. Yumoto, T. Koyama, H. Ohashi, S. Owada, K. Tono, M. Yabashi, E. Shigemasa, S. Yamamoto, M. Kotsugi, H. Wadati, H. Kumigashira, T. Arima, S. Shin and I. Matsuda: Phys. Rev. Lett.* ***120*** *(2018) 223902.*

[2] *R.K. Lam, S.L. Raj, T.A. Pascal, C.D. Pemmaraju, L. Foglia, A. Simoncig, N. Fabris, P. Miotti, C.J. Hull, A.M. Rizzuto, J.W. Smith, R. Mincigrucci, C. Masciovecchio, A. Gessini, E. Allaria, G. De Ninno, B. Diviacco, E. Roussel, S. Spampinati, G. Penco, S. Di Mitri, M. Trovò, M. Danailov, S.T. Christensen, D. Sokaras, T.-C. Weng, M. Coreno, L. Poletto, W.S. Drisdell, D. Prendergast, L. Giannessi, E. Principi, D. Nordlund, R.J. Saykally, C.P. Schwartz: Phys. Rev. Lett.* ***120*** *(2018) 023901.*

X-ray two-photon absorption spectroscopy

Successful lasing at SACLA has opened up a new frontier of nonlinear optics, i.e., X-ray nonlinear optics. Up to now, various nonlinear optical phenomena [1], such as two- and multiphoton absorption, saturable absorption, second harmonic generation, superradiance, stimulated emission, and sum-frequency generation, have been observed in the hard X-ray region.

Since nonlinear optical processes originate from different mechanisms from linear processes, they can access different information of materials. For example, the selection rule of direct two-photon absorption (TPA) is the opposite of one-photon absorption. As a result, direct TPA can use the 1*s*-3*d* transition, whereas the conventional X-ray absorption spectroscopy relies on the 1*s*-4*p* transition [2]. The 3*d* electrons play important roles in the 3*d* transition metal compounds, which include valuable functional materials, such as high-temperature superconductors. The ability of direct TPA to access the 3*d* orbital may provide a better understanding of the physical properties.

However, none of the X-ray nonlinear optical phenomena have been applied to novel spectroscopic and diffractive techniques. One reason is the need for intense X-rays. In fact, we employed intense X-rays with peak intensities beyond 10^{19} W/cm^2 to observe direct TPA and found that the electronic state of the sample changes within the femtosecond pulse duration [3]. Therefore, we cannot measure the sample as it is, i.e., in the ground state, when we use high intensity X-rays.

In this study [4], we determined the threshold above which a change in electronic state appears in the absorption spectrum and measured the direct TPA spectrum of metallic copper around the threshold at SACLA **BL3**. This is the first application of an X-ray nonlinear optical process to nonlinear spectroscopy.

First, we discuss the threshold. Figure 1 shows the absorption spectra (XANES, X-ray absorption near-edge structure) of copper measured with intense X-rays in transmission geometry. The pulse energies range from 0.5 to 20 μJ. The peak intensity is estimated to be around 10^{15} W/cm^2 from the focus size of 1.5×1.6 μm^2 and the pulse duration of 8 fs. The spectrum starts to change in the vicinity of the absorption edge. At higher pulse energies, the absorption edge shifts toward the higher photon-energy side. We consider that the spectral change is caused by impact ionization, where a fast photoelectron created by X-ray absorption ionizes the surrounding atoms. Simultaneous X-ray absorption within the small focal spot quickly creates a number of energetic free electrons, which change the absorption coefficient and spectrum.

The analysis of the pulse energy dependence of XANES is not straightforward because the X-ray intensity decreases as the beam propagates in the sample. X-ray absorption with different absorption coefficients contributes to the measured transmittance. Detailed analysis [4] gives the threshold for measuring the unchanged spectrum to be an energy density of 0.02 μJ/μm^3 (1.5 eV/atom). It is interesting to compare this threshold with the energy density of melting, which is 0.3 eV/atom for copper and is five times lower than the threshold. The melt limit may give a rough estimation of the threshold.

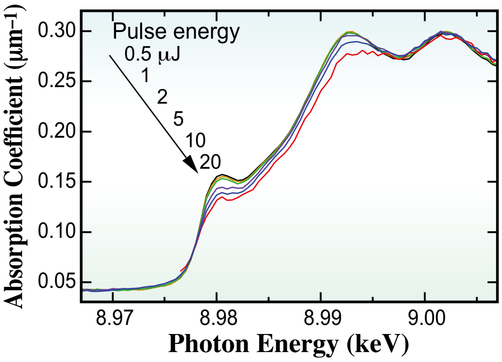

Fig. 1. Pulse energy dependence of XANES of metallic copper.

Now, we consider the experimental difficulties caused by the low threshold. The peak intensity, which can be used to measure the TPA signal, becomes much lower than that in the previous observation [3]. Since the contribution of TPA to the total absorption is negligible, we measure the weak X-ray fluorescence from the excited state by TPA as the signal. Thus, it is crucial to suppress the background sources, such as the elastic scattering, the Compton scattering, and the fluorescence due to higher harmonics. The scattering can be suppressed by measuring the TPA fluorescence signal at a right angle to the incidence within the polarization plane. It is more important to eliminate the higher harmonics, because they can produce a strong fluorescence by the linear absorption. The third-harmonic radiation was reduced by using cutoff mirrors. The second harmonic was eliminated by the forbidden 222 reflection of a double channel-cut Si 111 monochromator.

Figure 2 shows the TPA spectrum, which is the photon energy dependence of the TPA cross section. The cross section is deduced from the pulse energy dependence of the TPA fluorescence count at each photon energy. The TPA spectrum is considerably different from the one-photon absorption (XANES). The absorption edge in the TPA spectrum is lower than that in XANES. The shift of the absorption edge is consistent with the fact that the 1*s*-3*d* transition is allowed for TPA. The 3*d* orbital is closer to the nucleus than the 4*p* orbital and is subjected to a stronger potential. The creation of a *K*-shell core hole increases the binding energy of the 3*d* orbital and moves the TPA edge toward the lower-photon-energy side. Unfortunately, there is no quantitative theory to interpret the TPA spectrum. However, divergence toward the edge can be explained by the Anderson orthogonality catastrophe in metals with an incomplete shell [2].

In summary, we determined the threshold above which the intrinsic absorption spectrum cannot be measured owing to impact ionization. The threshold is found to be an absorbed energy density of 0.02 μJ/μm³ for metallic copper, which may be reached under typical experimental conditions with X-ray free-electron lasers. Thus, an extended survey of the threshold in various materials is needed to design experimental conditions. We successfully measured the direct TPA spectrum of metallic copper around the threshold, in spite of four-orders-of-magnitude lower peak intensities than those used for the direct TPA experiment. Our achievement is expected to encourage further investigation of the X-ray nonlinear optical process for novel application to nonlinear spectroscopy.

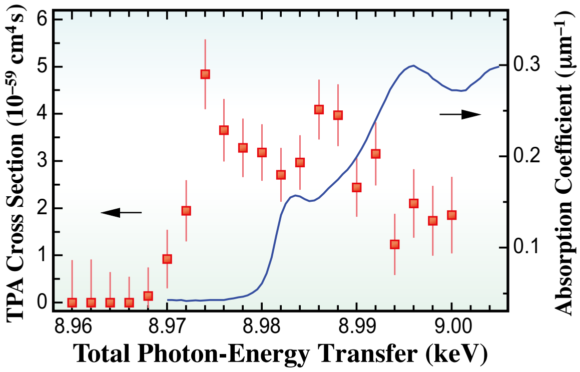

Fig. 2. Direct TPA spectrum (filled squares) and XANES (solid line) of metallic copper. Vertical bars represent the fitting error.

Kenji Tamasaku

RIKEN SPring-8 Center

Email: tamasaku@riken.jp

References

[1] R.W. Boyd: Nonlinear Optics (Academic Press, London, 2003).
[2] F. de Groot and A. Kotani: Core Level Spectroscopy of Solids (CRC Press, New York, 2008).
[3] K. Tamasaku *et al.*: Nat. Photon. **8** (2014) 313.
[4] *K. Tamasaku, E. Shigemasa, Y. Inubushi, I. Inoue, T. Osaka, T. Katayama, M. Yabashi, A. Koide, T. Yokoyama and T. Ishikawa: Phys. Rev. Lett.* ***121*** *(2018) 083901.*

Different quark-antiquark production mechanism of $u\bar{u}$ from $d\bar{d}$ and $s\bar{s}$ studied by linearly polarized high energy photon beams at BL33LEP

We carried out meson (quark-antiquark) and baryon (three quarks) production experiments from a proton target using high energy photon (γ) beams of 1.5-2.95 GeV. According to the well-known formula $E = mc^2$ of Einstein, the high energy photon beams produce masses. In our experiments, lepton-antilepton(e^-e^+) or quark-antiquark($u\bar{u}$, $d\bar{d}$, and $s\bar{s}$) pairs are produced. We would like to clarify the structure of mesons and baryons and understand the production mechanisms of quark-antiquark pairs. At forward meson angles, we measured differential cross sections and photon beam asymmetries for the γ+proton → (a) $\pi^-+\Delta^{++}$ [1], (b) π^++neutron [2], and (c) $K^+ + \Lambda$ [3] reactions at SPring-8 **BL33LEP**. There are six types of quarks: u, d, s, c, b, and t, and six types of antiquarks: $\bar{u}$, $\bar{d}$, $\bar{s}$, $\bar{c}$, $\bar{b}$, and $\bar{t}$. On the basis of the quark model, the proton, Δ^{++}, neutron, and Λ baryons are composed of uud, uuu, udd, and uds quarks, and the π^-, π^+, and K^+ mesons are composed of $d\bar{u}$, $u\bar{d}$, and $u\bar{s}$ quark-antiquark pairs, respectively. These reactions produce pure (a) $u\bar{u}$, (b) $d\bar{d}$, and (c) $s\bar{s}$ pairs in the final state. We compare the results of these quark-antiquark productions precisely for the first time, which is essential to understand how mesons and baryons are produced.

Figure 1 shows the missing mass of the γ + proton → π^- + X reaction. The missing mass is calculated from the photon beam energy and the momenta of π^- in the x, y, and z directions. The law of conservation of momentum and energy is assumed. The Δ^{++} peak is predominantly observed and is fitted with a relativistic Breit-Wigner shape to obtain the yield. The contributions from 2π, 3π, and ρ productions and electron contamination in the π^- selection are considered as the background under the Δ^{++} peak. Figure 2 shows the first-ever high statistics differential cross sections for the γ+proton → $\pi^- + \Delta^{++}$ reaction [1]. As the photon energy increases, the cross sections decrease gradually. The result of the theoretical calculations by Nam [4] well reproduces the data for the photon energies above 1.9 GeV. Since the calculations do not introduce a nucleon or Δ resonance in the intermediate state, the bump (1.5-1.8 GeV) might be due to a contribution from the resonance.

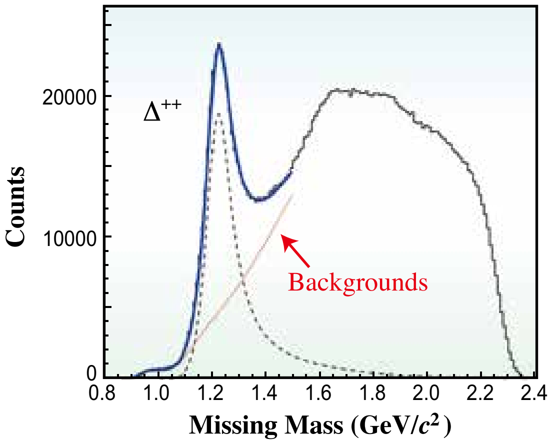

Fig. 1. Missing mass of the γ+proton → π^-+X reaction for E_γ = 1.5-2.95 GeV [1]. The thick solid curve is the result of the fit. The dashed curve is the Δ^{++} contribution.

The photon beam asymmetries measured by using linearly polarized photon beams are sensitive to quark-antiquark production mechanisms. When mesons are produced at forward angles, meson exchanges are dominant in the production mechanisms. Figure 3 shows the asymmetries for the γ+proton → $\pi^-+\Delta^{++}$ [1], π^++neutron [2], and $K^+ + \Lambda$ [3] reactions. The π^++ neutron and $K^+ + \Lambda$ reactions have positive asymmetries, which suggests the dominance of ρ-meson and K^*-meson exchanges, respectively, in the production mechanisms. In other similar meson productions, such as π^0+proton, η+proton, and $K^+ + \Sigma^0$, positive asymmetries were also observed. On the other hand, the $\pi^- + \Delta^{++}$ reaction is found to have negative asymmetries, which suggests the dominance of π-meson exchange. The result of the theoretical calculation by Nam [4] reproduces the negative asymmetries for the $\pi^- + \Delta^{++}$. It is quite interesting that only the $u\bar{u}$ production seems to have a different production mechanism from the $d\bar{d}$ and $s\bar{s}$ productions.

The π^++neutron reaction exchanges a u-quark in a proton(uud) for a d-quark, producing a neutron(udd). The $K^+ + \Lambda$ reaction also exchanges a u-quark for an s-quark, which produces a Λ(uds) baryon. Only the $\pi^- + \Delta^{++}$ reaction exchanges a d-quark for a u-quark and produces a Δ^{++} (uuu) baryon. The author's naive interpretation is that the spatial distribution of the d-quark might be different from that of the u-quark in the proton. The ρ-meson and K^*-meson have relatively heavy masses of 770 and 890 MeV/c^2, respectively. The well-known theory by Yukawa suggests that the interaction of these heavy mesons is limited to short distances, for example, a few 0.1 fm. The π-meson has a low mass of 140 MeV/c^2 and its interaction can reach large distances of 1-2 fm, which are comparable

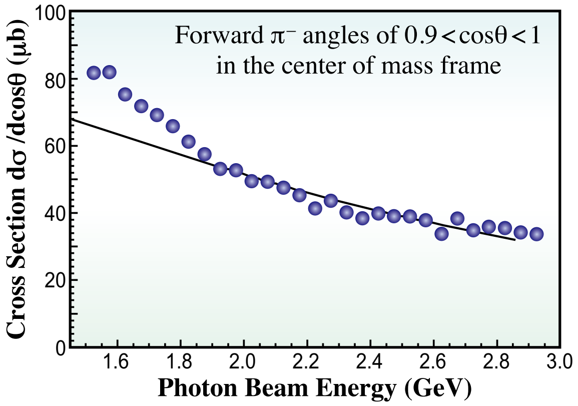

Fig. 2. Differential cross sections for the γ+proton → $\pi^-+\Delta^{++}$ reaction [1]. The solid curve is the theoretical calculation by Nam [4].

to the proton's radius of ~1 fm. Since we detected the mesons at forward angles of $0.9<\cos\theta<1$, the reactions are inferred to occur on the surface of the proton. If we assume that the *u*-quark is located near the surface and the *d*-quark remains in the central region of the proton, these asymmetry results are reasonably explained.

We are developing polarized HD (hydrogen-deuteride) targets. Longitudinally and transversely polarized proton targets are used in combination with circularly and linearly polarized photon beams. Many polarization observables for various reactions can be measured. We expect that new measurements will provide us with further interesting understanding of the proton structure and the quark-antiquark production mechanisms.

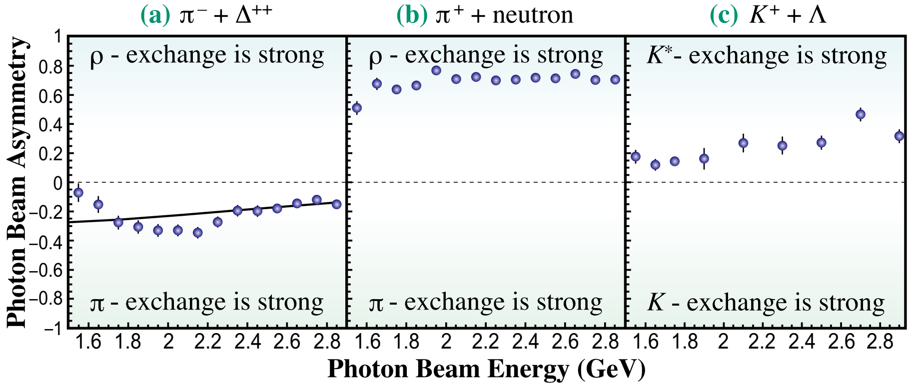

Fig. 3. Photon beam asymmetries for the γ+proton → **(a)** $\pi^-+\Delta^{++}$ [1], **(b)** π^++neutron [2], and **(c)** K^++Λ [3] reactions for forward meson angles of $0.9<\cos\theta<1$. The solid curve in (a) is the theoretical calculation by Nam [4].

Hideki Kohri for the LEPS collaboration

Research Center for Nuclear Physics,
Osaka University

Email: kohri@rcnp.osaka-u.ac.jp

References

[1] *H. Kohri, S.H. Shiu, W.C. Chang, Y. Yanai, D.S. Ahn, J.K. Ahn, J.Y. Chen, S. Daté, H. Ejiri, H. Fujimura, M. Fujiwara, S. Fukui, W. Gohn, K. Hicks, A. Hosaka, T. Hotta, S.H. Hwang, K. Imai, T. Ishikawa, K. Joo, Y. Kato, Y. Kon, H.S. Lee, Y. Maeda, T. Mibe, M. Miyabe, Y. Morino, N. Muramatsu, T. Nakano, Y. Nakatsugawa, S.i. Nam, M. Niiyama, H. Noumi, Y. Ohashi, T. Ohta, M. Oka, J.D. Parker, C. Rangacharyulu, R.Y. Ryu, T. Sawada, H. Shimizu, E.A. Strokovsky, Y. Sugaya, M. Sumihama, T. Tsunemi, M. Uchida, M. Ungaro, S.Y. Wang, M. Yosoi: Phys. Rev. Lett.* ***120*** *(2018) 202004.*
[2] H. Kohri *et al.*: Phys. Rev. C **97** (2018) 015205.
[3] S.H. Shiu *et al.*: Phys. Rev. C **97** (2018) 015208.
[4] S-I. Nam and B.G. Yu: Phys. Rev. C **84** (2011) 025203.

Observation of weak interlayer interaction in layered 2D material TiS_2

The nature of the weak interlayer interaction that holds together two-dimensional (2D) materials is decisive for realizing layered materials with unique properties. 2D materials and their layered materials such as graphene and transition metal dichalcogenides (TMDs) are attracting much attention owing to their many energy applications, such as electrode materials for ion batteries, as well as their physically interesting properties such as topological insulators. It is commonly assumed that the layers are held together by the van der Waals (vdW) force, which is caused by fluctuations in electron clouds. Since the vdW force is not described in ground states, it is very difficult for current theory to describe the weak interlayer interaction in layered 2D materials [1]. In addition, an unexpectedly strong interlayer interaction in layered PtS_2 was reported using spectroscopy [2].

The structure of the archetypal layered 2D material 1*T*-TiS_2, where 1*T* represents a trigonal phase, is shown in Fig. 1. The TiS_2 slabs are constructed by covalent Ti–S interactions, which should be accurately described by current theory. The slabs are stacked by weak interlayer interactions. Observation of the electron distribution in TiS_2 enables us to investigate the intralayer and interlayer interactions simultaneously. We have accurately observed the electron distribution using high-resolution diffraction data [3,4].

We observed the distribution of electrons between layers in TiS_2 with high resolution using synchrotron X-rays [5]. The electron density in TiS_2 was determined by Hansen-Coppens multipole modeling of the experimental and theoretical structure factors with a resolution of $d > 0.3$ Å. To obtain the experimental structure factors, we measured single-crystal diffraction data at 20 K using an imaging plate detector at SPring-8 **BL02B1**. The wavelength of the X-rays was 0.248 Å. To obtain the theoretical structure factors, we carried out density functional theory (DFT) calculations. The experimental lattice parameters and atomic positions were used for the calculations. The SCAN, LDA and PBE functionals coupled with several vdW functionals including rVV10, rev-vdW-DF2, vdW-DF2 and optB86b-vdW were used for the calculations. The theoretical structure factors were obtained by Fourier transform of the DFT electron densities.

Figure 2 shows the static deformation density in the intralayer of TiS_2. The deformation density was obtained by subtracting the independent atom model (IAM) electron density from the true electron density. Thus, the deformation density enhances interaction features that are unclear in electron density maps. Good agreement is observed between the experimental and theoretical deformation densities. The covalent nature of the Ti-S bond is confirmed from the electron accumulation. The quantitative agreement between the experimental and theoretical electron densities for the intralayer Ti–S interactions mutually validates both the experimental and theoretical approaches.

Figure 3 shows the static deformation density in the interlayer of TiS_2. The experimental interlayer S···S deformation density is significantly higher than the theoretical one. This indicates that a stronger interlayer interaction is observed in the experiment than that according to the theory at this DFT level. The discrepancy in the interlayer interaction is quantitatively evaluated by the dipole moment of the

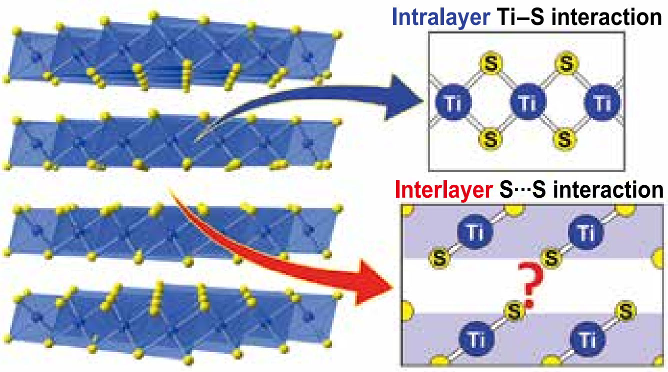

Fig. 1. Structure of 1*T*-TiS_2.

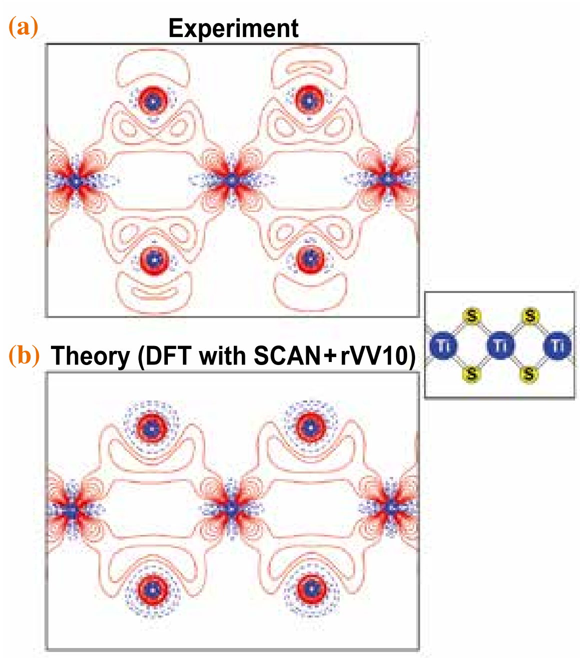

Fig. 2. Static deformation density for intralayer Ti–S interaction. Static deformation map from multipole modeling of **(a)** experimental and **(b)** theoretical structure factors. The contour interval is 0.05 eÅ^{-3}, with positive and negative contours drawn as solid red and dotted blue lines, respectively.

S atom. The magnitude of the atomic dipole moment of S obtained experimentally, $\mu = 0.03$ *e*Å, is 1/10 of the value obtained theoretically, $\mu = 0.34$ *e*Å. This difference is consistent with the electron density distribution in the interlayer, which is more pronounced in the experiment. This indicates that more attractive interlayer forces are observed in the experiment. While the DFT electron density is purely ground state, the experimental electron density is inherently time-averaged even when the thermal vibration is deconvoluted. This makes the experimental static electron density reflect all the chemical interactions, including the vdW forces. Therefore, it is reasonable to conclude that the observed difference between the experimental and theoretical electron distributions emerges from the existence of vdW interactions in the layered 2D material TiS$_2$.

Our X-ray electron density study revealed the nature of the weak interlayer interaction that holds together 2D materials. The high quality of the observation was confirmed by the quantitative agreement between the experiment and theory in the description of the intralayer Ti–S interaction. We observed substantial differences in the interlayer S···S interaction between the experiment and theory. This is attributed to the significant vdW interactions, which are poorly modeled by DFT using conventional functionals. Thus, the observed distribution of electrons provides a useful benchmark for theory in developing methods that accurately describe vdW interactions. The proper description of the weak interlayer interactions in layered materials is very important not only for science but also for the future engineering of layered 2D materials.

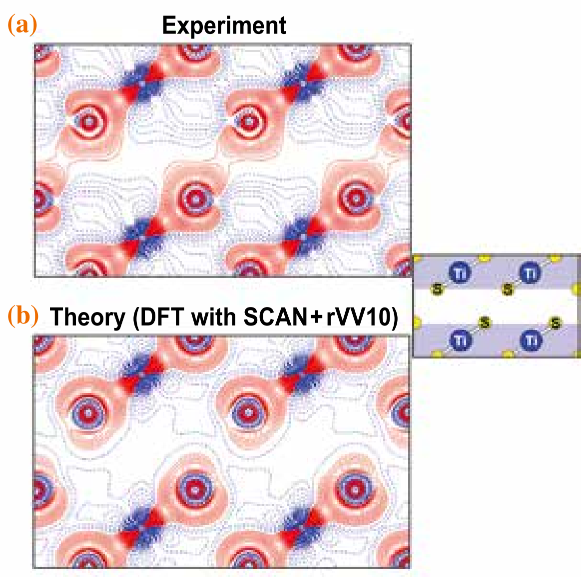

Fig. 3. Static deformation density for interlayer S···S interaction. Static deformation map from multipole modeling of **(a)** experimental and **(b)** theoretical structure factors. The contour interval is 0.01 eÅ^{-3}, with positive and negative contours drawn as solid red and dotted blue lines, respectively.

Hidetaka Kasai[a,*], Eiji Nishibori[a] and Bo B. Iversen[b]

[a] Faculty of Pure and Applied Sciences and Tsukuba Research Center for Energy Materials Science (TREMS), University of Tsukuba
[b] CMC, Dept. of Chemistry and Interdisciplinary Nanoscience Center (iNANO), Aarhus University, Denmark

*Email: kasai.hidetaka.fw@u.tsukuba.ac.jp

References

[1] L. Shulenburger *et al*.: Nano Lett. **15** (2015) 8170.
[2] Y. Zhao *et al*.: Adv. Mater. **28** (2016) 2399.
[3] H. Kasai and E. Nishibori: Phys. Scr. **91** (2016) 043009.
[4] H. Kasai and E. Nishibori: Sci. Rep. **7** (2017) 41375.
[5] *H. Kasai, K. Tolborg, M. Sist, J. Zhang, V.R. Hathwar, M.Ø. Filsø, S. Cenedese, K. Sugimoto, J. Overgaard, E. Nishibori and B.B. Iversen: Nat. Mater.* ***17*** *(2018) 249.*

Arrayed CH-π hydrogen bonds in a circle for single-axis rotation of a bowl in a tube

Designing unique molecules is one of the most indispensable roles of chemists, who strive to understand physical science through the language of molecules. Through the molecular design of rigid cylindrical molecules, we previously discovered unique behaviors of cylindrical molecules such as the intense circularly polarized luminescence and the solid-state, inertial rotational motion of a spherical guest in the cylinder [1,2]. With the aid of crystallographic analyses associated with another supramolecular complex with cylindrical molecules, we have now revealed the presence of CH-π hydrogen bonds [3]. As has been described by one of the reviewers of our paper [4], the CH-π hydrogen bond has "hovered around the border between a true hydrogen bond and a nonspecific dispersive interaction for some years," "but conclusive evidence has been elusive." The 2011 version of the International Union of Pure and Applied Chemistry (IUPAC) definition of hydrogen bonds states that "the evidence of bond formation" is indispensable for any type of hydrogen bond [5], and we are pleased to "supply strong evidence" (comment by the same reviewer) "with solid quantitative evidence for the strength of the complexation and for the conclusion that complexation is enthalpy driven" (by another reviewer). Additional findings of solid-state, single-axis rotation of bowl-shaped guests in a cylindrical host further highlight the uniqueness of the weak yet directional forces of CH-π hydrogen bonds.

The unique CH-π supramolecular complex was assembled with a cylindrical host molecule, (*P*)-(12,8)-[4]cyclo-2,8-chrysenylene ([4]CC), and a bowl-shaped guest, corannulene (COR) (Fig. 1 (a)). Through thermodynamics analyses with NMR and isothermal titration calorimetry (ITC), we obtained an association constant of $K_a = 2.94 \times 10^3 \cdot M^{-1}$ for the 1:1 complex, which was driven by favorable enthalpy with $\Delta H = -6.76$ kcal·mol^{-1}. There are 10 hydrogen atoms at the periphery of the bowl guest, and we estimate the enthalpy gain to be –0.7 kcal·mol^{-1} for one CH-π contact.

Theoretical studies further deepened our understanding of the chemical bonds in our bowl-in-tube supramolecular system. Density functional theory (DFT) calculations and atoms-in-molecule (AIM) analyses were useful for this investigation. The DFT calculations first reproduced experimental results such as association energetics and NMR chemical shifts. The subsequent AIM analyses then clarified the presence of the "CH-π hydrogen bonds." As can be seen in Fig. 1(b), the AIM analyses showed the presence of bond critical points (blue) and bond paths (orange), which anchor the bowl in the cylindrical space of the host. "For systems of this sort, this type of analysis is probably among the best evidence that can be expected" (by the reviewer).

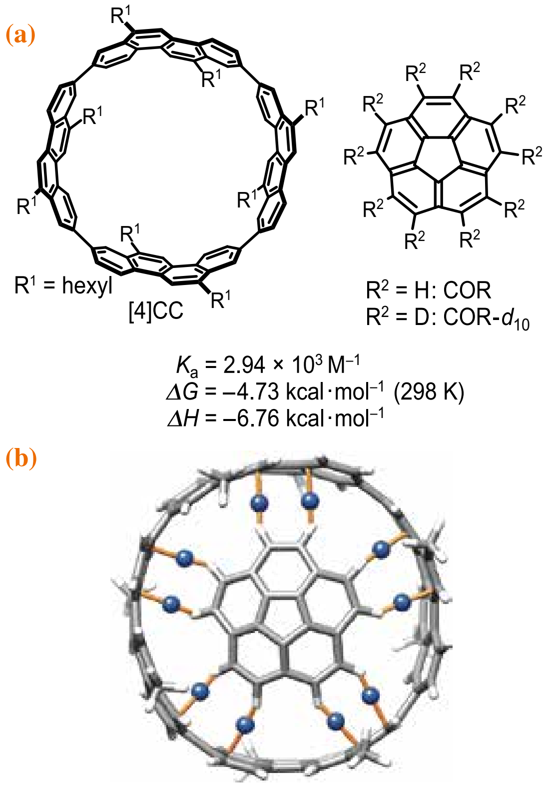

Fig. 1. Bowl-in-tube complex assembled with CH-π hydrogen bonds. **(a)** Molecular structures. **(b)** AIM analysis of the DFT structure of [4] CC⊃COR: bond critical points (blue) and bond paths (orange) are shown.

The solid-state structure of the bowl-in-tube complex was then revealed by crystallographic analysis. The diffraction analysis was carried out at SPring-8 **BL38B1**. Unexpectedly, in the crystalline solid state, the [4]CC guest and the COR host were present at a 1:2 ratio in the form of [4]CC⊃(COR)$_2$ (Fig. 2(a)). In this complex, one COR molecule occupied the central position of the cylindrical host (COR$_{\text{cent}}$) and the other molecule was stacked above it (COR$_{\text{edge}}$). These COR molecules were solved as disordered structures of three different orientations (Fig. 2(b)). The electron density mapping of COR indicates concentric distributions of electrons, indicating single-axis rotation of the COR guests. The structural parameters from the crystal data of the CH-π contacts were within the expected range for the CH-π hydrogen bonds.

One of the most intriguing findings of this study was the presence of dynamic motion of the COR guests. Anomalous single-axis rotation of the bowl-shaped guests was spectroscopically observed in the solid state. We prepared a crystalline solid of a complex composed of [4]CC and deuterated COR (COR-d_{10}) and measured solid-state ^{2}H NMR spectra under static conditions without magic angle spinning. The typical Pake doublet of ^{2}H resonance with quadrupolar splitting of 42 kHz was observed (Fig. 3(b)). This small splitting indicated the dynamic motion of COR-d_{10}, because the splitting for a static molecule should be 135 kHz. Simulation of the ^{2}H NMR line shape revealed that the COR guest rotated along a single C_5 axis of the molecule within the cylinder (Fig. 3(b)). The rotational frequency of this single-axis rotation was estimated to be 2.26 GHz at 298 K. Moreover, the precise energetics for the rotation was disclosed: the energy barrier $\Delta G^\ddagger$ was +4.67 kcal·mol^{-1}, which originated from the enthalpy barrier $\Delta H^\ddagger = +1.40$ kcal·mol^{-1} and the entropy barrier $-T\Delta S^\ddagger = +3.27$ kcal·mol^{-1} (298 K). The energetics showed the unique weak yet directional characteristics of the CH-π hydrogen bonds.

We found a novel CH-π complex in the form of a bowl-in-tube complex. This unique supramolecular system supplied the first firm evidence for the presence of CH-π hydrogen bonds with quantitative measures. The uniqueness of this weak yet directional force was noted with the dynamic motion within the complex, which, we believe, should provide a new design concept for molecular machinery.

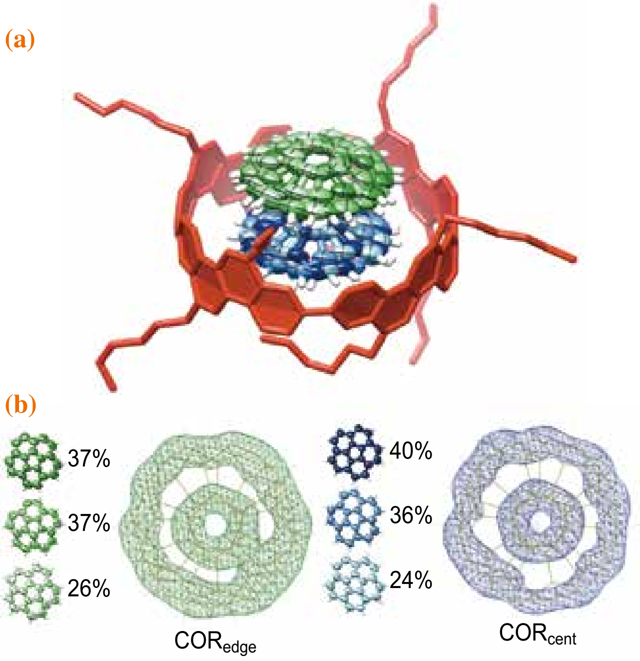

Fig. 2. Crystal structure of the bowl-in-tube complex, [4]CC⊃COR. **(a)** Molecular structures. **(b)** Contour electron density mappings ($2F_o-F_c$ contoured at 1.5σ, root mean square deviation) and disordered structures of COR.

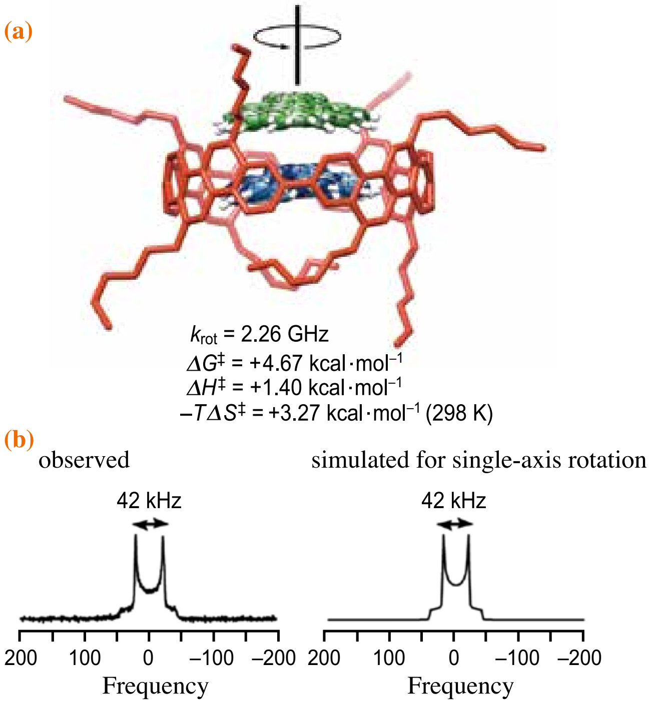

Fig. 3. Solid-state single-axis rotation of the bowl guests in a cylindrical host. **(a)** Axis of the single-axis rotation and kinetic parameters. **(b)** Observed and simulated solid-state ^{2}H NMR spectra under static conditions without magic angle spinning.

Taisuke Matsuno, Sota Sato and Hiroyuki Isobe*

Department of Chemistry, The University of Tokyo

*Email: isobe@chem.s.u-tokyo.ac.jp

References

[1] S. Sato *et al.*: Proc. Natl. Acad. Sci. USA **114** (2017) 13097.
[2] T. Matsuno *et al.*: Nat. Commun. **9** (2018) 1907.
[3] M. Nishio: Phys. Chem. Chem. Phys. **13** (2011) 13873.
[4] *T. Matsuno, M. Fujita, K. Fukunaga, S. Sato and H. Isobe: Nat. Commun.* ***9*** *(2018) 3779.*
[5] G.R. Desiraju: Angew. Chem. Int. Ed. **50** (2011) 52.

High-pressure synthesis of novel hydrides with high hydrogen densities – Li_3AlFeH_8 and $LiAlFeH_6$

Recent progress in synthesis techniques and theoretical calculations has enabled us to obtain novel hydrides with high hydrogen densities. Such hydrogen-rich materials are expected to be used as hydrogen storage materials. Some of them may show functionalities such as high-temperature superconductivity and fast ionic conductivity. We are synthesizing iron-containing complex hydrides because this class of materials consist of $[FeH_6]^{4-}$ complex anions and tend to have high hydrogen densities, and iron is one of the most common metals. As example of iron-containing complex hydrides, we have already synthesized $YLiFeH_6$ and Li_4FeH_6.

We are attempting to synthesize other iron-containing complex hydrides with higher hydrogen densities by incorporating H^- anions into iron-containing complex hydrides. Since the $[FeH_6]^{4-}$ complex anion is tetravalent and it is necessary to follow the 18-electron rule, possible combinations of countercations are limited to four types (Fig. 1(a)). When we try to synthesize a lightweight hydride, the combinations are severely limited. If we can incorporate H^- anions into an iron complex hydride, the number of combinations of countercations will markedly increase as shown in Fig. 1(b). The purpose of the present study [1] is to synthesize the theoretically predicted Li_3AlFeH_8 [2] using a high-pressure technique, which is a powerful technique for synthesizing novel hydrides.

The starting material was a powder mixture of LiH, AlH_3, and pure iron with a molar ratio of 3:1:1. The starting material was compacted into a small disk and was placed in a sample capsule made of boron nitride. The sample was pressurized to a target pressure ranging from 4-7 GPa at room temperature and then heated 600-800°C. We changed the pressure and temperature to find the synthesis conditions with the aid of *in situ* measurements.

Hydrogenation of the sample was achieved using a high-pressure cell developed by Fukai and Okuma [3]. A capsule made of NaCl was used as the hydrogen-sealing capsule. Hydrogen was evolved from a powder mixture of $NaBH_4$ and $Ca(OH)_2$ at around 400°C and confined in the hydrogen-sealing capsule. The sample was hydrogenated in a boron nitride capsule, in which hydrogen can permeate but other by-products from the internal hydrogen source cannot permeate.

We observed the structural changes of the sample during the hydrogenation reaction *in situ* by synchrotron radiation X-ray diffraction (SR-XRD) measurement at SPring-8 **BL14B1**. After the high-pressure treatment, the sample was quenched to room temperature and depressurized to ambient pressure. The recovered sample under ambient conditions was characterized by a conventional X-ray diffractometer.

We searched for hydrogenation conditions of the powder mixture by *in situ* SR-XRD measurement. Figure 2 shows a series of X-ray diffraction profiles of the sample hydrogenated at 5 GPa and 600°C. New Bragg peaks were observed approximately 50 min after the sample was heated to 600°C in hydrogen fluid. The Bragg peaks were indexed by the unit cell of the theoretically predicted Li_3AlFeH_8, indicating that the powder mixture was hydrogenated to form Li_3AlFeH_8. The inset of Fig. 2 shows the time evolution of the peak intensity of the 011 Bragg peak from Li_3AlFeH_8. The increase in the peak intensity finished at around 300 min. Unreacted iron was still observed at this stage, indicating that a single phase of Li_3AlFeH_8 cannot be obtained by a further hydrogenation reaction at 5 GPa and 600°C.

The hydrogenated sample was recovered under ambient conditions. Figure 3(a) shows the powder X-ray diffraction profile of the sample and the calculated profile for theoretically predicted Li_3AlFeH_8

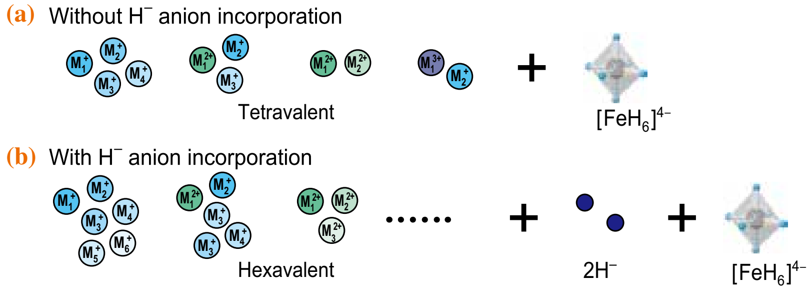

Fig. 1. Schematics of charge neutrality in iron-containing complex hydrides **(a)** without H^- anion incorporation and **(b)** with H^- anion incorporation.

(crystal structures shown in this article were drawn using the VESTA program [4]). The calculated profile reproduces the experimentally obtained one; we confirmed that the theoretically predicted Li_3AlFeH_8 was synthesized.

We searched for synthetic conditions where the single phase of Li_3AlFeH_8 can be obtained. Unfortunately, we could not obtain a single phase of Li_3AlFeH_8 up to 9 GPa and 900°C.

Another novel hydride, $LiAlFeH_6$, was found while optimizing the synthesis conditions of Li_3AlFeH_8. Figure 3(b) shows an X-ray diffraction profile of the recovered sample hydrogenated at 9 GPa and 900°C. The observed Bragg peaks were indexed by a hexagonal lattice. The chemical composition of the novel hydride was predicted to be $LiAlFeH_6$ based on the relationship between the constituent ions and the crystal structure volume reported by Sato *et al.* [5]. The crystal structure obtained by the first-principles calculations is shown in the inset of Fig. 3(b). The experimentally obtained X-ray diffraction profile was reproduced by the calculated profile for the theoretically predicted crystal structure.

The theoretically predicted Li_3AlFeH_8 was synthesized at 5 GPa. We did not obtain single-phase Li_3AlFeH_8; however, another novel hydride, $LiAlFeH_6$, was also synthesized while optimizing the reaction pressure-temperature conditions for Li_3AlFeH_8.

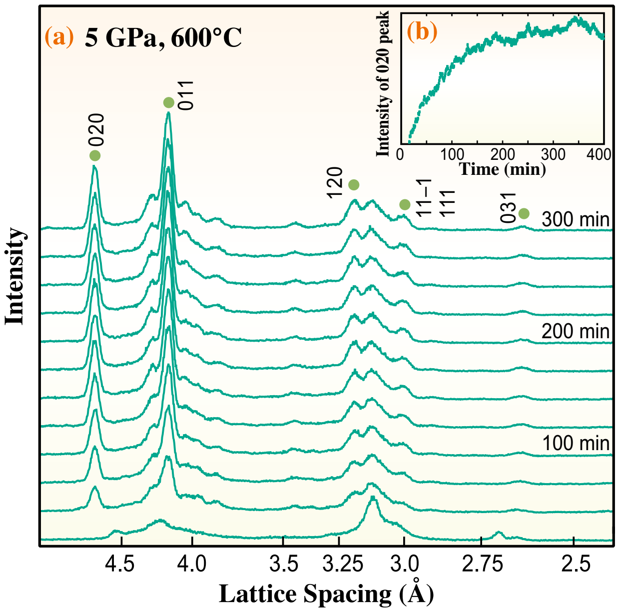

Fig. 2. **(a)** Series of synchrotron radiation powder X-ray diffraction profiles of the powder mixture hydrogenated at 5 GPa and 600°C. Bragg peaks with filled circles and Miller indices are from Li_3AlFeH_8. **(b)** Time dependence of the integrated intensity of the 110 Bragg peak of Li_3AlFeH_8.

We demonstrated that the combination of high-pressure synthesis and *in situ* SR-XRD is a powerful approach for obtaining novel hydrogen-rich materials. We are currently investigating the properties of the obtained hydrides.

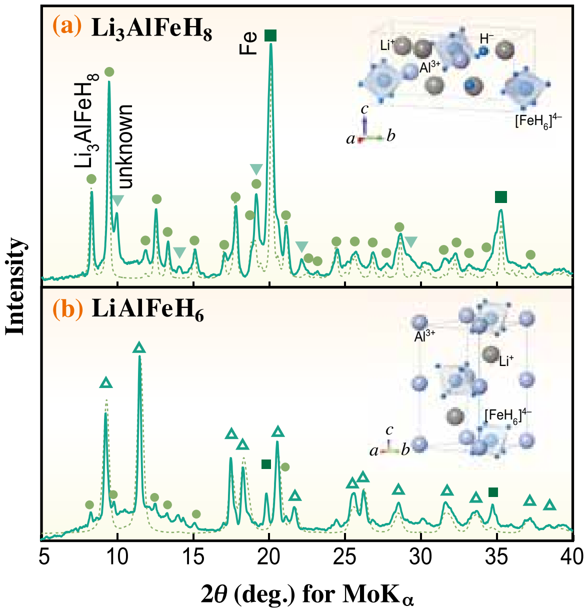

Fig. 3. Powder X-ray diffraction profiles of recovered samples hydrogenated at **(a)** 5 GPa and 650°C and **(b)** 9 GPa and 900°C. The insets show the schematics of the crystal structures of (a) Li_3AlFeH_8 and (b) $LiAlFeH_8$. Calculated profiles for the theoretically predicted crystal structures are shown in dashed lines. Bragg peaks with filled circles, filled squares, up-pointing triangles, and down-pointing triangles are from Li_3AlFeH_8, pure iron, $LiAlFeH_6$, and an unknown phase, respectively.

Hiroyuki Saitoh

National Institutes for Quantum and Radiological Science and Technology (QST)

Email: saito.hiroyuki@qst.go.jp

References

[1] *H. Saitoh, S. Takagi, T. Sato, Y. Iijima and S. Orimo: Int. J. Hydrogen Energy* ***42*** *(2017) 22489.*
[2] S. Takagi *et al.*: Appl. Phys. Lett. **104** (2014) 203901.
[3] Y. Fukai and N. Okuma: Jpn. J. Appl. Phys. **32** (1993) L1256.
[4] K. Momma and F. Izumi: J. Appl. Crystallogr. **41** (2008) 653.
[5] T. Sato *et al.*: Sci. Rep. **6** (2016) 23592.

Microscopic mechanisms of the electric-field effect on proximity-induced magnetism in Pt revealed by X-ray absorption spectroscopy

Carrier doping in condensed matter by an electric field is a principal technology for operating electronic devices. Electric fields are also used to control the magnetic properties of not only ferromagnetic semiconductors [1] but also thin ferromagnetic metals [2], such as Fe and Co. In particular, electric-field-assisted magnetization switching in ferromagnetic metals [3] is promising for the energy-efficient operation of magnetic memory devices. However, despite the potential applications, the mechanisms of the electric-field effect on ferromagnetism are still controversial because of the lack of experimental study.

In this research [4], we unraveled the microscopic mechanisms of the electric-field effect on proximity-induced magnetism in Pt by X-ray magnetic circular dichroism (XMCD) and X-ray absorption spectroscopy (XAS) performed at SPring-8 **BL39XU**. Pt atoms in the proximity of a ferromagnetic layer can be ferromagnetic. "Ferromagnetic Pt" has interesting characters: a small exchange splitting and strong spin-orbit interaction. Because the coexistence of the two factors can enhance the electric-field effect on the magnetic anisotropy [5], ferromagnetic Pt has been attracting attention. XMCD and XAS spectroscopy are powerful tools for scrutinizing the electric-field effect. An XMCD spectrum contains information about the magnetic polarization of a specific element and, importantly, enables us to evaluate the spin and orbital magnetic moments by using the sum rules. By analyzing the XAS spectrum obtained under the application of an electric field, one can examine how the applied electric field affects the unoccupied electronic states.

In our experiments, we employed an ionic liquid to apply a large electric field to a Pt channel of an electric-double-layer transistor formed on a synthetic quartz glass substrate (see Fig. 1). By applying a gate voltage (V_G) between the channel and lateral gate electrodes, the ions move onto the channel surface to form an electric double layer, equivalent to a nanogap capacitor. Here, applying a positive V_G causes the accumulation of electrons at the Pt/MgO interface. The experimental configuration is schematically shown in Fig. 1. A magnetic field was applied perpendicular to the device surface and a circularly polarized X-ray propagated parallel to the magnetic field direction. We measured the fluorescence yields of the Pt L_α and L_β lines as a function of X-ray energy at the Pt L_3 and L_2 edges, respectively. The XAS and XMCD intensities are defined as $I_{XAS} = [I(\sigma^+) + I(\sigma^-)]/2$ and $I_{XMCD} = I(\sigma^+) - I(\sigma^-)$, where $I(\sigma^+)$ and $I(\sigma^-)$ indicate the intensities of X-ray fluorescence when the incident photon momentum and magnetization vectors are antiparallel and parallel, respectively. Throughout the X-ray measurements, the device was located in an evacuated chamber of a He-flow cryostat and the measurement temperature was fixed at 100 K.

Figure 2 shows I_{XMCD} and I_{XAS} at $V_G = +6$ and -4 V together with their differences, ΔI_{XMCD} and ΔI_{XAS}, between the two voltages. The significant changes in I_{XMCD} and I_{XAS} indicate that the applied electric field modulates the magnetic moments and electronic states of Pt. By applying the sum rules to values of the I_{XMCD} measured at different V_G's, the perpendicular components of the effective spin and orbital moments are estimated to be 0.222 ± 0.001 $(0.232 \pm 0.002)\mu_B$ and 0.043 ± 0.001 $(0.047 \pm 0.001)\mu_B$ at $V_G = +6$ (-4) V, respectively. The voltage-induced changes in I_{XAS} indicate that the electronic states above the Fermi

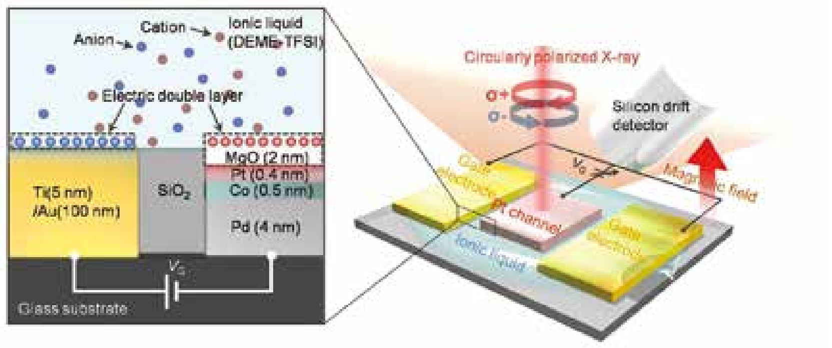

Fig. 1. Schematic illustration of the experimental configuration.

energy (E_F), i.e., the number of 5*d* holes, change upon the application of an electric field. The total number of 5*d* holes of Pt increases by ~0.009 when V_G is switched from +6 V to −4 V. Note that the spectral profile of the XAS difference (ΔI_{XAS}) is not monotonic with the X-ray energy; ΔI_{XAS} changes sign around 11.571 and 13.290 eV for the L_3 and L_2 absorption edges, respectively. The reductions of ΔI_{XAS} near the absorption edges are mostly due to the electric-field-induced shift of E_F, simply corresponding to the electrostatic charge accumulation. Then, ΔI_{XAS} becomes positive at the high-energy sides of the absorption edges, which cannot be explained by the electrostatic charge accumulation. The electric field can also alter the hybridizations between the *sp* and *d* orbital of Pt. This mechanism is considered to increase (decrease) the number of 5*d* holes of the Pt atoms under a positive (negative) electric field. The changes in I_{XMCD} and I_{XAS} were well reproduced by a density functional theory calculation. Scrutinizing the electronic structures under electric fields, we find that the two mechanisms (electric-field-induced shift of E_F and changes in the orbital hybridizations) indeed give rise to the nonmonotonic changes in I_{XAS} and are relevant to the modulated magnetic moments of the Pt atom.

The experimentally unveiled mechanisms of the electric-field effects in ferromagnetic Pt are expected to give us a fundamental model applicable to a wide range of ferromagnetic metals, represented by Fe and Co. Furthermore, the highly sensitive XMCD and XAS measurements under the application of electric fields enabled us to correlate the changes in the magnetism with the microscopic picture. This research has demonstrated the significant benefit of XAS for investigating magnetic phenomena induced by external fields.

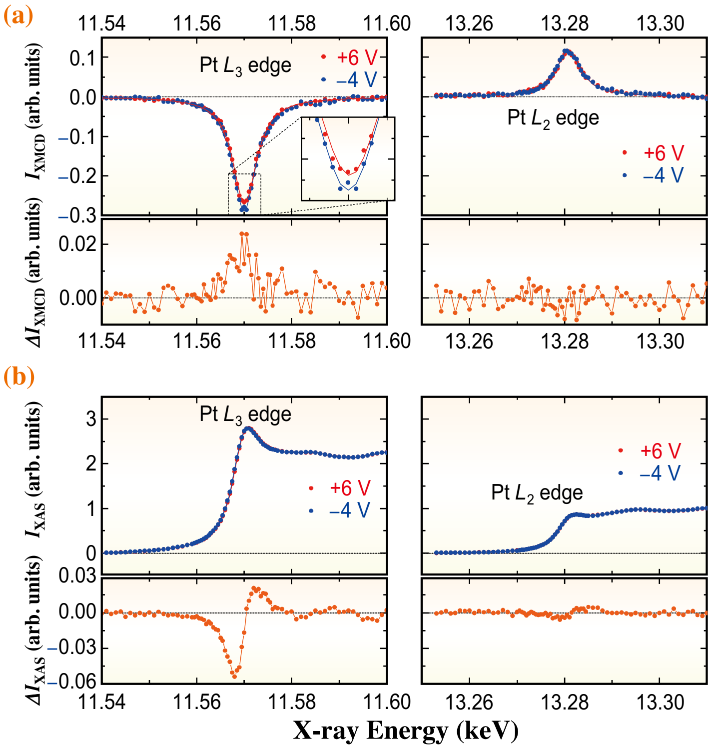

Fig. 2. (**a**) XMCD (I_{XMCD}) and (**b**) XAS (I_{XAS}) intensities at Pt L_3 and L_2 edges for $V_G = +6$ and −4 V and their difference $\Delta I_{XMCD(XAS)}$ [= $I_{XMCD(XAS)}$ (+6 V) − $I_{XMCD(XAS)}$ (−4 V)].

Kihiro Yamada[a,b,*], Motohiro Suzuki[c] and Teruo Ono[a,d]

[a] Institute for Chemical Research, Kyoto University
[b] Institute for Molecules and Materials, Radboud University, The Netherlands
[c] Japan Synchrotron Radiation Research Institute (JASRI)
[d] Center for Spintronics Research Network (CSRN), Osaka University

*Email: K.Yamada@science.ru.nl

References

[1] H. Ohno *et al.*: Nature **408** (2000) 944.
[2] M. Weisheit *et al.*: Science **315** (2007) 349.
[3] Y. Shiota *et al.*: Nat. Mater. **11** (2012) 39.
[4] *K.T. Yamada, M. Suzuki, A.-M. Pradipto, T. Koyama, S. Kim, K.-J. Kim, S. Ono, T. Taniguchi, H. Mizuno, F. Ando, K. Oda, H. Kakizakai, T. Moriyama, K. Nakamura, D. Chiba and T. Ono: Phys. Rev. Lett.* ***120*** *(2018) 157203.*
[5] S. Miwa *et al.*: Nat. Commun. **8** (2017) 15848.

Visualization of heterogeneous oxygen storage in platinum-supported cerium-zirconium oxide three-way catalyst particles by hard X-ray spectro-ptychography

Heterogeneous solid catalysts are key materials in various chemical processes in modern industry, and the intrinsic nanoscale complexity of their heterogeneous structures has led to various discussions on their structure–activity relationships. The most typical form of solid catalyst is a powder, which is an assembly of nonuniform particles with different sizes, morphologies, atomic components, surface structures, and mesoscopic domains. The nanoscale complexity of their structural parameters is considered to be a reason for their unique catalytic performances.

Ce-based mixed oxides such as $CeZrO_x$ are widely used as co-catalysts in three-way exhaust processes to expand the operation window. In particular, $Ce_2Zr_2O_x$ ($7 \leq x \leq 8$) solid-solution oxide with an ordered arrangement of Ce and Zr has been reported to exhibit excellent oxygen storage capacity (OSC) performance, where approximately 90% of the bulk Ce atoms are used in the redox process between κ-phase $Ce_2Zr_2O_8$ and pyrochlore $Ce_2Zr_2O_7$. Their oxygen storage behavior inside the bulk of the solid solution is a key factor in its OSC.

X-ray imaging techniques, such as scanning X-ray microscopy using highly focused beams, are promising tools for imaging both structures and chemical states by combining them with the X-ray absorption fine structure (XAFS) method, i.e., using multiple energies around the absorption edge of a target element. The minimum probe size, which corresponds to the spatial resolution, in practical use is roughly 100 nm in the hard X-ray region, which is limited by the difficulty of fabricating optical devices. X-ray ptychography can in principle overcome the limitations. In this approach, a sample is scanned across a coherent X-ray probe to collect the far-field coherent diffraction pattern at each beam position, and then images of both the sample and probe are reconstructed by iterative phase retrieval calculation [1]. X-ray ptychography using multiple energies including the absorption edge of a specific element, often referred to as X-ray spectro-ptychography (ptychographic XAFS), has been demonstrated in the soft X-ray region [2]. Extending this approach to the hard X-ray region enables us to visualize the chemical state inside micrometer-size bulk samples (Fig. 1). However, the absorption of incident X-rays is significantly small in the hard X-ray region, which makes it challenging to reach convergence in the conventional phase retrieval calculation. Recently, a phase retrieval algorithm using a constraint based on the Kramers–Kronig relation (KKR) has been proposed, and more quantitative images as well as X-ray absorption spectra have been experimentally obtained in the hard X-ray region [3]. In this study, we demonstrate the visualization of the Ce valence distribution of micrometer-size Pt-supported $Ce_2Zr_2O_x$ (denoted as Pt/CZ-x, $7 \leq x \leq 8$) particles with better than 50 nm resolution by ptychographic XAFS in the hard X-ray region [4].

The ptychographic XAFS measurements were performed using X-rays (5.717–5.817 keV, including the Ce L_3 edge) at SPring-8 **BL29XUL**. 1 wt% Pt/CZ-x particles (average CZ-x particle size = 750 nm) were treated with H_2 or O_2 to prepare 1) $Pt/Ce_2Zr_2O_7$

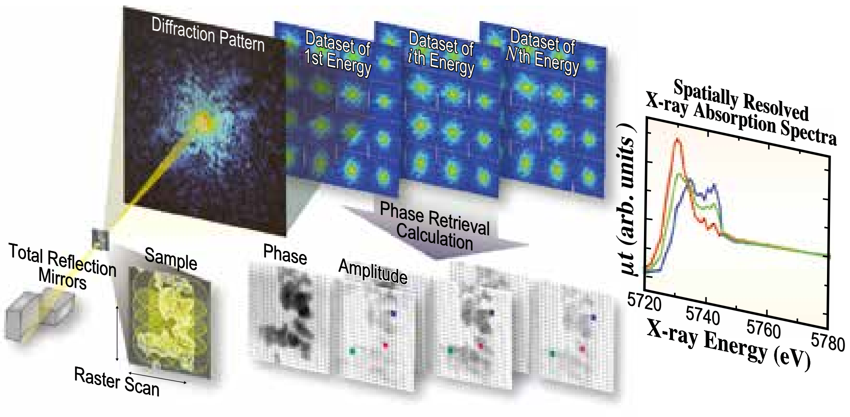

Fig. 1. Schematic of X-ray spectro-ptychography (ptychographic XAFS). A focused coherent X-ray beam is scanned across the specimen at multiple X-ray energies. Phase and amplitude images are reconstructed from diffraction patterns by phase retrieval calculation. By analyzing the energy dependence of the reconstructed images, spatially resolved X-ray absorption spectra are derived.

(denoted as Pt/CZ-7), fully reduced by H_2 at 873 K; 2) Pt/$Ce_2Zr_2O_8$ (denoted as Pt/CZ-8), fully oxidized by O_2 at 773 K; and 3) Pt/$Ce_2Zr_2O_{7.6}$ (denoted as Pt/CZ-7.6), prepared by the reaction of Pt/CZ-7 with O_2 at 423 K. Incident X-rays were two-dimensionally focused to a 500 nm (full width at half maximum) spot size by a pair of Kirkpatrick–Baez mirrors, and then the samples were scanned in 9-by-9 positions with a step width of 400 nm. Multiple coherent diffraction patterns were collected using an in-vacuum pixel array detector with an exposure time of 4.0 s at each scan.

The amplitude and phase images were reconstructed using the ePIE algorithm with the KKR constraint [3]. Figures 2(a) and 2(b) show phase and amplitude images at 5.732 keV above the Ce L_3 edge, respectively. On the basis of the phase retrieval transfer function, the full-period spatial resolution was estimated to be better than 50 nm at all X-ray energies. The shapes of the individual particles are in good agreement with the SEM and X-ray ptychography images. The Ce valence maps of each particle were then estimated by analysis of the ptychographic XAFS images. The XAFS spectra of Pt/CZ-x $(\mu t)_{CZx}$ can be approximately expressed by a linear combination of the normalized standard XAFS spectra of Pt/CZ-7 $(\mu t)_{CZ7}$ and Pt/CZ-8 $(\mu t)_{CZ8}$ as $(\mu t)_{CZx} = a(\mu t)_{CZ7} + b(\mu t)_{CZ8}$. The parameters a and b at each pixel were determined by a least-squares fit, and $(3a+4b)/(a+b)$ provides the Ce valence as presented in Fig. 2(c). While Pt/CZ-7 and Pt/CZ-8 particles were respectively almost fully reduced and oxidized as expected, partially oxidized Pt/CZ-7.6 particles exhibited a complicated valence distribution. The differences were thought to be caused by the inhomogeneous reactivity in the domain structures formed inside the particles.

In summary, we successfully reconstructed amplitude and phase images by ptychographic XAFS at 27 X-ray energies to obtain two-dimensional mappings of the Ce valence of Pt/CZ-x particles with spatial resolution better than 50 nm. By coupling ptychographic XAFS with computed tomography measurement, three-dimensional structural and chemical nanoimaging is possible, which will elucidate the unrevealed intrinsic heterogeneous reaction behaviors of the material. We believe that the present approach will be a more promising and powerful tool in future synchrotron facilities, where a high coherent flux will be obtained.

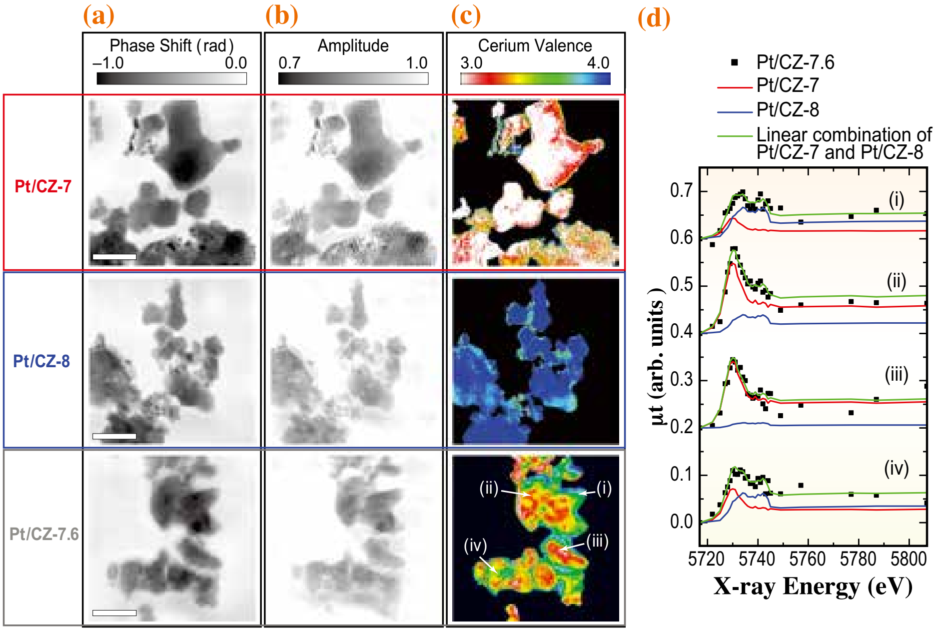

Fig. 2. **(a, b)** Phase and amplitude images at 5.732 keV. **(c)** Ce valence images. The pixel resolution is 13 nm and the scale bars represent 1 μm. **(d)** One-pixel XANES spectra of Pt/CZ-7.6 at positions (i)-(iv) in (c). Red, blue, and green lines represent the fitted spectra of Pt/CZ-7 and Pt/CZ-8 and their linear combination, respectively.

M. Hirose[a,b], N. Ishiguro[b], M. Tada[b,d] and Y. Takahashi[a,b,c,*]

[a] Graduate School of Engineering, Osaka University
[b] RIKEN SPring-8 Center
[c] Institute of Multidisciplinary Research for Advanced Materials, Tohoku University
[d] Graduate School of Science, Nagoya University

*Email: ytakahashi@tohoku.ac.jp

References

[1] P. Tihibault *et al.*: Science **321** (2008) 379.
[2] D.A. Shapiro *et al.*: Nat. Photonics **8** (2014) 765.
[3] M. Hirose *et al.*: Opt. Express **25** (2017) 8593.
[4] *M. Hirose, N. Ishiguro, K. Shimomura, N. Burdet, H. Matsui, M. Tada, Y. Takahashi: Angew. Chem. Intern. Ed.* ***130*** *(2018) 1490.*

Simultaneous operando time-resolved XAFS-XRD measurements of a Pt/C cathode catalyst in a polymer electrolyte fuel cell under transient potential cyclic operations

Crucial issues in developing next-generation polymer electrolyte fuel cells (PEFCs) are improving the oxygen reduction reaction (ORR) activity and long-term durability, and reducing the cost of cathode catalysts. To resolve these issues, it is necessary to determine and understand the dynamic aspects of the structures and electronic states of cathode catalysts and also the reaction mechanisms at the cathode catalyst surface under PEFC operating conditions by operando time-resolved analysis methods. Time-resolved quick X-ray absorption fine structure (QXAFS) enables the element-selective investigation of the dynamic transformations of the local structures and oxidation states of Pt nanoparticles in Pt/C cathode catalysts. Time-resolved X-ray diffraction (XRD) enables measurements of the dynamic transformation of the crystalline structures of Pt nanoparticles in Pt/C cathode catalysts. Thus, we have designed a combined system for simultaneous time-resolved QXAFS-XRD measurements of Pt/C cathode catalysts in PEFCs [1,2]. Here, we summarize the simultaneous operando time-resolved QXAFS-XRD measurements and the application of the technique to determine the dynamic structural and electronic behavior of a Pt/C cathode catalyst in PEFC under transient voltage cyclic operations.

Simultaneous time-resolved QXAFS-XRD measurements at 60 ms time resolution (20 ms QXAFS ×2 + 20 ms XRD ×1 = 60 ms) were performed at SPring-8 **BL36XU** [3] by using a servomotor-driven Si channel-cut crystal monochromator. The experimental setup for the simultaneous operando time-resolved QXAFS-XRD measurements of a PEFC is shown in Figs. 1(A-C), where a high-speed regulation pattern of monochromator angles for the simultaneous QXAFS-XRD measurements is also shown. The cell voltage was changed from the open-circuit voltage (OCV) to 0.4 V_{RHE}, which was maintained for 300 s, followed by a rapid voltage jump from 0.4 to 1.4 V_{RHE}. This voltage was maintained for 300 s, and then reversely the cell voltage was changed rapidly from 1.4 to 0.4 V_{RHE} (anode: H_2, cathode: N_2).

The series of time-resolved QXANES spectra, QEXAFS Fourier transforms and XRD patterns of the Pt/C in the transient potential operations are respectively shown in Figs. 1(D–F). The transient response time profiles of the QXANES white line peak height (proportional to Pt valence), CN(Pt-Pt), and CN(Pt-O) are plotted against the reaction time after the voltage jump in Figs. 1(G–I), respectively, and the Pt metallic phase size estimated using Scherrer's formula with the XRD (220) peak is also shown in Fig. 1(J). All transient responses to the voltage cyclic operations 0.4 V_{RHE}→1.4 V_{RHE}→0.4 V_{RHE} were analyzed by the following one- or two-exponential functions: $f(t) = y_0 + a_1\exp(-k_1 t)$ or $f(t) = y_0 + a_1\exp(-k_1 t) + a_2\exp(-k_2 t)$, as shown by red curves in Figs. 1(G–J). The parameters k_1, k_2, a_1, a_2, and t are the rate constants

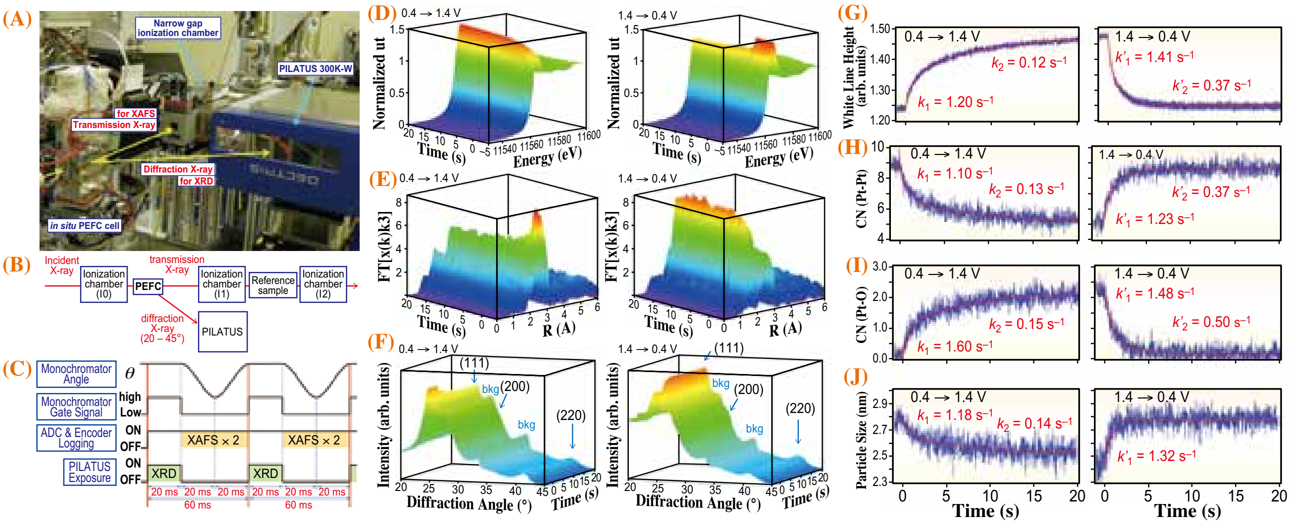

Fig. 1. (Left) Experimental setup for operando simultaneous time-resolved XAFS-XRD measurements of PEFC. **(A)** XAFS-XRD measurement setup, **(B)** schematic diagram of the setup, and **(C)** high-speed regulation pattern of monochromator angles with gate signals and recording time charts of detectors. (Center) Series of time-resolved **(D)** QXANES spectra, **(E)** QEXAFS Fourier transforms, and **(F)** XRD patterns. (Right) Transient response curves of **(G)** white line peak height, **(H)** CN(Pt-Pt), **(I)** CN(Pt-O), and **(J)** Pt metallic phase size. Potential cyclic operations, 0.4 V_{RHE}→1.4 V_{RHE}→0.4 V_{RHE}; gas, H_2(anode)-N_2(cathode); cell temp., 353 K; relative humidity, ~93%.

k_1 and k_2, the amounts of variations, a_1 and a_2, and the reaction time t for the two-stage (fast and slow) structural kinetics of the Pt nanoparticles. The Pt nanoparticles in the Pt/C cathode catalyst under the transient voltage operation 0.4 V_{RHE}→1.4 V_{RHE} transform at the fast and slow successive steps with the rate constants k_1 and k_2, respectively. The surface Pt-O bond formation event was followed by decreases in Pt metallic phase size and CN(Pt-Pt), and an increase in Pt valence. The results suggest that the surface Pt-O bond formation induces the partial disordering (rearrangement) of the outermost Pt layer, resulting in an apparent half-layer decrease in metallic phase size at the saturated O layer from 2.78 to 2.64 nm as shown in Fig. 2. The first fast surface event was followed by the second slow transformations of Pt-O bond formation, Pt charging, Pt-Pt bond dissociation, and the decrease in Pt metallic phase size. These rate constants are similar to each other within the error ranges, suggesting that these slow events occur concertedly to finally produce the tetragonal Pt^{2+}-O layer (Pt-O = 0.201 nm) at the Pt surface (Fig. 2). At the transient voltage operation 1.4 V_{RHE}→0.4 V_{RHE}, the first fast steps of Pt-O bond dissociation, the decrease in Pt valence, Pt-Pt bond reformation, and the increase in Pt metallic phase size proceed concertedly at similar rates within the experimental error range as shown in Fig. 2. The second slow steps of Pt-O bond dissociation, the decrease in Pt valence, and Pt-Pt bond reformation under 1.4 V_{RHE}→0.4 V_{RHE} also occur concertedly. However, the XRD data indicated a one-step event as shown by the one-wave fitting (Fig. 1(J)). These results suggest that the size of the Pt metallic phase increases in one step under 1.4 V_{RHE}→0.4 V_{RHE}, unlike the two-stage decrease under 0.4 V_{RHE}→1.4 V_{RHE}. The change in metallic phase size is completed in the fast step, and the changes in Pt valence, Pt-O bond dissociation, and Pt-Pt bond reformation at the surface proceed further at lower rates as shown in Fig. 2. Although the Pt/C cathode catalysis in a PEFC for the ORR performance is reversible under the voltage operations 0.4 V_{RHE}→1.4 V_{RHE} and 1.4 V_{RHE}→0.4 V_{RHE}, note that the structural and electronic transformations and reaction kinetics for the 15 elementary steps did not trace similar transformations and kinetics in the forward and backward voltage operation processes, and revealed different structural transformations and kinetics and a definite hysteresis as illustrated in Fig. 2.

The simultaneous operando time-resolved QXAFS-XRD approach to the Pt/C cathode catalysis in PEFCs provide a new insight into the molecular-level reaction mechanism and dynamic transformations in the Pt surface layer and bulk under the transient potential operations. The simultaneous operando time-resolved QXAFS-XRD technique is promising and powerful, and can promote further understanding and improvement of next-generation PEFC performance and durability by providing the key material properties and the relationship of the macroscopic electrochemical data with the structural kinetics.

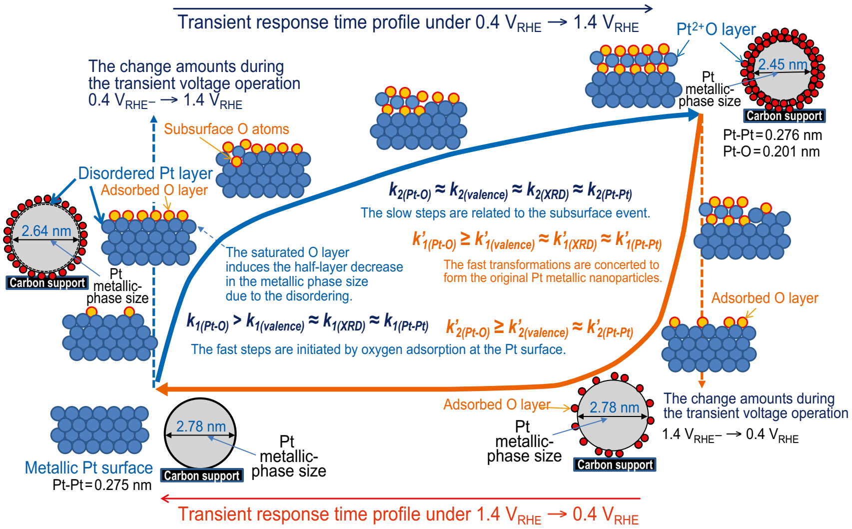

Fig. 2. Reaction mechanism and structural kinetics for Pt surface events of Pt/C cathode catalyst under transient voltage cyclic operations 0.4 V_{RHE}→1.4 V_{RHE}→0.4 V_{RHE} under H_2(anode)-N_2(cathode). $k_{1(Pt\text{-}O)}$ and $k_{2(Pt\text{-}O)}$, Pt-O bond formation; $k_{1(valence)}$ and $k_{2(valence)}$, Pt charging; $k_{1(Pt\text{-}Pt)}$ and $k_{2(Pt\text{-}Pt)}$, Pt-Pt bond dissociation; $k_{1(XRD)}$ and $k_{2(XRD)}$, decrease in Pt metallic phase size; $k'_{1(Pt\text{-}O)}$ and $k_{1(Pt\text{-}O)}$, Pt-O bond dissociation; $k'_{1(valence)}$ and $k'_{2(valence)}$, Pt discharging; $k'_{1(Pt\text{-}Pt)}$ and $k'_{2(Pt\text{-}Pt)}$, Pt-Pt bond reformation; $k'_{1(XRD)}$, increase in Pt metallic phase size.

Oki Sekizawa[a,b,*], Tomoya Uruga[a,b] and Yasuhiro Iwasawa[b]

[a] Japan Synchrotron Radiation Research Institute (JASRI)
[b] Innovation Research Center for Fuel Cells,
The University of Electro-Communications

*Email: sekizawa@spring8.or.jp

References

[1] *O. Sekizawa, T. Uruga, K. Higashi, T. Kaneko, Y. Yoshida, T. Sakata, Y. Iwasawa: ACS Sus. Chem. Eng.* **5** *(2017) 3631.*
[2] O. Sekizawa *et al.*: Top. Catal. **61** (2018) 889.
[3] O. Sekizawa *et al.*: J. Phys. Conf. Ser. **712** (2016) 012142.

Complete agreement of the post-spinel transition pressure with the 660-km seismic discontinuity depth

The 660-km seismic discontinuity is a global feature dividing the Earth's upper and lower mantle. Geophysical observations of this discontinuity have revealed the following features. (1) The reported global average depth of this discontinuity is 660 km, corresponding to a pressure of 23.4 GPa (e.g., [1]). (2) The jumps of the compressional and shear velocities are both 6%. (3) The 660-km discontinuity has a topography of ±20 km. In particular, the 660-km discontinuity is depressed under the circum-Pacific subduction zones [1]. (4) The 660-km discontinuity produces strong reflection. The reflection of short P waves suggests that the thickness of the discontinuity is less than 2 km [2]. (5) Seismic tomography studies observed the stagnation of subducted slabs around the 660-km discontinuity (e.g., [3]). These observations should be interpreted in terms of mineral physics. Mg_2SiO_4 olivine is the most abundant mineral in the Earth's upper mantle, which transforms to a high-pressure polymorph of ringwoodite at pressures corresponding to the base of the upper mantle. At a pressure near that at the 660-km discontinuity, ringwoodite decomposes to bridgmanite + periclase, which is called the post-spinel transition. Therefore, the post-spinel transition is commonly accepted to be the cause of the 660-km discontinuity.

Since the late 1990s, the post-spinel transition pressure in Mg_2SiO_4 has been investigated using a combination of Kawai-type multi-anvil presses and synchrotron-based *in situ* X-ray diffraction, which enabled the most precise and accurate determination of the phase boundary. Nevertheless, these studies have located the post-spinel transition at pressures of 21.4–22.9 GPa at temperatures of 1900–2000 K (the geotherm at a depth of 660 km [3]), which are 0.5–2.0 GPa lower than the actual pressure at a depth of 660 km. This discrepancy is distinctive considering the pressure precision in a Kawai-type multi-anvil press. If these results were correct, the 660-km discontinuity could not be attributed to the post-spinel transition. Consequently, ringwoodite and bridgmanite + periclase would not be the dominant minerals in the transition zone and lower mantle, respectively. This is highly unlikely because, if this were the case, the mantle composition would be completely different from those suggested on the basis of geochemical and petrological observations, such as the ferromagnesium silicates $(Mg,Fe)_2SiO_4$ and $(Mg,Fe)SiO_3$. Therefore, the discrepancy between the reported results and expected pressures requires critical experimental investigations.

We revisited the PSp transition pressure in Mg_2SiO_4 at 1700 K by employing a combination of advanced multi-anvil techniques and *in situ* X-ray diffraction using the Kawai-type multi-anvil press SPEED-Mk.II at SPring-8 **BL04B1** [4]. This approach is, for the most part, identical to that followed in previous studies. However, we detected a significant drop in pressure in the samples after reaching the target temperature. This finding suggests a likely cause of the unexpectedly low transition pressures reported in previous studies. Accordingly, we minimized this decrease in pressure by increasing the press load during heating (forced pumping), something that no other research group has yet attempted.

We performed seven runs to determine the transition pressure at 1700 K. The PSp transition pressure at 1700 K was constrained to be between 23.72 GPa and 23.86 GPa (Fig. 1) according to the MgO scales based on the equations of states reported in Ref. 5 (hereafter the Tange MgO scales). Our results showed 0.5–2 GPa higher transition pressures than those previously determined.

We examine the correspondence of the post-spinel transition with the 660-km discontinuity using the new transition pressures obtained in this study. The temperature at the 660-km discontinuity is estimated to be 1900–2000 K [3]. The transition pressure was extrapolated to 2000 K using the Clapeyron slope of Ref. 5 corrected by the Tange MgO scale (–0.0016 GPa/K), which gave 23.4 GPa at 2000 K (Fig. 1). Given these facts, the present findings are entirely consistent with the depth of the 660-km discontinuity.

Previous studies likely underestimated the transition pressure owing to insufficient pressure control at high temperatures. The phase transition is completed within minutes after the target temperature is reached. Reference 6 reported a typical pressure decrease of ~0.5 GPa at a constant temperature of 1873 K; however, having adopted the final pressure before quenching in order to constrain the phase boundary, the authors significantly underestimated the transition pressure. We avoided a pressure drop at a high temperature via forced pumping and, therefore, obtained a more accurate transition pressure. Therefore, the forced-pumping technique is essential to determine a phase boundary. Notably, we observed a lower transition pressure (22.8 GPa) in preliminary experiments without the forced pumping techniques.

The problem of pressure drops is obvious when a Kawai-type multi-anvil press is combined with *in situ* X-ray diffraction at high temperatures, even though it is in fact attributable to the high precision of the Kawai-type multi-anvil press experiments. Experiments in a laser-heated diamond anvil cell would therefore encounter similar difficulties. This issue has never been seriously considered when investigating phase relations at high pressures and high temperatures. Therefore, there is a pressing need to reinvestigate every high P–T phase boundary that has been determined by X-ray diffraction without considering this problem. In particular, the determination of mantle mineral phase boundaries that are inseparably linked to other seismic discontinuities should be carefully investigated to improve our knowledge of the structure of the mantle.

Thus, owing to our innovation of the Kawai-type multianvil technology, we obtained a transition pressure that is in complete agreement with that of the 660-km discontinuity. The present study validates the applicability of widely accepted mantle compositional models such as the pyrolite and CI chondrite models.

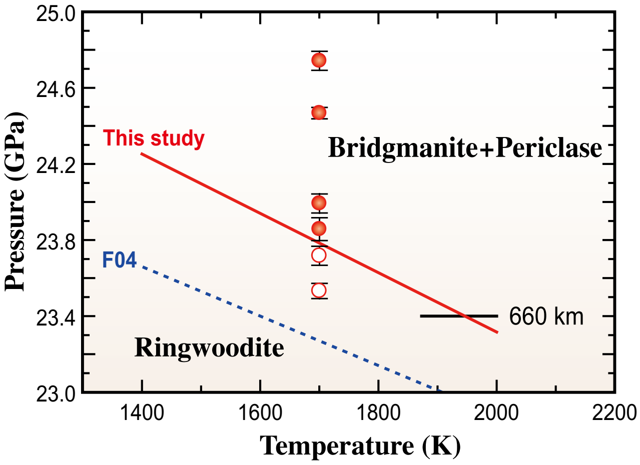

Fig. 1. Phase boundaries of the post-spinel transition in Mg_2SiO_4. Data points were calculated on the basis of the Tange MgO scale (red circle). Open and solid circles with error bars identify the stable phases as ringwoodite and bridgmanite+periclase, respectively. The black solid line is the expected condition of the 660-km discontinuity. The red solid line is a phase boundary evaluated using the fixed points obtained in this study and the Clapeyron slopes of Ref. 6 after recalculation with the Tange MgO scale. The blue dashed line (F04) is the phase boundary determined by Ref. 6 using MgO scale. The recalculated boundaries of the previous study with the Tange MgO scale are shifted to an even lower pressure.

Takayuki Ishii* and Tomoo Katsura

Bayerisches Geoinstitut, University of Bayreuth, Germany

*Email: Takayuki. ishii@uni-bayreuth.de

References

[1] M.P. Flanagan & P.M. Shearer: J. Geophys. Res. **103** (1998) 2673.
[2] F. Xu *et al.*: J. Geophys. Res. **108** (2003).
[3] T. Katsura *et al.*: Phys. Earth Planet. Sci. **183** (2010) 212.
[4] *T. Ishii, R. Huang, H. Fei, I. Koemets, Z. Liu, F. Maeda, L. Yuan, L. Wang, D. Druzhbin, T. Yamamoto, S. Bhat, R. Farla, T. Kawazoe, N. Tsujino, E. Kulik, Y. Higo, Y. Tange and T. Katsura: Sci. Rep.* ***8*** *(2018) 6358.*
[5] Y. Tange *et al.*: J. Geophys. Res. Solid Earth **114** (2009) B03208.
[6] Y. Fei *et al.*: J. Geophys. Res. Solid Earth **109** (2004) B02305.

Moganite in a lunar meteorite NWA 2727 as a trace of water ice in the Moon's subsurface

Moganite (monoclinic SiO_2 phase that belongs to the *I2/a* space group) is a mineral of silicon dioxide and has a similar but different crystal structure from quartz [1]. It forms on Earth as a precipitate when alkaline water including SiO_2 is evaporated under high-pressure conditions, as in the formation of sedimentary rocks (e.g., evaporite, chert, and breccia) [1,2]. In contrast, moganite has not at all been expected to be found in extraterrestrial materials since it originates only from recent alkaline water activity. We have discovered moganite in a lunar meteorite named NWA 2727 found in a desert in northwest Africa (Fig. 1) by performing various microanalyses [3]. This is significant because moganite requires alkaline water to form, reinforcing the conclusion of recent remote-sensing spacecraft observations (e.g., LCROSS and Deep Impact) that water exists on the Moon [4,5]. The existence of moganite in NWA 2727 strongly implies that there has been recent water activity on the lunar surface. Here, a new history of lunar water can be interpreted by our discovery of moganite using synchrotron X-ray diffraction (SR-XRD) measurements at SPring-8 **BL10XU**, combined with Raman spectrometry and electron microscopy.

Thirteen different lunar meteorites with various lithologies (gabbro, basalt, anorthositic regolith, troctolite, and their breccias) were investigated in the microanalyses, and moganite coexisting with coesite and stishovite (high-pressure SiO_2 phases formed above 3 and 8 GPa, respectively) was found only in NWA 2727, which may have originated from the local sites within the Procellarum terranes. NWA 2727 was found to be mainly composed of gabbroic and basaltic clasts containing a breccia matrix (Fig. 1), where the breccia matrix contains several silica micrograins (2 to 13 mm in radius) between the constituent minerals (olivine, pyroxene, and plagioclase). The SR-XRD analyses of these silica micrograins in the breccia matrix show characteristics of moganite (Figs. 2(a) and 2(b)) (X-ray wavelength of 0.41569(9) Å). The strong peaks at *d* values of 4.46 and 3.36 Å and weak peaks at 2.31, 2.19, 2.04, 1.97, 1.83, and 1.66 Å can be indexed to a monoclinic lattice with the cell parameters: a = 8.77(1) Å, b = 4.90(1) Å, c = 10.77(3) Å, b = 90.38(3)°, and V = 463.0(6) Å as the space group *I2/a*. This is in good agreement with the structure of moganite. The SR-XRD signatures corresponding to coesite and stishovite can also be obtained from the silica micrograins with moganite. However, we did not discover moganite in the basaltic and gabbroic clasts of NWA 2727 or in the other lunar meteorites examined here. Raman spectrometry and transmission electron microscopy also demonstrated the same tendency as the result of the SR-XRD analyses.

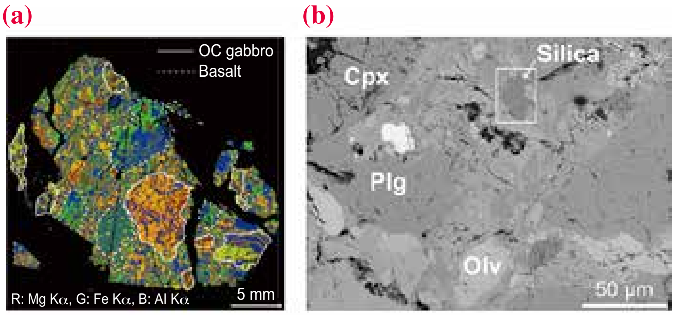

Fig. 1. **(a)** Petrological photographs of NWA 2727. False-color elemental X-ray map of thin section of NWA 2727 with red (R) = Mg Ka, green (G) = Fe Ka, and blue (B) = Al Ka X-rays obtained by the electron probe microanalysis. Areas enclosed by white solid and dashed lines indicate olivine-cumulate (OC) gabbroic clasts and basaltic clasts, respectively. The other areas filling the interstices between these clasts represent the breccia matrix. **(b)** Backscattered electron image of moganite-bearing silica micrograin adjacent to olivine (Olv), clinopyroxene (Cpx), and plagioclase (Plg) in the breccia matrix.

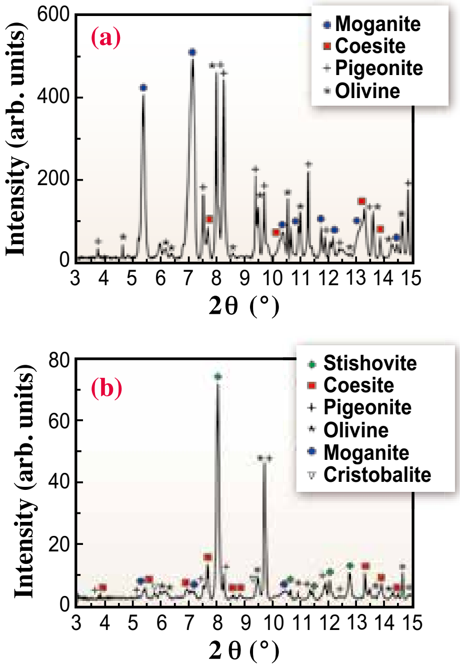

Fig. 2. SR-XRD pattern of the silica micrograins **(a)** with moganite and coesite and **(b)** moganite, coesite, and stishovite in the breccia matrix.

Moganite was found in only one of the 13 samples. If terrestrial weathering had produced moganite in the lunar meteorites, there would have been moganite present in all the samples that fell to Earth around the same time, but this was not the case. Furthermore, many previous publications on natural occurrences and laboratory experiments concluded that moganite can only be formed by precipitating from alkaline water under high-pressure consolidation at >100 MPa [1,2], which is a distinctly different environment from the desert. Part of the moganite had changed into coesite and stishovite, indicating their formation through heavy impact collisions on the Moon. These facts confirm our theory that it could not have formed in the African desert.

We interpreted the results as follows (Fig. 3) [3]. Alkaline water-bearing carbonaceous chondrite collisions delivered abundant alkaline water to the lunar surface <2.67 billion years ago. After the collisions, the delivered water was captured as fluid inside the breccia during the shock-induced consolidation. On the sunlit surface, lunar moganite precipitated from this captured alkaline water. Simultaneously, such captured water became cold-trapped in the subsurface and still remains as ice underneath the Procellarum terranes. Lunar moganite coexists with coesite and stishovite, thereby implying that a trace of the subsurface water ice was brought from the Moon by the recent impact <1–30 million years ago. Our moganite-precipitation simulation modeling concluded that a subsurface H_2O concentration higher than the estimated bulk content of 0.6 wt% (18.8 L/m^3 H_2O in a rock) is expected to still remain as ice. This value is in excellent agreement with the concentrations of H_2O ice (5.6±2.9% by mass) excavated from the Cabeus crater in the South Pole observed by LCROSS [4] and those of OH and H_2O molecules (~0.3 wt%) on the North Pole observed by Deep Impact [5]. Thus, the subsurface is expected to be an abundant and available water resource for future lunar explorations (e.g., water for drinking, oxygen for breathing, and hydrogen for fuel). Furthermore, moganite can serve as an excellent marker of the existence of water in the Moon's subsurface, which can be used for astronomy and spacecraft searching for water in Earth's satellite.

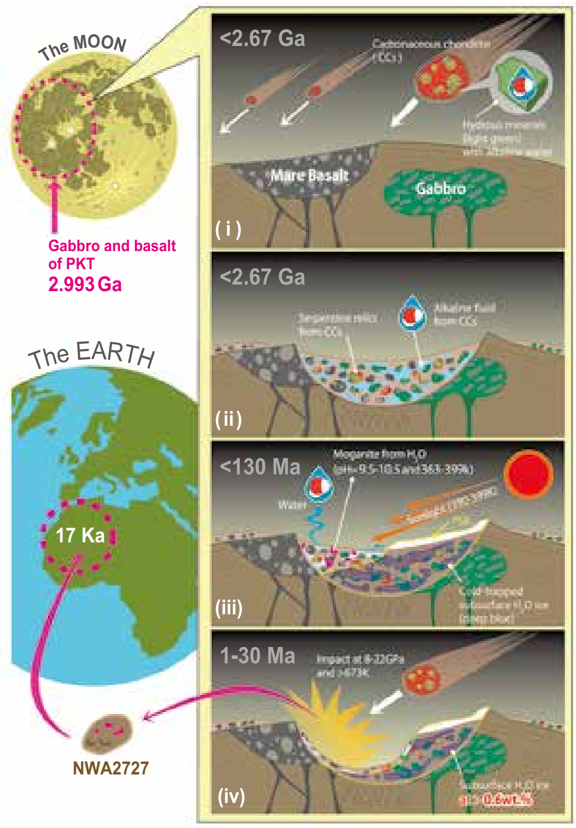

Fig. 3. Schematic of the history of subsurface H_2O in the Moon and the formation of moganite. About 3 billion years ago, mare basalt solidified on the lunar surface, and a gabbroic intrusive chamber crystallized in the anorthositic crust of the Procellarum terrane. (i) Carbonaceous chondrite (CCs) collisions are considered to have occurred <2.67 billion years ago, which led to the delivery of alkaline water to the Procellarum terrane. (ii) After these collisions, constituent rocks of the Procellarum terrane and CCs fragments are considered to have been ejected and brecciated in the impact basin. During breccia consolidation, water delivered by the CCs was captured as fluid inside the breccia. (iii) On the sunlit surface, the captured H_2O is likely to have become a silicic acid fluid, part of which migrated to space and the colder regions. Then, moganite should have precipitated under high consolidation pressure after (ii) the first collisions <2.67 billion years ago and before (iv) the most recent impact 1 to 30 million years ago as expressed below. Below its freezing point, it should have been simultaneously cold-trapped in the subsurface down to the depth of the impact basin. (iv) A subsequent heavy impact event may have launched NWA 2727 from the Moon. NWA 2727 eventually may have fallen to Earth 17±1 thousand years ago. A subsurface H_2O concentration higher than the estimated bulk content of 0.6 wt% is expected to still remain as ice.

Masahiro Kayama[a,b,*], Naotaka Tomioka[c] and Eiji Ohtani[b]

[a] Frontier Research Institute for Interdisciplinary Sciences, Tohoku University
[b] Department of Earth and Planetary Materials Science, Tohoku University
[c] Kochi Institute for Core Sample Research, Japan Agency for Marine-Earth Science and Technology

*Email: masahiro.kayama.a3@tohoku.ac.jp

References

[1] P.J. Heaney, J.E. Post: Science **255** (1992) 441.
[2] O. Schäf *et al.*: Solid State Sci. **8** (2006) 625.
[3] *M. Kayama, N. Tomioka, E. Ohtani, Y. Seto, H. Nagaoka, J. Götze, A. Miyake, S. Ozawa, T. Sekine, M. Miyahara, K. Tomeoka, M. Matsumoto, N. Shoda, N, Hirao, T. Kobayashi: Sci. Adv.* ***4*** *(2018) eaar4378.*
[4] A. Colaprete *et al.*: Science **330** (2010) 463.
[5] J.M. Sunshine *et al.*: Science **326** (2009) 565.

Synchrotron Mössbauer spectroscopy measurements of Fe-Si alloys: Implication for planetary cores

Earth's core is divided into an outer liquid core and an inner solid core according to seismological observations. These cores are less dense than pure metallic iron under the high-pressure and -temperature conditions corresponding to the core conditions. This density deficit of the cores suggests the presence of one or more light elements in addition to Fe. Silicon has been proposed as a viable candidate for one of the light elements in the cores as it is one of the most abundant elements on Earth. Phase relationships in Fe and Fe-Si systems have been investigated and a hexagonal-close-packed (hcp) structure was revealed to be stable under the pressure and temperature conditions corresponding to Earth's cores. The compressional behavior [1] and sound velocities of hcp Fe-Si alloys [2] have been measured at high pressures and temperatures to evaluate the contribution of Si to the density deficit and seismic velocity in the inner core. In previous studies, the amount of Si in Earth's core was estimated to be at most 5 wt.%.

An electronic topological transition (ETT) in Fe and Fe-Ni alloy was reported by observations of the pressure dependences of the *c*/*a* axial ratio for the hcp structure, Mössbauer center shifts (CS), sound velocities, and theoretical calculations [3]. As the ETT affects elasticity, this transition could change the physical properties of the core. Therefore, the ETT must be investigated under conditions corresponding to terrestrial planetary cores. As the planetary cores have high temperatures, it is also important to consider this relationship at high temperatures. Ono [4] reported that a change in the pressure dependence of the *c*/*a* ratio of hcp Fe occurs at room temperature at around 50 GPa and at 2000 K at around 150 GPa. Thus, there is a possibility that the ETT and a change in *c*/*a* may occur in the Earth and planetary cores. Although the ETT in Fe and Fe-Ni alloys was previously reported to occur at high pressures and temperatures, the electronic properties and *c*/*a* ratios have not yet been investigated in Fe–light-element alloys under hydrostatic conditions. Since Si is a prime candidate for a light element in the core and substitutes Fe in the same way as Ni, we examined the structural, electronic, and compression properties of Fe-Si alloys with the hcp structure up to 60 GPa under quasi-hydrostatic conditions using a combination of XRD and synchrotron-based Mössbauer spectroscopy (SMS) [5].

The starting materials were Fe-2.8wt.%Si and Fe-6.1wt.%Si, which were 33% enriched with ^{57}Fe. Chips from the starting materials were used for energy-domain SMS at SPring-8 **BL10XU** (Fig. 1) and **BL11XU**, and for *in situ* XRD experiments at high pressures at BL10XU. A chip of Fe-2.8wt.%Si or Fe-6.1wt.%Si with a ruby chip as a pressure gauge was loaded into a sample chamber with helium gas as the pressure medium.

Mössbauer spectra and XRD patterns from hcp phases of Fe-2.8wt.%Si or Fe-6.1wt.%Si were obtained up to 60 GPa at room temperature. Typical SMS spectra are shown in Figs. 2(a,b) and a single peak was observed in each spectrum from Fe-2.8wt%Si or Fe-6.1wt%Si at all pressures, suggesting that they are nonmagnetic within the present experimental resolution. Only hcp-structured phases in Fe-2.8wt.%Si and Fe-6.1wt.%Si were observed above 21 GPa and 29 GPa, respectively. The relationships between the CS–pressure and *c*/*a*–pressure for the present Fe-Si alloys are shown in Figs. 2(c,d), together with those of pure Fe and $Fe_{0.9}Ni_{0.1}$ [3]. Both relationships showed changes in pressure dependence at high pressures. The pressures where the changes occurred increased with the amount of Si in Fe.

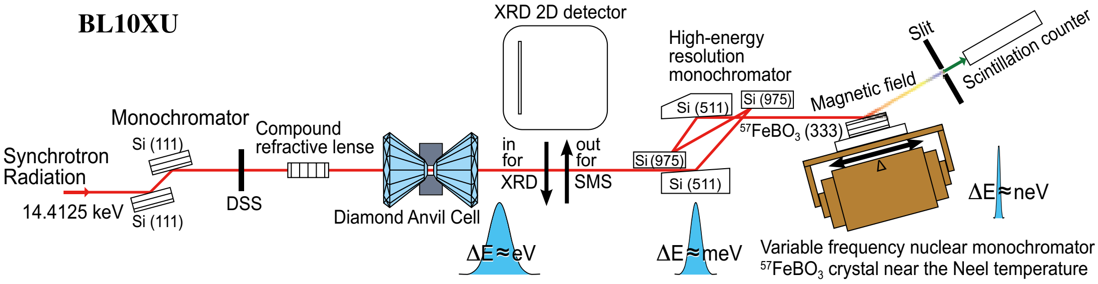

Fig. 1. Schematic view of Mössbauer spectroscopy system at BL10XU. Energy domain Mössbauer spectra and X-ray diffraction patterns can be taken with a typical collection time of 2 h.

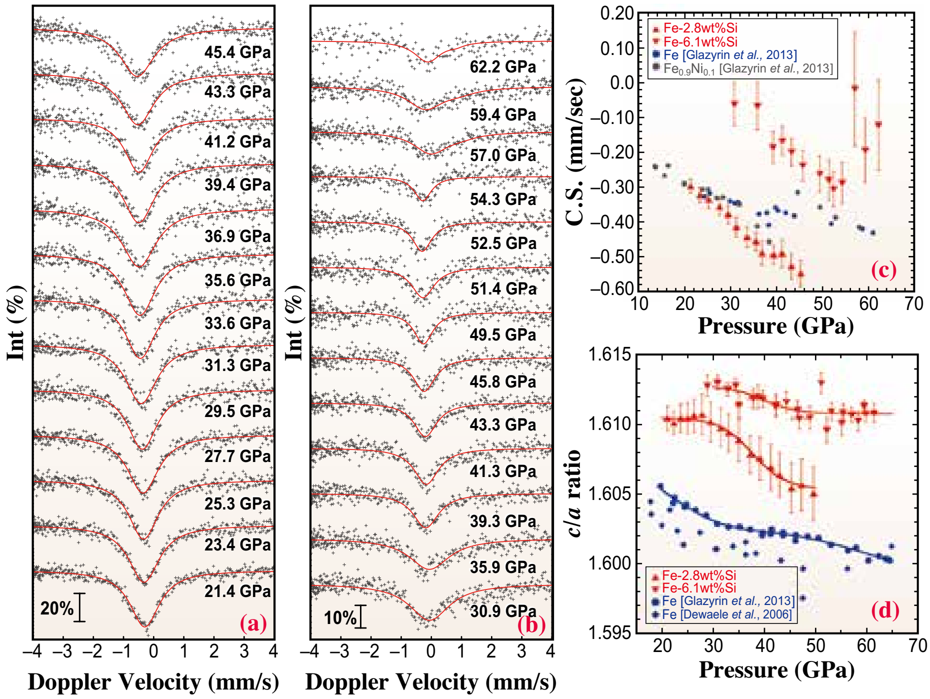

Fig. 2. **(a)** Obtained Mössbauer spectra from Fe–2.8wt%Si, **(b)** obtained Mössbauer spectra from Fe-6.1wt%Si. **(c)** C.S. of Fe–2.8wt%Si, Fe-6.1wt%Si, Fe, and Fe-10wt%Ni alloys are plotted against pressure. **(d)** *c*/*a* ratios as function of pressure.

Our results were used to estimate the effect of Si on the ETT and *c*/*a* evolution as a function of pressure in the interior of terrestrial cores [5]. The ETT pressure was regarded as a function of the amount of Si and temperature to discuss the interiors of terrestrial planets. The estimated pressure of the ETT is shown in Fig. 3 along with the Mercury, Venus, Earth, and Mars core conditions and the Fe phase relationship. Although we do not know exactly whether the terrestrial planets have solid inner cores owing to the lack of seismological data, our results indicate that only Venus's core could undergo a change in *c*/*a* ratio. If Venus has a solid inner core and the inner core intercepts the boundary of the *c*/*a* relationships as shown in Fig. 3, the inner core may have seismic wave velocities lower than those estimated under pressures lower than the ETT pressure [3].

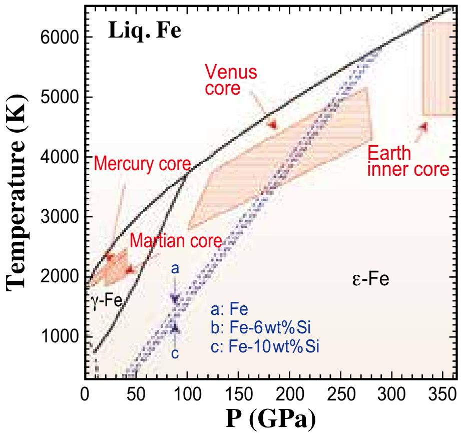

Fig. 3. Phase diagram of Fe with terrestrial planet core conditions and the transition boundary where *c*/*a* changes according to this study and previous studies. The ETT boundaries were estimated from the results for Fe, Fe-6wt%Si, and Fe-10wt%Si.

Seiji Kamada[a,b,*], Fumiya Maeda[b] and Naohisa Hirao[c]

[a] Frontier Research Institute for Interdisciplinary Sciences, Tohoku University
[b] Department of Earth Science, Tohoku University
[c] Japan Synchrotron Radiation Research Institute (JASRI)

*Email: seijikmd@m.tohoku.ac.jp

References

[1] S. Tateno *et al*.: EPSL **418** (2015) 11.
[2] J. Badro *et al*.: EPSL **254** (2007) 233.
[3] K. Glazyrin *et al*.: Phys. Rev. Lett. **110** (2013) 117206.
[4] S. Ono: Solid State Commun. **203** (2015) 1.
[5] *S. Kamada, N. Suzuki, F. Maeda, N. Hirao, M. Hamada, E. Ohtani, R. Masuda, T. Mitsui, Y. Ohishi and S. Nakano: Am. Mineral.* ***103*** *(2018) 1959.*

Application of X-ray computed tomography using synchrotron radiation to frozen food

Freezing is an essential method of preserving food for storage and logistics in food manufacturing. Control of the size, shape, and distribution of ice grains in frozen food is important for reducing damage to food. We investigated the capability of X-ray computed tomography (CT) as a nondestructive observation technique for the internal structures of frozen foods using SPring-8. It is difficult for a laboratory X-ray CT apparatus using white X-rays to distinguish ice grains from other substances in frozen food, because the difference in density between ice and other substances is not significant for white X-rays. Utilizing synchrotron radiation (SR) as the light source enables us to use a highly brilliant and monochromatic X-ray beam. Monochromatic X-rays improve the contrast of CT images, making the ice grains in frozen food distinguishable.

We developed a specimen freezer for keeping food specimens frozen on an X-ray CT apparatus as shown in Fig. 1. This equipment keeps the temperature of specimens at about –30°C by blowing liquid nitrogen (LN_2) vapor. The noncontact freezer does not disturb turning the specimen and accepts various shapes of specimen, whose horizontal thickness must be less than *ca.* 6 mm. Examples of CT images of frozen food are shown in Fig. 2; these are the tomograms of frozen tuna (Fig. 2(a): horizontal, Fig. 2(b): vertical) [1]. The measurement was carried out at SPring-8 **BL19B2**. The energy of the X-rays was 12.4 keV. The specimen was irradiated with the X-ray while turned at a speed of $1.2^\circ\,\mathrm{s}^{-1}$. A set of 256 transmission images was acquired during turning the specimen throughout 0-180 degrees. The exposure time for each image acquisition was 120 ms. The X-ray camera used for the image acquisition was an X-ray imaging system composed of an AA40 X-ray imaging unit and a C4880-41S CCD camera manufactured by Hamamatsu Photonics K.K. The distance from the specimen to the X-ray camera was set at 100 mm. The size of the pixels in the image data was $2.9 \times 2.9\ \mu\mathrm{m}^2$. These images indicate the linear X-ray absorption coefficient μ of the matter in the specimens with a gray scale, in which a dark area means a large value. Ice grains are clearly indicated as light gray areas, where the mean μ value of $2.59\ \mathrm{cm}^{-1}$ is consistent with that of ice. Because the specimen was frozen by slow cooling, ice grains were coarsened and the other substances shrank into the dark gray bands elongated vertically along the direction of the muscle fibers. The utilization of highly brilliant and monochromatic X-rays made it possible not only to improve the contrast of CT images but

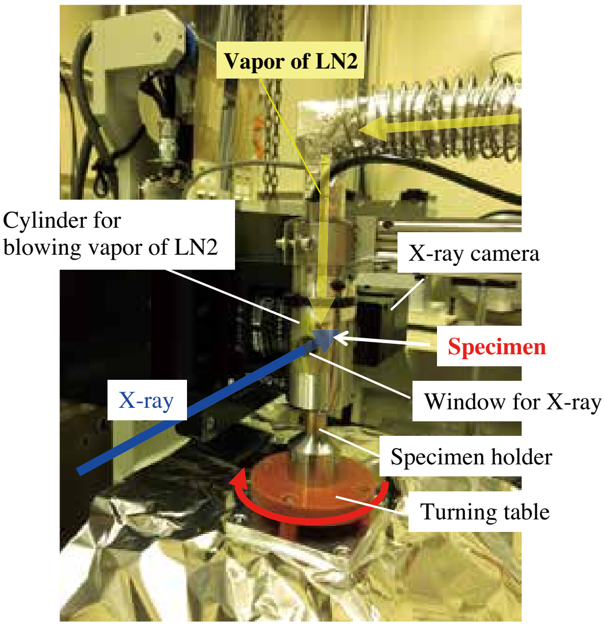

Fig. 1. View of the specimen freezer for the X-ray CT of frozen food.

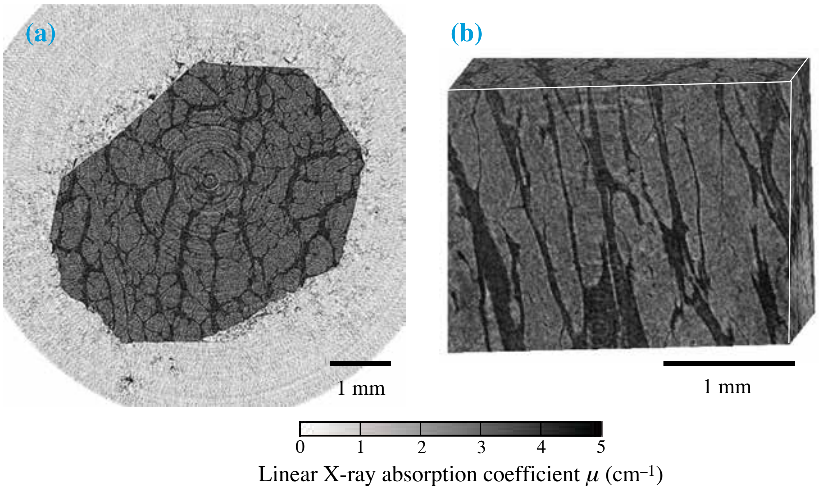

Fig. 2. Tomograms of frozen tuna. **(a)** Horizontal cross section. **(b)** Vertical cross section.

also to analyze the constituent distribution in the frozen food quantitatively. Figure 3 shows frequency distributions of the μ value at each pixel in tomograms of frozen tuna and raw tuna. The profile of data for raw tuna can be fitted to a single peak described with a Gaussian function as shown by the yellow line. The single peak reflected the fact that the substance in the raw tuna was homogeneous. On the other hand, the profiles of data for frozen tuna consisted of two peaks, as shown by the light blue line, whose profile was reproduced by the sum of the two Gaussian functions indicated by thick and dotted blue lines in the figure. The thick-line peak indicates ice grains and the dotted-line peak indicates the other substances. Comparison of the peak for the substances other than ice in frozen tuna with the peak for raw tuna shows that the center of the former peak is shifted to a larger value of μ from that of the latter peak. This means that the increase in the densities of the substances other than ice in frozen tuna was caused by freezing. The increased density suggests that the utilization of highly brilliant and monochromatic X-rays from SR in X-ray CT enables not only the morphological observation of ice grains but also quantitative analysis of the condensation of materials in frozen food.

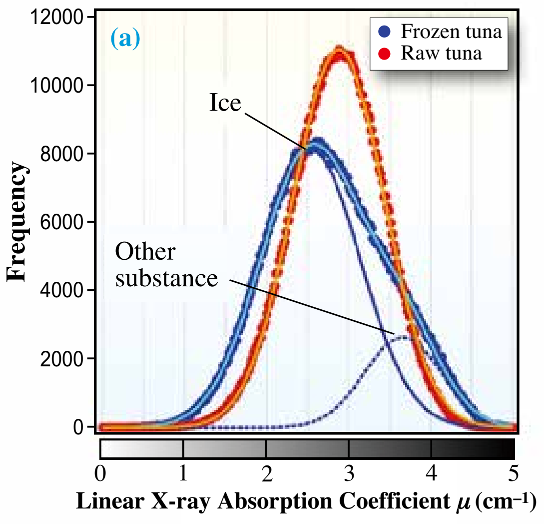

Fig. 3. Frequency distributions of value of μ of each pixel in the tomograms of frozen tuna (red circles) and raw tuna (blue circles).

This technique has been applied to various frozen foods, for example, frozen fruits [2], and frozen pasta [3]. The capability described here is currently available to users at BL14B2 and BL46XU.

Masugu Sato

Japan Synchrotron Radiation Research Institute (JASRI)

Email: msato@spring8.or.jp

References

[1] M. Sato, K. Kajiwara and N. Sano: Jpn. J. Food Eng. **17** (2016) 83.

[2] R. Kobayashi, T. Suzuki: Int. J. Refrig. **99** (2019) 94.

[3] J. Nonaka, T. Hirauchi, K. Irie: Refrigeration **93** 1086 (2018) 219. (in Japanese)

Investigation of collective dynamics of solvent molecules in nanofluids by inelastic X-ray scattering

A highly efficient heat transfer medium could be realized by increasing the thermal conductivity of fluids. Many studies have been conducted on the fabrication of nanofluids, in which nanoparticles are dispersed homogenously into a medium. By adding a small amount of copper (Cu), silver (Ag), or alumina (Al_2O_3) nanoparticles, the thermal conductivities of water and ethylene glycol (EG) are increased by 20 to 40% [1]. These thermal conductivities exceeded the theoretical values, and it was deduced that nanoparticles affect solvent molecules in some way. Several hypotheses, such as Brownian motion, clustering, ballistic transport, and the creation of an inter-nanoparticle potential, have been proposed to explain the high thermal conductivity of nanofluids [2]. However, the effect of nanoparticles on a solvent has not yet been clarified. It is essential to understand solvent behavior in nanofluids to develop an efficient heat transfer medium.

A high-resolution inelastic X-ray scattering (IXS) method has been used to investigate the collective dynamics of many liquids, such as water, organic solvents, ionic liquids, and liquid metals [3]. By analyzing coherent scattering from a nanofluid, collective dynamics of solvent molecules can be clarified. The excitation of acoustic phonons is observed in collective dynamics in the low-momentum-transfer region (2–20 nm^{-1}). The dispersion relation between the excitation energy and momentum transfer gives a high-frequency sound velocity (HFSV) that reflects the thermal conductivity and structural relaxation of solvent molecules. This leads to the elucidation of the effect of nanoparticles on the heat transfer and molecular dynamics of nanofluids.

Cu nanoparticles (Cu NPs) with 50 nm average diameter are prepared by the polyol method [4] and dispersed in EG. For comparison with the effect of Cu NPs, a nanofluid of EG in which other NPs, such as Ag or Al_2O_3, are dispersed, is desired. However, an EG dispersion of other NPs is difficult to fabricate and is not readily available. Therefore, a nanofluid with Al_2O_3 NPs in water is examined for comparison. The thermal conductivities of Cu NPs/EG and Al_2O_3 NPs/water are measured experimentally. It is found that Cu NPs are more effective than Al_2O_3 NPs for increasing the thermal conductivity of the medium. The thermal conductivities of Cu NPs/EG samples with different Cu NP concentrations exceed the estimated values obtained from the Maxwell-Garnett theory. In contrast, the thermal conductivities of Al_2O_3 NPs/water samples are less than or equal to the estimated values [5].

IXS measurements at SPring-8 **BL35XU** were conducted at room temperature for both Cu NPs/EG and Al_2O_3 NPs/water samples with the NP concentrations listed in Table 1. Dynamic structure factors, $S(Q,\omega)$, are obtained by subtracting the scattering from an empty cell. The normalized IXS spectrum of IXS-EG-3 obtained at $Q = 5.58\ nm^{-1}$ is shown in Fig. 1. Generally, a large peak around 0 meV is from quasi-elastic scattering, and side or shoulder peaks are caused by inelastic excitation. A shoulder peak is observed at 4.7 meV in Fig. 1, although peaks from Cu NPs should be observed at much higher energy than those from the solvent. The damped harmonic oscillation (DHO) method was adopted to separate the side or shoulder peaks from the main quasi-elastic scattering peak. Twenty-four data sets per sample for different Q values were analyzed and the inelastic excitation energy at each peak was obtained.

Figure 2 shows the dispersion relation between the Q value and excitation energy for IXS-EG-3. The HFSV is calculated from the slope of the dispersion

Table 1. High-frequency sound velocity of nanofluids

Exp. No.	NPs	Solvent	Concentration (vol%)	HFSV (km/s)	Increase Ratio/conc.
IXS-EG-1	–	EG	0	2.31 ± 0.01	
IXS-EG-2	Cu	EG	0.5	2.34 ± 0.02	2.60
IXS-EG-3	Cu	EG	1.32	2.56±0.03	8.41
IXS-WA-4	–	water	0	2.72±0.03	
IXS-WA-5	Al_2O_3	water	2.53	2.76±0.02	0.49
IXS-WA-6	Al_2O_3	water	7.60	2.84±0.03	0.50

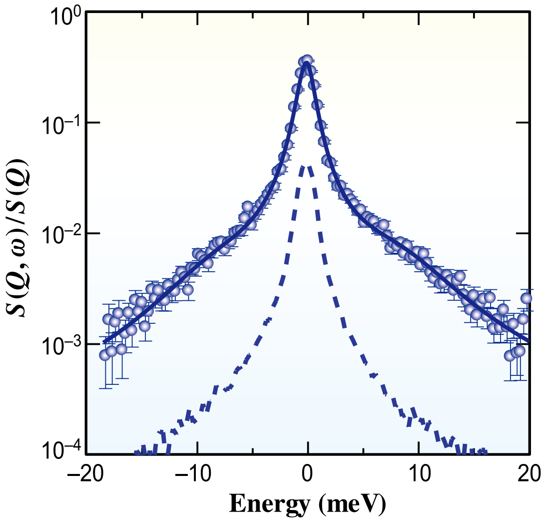

Fig. 1. Normalized inelastic X-ray scattering spectrum (IXS-EG-3, $Q = 5.58$ nm^{-1}). The solid line represents the DHO and Lorentzian fit including the convolution of the resolution function (dashed line).

relation. From Fig. 2, the HFSV is estimated to be 2.56 km/s for IXS-EG-3 by liner approximation using the least squares method. Since the HFSV of EG is 2.31 km/s, it is found that the existence of small amounts of Cu NPs increased the HFSV of EG 1.11-fold.

Table 1 summarizes the HFSVs of the samples. The HFSV increases with increasing amounts of Cu and Al_2O_3 NPs. The results indicate that the collective dynamics of EG and water is affected by the existence of NPs. The addition of 1.32 vol% Cu NPs brought about a 1.11-fold (2.56/2.31) increase in HFSV. On the other hand, in the case of the Al_2O_3/water system, the HFSV increases 1.04-fold (2.84/2.72) when 7.6 vol% Al_2O_3 NPs was added to water. To understand the effect of the NPs clearly, the relative increase is divided by the volume concentration of the NPs and the values are also listed in Table 1. It is clear from Table 1 that Cu NPs are over ten times more effective than Al_2O_3 NPs, although the solvent is different.

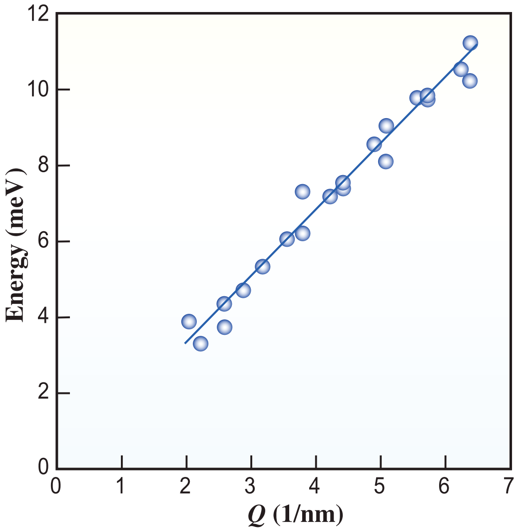

Fig. 2. Dispersion relation of the energy of the inelastic excitation (IXS-EG-3). The solid line is fitted by the least square method.

In summary, IXS measurements of two types of nanofluids (Cu NPs/EG, Al_2O_3 NPs/water) were conducted, and HFSVs of the series of samples were obtained. The effect of the NPs on the heat transfer and molecular dynamics of the medium of nanofluids was evaluated. The HSFV of EG was increased by 11% upon the addition of 1.32 vol% Cu NPs. It is suggested that the collective dynamics of EG is strongly affected by Cu NPs. In contrast, Al_2O_3 NPs had a limited effect on the dynamics of the solvent. It is found that the effect of Cu NPs on the solvent is significant.

The IXS method is a powerful tool for understanding the molecular behavior of a medium in nanofluids. The effect of NPs could be elucidated by the method, leading to the development of an efficient heat transfer medium.

Kazuhisa Yano[a,*] and Koji Yoshida[b]

[a] Sustainable Energy & Environment Dept.2,
Toyota Central R&D Labs
[b] Department of Chemistry, Fukuoka University

*Email: k-yano@mosk.tytlabs.co.jp

References

[1] J.A. Eastman *et al.*: Appl. Phys. Lett. **78** (2001) 718.
[2] P. Keblinski *et al.*: Int. J. Heat Mass Transfer **45** (2002) 855.
[3] T. Yamaguchi *et al.*: Nucl. Instrum. Meth. Phys. Res. B **238** (2005) 146.
[4] K. Yano *et al.*: J. Nanosci. Nanotech. **18** (2018) 5101.
[5] *K. Yano, K. Yoshida, K. Kamazawa, H. Uchiyama, S. Tsutsui, A.Q.R. Baron, Y. Fukushima, T. Yamaguchi: J. Mol. Liq.* ***248*** *(2017) 468.*

Structural change of cerium oxide-supported ruthenium catalyst during the biorefinery of platform chemicals

Current requirements to reduce carbon dioxide emissions have been the driving force for biorefinery utilizing renewable resources, such as plant biomass, as carbon-neutral feedstocks for commodity chemicals [1]. To utilize biomass feedstocks in place of fossil resources, the development of highly efficient catalytic methods is strongly desired [2]. To date, much effort has been devoted to the direct carbon–oxygen (C–O) bond cleavage of high-oxygen-containing biogenic polyols to produce valuable chemicals by hydrogenolysis and deoxydehydration. For example, there have been many attempts to achieve the selective hydrogenolysis of glycerol, which is readily obtained from fats and oils, to 1,2-propanediol and 1,3-propanediol as valuable polyester monomers and solvents using copper- and platinum-based heterogeneous catalysts, respectively. On the other hand, selective cleavage of carbon–carbon (C–C) bonds has not yet been widely researched despite its great potential for extending the utility of biomass-derived oxygenates to obtain the desired carbon chain length. However, these reactions often suffer from low selectivity toward the desired chemicals, limited substrate scope, and high reaction temperatures. Therefore, the development of selective and versatile C–C bond scission catalysts that can work under milder conditions is highly desired to open new routes for industrially important chemicals from a wide range of biomass derivatives.

Recently, we have found that cerium oxide-supported ruthenium (Ru/CeO_2) nanoparticles efficiently promoted the selective C–C bond scission of levulinic acid to 2-butanol in water [3]. Levulinic acid is one of the versatile platform chemicals obtained from biomass. There are many reports on the catalytic transformation of levulinic acid to valuable C5 chemicals, e.g., γ-valerolactone, 1,4-pentanediol, and 2-methyltetrahydrofuran. However, C–C bond scission reactions into valuable C4 chemicals such as 2-butanol have seldom been reported. Furthermore, Ru/CeO_2 showed high generality for the cleavage of C–C bonds of oxygenated compounds. The results provide a simple and more environmentally friendly method for the refinery of platform chemicals from biomass that are currently produced from petroleum feedstock.

The reaction of levulinic acid to 2-butanol was conducted using Ru/CeO_2 in water at 423 K under 3 MPa of H_2. To clarify the origin of the novel catalysis of Ru/CeO_2, several physicochemical analyses such as electron microscopy, X-ray diffraction (XRD), and X-ray absorption spectroscopy (XAS) were carried out. The XAS experiments were conducted at SPring-8 **BL14B2** and **BL01B1**.

The morphology of Ru/CeO_2 was determined by field-emission scanning electron microscopy (FE-SEM) analysis, which clearly showed the drastic change in the morphology after the catalytic reaction. The fresh Ru/CeO_2 nanoparticles (Ru/CeO_2_fresh) of 3–5 μm diameters were converted into an agglomeration of rodlike structures (Fig. 1(a)) on the used Ru/CeO_2 (Ru/CeO_2_used).

From the high-resolution TEM images of Ru/CeO_2_used, Ru nanoparticles of *ca.* 3 nm diameter were observed on CeO_2 nanorods (Figs. 1(b,c)). The nanorods consist of fine crystalline nanowires having a line spacing of 0.27 nm, which is consistent with the {002} reflection plane of CeO_2.

In situ XRD analysis of Ru/CeO_2 catalysts showed that the pristine CeO_2 support was transformed into $Ce(OH)_3$ (Fig. 2). No diffraction peaks derived from crystalline Ru oxide and Ru metal were observed in the fresh and used catalysts, suggesting the high dispersity of Ru species, respectively. The diffraction pattern of the Ru/CeO_2_used catalyst without exposure to air was similar to that of $Ce(OH)_3$

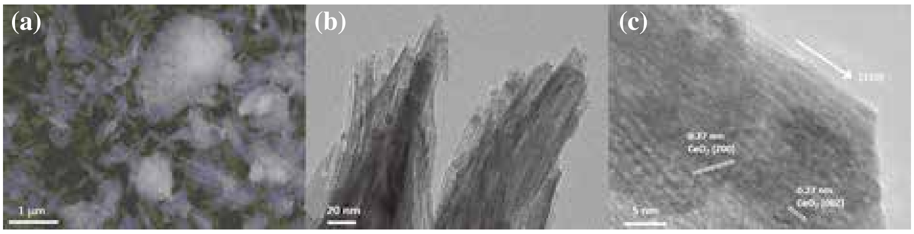

Fig. 1. FE-SEM image of Ru/CeO_2_used **(a)** and TEM images of Ru/CeO_2_used **(b)** and **(c)**.

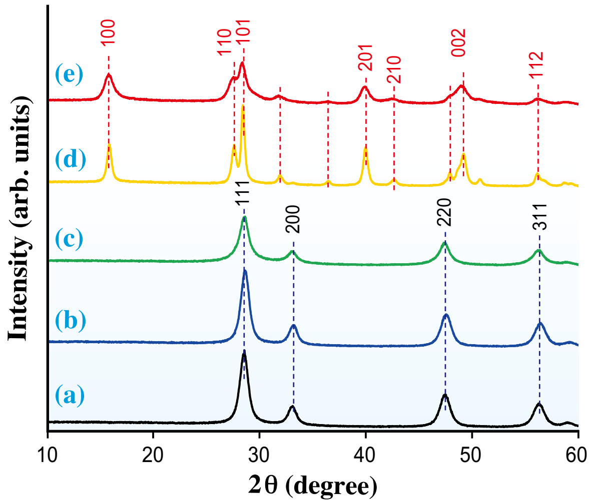

Fig. 2. XRD patterns of **(a)** pristine CeO_2, **(b)** Ru/CeO_2_fresh, **(c)** Ru/CeO_2_used after exposure to air and **(d)** $Ce(OH)_3$ and **(e)** Ru/CeO_2_used without exposure to air.

(Figs. 2(d) and 2(e)), indicating reduction and a phase transition from CeO_2 to $Ce(OH)_3$. After exposure to air, the $Ce(OH)_3$ was oxidized back to CeO_2 (Fig. 2(c)).

Ru *K*-edge XAS analysis revealed that the Ru oxide in the fresh catalyst was reduced under the operating conditions to afford metallic Ru species (Fig. 3(a)). FT-EXAFS and curve-fitting analysis of the peak at approximately 0.22 nm for the Ru-Ru shell revealed a Ru-Ru atomic distance of 0.267 nm and a coordination number of 8.6, indicating the formation of Ru nanoparticles with a mean diameter of *ca.* 3 nm [4]. The estimated particle size agreed well with that obtained from TEM observation (Figs. 3(b) and 1(b)).

Ce L_3-edge XANES analysis also confirmed the complete reduction of Ce^{4+} to Ce^{3+} species under the reaction conditions (Fig. 3(c)). After exposing the used Ru/CeO_2 to air, the $Ce(OH)_3$ nanorods were easily oxidized to CeO_2 nanorods [5]. On the other hand, neither the Ru/CeO_2 catalysts used in organic solvents nor the CeO_2 sample without the use of Ru suggested that CeO_2 was reduced to $Ce(OH)_3$ during the reaction.

Considering the above results, we proposed the following reaction mechanism. A particular type of CeO_2 was reduced to $Ce(OH)_3$ nanorods under H_2 pressure in water at 423 K. The RuNPs formed on the cerium nanorods activate molecular hydrogen, and the spillover hydrogen and water promote the reduction of Ce^{4+} to Ce^{3+} to form $Ce(OH)_3$ nanorods. Water is necessary to promote the reduction of Ce species under the relatively mild conditions. The selective C–C bond cleavage was promoted by the concerted effect of the RuNPs with the basic $Ce(OH)_3$ nanorods.

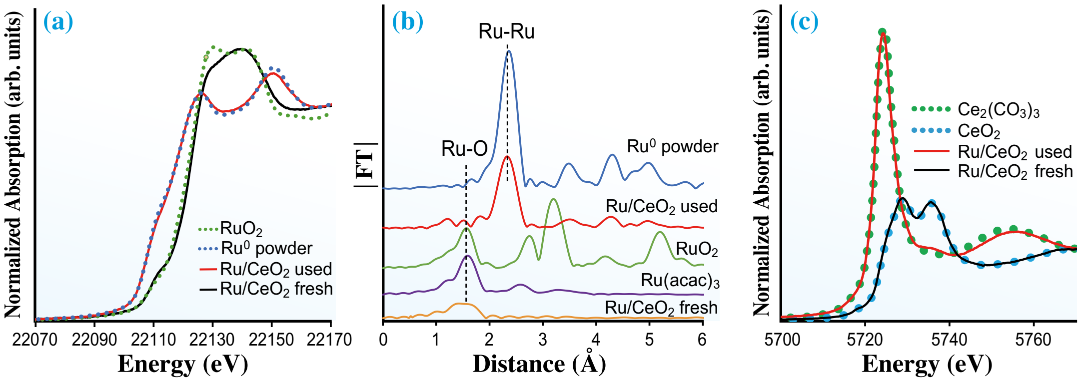

Fig. 3. Ru *K*-edge XANES **(a)** and FT of Ru *K*-edge EXAFS **(b)** of Ru/CeO_2 catalysts before and after catalytic reactions (H_2 3 MPa, 423 K in water). Ce L_3-edge XANES of Ru/CeO_2 catalyst **(c)**. (acac = acetylacetonate)

Tomoo Mizugaki

Graduate School of Engineering Science,
Osaka University

Email: mizugaki@cheng.es.osaka-u.ac.jp

References

[1] J.J. Bozell, G.R. Petersen: Green Chem. **12** (2010) 539.
[2] M.L. Besson *et al.*: Chem. Rev. **114** (2014) 1827.
[3] *T. Mizugaki, K. Togo, Z. Maeno, T. Mitsudome, K. Jitsukawa, K. Kaneda: Sci. Rep. 7 (2017) 14007.*
[4] L.S.R. Kumara *et al.*: Phys. Chem. Chem. Phys. **18** (2016) 30622.
[5] C.C. Tang *et al.*: Adv. Mater. **17** (2005) 3005.

ACCELERATORS & BEAMLINES FRONTIERS

SPring-8
BEAM PERFORMANCE

Recent update of accelerators

Renewal of the low-level radio-frequency (LLRF) system of the storage ring has been in progress. The LLRF system is distributed at four RF stations along the storage ring and has been dedicated to user operations since the SPring-8 accelerator complex was constructed in the 90 s. However, the analogue NIM modules have gradually become unreliable owing to their degradation over time. Also, one of our future concerns is that some of the electric parts inside the system will no longer be available on the market. Thus, we have developed a new LLRF system based on the modern standard MicroTCA.4 [1] and commenced user operations in fiscal year 2018 with one of the four RF stations, called the A-station, operated by the new LLRF system. So far, the new system has been working properly without any fatal errors, although several minor errors have been recognized and fixed. We plan to renew the LLRF system in the B- and C-stations in the summer of fiscal year 2019 and in the D-station at the end of the fiscal year.

At SPring-8, we have studied the possibility of applying permanent-magnet-based dipole magnets to next-generation light sources, especially SPring-8-II [2]. We have recently replaced one of the dipole magnets in the beam transport from the booster synchrotron to the storage ring with a newly developed permanent-magnet-based dipole magnet. Permanent magnets are advantageous over conventional electromagnets in that they consume less power and are physically more compact, and there is less risk of a magnet-related accelerator failure due to, for example, a power failure or water leakage. It follows that a permanent magnet could be beneficial to both the facility and its users. However, there are also practical challenges in using permanent magnets as the main magnets for light sources. For example, the behavior of a permanent magnet is known to be temperature-dependent, which may result in a shift in the electron energy caused by ambient temperature drift in the accelerator tunnel. Radiation damage of permanent magnets is also a concern when one considers the fact that the demagnetization of undulator permanent magnets has been observed at several accelerator facilities [3]. In recent years, we have designed, fabricated, and tested several kinds of permanent dipole magnets to overcome these challenges [2]. At the end of fiscal year 2017, we replaced one of the beam transport magnets between the booster synchrotron and the storage ring, SSBT-BM5, with a permanent dipole magnet that we had newly fabricated (Fig. 1). We designed the magnet so that the dipole magnetic field would be insensitive to temperature drift and the demagnetization due to radiation damage could be monitored using precise magnetic field measurement probes based on NMR. Although we do not expect significant demagnetization, we installed correction magnets just in case it occurs. The beam transport through the new dipole magnet has been stably carried out for a year, and no demagnetization due to radiation damage has been observed as we expected. We will continue to observe the performance to verify the reliability of the permanent dipole magnet we developed.

Fig. 1. C-shaped permanent dipole magnet newly installed in the beam transport between the booster synchrotron and the storage ring. The magnet consists of four segments; the first and third segments are made of a samarium-cobalt magnet, and the second and fourth segments are made of a neodymium-iron-boron (NdFeB) magnet.

Shiro Takano and Takahiro Watanabe*

Japan Synchrotron Radiation Research Institute (JASRI)

*Email: twatanabe@spring8.or.jp

References

[1] T. Ohshima *et al*.: Proc. IPAC2017(2017), THPAB117.
[2] T. Watanabe *et al*.: Phys. Rev. Acc. Beams **20** (2017) 072401.
[3] T. Bizen *et al*.: Sci. Rep. **6** (2016) 37937.

Ultraprecision ellipsoidal mirror with two-dimensional 100 nm focusing capability

High-precision X-ray optics are indispensable tools for supporting X-ray analytical technologies provided in synchrotron radiation and X-ray free electron laser facilities. X-ray focusing mirrors utilizing the total-reflection phenomenon play an extremely important role in X-ray microscopic analyses by taking advantage of a chromatic aberration-free characteristic. Advancement of fabrication technologies for high-precision X-ray mirrors is important to improve X-ray analytical technologies. Here, we report the development of an ellipsoidal mirror optics for two-dimensional focusing of hard X-rays to 100 nm size [1].

A pair of mirrors with an elliptical-cylinder surface in the Kirkpatrick-Baez (K-B) geometry is typically used as micro-/nano-focusing optics for hard X-rays. In the K-B geometry, two line-focusing mirrors are arranged in tandem to two-dimensionally focus X-rays. Using commercially available elliptical-cylinder mirrors with a sub-nanometer precision, focused beams with a beam size of 50 nm can be used for X-ray analysis. However, the 100 nm focusing of hard X-rays with ellipsoidal focusing mirrors, as shown in Fig. 1(a), which can produce a two-dimensional focused beam with a single reflection, is not accessible by conventional fabrication technologies. Our group addressed the challenge developing nanofocusing ellipsoidal mirrors by improving fabrication technologies including a high-precision machining method [2] and a surface measurement system [3].

Ellipsoidal focusing mirror optics have many advantages, such as highly efficient focusing properties and a simple mirror alignment mechanism, for application to X-ray microscopy compared with elliptical-cylinder mirrors in the K-B geometry. In particular, ellipsoidal mirrors have a major advantage over elliptical-cylinder mirrors that the spatial aperture of sagittal focusing, that is, the focusing in the short-axis direction, can be designed to be larger than that of meridional focusing, that is, the focusing in the long-axis direction. More specifically, an ellipsoidal focusing mirror can produce a smaller diffraction-limited focused beam size than elliptical-cylinder mirrors in the K-B geometry.

The optical parameters of the developed ellipsoidal focusing mirror were designed as follows. The distance between the light source and the mirror center is 50 m. The distance between the mirror center and the focal point is 200 mm. The incident angle at the mirror center is 9 mrad. The mirror surface has a radius of curvature of 44 m and 3.6 mm in the long- and short-axis directions at the mirror center, respectively. Difficulties in the fabrication process of ellipsoidal focusing mirrors are caused by this small radius of curvature in the short-axis direction. The ideal reflectivity is 75% with a platinum surface coating under the total-reflection conditions at an X-ray energy of 7 keV. The diffraction-limited focused beam size of 37 nm × 67 nm (full width at half maximum (FWHM)) is expected at an X-ray energy of 7 keV when the mirror surface has a reflection area of 93 mm × 0.45 mm in the long- and short-axis directions. It is estimated by a wave-optical simulator [4] that a surface figure accuracy of 1 nm (root-mean-square (RMS)) is required for nano-focusing with the ellipsoidal mirror.

The ellipsoidal shape was fabricated on a substrate surface of synthetic fused silica glass with a size of 100 mm × 50 mm × 30 mm as shown in Fig. 1(b). The ellipsoidal focusing mirror was fabricated by the following process. First, the ellipsoidal shape was roughly and efficiently formed by a precision multi-axis grinding machine using a diamond grinding wheel with an accuracy of about 1 μm (peak-to-valley). Then, the increase in the surface roughness on the mirror caused by the grinding was reduced

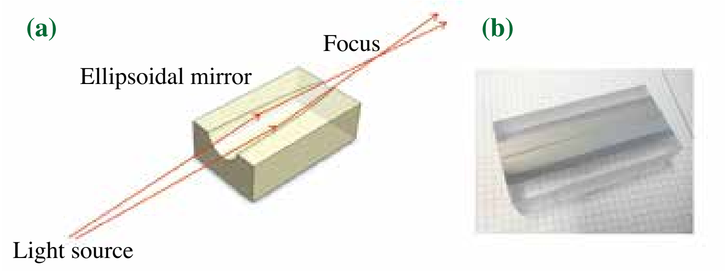

Fig. 1. Ellipsoidal focusing mirror. **(a)** Schematic view. **(b)** Photograph of the developed mirror.

to 0.2 nm (RMS), which is adequate for the X-ray mirror, using a processing machine with a rotational-type working head made by our group. In the next step, the surface figure error was removed to satisfy the accuracy of the estimated value by using a computer-controlled fabrication process employing a processing machine with a nozzle-type working head made by our group. After that, the mirror surface was uniformly coated with a platinum thin film by a DC magnetron sputtering system. The surface accuracy of the developed mirror was comparable to the reproducibility of our measurement system, which is based on a stitching interferometry developed by our group. The surface figure error of the finished ellipsoidal mirror was 1.0 nm (RMS) at an entire area of 93 mm × 0.45 mm and 0.8 nm (RMS) over the central area of 50 mm × 0.45 mm. The surface roughness of the mirror was 0.3 nm (RMS).

We evaluated the focused beam performances of the developed ellipsoidal mirror at SPring-8 **BL29XUL**. The mirror was set 50 m from a source slit with a size of 5 μm for the evaluation to obtain a sufficiently small focused beam size estimated by geometric demagnification. We made a dedicated alignment device for the ellipsoidal focusing mirror, which can align the incident angle and the in-plane rotation with a precision of 0.1 μrad. After the precision alignment using Foucault's knife-edge test, the focused beam profiles were measured by the knife-edge scanning method using a gold wire with a diameter of 200 μm. Figure 2 shows the measured focused beam profiles at an X-ray energy of 7 keV. We evaluated two focused beams reflected by two areas on the mirror surface: the entire area of 93 mm × 0.45 mm (Figs. 2(a) and 2(b)) and the central area of 50 mm × 0.45 mm (Figs. 2(c) and 2(d)). Figure 2 shows focused beam profiles in the meridional ((a) and (c)) and sagittal ((b) and (d)) directions. We achieved focused beam sizes of 95 nm × 132 nm and 85 nm × 125 nm (FWHM) from each reflection area. The obtained focused beam sizes were larger than the diffraction-limited size. This is due to the lack of the absolute accuracy of the surface measurement system.

The developed fabrication technologies for the ellipsoidal focusing mirror are applicable to other high-precision mirror optics with a two-dimensional aspherical surface, which are expected to be utilized in various advanced optical systems.

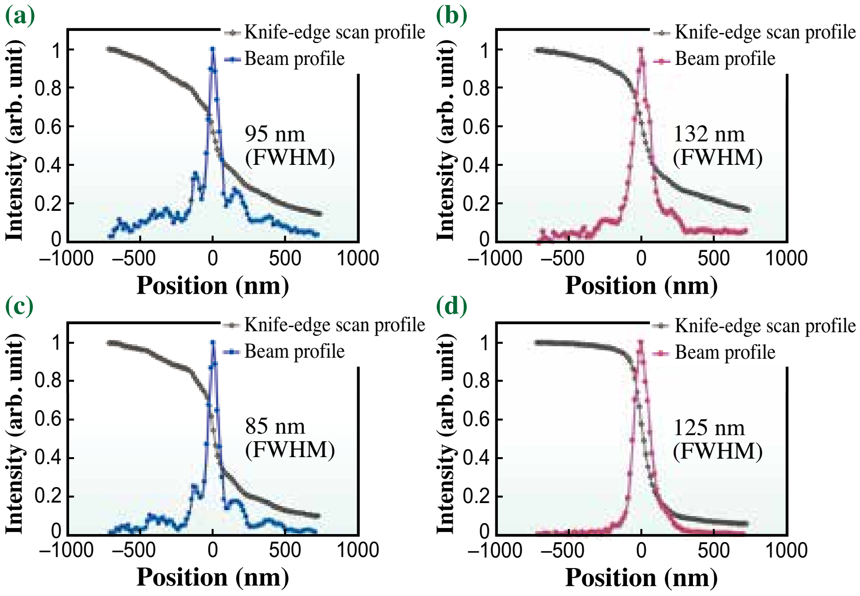

Fig. 2. Measured focused beam profiles. Two reflection areas on the mirror surface were evaluated: the entire area of 93 mm × 0.45 mm ((**a**) and (**b**)) and the central area of 50 mm × 0.45 mm ((**c**) and (**d**)). Beam profiles were measured in the meridional ((a) and (c)) and sagittal ((b) and (d)) focusing directions. [1]

Hirokatsu Yumoto

Japan Synchrotron Radiation Research Institute (JASRI)

Email: yumoto@spring8.or.jp

References

[1] *H. Yumoto, T. Koyama, S. Matsuyama, Y. Kohmura, K. Yamauchi, T. Ishikawa and H. Ohashi: Sci. Rep.* **7** *(2017) 16408.*
[2] H. Yumoto *et al.*: Proc. of SPIE **9206** (2014) 920605.
[3] H. Yumoto *et al.*: Rev. Sci. Instrum. **87** (2016) 051905.
[4] H. Yumoto *et al.*: AIP Conf. Proc. **1696** (2016) 020033.

High-resolution display-type retarding field analyzer

Photoelectron diffraction (PED) or photoelectron holography (PEH) is a powerful method for studying local atomic arrangements [1]. An advantage of these methods is the utilization of chemical shifts in core-level photoemission spectra. So far, however, such high-energy-resolution measurements have only been performable through time-consuming angular scans of samples using non-display-type analyzers. For more efficient measurements, high-energy-resolution display-type photoelectron analyzers are desired.

Display-type retarding field analyzers (RFAs) are one of the candidates for high-resolution PED or PEH. The simplest RFA optics is composed of three spherical grids, where a retarding voltage (RV) is supplied to the intermediate grid and the two exterior grids are grounded. Because the retarding grid is usually made of a wire mesh, a potential variation occurs across the space between the wires. This generates distortions of electron trajectories near the retarding grid from the normally incident trajectories, which are often called lens effects [2]. These effects usually limit the resolving powers ($E/\Delta E$) of three-grid RFAs to less than 100 [3]. In order to resolve chemical shifts, $E/\Delta E$ as high as or higher than 1000 is required.

In this work, we found a method for obtaining $E/\Delta E$ of 1000 or higher for three-grid spherical RFAs [4]. To find this method, we performed electron trajectory simulations where the trajectories in the vicinity of the retarding grid were calculated in detail. Because an RFA is a high-pass filter, the transmittance function of an RFA has a cutoff at the retarding potential energy. The electrons emitted from a sample with kinetic energy (E_K) values larger than the retarding potential energy can pass through the retarding grid, whereas the electrons with E_K values smaller than the retarding potential energy are repelled by the retarding grid. When using a conventional grid arrangement where the three spherical grids are deployed close together with the same distances, the RFA shows a very gradual transmittance cutoff because of the lens effects, which results in $E/\Delta E$ of about 100. We found that a much steeper cutoff can be obtained by deploying the three grids with very different distances as shown in Fig. 1(a). The lens effects still exist even in this devised arrangement, but they are optimized so as to sharpen the cutoff. The detailed reason for this is given in Ref. 4. $E/\Delta E$ of 3200 was theoretically expected when the mesh number was 250 and the grid radii were 12, 40, and 42 mm. [4].

We constructed an RFA employing the devised grid arrangement at the soft X-ray beamline **BL25SU** [5] as shown in Fig. 1(b). To evaluate $E/\Delta E$ of the RFA, we measured angle-integrated 4*f* core-level photoemission spectra of evaporated gold. A photon energy ($h\nu$) of 700 eV was used. The energy resolution (ΔE) of the beamline monochromator was set at 82 meV. First, we used a conventional RFA, where the grid radii were 32.5, 36.5, and 39.5 mm. The measured spectrum is shown in Fig. 2(a). Although the spin-orbit splitting of $4f_{5/2}$ and $4f_{7/2}$ is barely recognized, the spectral shape is very broad. Then, we used the RFA with the devised grid arrangement in which the grid radii were 12, 40, and 42 mm. The measured spectral widths in Fig. 2(b) are clearly narrower than those in Fig. 2(a), indicating an improved $E/\Delta E$. We compared the Au 4*f* spectrum in Fig. 2(b) with that measured using a concentric hemispherical analyzer with a known energy resolution and estimated $E/\Delta E$ of the RFA to be 1100 [4]. For PEH, photoelectron E_K values of more than 400 eV are required [1]. If the smallest available E_K of 400 eV is used, $E/\Delta E$ of 1100 results in ΔE of 0.36 eV, which allows one to resolve relatively large chemical shifts caused by, for example, different valencies.

To verify the ability to observe PED patterns, we performed PED measurements for single-crystal

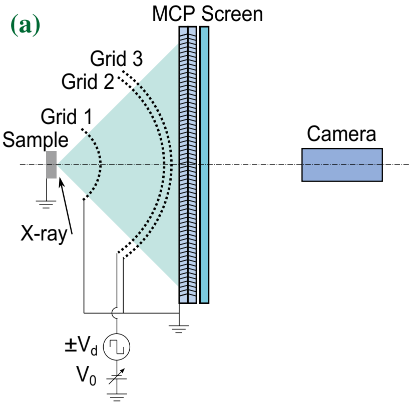

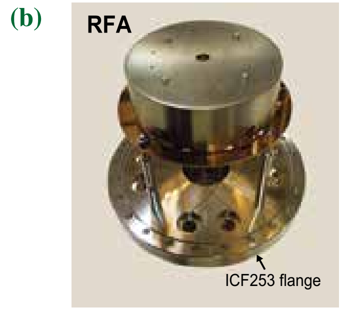

Fig. 1. **(a)** Schematic of the developed 3-grid RFA. **(b)** Photo of the developed 3-grid RFA.

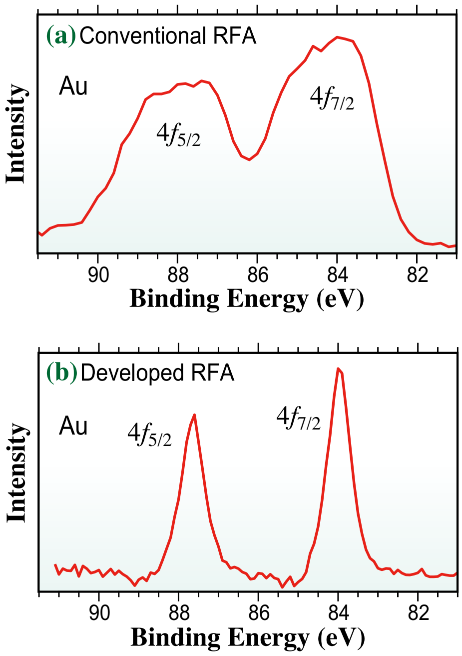

Fig. 2. Comparison of Au 4*f* photoemission spectra measured with **(a)** a conventional three-grid RFA and **(b)** the developed three-grid RFA. *hν* of 700 eV was used.

graphite. *hν* of 900 eV was used, at which C 1*s* photoelectrons had E_K values comparable to those of the Au 4*f* photoelectrons in Fig. 2. Figure 3(a) shows an angle-integrated photoemission spectrum measured in the C 1*s* region. In this figure, the horizontal axis represents the RV. Because $E/\Delta E$ of the RFA was 1100, the ΔE was approximately 0.55 eV in this E_K region. The ΔE of the beamline monochromator was set at 0.18 eV. Thus, the total ΔE was approximately 0.58 eV. Figure 3(b) shows a result of the PED measurements. A C 1*s* PED pattern with sharp Kikuchi lines was clearly observed. Since an RFA is a high-pass filter, to observe a PED pattern in a certain E_K bandwidth, it is necessary to take a difference image between two images corresponding to two different RVs. For the difference image acquisition, as shown in Fig. 1(a), we periodically switched the RV with a rectangular time profile between V_0+V_d and $V_0–V_d$, where V_0 is the static bias and $\pm V_d$ are voltages superimposed on V_0. The camera observing the screen was synchronized with the periodic RV switching. For the measurement in Fig. 3(b), V_0 was set at the C 1*s* peak and V_d was 0.5 V. The acceptance angle of the RFA was ±49°. The acquisition time of the raw difference image was 80 min. The developed RFA is now open to public use at SPring-8 BL25SU.

Although $E/\Delta E$ of 1100 for our RFA is higher than those of conventional RFAs by one order of magnitude, higher $E/\Delta E$ values are still desired for resolving small chemical shifts of a few hundred meV. Woven wire meshes inherently have inhomogeneities of grid openings, which affect $E/\Delta E$. One possibility is to fabricate a spherical grid by making a large number of radially directed holes through a partial spherical shell like a spherical cap with a sufficient thickness to maintain the spherical shape. We are now developing such a holed grid with a wide acceptance angle.

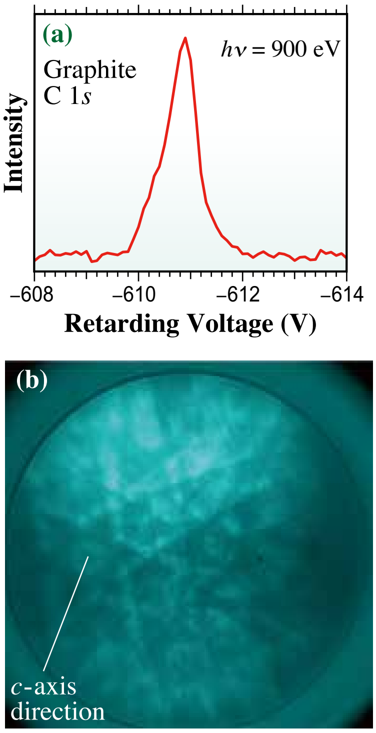

Fig. 3. **(a)** C 1*s* photoemission spectrum measured with the developed RFA for a single crystal of graphite. *hν* of 900 eV was used. The horizontal axis represents the RVs that is, V_0. **(b)** Image obtained by dividing the raw difference image by a background image. The acceptance angle is ±49°. For the difference image measurement, V_0 was set at the C 1*s* peak and V_d was 0.5 V. The *c*-axis direction is indicated in the figure.

Takayuki Muro* and Tomohiro Matsushita

Japan Synchrotron Radiation Research Institute (JASRI)

*Email: muro@spring8.or.jp

References

[1] T. Matsushita *et al*.: J. Electron Spectrosc. Relat. Phenom. **178-179** (2010) 195.
[2] Y. Sakai and I. Katsumata: Jpn. J. Appl. Phys. **24** (1985) 337.
[3] N.J. Taylor: Rev. Sci. Instrum. **40** (1969) 792.
[4] *T. Muro, T. Ohkochi, Y. Kato, Y. Izumi, S. Fukami, H. Fujiwara and T. Matsushita: Rev. Sci. Instrum.* ***88*** *(2017) 123106.*
[5] Y. Senba *et al*.: AIP Conf. Proc. **1741** (2016) 030044.

SACLA Beam Performance

Our facility has provided simultaneous operations of three FEL beamlines (BL1, BL2, and BL3) using pulse-by-pulse switching of the beam route and maintained stable and high-performance soft and hard XFELs for user experiments throughout the year [1-3]. The net user time in FY2018 across user shifts for these beamlines is expected to exceed 6000 hours, with high levels of laser performance and availability. In order to provide innovative experimental opportunities and to improve the experimental efficiency using XFELs with a narrow bandwidth, a self-seeded XFEL scheme with a reflective geometry was developed [4]. Test experiments using self-seeded XFELs began in autumn 2018 with a plan to release this optional mode to experimental users in early 2019. Figures 1 and 2 show schematic drawings of the reflection self-seeding scheme and the typical spectrum of the self-seeded XFEL, respectively.

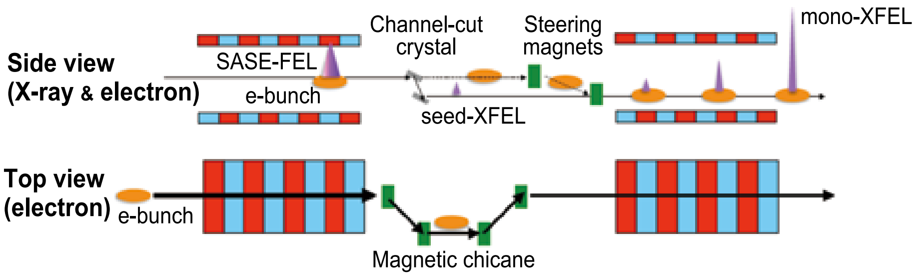

Fig. 1. Schematic drawings of the reflection self-seeding scheme.

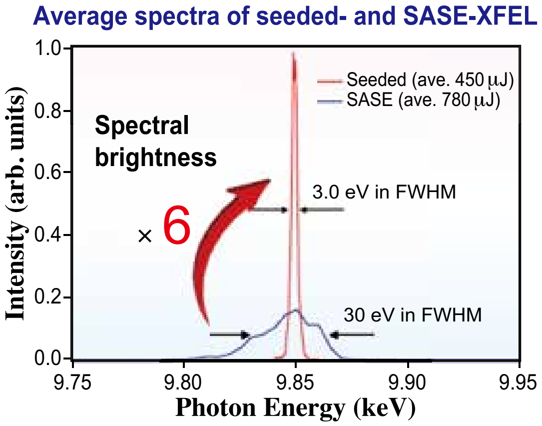

Fig. 2. Typical spectrum of the self-seeded XFEL. The red and blue lines show the averaged spectra of seeded and SASE XFELs, respectively.

Hitoshi Tanaka

RIKEN SPring-8 Center

Email: tanaka@spring8.or.jp

References

[1] T. Hara *et al.*: Proc. IPAC2018, Vancouver, Canada (2018) pp. 1740.
[2] T. Hara *et al.*: Phys. Rev. Accel. Beams **21** (2018) 040701.
[3] C. Kondo *et al.*: Rev. Sci. Instrum. **89** (2018) 064704.
[4] I. Inoue *et al.*: SRI 2018, Taipei, Taiwan (2018).

FACILITY STATUS

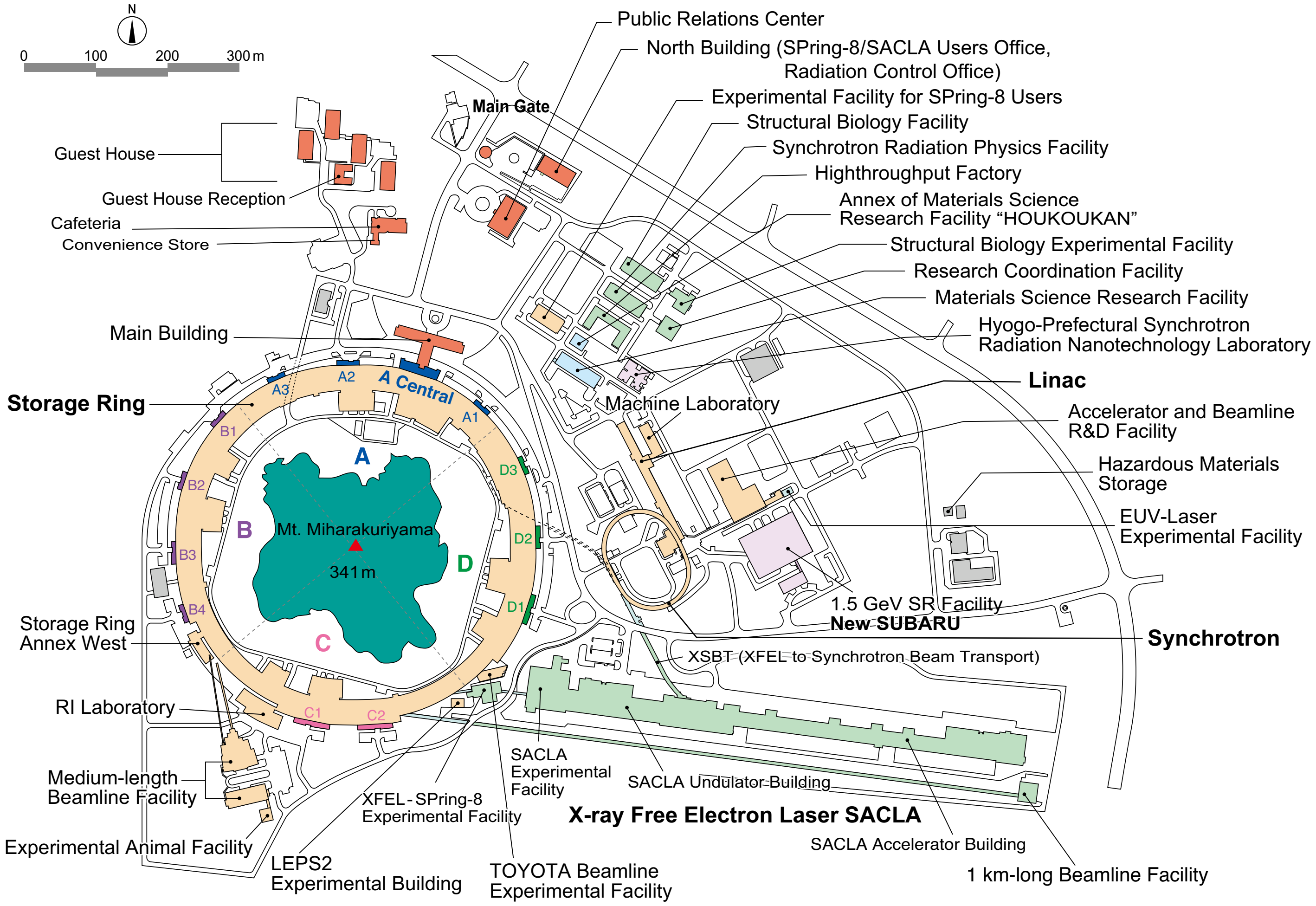

SPring-8

I. Introduction

SPring-8 was stably operated throughout FY2018 with the total operation time of the accelerator complex and the total user beam time of 5316.7 h and 4559.6 h, respectively, and a total downtime of 43.1 h. SPring-8 completed all its operations by the middle of February 2019.

Regarding its research proposal system, SPring-8 designated Industrial Application Using Advanced Technology as a field of the priority research program on 19 September 2018. Concerning the contract beamlines, there were five interim reviews conducted for JAEA Actinide Science (BL22XU), JAEA Actinide Science II (BL23SU), QST Quantum Dynamics I (BL11XU), QST Quantum Dynamics II (BL14B1), and Catalytic Reaction Dynamics for Fuel Cells (BL36XU, The University of Electro-Communications), and all projects were authorized to continue.

At present, the number of SPring-8 users is as many as 15,000, all of whom are members of the SPring-8 User Community (SPRUC). It is important for SPring-8 to jointly organize scientific events with SPRUC, such as the SPring-8 Symposium, to facilitate dialogue between users and the facility staff. In 2018, the SPring-8 Symposium was held at Himeji City Civic Center on August 25–26, with 345 participants. SPring-8 also promotes communication between users and industry. The Joint Conference on Industrial Applications of SPring-8 was held in Kobe on September 6–7, 2018, with 240 participants. As part of its continuous effort towards fostering of human resources in synchrotron sciences, SPring-8 organized the 18th SPring-8 Summer School with 60 students of graduate schools nationwide, in cooperation with Hyogo University, Kwansei Gakuin University, The University of Tokyo, Okayama University, Osaka University, Japan Atomic Energy Agency, National Institutes for Quantum and Radiological Science and Technology, and RIKEN. Furthermore, SPring-8 and SPRUC organized the 2nd SPring-8 Autumn School with 45 participants, which included 3rd year university students and researchers from companies.

II. Machine Operation

The operation statistics for the last five fiscal years are shown in Fig. 1. In FY2018, the total operation time of the accelerator complex was 5329.8 h. The operation time of the storage ring was 5316.7 h, 85.8% of which (4559.6 h) was for SR experiments. This excellent figure for the user time represents a storage ring availability of 98.9%. The downtime resulting from failure accounted for 43.1 h (0.95% of the total user time), which was 50% greater than the figure for last year owing to problems with the magnet system. The intensity of the light source, i.e., the stored current, was kept extremely stable within 0.1% owing to the top-up operation, in which the current is filled up at any time on demand. For 99.9% of the user time in FY2018, the stored current was kept at 100 mA by the top-up operation.

The variety of operation modes for SR experiments is one of the characteristics of SPring-8. The operation modes are grouped into several-bunch and hybrid filling modes. The several-bunch mode consists of equally spaced bunches or bunch trains, i.e., 203 bunches, or 29 trains of 11 bunches, and the hybrid filling mode is composed of a long bunch train and isolated single bunches as shown in Table 1, where the share of each operation mode is also shown. The isolated bunch impurity is routinely maintained better than 10^{-8} in the top-up operation by bunch cleaning in the booster. The bunch current is also kept constant within 1% by the top-up operation. Table 2 summarizes the beam parameters of the storage ring.

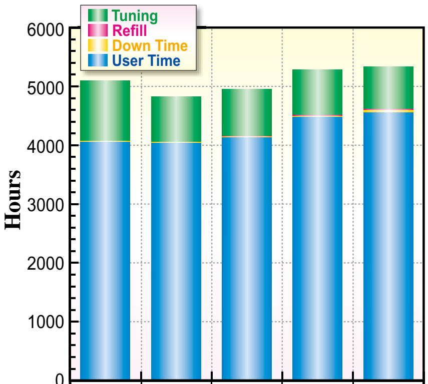

	FY2014	FY2015	FY2016	FY2017	FY2018
Accelerator Operation Time	5099.3	4817.9	4951.7	5281.6	5329.8
Storage Ring Operation Time	5080.7	4804.8	4941.1	5270.4	5316.7
Tuning & Study (Acc. & BL)	1019.3	767.2	803.1	769.6	721.8
Refill	5.1	5.3	3.4	4.6	5.3
Down Time	17.1	16.8	23.1	28.7	43.1
Mean Time Between Failures	163.2	202.8	229.2	194.7	168.9
Achieved User Time	4057.8	4033.9	4125.5	4478.7	4559.6
Planning User Time	4080.0	4056.0	4152.0	4512.0	4608.0
Availability (%)	99.5	99.5	99.4	99.3	98.9

Fig. 1. Operation statistics for last five fiscal years.

Table 1. Operation modes in FY2018

	Single bunch current (mA)	Share of operation time (%)
203 bunches		29.2
4 bunch-train × 84		3.7
11 bunch-train × 29		22.9
1/7-filling + 5 single bunches	3	6.8
2/29-filling + 26 single bunches	1.4	3.1
1/14-filling + 12 single bunches	1.6	13.5
11/29-filling + 1 single bunch	5	20.8

Table 2. Beam parameters of SPring-8 storage ring

Energy [GeV]	8
Number of buckets	2436
Tunes (ν_x / ν_y) 41.14 / 19.34	
Current [mA]:	
single bunch	12
multi bunch	100
Bunch length (σ) [psec]	13
Horizontal emittance [nm·rad]	2.4 *
Vertical emittance [pm·rad]	4.8 *
Coupling [%]	0.2
RF Voltage [MV]	14.4 ** ~ 16
Momentum acceptance [%]	3.2 (~256 MeV)
Beam size (σ_x / σ_y)* [μm]	
Long ID section	333 / 7
ID section	316 / 5
BM1 section	94 / 12
BM2 section	100 / 12
Beam divergence (σ_x' / σ_y')* [μrad]	
Long ID section	8 / 0.7
ID section	9 / 1.0
BM1 section	58 / 0.5
BM2 section	68 / 0.5
Operational chromaticities (ξ_x / ξ_y)	+2 / +2 ***
Lifetime [hr]:	
100 mA (multi bunch)	~ 250
1 mA (single bunch)	~ 30
Horizontal dispersion [m]:	
Long ID section	0.153
ID section	0.146
BM1 section	0.039
BM2 section	0.059
Fast orbit stability (0.1 – 200 Hz) [μm]	
horizontal (rms)	~ 4
vertical (rms)	~ 1

* Assuming 0.2% coupling
** Power saving mode
*** With bunch-by-bunch feedback

III. Beamlines

The SPring-8 storage ring can accommodate up to 62 beamlines: 34 insertion devices, 4 long undulators, and 24 bending magnets. At present, 57 beamlines are in operation, covering a wide variety of research fields involving synchrotron radiation science and technology. The beamlines are classified into the following three types:

(1) Public Beamlines (26 beamlines operating),
(2) Contract Beamlines (19 beamlines operating), and
(3) RIKEN Beamlines (12 beamlines operating).

There are now 26 public beamlines in full operation. The beamlines that are proposed and constructed by external organizations, such as universities, research institutes, private companies, and consortiums, are called contract beamlines and are exclusively used by contractors for their own research purposes. At present, 19 contract beamlines are in operation. The beamlines constructed by RIKEN that are not public beamlines are called RIKEN beamlines, and are mainly used for RIKEN's own research activities, with partial availability for public use. RIKEN is now operating 12 beamlines.

From 2019A, BL45XU is newly available as a public beamline and added to Macromolecular Crystallography Beamlines (PX-BLs), while BL38B1 becomes RIKEN Beamline and no longer available as a PX-BL.

To illustrate the beamline portfolio of SPring-8, a beamline map is shown in Fig. 2 together with the beamline classification. The research fields of each beamline are presented in Table 3.

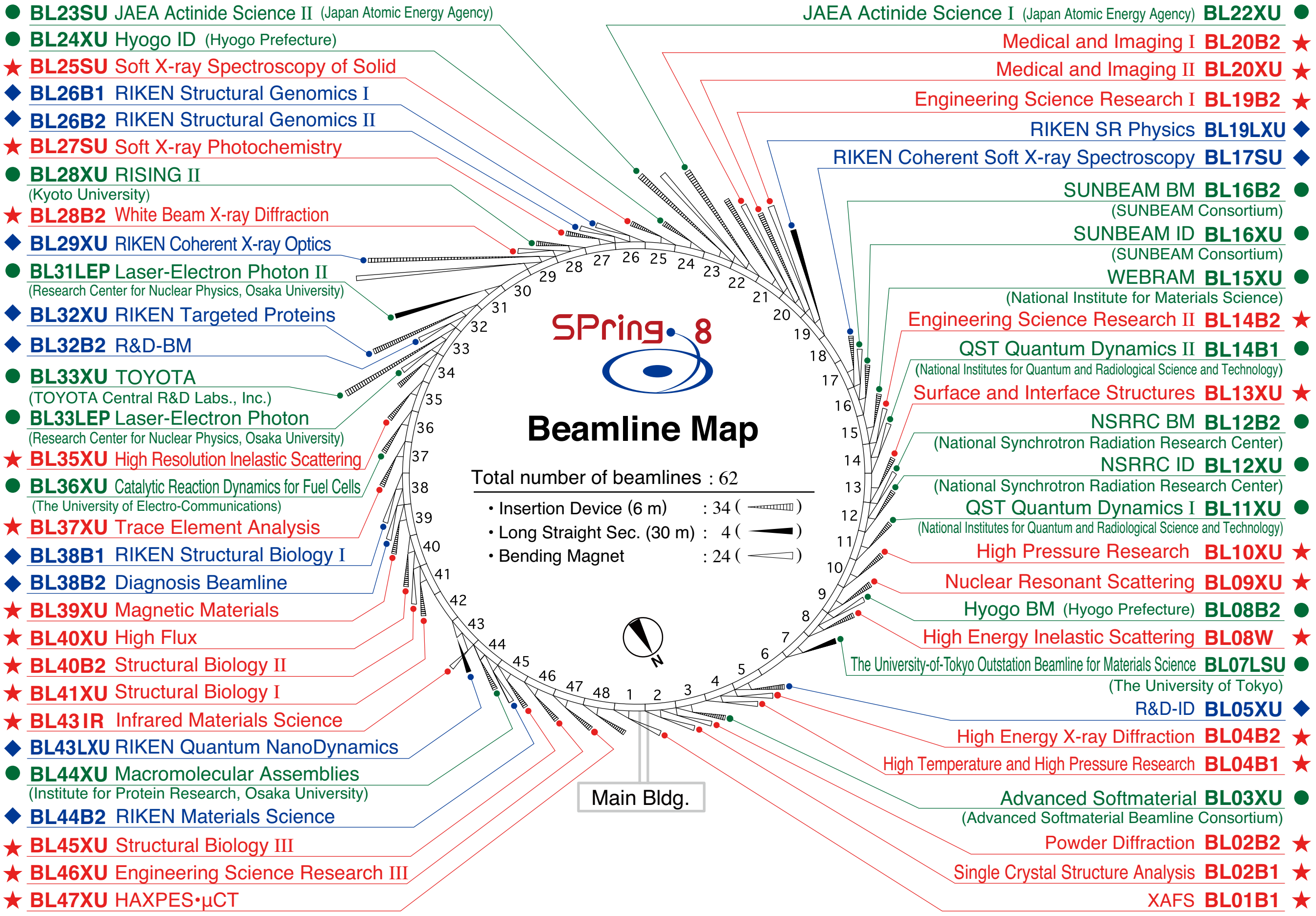

BL: Beamline
B1, B2: Bending Magnets
XU: X-ray Undulator
SU: Soft X-ray Undulator
W: Wiggler
IR: Infrared Radiation
LEP: Laser-Electron Photon
LXU: Long-length X-ray Undulator
LSU: Long-length Soft X-ray Undulator

★ : Public Beamlines
● : Contract Beamlines
◆ : RIKEN Beamlines

WEBRAM: Wide Energy Range Beamline for Research in Advanced Materials
NSRRC: National Synchrotron Radiation Research Center, Taiwan
RISING: Research & Development Initiative for Scientific Innovation of New Generation Batteries

Fig. 2. Beamline map.

Table 3. List of beamlines

BL #	Beamline Name	(Public Use) or (First Beam)	Areas of Research and Available Techniques
			★ Public Beamlines
BL01B1	**XAFS**	(Oct. 1997)	XAFS in wide energy region (3.8 to 113 keV). XAFS of dilute systems and thin films. Quick XAFS with a time resolution of seconds to tens of seconds.
BL02B1	**Single Crystal Structure Analysis**	(Oct. 1997)	Charge density study and crystal structure analysis from single crystal X-ray diffraction. (X-ray energy range: 8 – 115 keV)
BL02B2	**Powder Diffraction**	(Sept. 1999)	Charge density study and phase identification of crystalline materials from accurate powder diffraction measurements. (X-ray energy range: 12.4 – 35 keV)
BL04B1	**High Temperature and High Pressure Research**	(Oct. 1997)	High temperature and high pressure research with the multi-anvil press by powder X-ray diffraction, radiography and ultrasonic measurement.
BL04B2	**High Energy X-ray Diffraction**	(Sept. 1999)	Pair distribution function analysis for glass, liquid, and amorphous materials. High-energy X-ray total scattering. Containerless levitation.
BL08W	**High Energy Inelastic Scattering**	(Oct. 1997)	Magnetic Compton scattering. High-resolution Compton scattering. High-energy Bragg scattering. High-energy fluorescent X-ray analysis.
BL09XU	**Nuclear Resonant Scattering**	(Oct. 1997)	Lattice dynamics using nuclear inelastic scattering. Mössbauer spectroscopy, especially for the surface/interface study and under the extreme conditions. Hard X-ray photoelectron spectroscopy (HAXPES). Depth analysis of HAXPES with high flux and energy resolution.
BL10XU	**High Pressure Research**	(Oct. 1997)	Structure analysis and phase transitions under ultra high pressure (DAC experiment). Earth and planetary science.
BL13XU	**Surface and Interface Structures**	(Sept. 2001)	Atomic-scale structural analysis of surfaces and interfaces of crystalline materials, ultra-thin films, and nanostructures. Surface X-ray diffraction (SXRD). Microbeam diffraction.
BL14B2	**Engineering Science Research II**	(Sept. 2007)	X-ray Imaging. XAFS in wide energy region (3.8 to 72 keV). XAFS of dilute systems and thin films.
BL19B2	**Engineering Science Research I**	(Nov. 2001)	Residual stress measurement. Structural analysis of thin film, surface, interface. Powder diffraction. X-ray topography. Ultra-small angle X-ray scattering.
BL20XU	**Medical and Imaging II**	(Sept. 2001)	Microimaging. Micro-/nano-tomography, phase-contrast microtomography, X-ray diffraction tomography (XRD-CT), hard X-ray microbeam/scanning microscopy, imaging microscopy, coherent X-ray optics, and other experiments on X-ray optics and developments of optical elements. Refraction-enhanced imaging. Ultra-small angle scattering.
BL20B2	**Medical and Imaging I**	(Sept. 1999)	Microimaging: microtomography, phase-contrast microtomography with grating interferometer for biological specimen and other kinds of specimen. Evaluation and development of various kinds of optical elements for novel imaging techniques. Large field X-ray topography.
BL25SU	**Soft X-ray Spectroscopy of Solid**	(Apr. 1998)	Study of electronic state of solids by soft X-ray photoemission spectroscopy (PES) including angle-resolved PES (ARPES). Atomic arrangement analysis of surfaces by photoelectron diffraction (PED) technique using two-dimensional photoemission analyzer. Magnetic state analysis by magnetic circular dichroism (MCD) of soft X-ray absorption and its element-specific magnetization curve measurements.
BL27SU	**Soft X-ray Photochemistry**	(May 1998)	Ambient atmospheric pressure soft X-ray photoabsorption spectroscopy. Chemical state analysis of light elements in dilute samples (NEXAFS). Elemental and chemical mapping using micro soft X-ray beam. Soft-X-ray emission spectroscopy.
BL28B2	**White Beam X-ray Diffraction**	(Sept. 1999)	White X-ray diffraction and topography. Time-resolved energy-dispersive XAFS (DXAFS) for studies of chemical and/or physical reaction process. Biomedical imaging and radiation biology studies. High energy X-ray microtomography.
BL35XU	**High Resolution Inelastic Scattering**	(Sept. 2001)	Materials dynamics on ~meV energy scales using inelastic X-ray scattering (IXS).
BL37XU	**Trace Element Analysis**	(Nov. 2002)	X-ray microbeam spectrochemical analysis. Ultra trace element analysis. High energy X-ray fluorescence analysis.
BL39XU	**Magnetic Materials**	(Oct. 1997)	X-ray magnetic circular dichroism (XMCD) spectroscopy and element-specific magnetometry under multiple-extreme conditions. XMCD/XAS using a 100 nm focused X-ray beam. X-ray emission spectroscopy.
BL40XU	**High Flux**	(Apr. 2000)	Time-resolved diffraction and scattering experiments. Microbeam X-ray diffraction and scattering experiments. X-ray photon correlation spectroscopy. Fluorescence analysis. Quick XAFS. Submicrometer-scale single crystal structure analysis with high flux and zone plate focused X-ray beam. Single shot imaging with X-ray choppers. Laser pump-X-ray probe experiment.
BL40B2	**Structural Biology II**	(Sept. 1999)	Noncrystalline small and wide angle X-ray scattering.
BL41XU	**Structural Biology I**	(Oct. 1997)	Structural biology. Macromolecular crystallography. Microcrystallography. High resolution data collection.
BL43IR	**Infrared Materials Science**	(Apr. 2000)	Infrared microspectroscopy.
BL45XU	**Structural Biology III**	(Apr. 2019)	Structural biology. Macromolecular crystallography. Automation & High throughput data collection. Microcrystallography.
BL46XU	**Engineering Science Research III**	(Nov. 2000)	Structural characterization of thin films by X-ray diffraction and X-ray reflectivity measurement. Residual stress measurement. Time resolved X-ray diffraction measurement. Hard X-ray Photoemission Spectroscopy. X-ray Imaging.
BL47XU	**HAXPES・μCT**	(Oct. 1997)	Hard X-ray photoelectron spectroscopy (HAXPES). Depth analysis of angle resolved HAXPES with wide acceptance lens. Projection type microtomography. Imaging type microtomography. Hard X-ray microbeam/scanning microscopy.

BL #	Beamline Name	(Public Use) or (First Beam)	Areas of Research and Available Techniques
			● Contract Beamlines
BL03XU	**Advanced Softmaterial** (Advanced Softmaterial Beamline Consortium)	(Nov. 2009)	Structural characterization of softmaterials using small- and wide-angle X-ray scattering. Grazing-incidence small- and wide-angle X-ray scattering for thin films. X-ray diffraction and reflectivity measurements for softmaterials.
BL07LSU	**The University-of-Tokyo Outstation Beamline for Materials Science** (The University of Tokyo)	(Oct. 2009)	Time-resolved soft X-ray spectroscopy, nano-beam photoemission spectroscopy, ultra high-resolution soft X-ray emission spectroscopy, and any methods requiring the highly brilliant soft X-ray beam.
BL08B2	**Hyogo BM** (Hyogo Prefecture)	(Jun. 2005)	XAFS in a wide energy region. Small angle X-ray scattering. X-ray topography. Imaging. X-ray diffraction for multipurpose.
BL11XU	**QST Quantum Dynamics I** (National Institutes for Quantum & Radiological Science & Technology)	(Oct. 1998)	Synchrotron radiation Mössbauer spectroscopy. XAFS. Resonant inelastic X-ray scattering spectroscopy. *In situ* X-ray diffraction during molecular-beam epitaxial growth.
BL12B2	**NSRRC BM** (National Synchrotron Rad. Res. Center)	(Oct. 2000)	X-ray absorption spectroscopy. Powder X-ray diffraction. High resolution X-ray scattering. Protein crystallography.
BL12XU	**NSRRC ID** (National Synchrotron Rad. Res. Center)	(Dec. 2001)	Non-resonant or resonant inelastic X-ray scattering. Hard X-ray photoemission spectroscopy.
BL14B1	**QST Quantum Dynamics II** (National Institutes for Quantum & Radiological Science & Technology)	(Dec. 1997)	Materials science under high-temperature and high-pressure, Energy-dispersive XAFS. X-ray diffraction for surface structure analyses.
BL15XU	**WEBRAM** (National Institute for Materials Science)	(Jan. 2000)	Hard X-ray photoelectron spectroscopy. High-precision X-ray powder diffraction. Structural analysis of thin film, surface and interface.
BL16B2	**SUNBEAM BM** (SUNBEAM Consortium)	(Oct. 1998)	Characterization of secondary battery related materials, semiconductors, fuel cells, catalysts, and several industrial materials with using X-ray absorption fine structure measurements, X-ray diffraction (including X-ray reflectivity technique), X-ray topography and computed tomography/laminography.
BL16XU	**SUNBEAM ID** (SUNBEAM Consortium)	(Oct. 1998)	Characterization of secondary battery related materials, semiconductors, fuel cells, catalysts, and structural materials using X-ray diffraction, X-ray microbeam based evaluation techniques (including X-ray magnetic circular dichroism), hard X-ray photoelectron spectroscopy and fluorescence X-ray analysis.
BL22XU	**JAEA Actinide Science I** (Japan Atomic Energy Agency)	(May 2002)	HAXPES. XAFS. Residual stress/strain distribution analysis. Materials science under high-pressure. Resonant X-ray scattering. Speckle scattering.
BL23SU	**JAEA Actinide Science II** (Japan Atomic Energy Agency)	(Feb. 1998)	Surface chemistry with supersonic molecular beam. Biophysical spectroscopy. Photoelectron spectroscopy. Magnetic circular dichroism.
BL24XU	**Hyogo ID** (Hyogo Prefecture)	(May. 1998)	Microbeam small- and wide-angle X-ray scattering for local structure analysis. Scanning and imaging microscope, micro-tomography, coherent diffraction. Microbeam X-ray diffraction and bright field X-ray topography for electronic device materials. Near-ambient pressure hard X-ray photoelectron spectroscopy.
BL28XU	**RISING II** (Kyoto University)	(Apr. 2012)	Characterization of rechargeable battery reactions and battery related materials by resonance X-ray diffraction, X-ray absorption spectroscopy (XAS), X-ray diffraction spectroscopy (XDS), and hard X-ray photoemission spectroscopy (HAXPES).
BL31LEP	**Laser-Electron Photon II** (RCNP, Osaka University)	(Oct. 2013)	Production of high intensity GeV photon beam by laser-backward Compton scattering. Hadron physics via photonucleon and photonuclear reactions. Test and calibration of detectors with GeV gamma-ray and converted electrons/positrons.
BL33LEP	**Laser-Electron Photon** (RCNP, Osaka University)	(Jun. 1999)	Meson photoproduction from nucleon and nucleus. Photoexcitation of hyperons, nucleon resonances, and other exotic states. Photonuclear reactions. Beam diagnoses. Test and calibration of detectors with GeV photon beam.
BL33XU	**TOYOTA** (TOYOTA Central R&D Labs., Inc.)	(Apr. 2009)	Time-resolved XAFS. Characterization of industrial materials, such as catalysts, secondary batteries, fuel cells.
BL36XU	**Catalytic Reaction Dynamics for Fuel Cells** (The University of Electro-Communications)	(Jan.2013)	Real time analysis of catalytic reaction dynamics for fuel cells: time resolved XAFS and X-ray diffraction, 2D scanning microscopic XAFS, 3D computed tomography/laminography XAFS, ambient pressure hard X-ray photoelectron spectroscopy.
BL44XU	**Macromolecular Assemblies** (IPR, Osaka University)	(May 1999)	Crystal structure analysis of biological macromolecular assemblies (e.g., membrane protein complexes, protein complexes, protein-nucleic acid complexes, and viruses).
			◆ RIKEN Beamlines
BL05XU	**R&D-ID**	(Mar. 2004)	Structural and dynamical research using small and wide angle scattering, R&D of SR instruments.
BL17SU	**RIKEN Coherent Soft X-ray Spectroscopy**	(Sept. 2003)	High resolution photoemission spectroscopy. Soft X-ray emission spectroscopy. Soft X-ray diffraction spectroscopy. Soft X-ray microspectroscopy.
BL19LXU	**RIKEN SR Physics**	(Oct. 2000)	SR science with highly brilliant X-ray beam.
BL26B1	**RIKEN Structural Genomics I**	(Apr. 2002)	Structural biology research based on single crystal X-ray diffraction.
BL26B2	**RIKEN Structural Genomics II**	(Apr. 2002)	Structural biology research based on single crystal X-ray diffraction.
BL29XU	**RIKEN Coherent X-ray Optics**	(Dec. 1998)	X-ray optics, especially coherent X-ray optics.
BL32XU	**RIKEN Targeted Proteins**	(Oct. 2009)	Protein microcrystallography.
BL32B2	**R&D-BM**	(May 2002)	X-ray diffraction, X-ray absorption fine structure, R&D of SR instruments.
BL38B1	**RIKEN Structural Biology I**	(Oct. 2000)	Time-resolved and static structures of non-crystalline biological materials using small-angle scattering and diffraction techniques.
BL38B2	**Diagnosis Beamline**	(Sept. 1999)	Accelerator beam diagnostics.
BL43LXU	**RIKEN Quantum NanoDynamics**	(Oct. 2011)	High resolution inelastic X-ray scattering for investigating atomic and electronic dynamics.
BL44B2	**RIKEN Materials Science**	(Feb. 1998)	Structural materials science research using powder X-ray diffraction.

IV. User Program and Statistics

SPring-8 calls for public use proposals twice a year, in principle. The submitted proposals are reviewed by the SPring-8 Proposal Review Committee (SPring-8 PRC). Since 1997, SPring-8 has accepted a variety of proposals. For the promotion of research on industrial applications at SPring-8, the Industrial Application Division was established in 2005. With consultation support for industrial users provided by the division's coordinators, Industrial Application Proposals currently account for approximately 16%-20% of the total number of proposals conducted at the public beamlines. In addition, the Measurement Services were introduced in 2007B, wherein personnel of the Industrial Application Division carry out XAFS measurements on behalf of users at BL14B2. SPring-8 also launched a Protein Crystallography Data Collection Service at BL38B1 and a Powder X-ray Diffraction Measurement Service at BL19B2 in 2009B, a Hard X-ray Photoemission Spectroscopy (HAXPES) Measurement Service and a Thin Film Analysis (GIXD/XRR) Measurement Service at BL46XU in 2012B, and a Small Angle Scattering (SAXS) Measurement Service at BL19B2 in 2014B.

In FY2018, JASRI started to call for Cross-SR Facility Use Proposals for Industrial Application. These are intended to produce outstanding results through the research results from other domestic synchrotron radiation facilities.

SPring-8 has consistently provided ~4,500 h of user beamtime per year. Since the start of its operation in 1997, SPring-8 has succeeded in providing users with a total beamtime of 83,961 h. The beamtime available to users, the number of experiments conducted, and the number of user visits at the public and contract beamlines are summarized in Fig. 3. Some of the proposals are for proprietary use, for which refereed reports are not required. Figures 4 to 13 show the information on user programs.

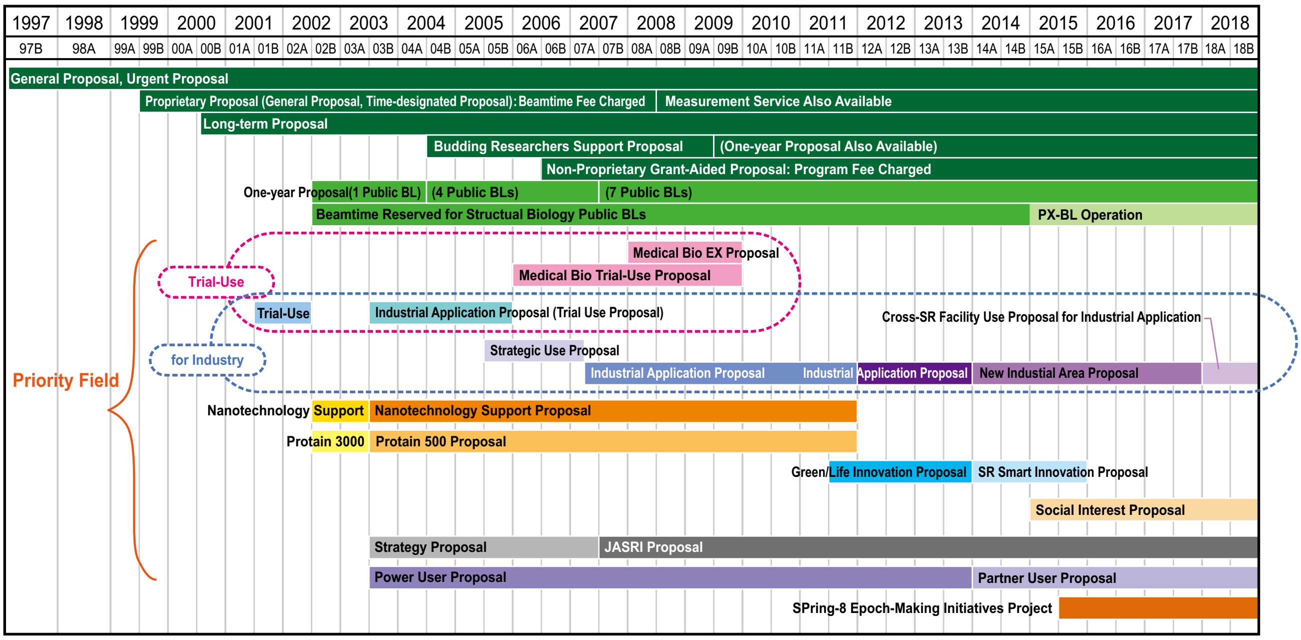

Fig. 3. Categories of proposals for the public beamlines.

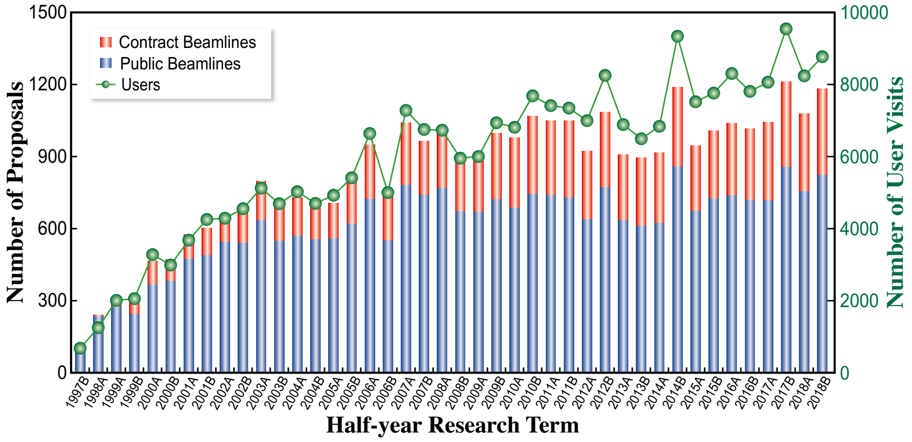

Fig. 4. Numbers of conducted experiments.

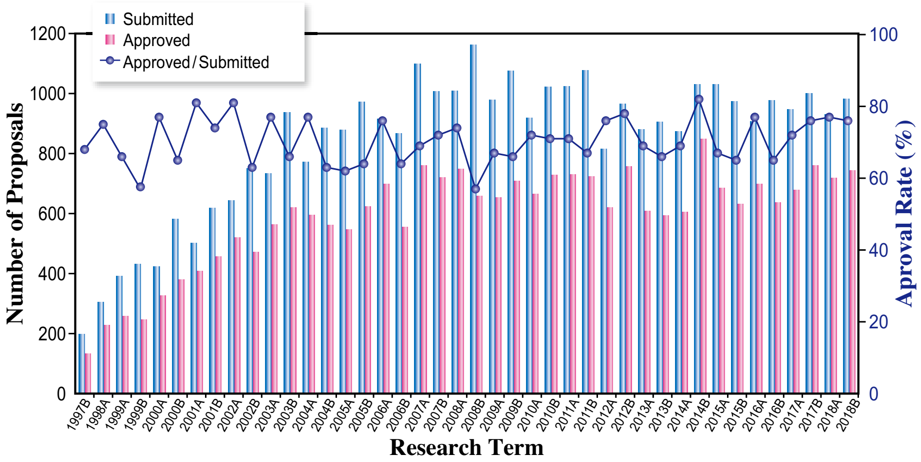

Fig. 5. Numbers of submitted proposals and approved proposals by research term (public beamlines).

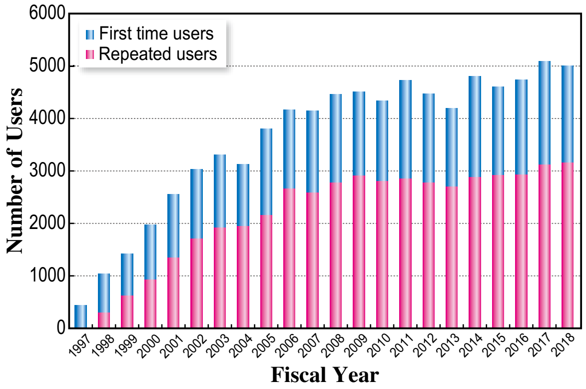

Fig. 6. Numbers of users by fical year.

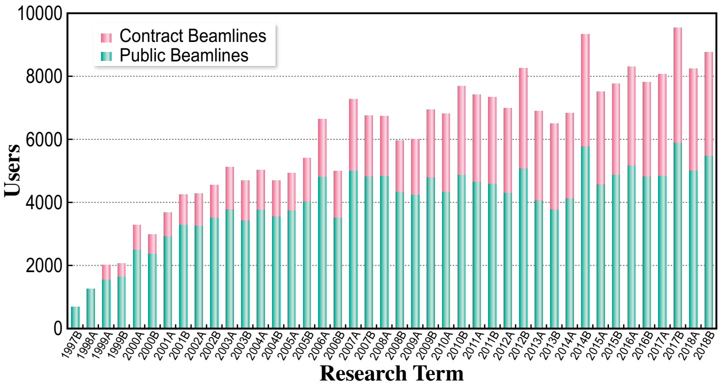

Fig. 7. Numbers of users visits by research term.

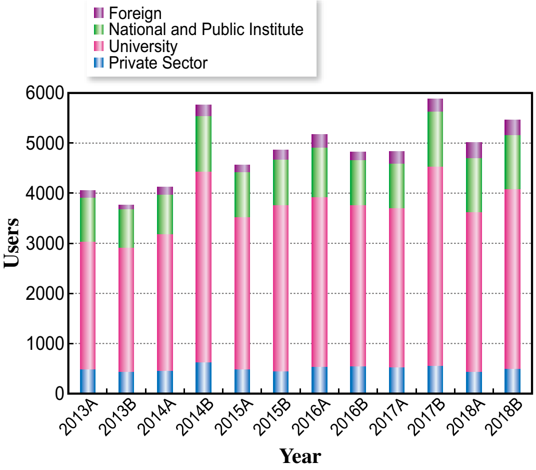

Fig. 8. Numbers of users by affiliation categories (public beamlines).

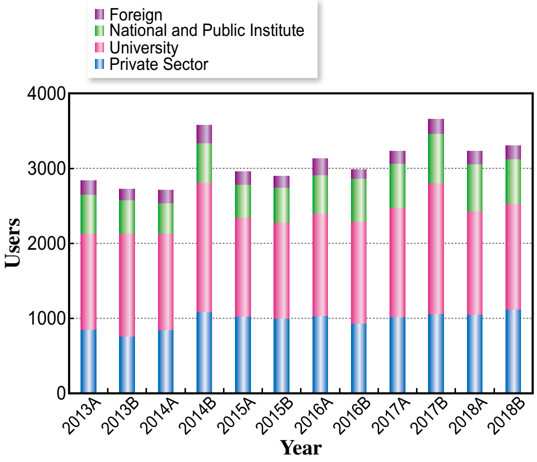

Fig. 9. Numbers of users by affiliation categories (contract beamlines).

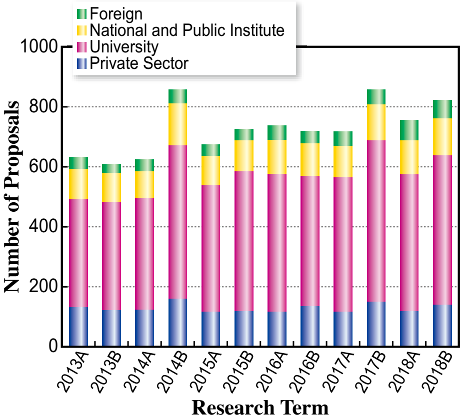

Fig. 10. Numbers of conducted proposals by affiliation (public beamlines).

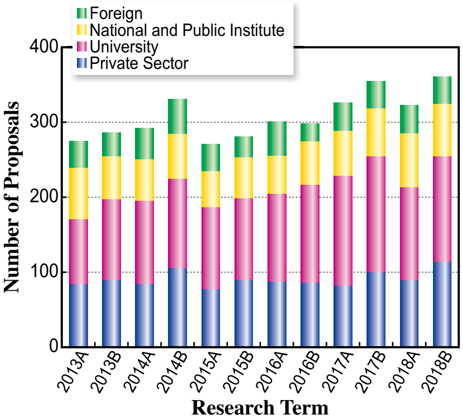

Fig. 11. Numbers of conducted proposals by affiliation categories (contract beamlines).

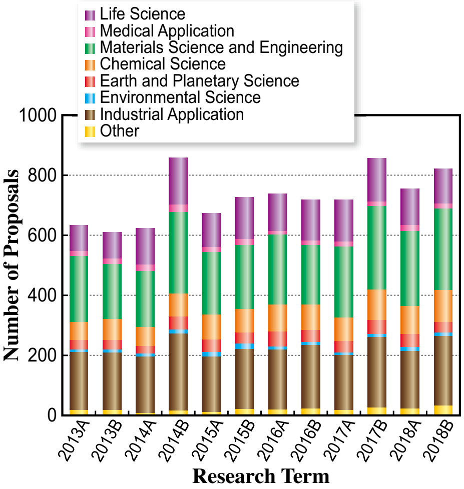

Fig. 12. Numbers of conducted proposals by research area (public beamlines).

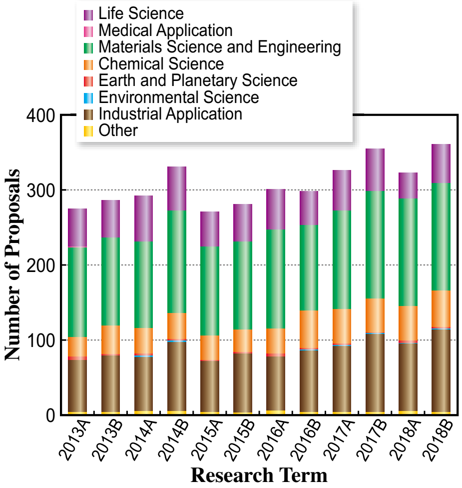

Fig. 13. Numbers of conducted proposals by research area (contract beamlines).

V. Research Outcome

As of March 2019, the total number of registered refereed papers from SPring-8 was 14,874. Figure 14 shows the annual statistics of refereed papers.

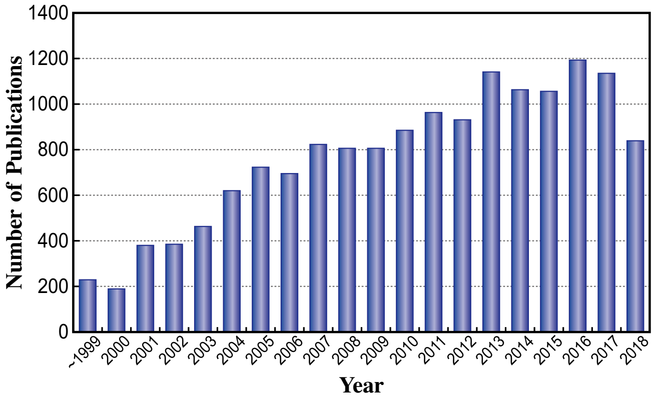

Fig. 14. Number of refereed publications.

VI. Budget and Personnel

When SPring-8 started operation in 1997, it was jointly managed by RIKEN, JAERI (now JAEA), and JASRI. However, JAERI withdrew from the management of SPring-8 on September 30, 2005. SPring-8 is currently administered by RIKEN and JASRI collaboratively.

The total budget for the operation of SPring-8 in FY2018 was about 9.5 billion yen. As of October 2018, RIKEN and JASRI have a total of 427 staff members. Figure 15 shows the annual budget allocated to operations, maintenance, and promotion of SPring-8. Figure 16 shows the manpower of RIKEN and JASRI.

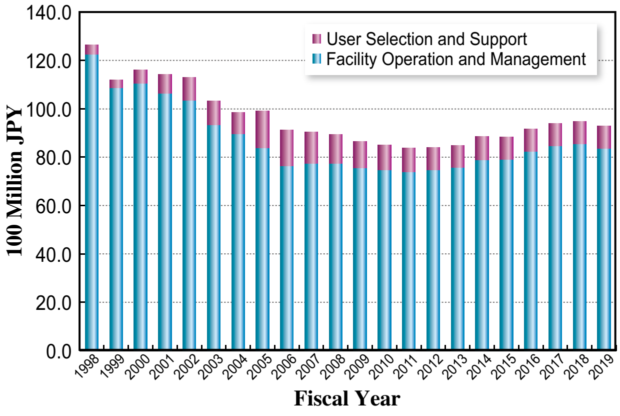

Fig. 15. SPring-8 budget.

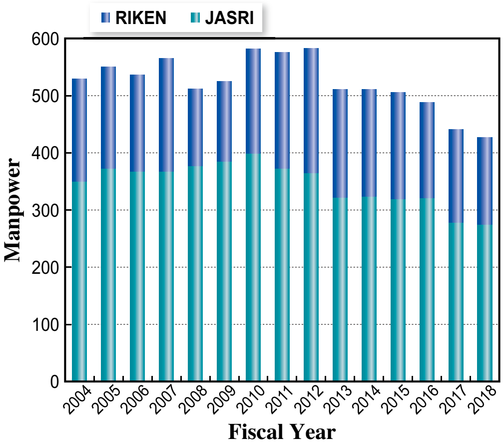

Fig. 16. Personnel at SPring-8: JASRI and RIKEN.

VII. Research Complex

The facilities of SPring-8, SACLA, and NewSUBARU form the Center of Excellence (COE) at the SPring-8 campus where JASRI, public beamline users, the contractors of contract beamlines, RIKEN, and the University of Hyogo work in close cooperation, forming a research complex where each member has their own role in delivering high-quality results to the field of synchrotron radiation science and technology. The organizational charts of RIKEN and JASRI, which are at the center of this research complex, are shown in Fig. 17 and Fig. 18, respectively.

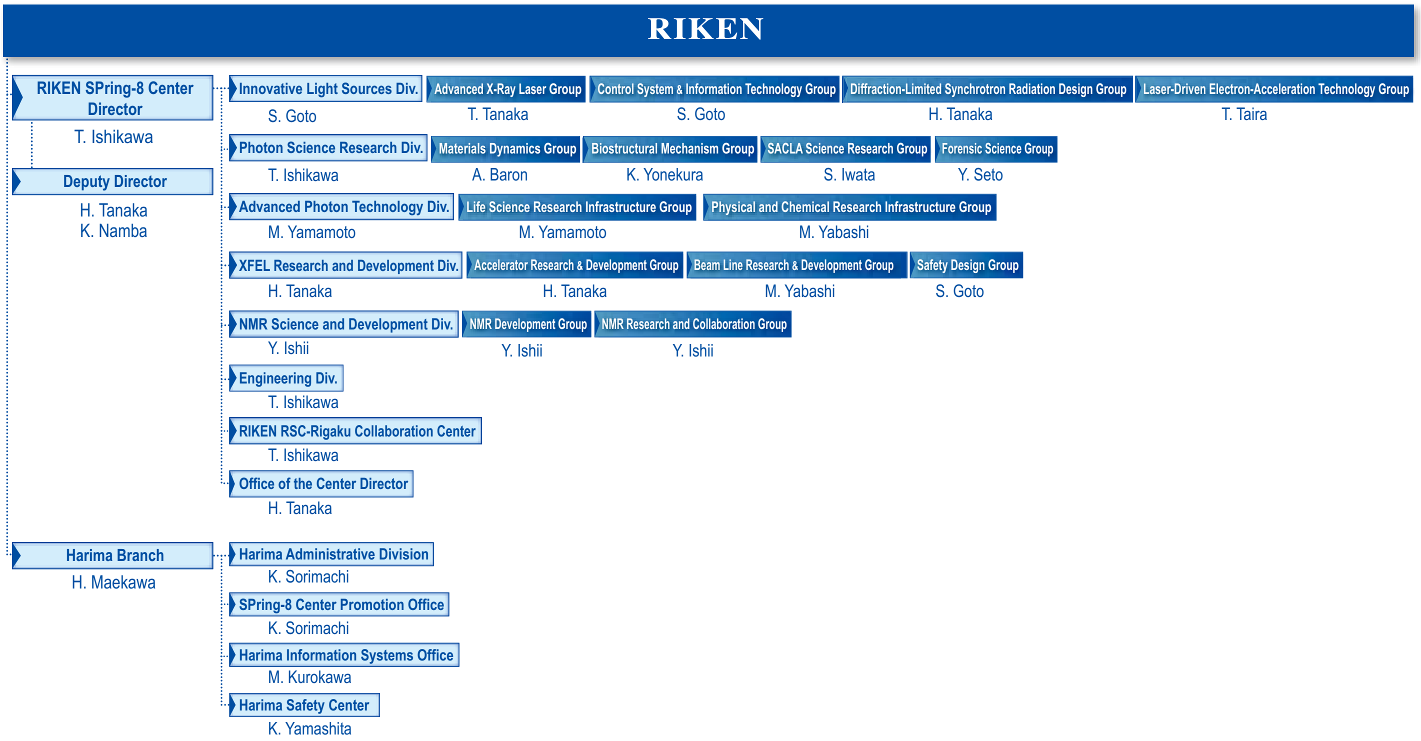

Fig. 17. RIKEN Harima Branch chart as of July 2019.

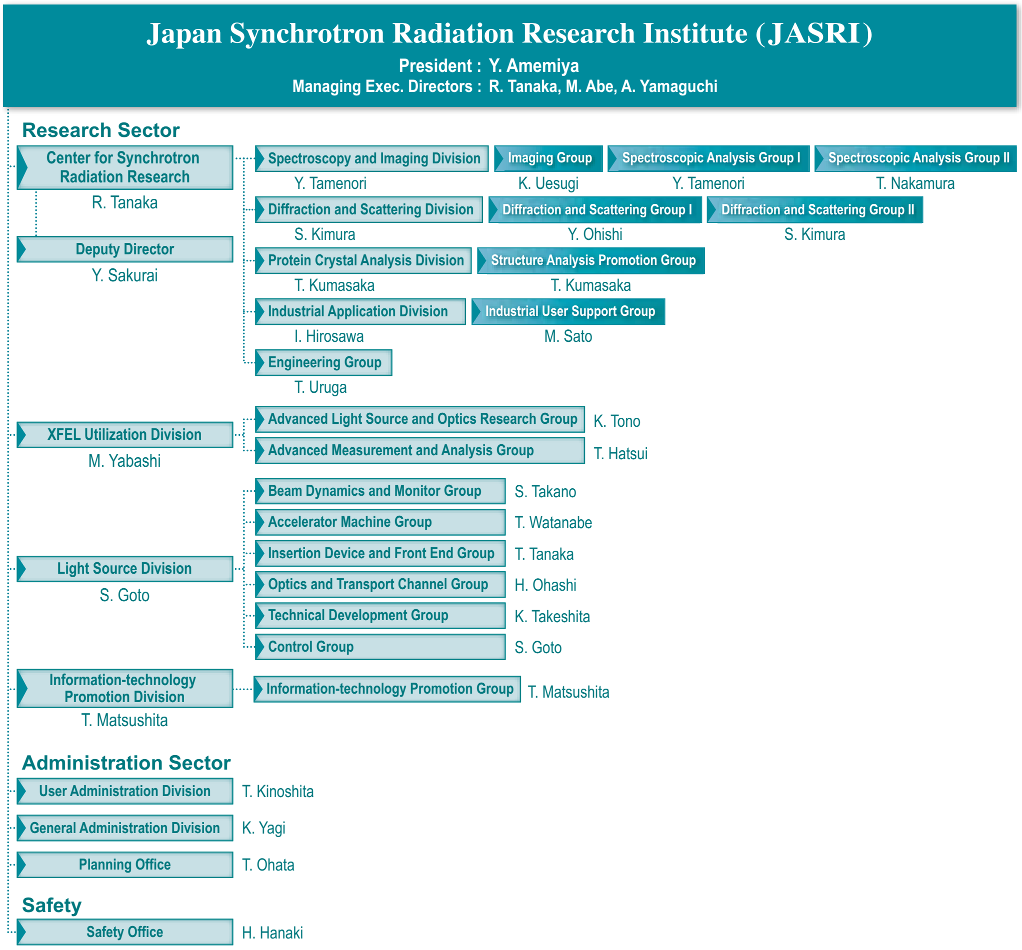

Fig. 18. JASRI chart as of July 2019.

VIII. SPring-8 Users Community (SPRUC)

The SPring-8 Users Community (SPRUC) is a user society that includes not only all users but also potential users who are interested in using SPring-8. In addition to these individuals, representative organizations comprising 26 institutes (principal universities, national/international research institutes, industries, and beamline consortiums) participate in SPRUC to discuss further promotion of the utilization of SPring-8 from strategic and perspective viewpoints.

As one of the key activities of SPRUC, the SPring-8 Symposium is held annually at the site of one of the representing organizations jointly with RIKEN and JASRI. SPring-8 Symposium 2018 with the theme "Starting movements toward the innovative leap of SPring-8" was held at Himeji Civic Auditorium on August 25 and 26. A panel discussion was held to debate this theme. This debate led to a workshop on the upgrade of beamlines toward the SPring-8 upgrade, which was co-hosted by RIKEN, JASRI, and SPRUC in March 2019. The award ceremony of the SPRUC 2018 Young Scientist Award, which was conferred on Dr. Makina Saito, Kyoto University and Dr. Keitaro Yamashita, Tokyo University, was also held. SPring-8 Symposium 2019 is scheduled to be held on August 30 and 31 at 50th Anniversary Hall, Okayama University, jointly hosted by Okayama University.

SPRUC has continued to promote the activities of SPRUC Multidisciplinary Research Groups in order to develop the use of SPring-8 in new research areas that will be important for future science and technology. Two research groups, one for nanodevice science and the other for practical application, have operated actively since their launching in 2015. The nanodevice science research group led by Dr. Teruo Ono, Kyoto University, which is at the end of the midterm of the research period, held a special session to discuss advanced results and future perspectives of spintronics research in JSR2019 (annual meeting of the Japanese Society for Synchrotron Radiation Research, held in January). The practical application research group successfully finished the first term led by Dr. Masatoshi Takao, project officer, and received an ex-post evaluation. The second term of the research project with a two-year research period, led by Dr. Masatoshi Takao as the program officer and Dr. Akihiko Fujiwara as the executive officer, started in the period 2018B.

The 4th-term SPRUC research groups were voluntarily organized in more than 30 research fields, and each research group actively conducted research meetings. For the research meetings, SPRUC supported the travel expenses of lecturers who contributed to promoting intercommunication between research fields. SPRUC supported the SPring-8 Summer School for enhancing users' research competency and also hosted the SPring-8 Autumn School with JASRI to acquire new users. In the latter school, the SPRUC research groups contributed to planning the lectures.

There were three modifications in the SPRUC organizational structure and related rules. One was the founding of SACLA Utilization Committee and its subsidiary organization XFEL Utilization Research Group. This will enhance the collaboration between SPRUC and the SACLA user community, and lead

SPRUC 2018 Young Scientist Award
Prof. Y. Amemiya, Dr. M. Saito, Dr. K. Yamashita, and Prof. J. Mizuki

to the creation of new research fields. The second was the changing of the advisers for the utilization committee to those for the SPRUC chair. This is to strengthen the planning ability in SPRUC steering. The third was the modification of the election rules of the SPRUC chair.

Prof. J. Mizuki
Kwansei Gakuin University
SPRUC Chairman FY2018

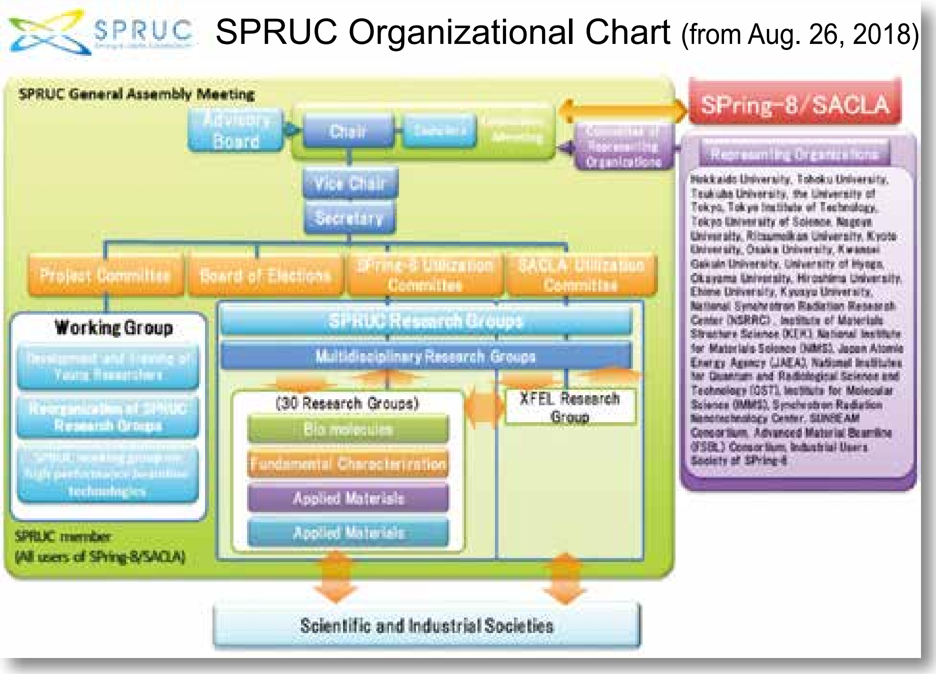

Chart of SPRUC organizational structure reorganized.

IX. Outreach Activities

To find new users in unexplored fields of application, SPring-8 holds various serialized seminars named Workshop on Advanced Techniques and Applications at SPring-8. Here are some representatives.

- 26th SPring-8 as a research tool for the drug delivery system (DDS)
  June 22, 2018 • Nagasaki Brick Hall (Nagasaki)

- 27th Cultural property analysis with SPring-8
  July 7, 2018 • Nara Women's University (Nara)

- 30th Current status and future prospects of protein structural biology research at SPring-8
  August 9-10, 2018 • Osaka University (Osaka)

SACLA

I. Machine Operation & Beamlines

Our seventh year of operations proceeded without any significant issues. Operation statistics are summarized in Table 1. The ratio of downtime to user time was kept below 4%, a reasonably low rate for linac-based light sources.

Table 1. Operation Statistics for FY2018

	Time (h)
Total operation time	6281
User time	
BL1	1224
BL2	1854
BL3	3192
Total	6270
Facility tuning time	672
Downtime	221

In 2012, two beamlines, BL3 for XFEL and BL1 for broadband spontaneous light, were open for users, while all experiments were conducted with BL3. As the newest beamline, construction of BL2 was completed during the summer shutdown of 2014, and first laser amplification was achieved on October 21. An upgraded beamline for soft X-ray FEL, BL1, which combines the prototype accelerator of SACLA (SCSS), started operation in 2016. For more details, please refer to SACLA Beam Performance in this volume.

II. User Program and Statistics

SACLA calls for public user proposals twice per year.

In FY2016, JASRI introduced the proprietary research of General Proposals and the Proprietary Time-Designated Proposals. The project leaders of these proprietary proposals are not required to publish their research results, but required to pay each beamtime fee. In addition, to apply for the proprietary research the project leaders should be affiliated with a corporate enterprise located and registered in Japan.

Table 2, Figs. 1 and 2 provide statistics on proposals, users, and beamtime.

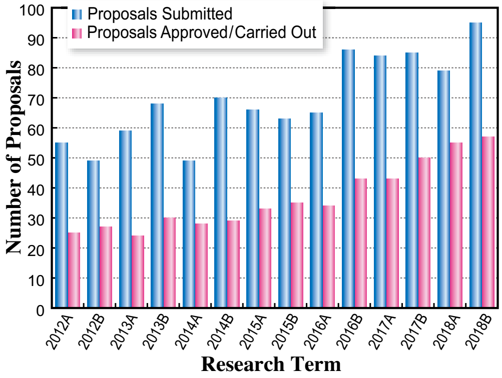

Fig. 1

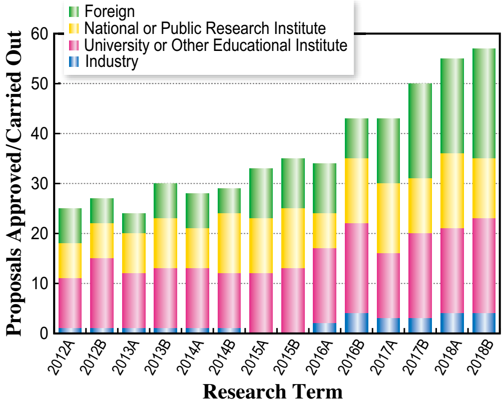

Fig. 2

Table 2. Number of proposals submitted, proposals approved/carried out, cumulative users, and beamtime available by research term

Half-year Research Term	Proposals Submitted	Proposals Approved / Carried Out					Cumulative Users	Beamtime Carried Out (Shifts)
			Priority Strategy Proposals	Non-proprietary	Proprietary			
				General Proposals	General Proposals	Time-Designated Proposals		
2012A	55	25	(12)	(13)	–	–	297	126
2012B	49	27	(19)	(8)	–	–	461	154
2013A	59	24	(15)	(9)	–	–	268	117
2013B	68	30	(19)	(11)	–	–	410	139
2014A	49	28	(20)	(8)	–	–	400	147
2014B	70	29	(17)	(12)	–	–	430	140
2015A	66	33	(23)	(10)	–	–	527	144
2015B	63	35	(23)	(12)	–	–	552	152
2016A	65	34	(21)	(12)	(1)	–	538	158
2016B	86	43	(21)	(20)	(1)	(1)	650	197
2017A	84	43	–	(43)	(0)	(0)	577	210
2017B	85	50	–	(50)	(0)	(0)	642	244
2018A	79	55	–	(55)	(0)	(0)	643	257
2018B	95	57	–	(56)	(0)	(1)	653	264

One shift = 12 hours at SACLA beamlines

Editor
Naoto Yagi
Japan Synchrotron Radiation Research Institute (JASRI)

Editing, Design & Layout
Marcia M. Obuti-Daté
Japan Synchrotron Radiation Research Institute (JASRI)

Printing
Hokuoh Printing Co.

JASRI
Information & Outreach Section
Users Administration Division

1-1-1 Kouto, Sayo-cho, Sayo-gun
Hyogo 679-5198 • JAPAN
Tel: +81-(0)791-58-2785   Fax: +81-(0)791-58-1869

Email: frontiers@spring8.or.jp
http://www.spring8.or.jp/

http://www.spring8.or.jp

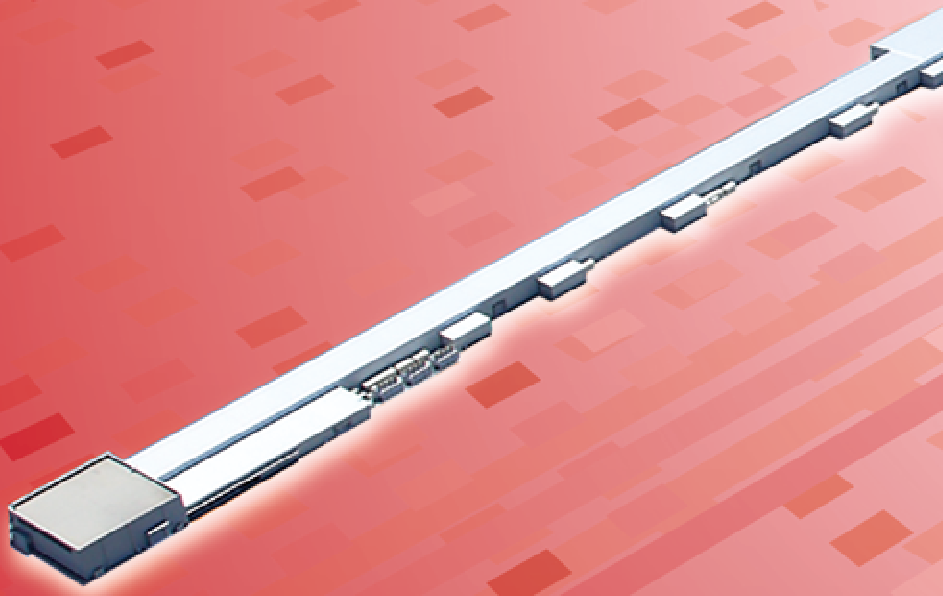

Japan Synchrotron Radiation Research Institute (JASRI)
1-1-1 Kouto, Sayo-cho, Sayo-gun, Hyogo 679-5198, Japan